Acoustic properties of natural materials

Weichun Huang

UNIVERSITE BRETAGNE SCIENCES LOIRE POUR L'INGENIEUR

Le Mans Université

THESE DE DOCTORAT DE

LE MANS UNIVERSITE
COMUE UNIVERSITE BRETAGNE LOIRE

ECOLE DOCTORALE N° 602
Sciences pour l'Ingénieur
Spécialité : *« Acoustique »*

Par
Weichun HUANG

Acoustic Properties of Natural Materials

Thèse présentée et soutenue à LE MANS le 4 décembre 2018
Unité de recherche : Laboratoire d'Acoustique de l'Université du Mans
Thèse N° : 2018LEMA1031

Rapporteurs avant soutenance :

Kirill HOROSHENKOV Professor, University of Sheffield, UK
Yong LI Professor, Tongji University, Chine

Composition du Jury :

Présidente :
Catherine POTEL — Professeur des Universités, LAUM – Le Mans Université
Examinateurs :
Vicente CUTANDA-HENRIQUEZ — Associated Professor, Danmarks Tekniske Universitet, Danmark
Benoit NENNIG — Maître de Conférence, SUPMECA Paris
Invité :
Logan SCHWAN — Post-Doc, LAUM - Le Mans Université

Dir. de thèse : Jean-Philippe GROBY — Chargé de Recherche CNRS, LAUM - Le Mans Université
Co-dir. de thèse : Jean-Michel GÉNEVAUX — Professeur des Universités, LAUM - Le Mans Université
Co-encadrant : Vicent ROMERO-GARCÍA — Chargé de Recherche CNRS, LAUM - Le Mans Université

Académie de Nantes

Le Mans Université

École Doctrorale Sciences pour l'Ingénieur

Doctoral Thesis

by

Weichun Huang

to obtain the degree of

Doctor of Le Mans Université
in Acoustics

Acoustic Properties of Natural Materials

---

defended on

4th December 2018

To the panel composed of

K. Horoshenkov	Professor, University of Sheffield, UK	*Reviewer*
Y. Li	Professor, Tongji University, China	*Reviewer*
C. Potel	Professeur des Universités, Le Mans University	*President*
V. Cutanda-Henriquez	Associate Professor, Danmarks Tekniske Universitet, Danmark	*Examiner*
B. Nennig	Maître de Conférence, SUPMECA Paris	*Examiner*
L. Schwan	Post-Doc, LAUM - Le Mans Université	*Invited*
J.-P. Groby	Chargé de Recherche CNRS, LAUM - Le Mans Université	*Supervisor*
J.-M. Génevaux	Professeur des Universités, LAUM - Le Mans Université	*Co-Supervisor*
V. Romero-García	Chargé de Recherche CNRS, LAUM - Le Mans Université	*Co-advisor*

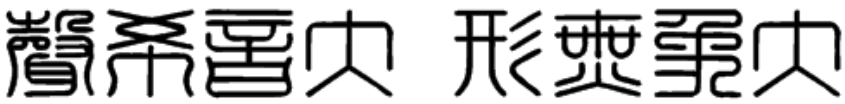

“. . . la grande optique est de la transparence, la grande acoustique est du silence . . . ”

Lao-Tseu

Acknowledgements

It has been a wonderful journey for me, starting in Hangzhou, then to Harbin, and now in Le Mans. And I am never alone on the road ...

First of all, I would like to give my thanks with much respect and admiration to my thesis advisors Jean-Philippe Groby, Vicente Romero-García and Jean-Michel Génevaux for giving me this opportunity to work on such an interesting topic and great projects, and more importantly showing me the true meaning of scientific research.

I would like to express my gratitude to Jean-Philippe Groby, for letting me into the fantastic realm of "Metamaterials" since our first meeting in 2013, and for accompanying me in every step of the way ever since, and most of all in the hardest time of my PhD years.

I would like to give my thanks to Jean-Michel Génevaux, for his special charm in daily life, inspiring me to look for better understanding in the small details, and especially for harvesting the wheat straws used in this project.

I would like to thank Vicente Romero-García, who has taught me a lot by example, with his patience, kindness, and professionalism during these years.

Especially, I want to offer my sincere thanks to my co-authors, Noé Jiménez and Logan Schwan, for sharing with me without reservation their experiences on scientific writing and knowledge on complex media, and for helping me at different stages during Project "Metaudible" and "PavNat".

And special thanks should be given to Thibault Devaux, who introduced me to Jean-Philippe for Master research project.

Equally, I want to express my sincere thanks to the jury members of my PhD defence, for sharing your precious time with me.

I would like to acknowledge Kirill Horoshenkov and Yong Li for having accepted to review this thesis, and giving me crucial opinions on the thesis.

I would also like to acknowledge Catherine Potel, Vicente Cutanda-Henriquez and Benoit Nennig, for having accepted to be the examiners of the defence as well as sharing with me their pertinent opinions on the subject of this thesis.

I am also grateful to Denis Lafarge and again Benoit Nennig, for having helped me as members of my *Commité de Suivi de Thèse*, with useful advises and scientific discussions throughout my doctoral years.

During the last 5 year, LAUM has been my second home. I would like to thank all the members of LAUM, for offering such a great work environment.

A special note goes to the colleagues of *l'Équipe Matériaux* and *l'Axe Métamatériaux*, for sharing their experience, knowledge and insights on acoustic metamaterials and porous materials.

Also, I want to acknowledge all fellow doctoral students of LAUM, for sticking together and encouraging each other, therefore creating a positive ambience.

Moreover, my thanks especially go to the office of "*Le Mans Acoustique*", and to James Blondeau and Stéphane Lebon for helping me with 3D printers and measurement systems.

As an old Chinese proverb says "*Fate pulls friends together no matter how far away*", I want to thank all my friends from different parts of my life.

I would acknowledge my friends and colleagues from both the local and national offices of *Union des Chercheurs et des Étudiants Chinois en France*, for supporting my work in helping fellow Chinese students in need.

I would also acknowledge my friends and classmates from *Licence SPI* and *Master Acoustique*, for the comradeship shared among us, also for helping me with my French.

Most importantly, I shall never forget to mention my comrades from the double diploma program. Together, we went through much hardship and difficulties, helping and caring for each other, since the French class in Harbin, and much more upon our arrival in France in 2011.

Furthermore, I want to pay special tributes to the Professors, Deans and Presidents, of *Harbin Engineering University* and its *College of Underwater Acoustic Engineering*, of *Le Mans Université* and its *Faculté des Sciences et Techniques* who had worked together on the collaboration agreement of the double diploma program between the two universities. Without their efforts, I would have never come to Le Mans, and have the chance of working with such nice people, on such a great project

Last but not least, I want to express my deepest gratitude to my parents Mr Huang Xian-qiang and Ms Song Hua, and to my extended families, friends back home in China, for loving, caring for, and supporting me throughout my long period of study, especially for that I was hardly home, was never able to be helpful at any occasions for the last decade.

Huang Weichun

黄唯纯

List of Figures

Physical Constants

Air density	$\rho_0 = 1.213$ kg.m^{-3}
Atmospheric pressure	$P_0 = 101325$ Pa
Temperature	$T_0 = 273.15$ K
Prandtl number	$\mathrm{Pr} = 0.715$
Dynamic viscosity	$\eta = 1.839 \times 10^{-5}$ Pa.s
Kinematic viscosity	$\mu_v = \eta/\rho_0 = 1.5161 \times 10^{-5}$ m^2.s^{-1}
Heat capacity (constant pressure)	$c_p = 1.005 \times 10^3$ J. kg^{-1}.K^{-1}
Heat capacity (constant volume)	$c_v = 717.8571$ J. kg^{-1}.K^{-1}
Heat capacity ratio (adiabatic)	$\gamma = c_p/c_v = 1.4$
Bulk modulus	$B_0 = \gamma P_0 = 141855$ Pa
Thermal conductivity	$\lambda = 0.0260$ W.m^{-1}.K^{-1}
Thermal viscosity	$\mu_t = \mu_v/\mathrm{Pr} = 2.120 \times 10^{-5}$ m^2.s^{-1}
Sound speed	$c_0 = \sqrt{B_0/\rho_0} = 343.3$ m.s^{-1}

Contents

General Introduction

Noise has been reported as an annoyance since the invention of wheels at the early stage of the human civilisation [1]. In modern Society, noise pollution exponentially increases because of fast population growth, urbanisation, technological developments, and sustained growth in infrastructure, to cite a few. Each of them is a major source of environmental noise [2].

Noise has become one of the most complained problems by the public [3]. Health hazards brought by long-term noise exposure include but not exclude hearing impairment, sleep disturbance, cardiovascular disease, etc. [4]. More importantly, noise annoyance also changes social behaviour, reducing helpfulness and increasing aggressiveness [5]. Occupational noise also reduces productivity and increases the risk for psychiatric illness [6].

To solve the noise problem, acousticians and engineers seek to either reduce the emitting sound level of the sources, which requires further studies on the internal mechanism of noise generation by specific sources (vehicles , rotary machines, etc.), or cut off the sound transmission path, which requires the design of absorbing sound-proofing materials.

Conventionally, porous materials are used for sound absorption and insulation in practice. Acoustic wave propagation in these porous materials is usually modelled through semi-phenomenological fluid models [7–10], considering a rigid-frame approximation. These equivalent fluid models rely on complex and frequency dependent equivalent density and compressibility, which respectively account for the viscous and thermal losses [11].

Among the different regimes considered, the viscous and inertial regimes, which are only related to the viscous losses, are particularly interesting. These two regimes are separated by the viscous-inertial transition frequency, i.e. the Biot frequency f_B. Below f_B, in the viscous regime, the density is mainly imaginary and the pressure field satisfies a diffusion equation [12]. Above f_B, in the inertial regime, the density is mainly real and the pressure field satisfies a Helmholtz equation with losses [13].

The lowest frequency absorption peak of a rigidly backed porous layer corresponds to the so-called quarter-wavelength resonance [9]. The first order Taylor expansion of the numerator of the reflection coefficient of the rigidly backed layer around this quarter-wavelength resonance leads to an optimum in terms of absorption-thickness ratio.

This optimum imposes a purely imaginary value of the effective density and a purely real value of the effective sound speed. In other words, the optimum can only be achieved for a frequency which is slightly above the Biot frequency. Therefore, this translates to two observations. First, rigidly backed porous materials can only absorb sound for wavelength smaller than 4 times their thickness. Second, the perfect absorption of sound can only occur at frequencies higher than the quarter wavelength resonance when the Biot frequency equals to the quarter-wavelength resonance frequency.

Consequently, bulky and heavy structures are required to absorb sound at low frequency. Thicker layer means that the indoor useable surface is further shrunken, and implies much more material consumption. Inversely, this means that the low-frequency sound cannot be efficiently absorbed if the absorbing material thickness is less than the required value.

Furthermore, it is worth mentioning that the most used porous materials for insulation are plastic foam and glass-fibre wool. These two kinds of materials have evident shortcomings. The plastic foam material is a petrol product. Its production is related to pollution and plausible health hazards [14]. Also, the installation of this material, particularly instantaneous foam spray may cause health hazards to workers and to residents as well [14]. The glass-fibre wool material is made of man-made micro-fibres from glass or rock. It has been listed as a carcinogenic agent [15, 16].

In acoustics, a metamaterial is an artificial material, which is composed of resonant scatterers that are arranged in a controlled (or not) pattern (periodic, semi-periodic, or super-uniform). Its performance is extraordinary in terms of wave manipulation, in our case, absorption. These properties should be independent of or drastically different from the acoustic and mechanic properties of the composing elements.

Particularly, for the purpose of sound absorption, an efficient design of acoustic metamaterial should provide one or several of the following features

- low-frequency response: the first absorption peak should appear at a frequency lower than the quarter wavelength resonance of the effective layer;
- high absorption: absorption coefficient should be higher than 90% or perfect, i.e. the structured material should absorb 100% of the impinging energy;
- wide frequency range: broad-band absorption;
- tunable geometry: possible tunability for the targeted frequency range.

In addition, the above goals should be achieved with a material thickness much smaller than that required by a conventional material, for the same or much lower frequency . This feature is also known as the sub-wavelength absorber.

Different designs of acoustic metamaterial for absorption have been conceived over the last years. In principle, we seek to increase the density of the states at low frequencies by the means of localised resonances [17–24]. For example, membrane-type metamaterials can concentrate the sound energy at the edges of the decorated rigid plates [18]. When rigidly backed, this kind of structure can lead to total absorption at very low frequency [19]. Coiled quarter-wavelength resonators are used to design a perfectly absorbing sub-wavelength system [20, 21]. The conventional porous materials can also be improved by introducing resonances and achieve total absorption with rigid backing [22–24], i.e. meta-porous surface.

Moreover, all these studies deal with the interaction of an incoming wave with a lossy open resonant structure, in order to achieve perfect absorption. To do so, the condition of impedance matching with the background field should be fulfilled [25–27]. Another way to achieve impedance matching is the critical coupling condition [28].

These open resonant systems, at their resonant frequency, are characterised by both the leakage rate of energy and the intrinsic losses of the resonator. The balance between the leakage and the losses activates the condition of critical coupling, trapping the energy around the resonant elements and generating a maximum of energy absorption [28–30].

Although most materials with unconventional properties are man-made, the existence of metamaterials in nature has been proven in the fields of optics and electromagnetism [31]. It paves the way to natural metamaterials, as existing meta-structure in nature.

Nevertheless, acoustic metamaterial also has its own disadvantages. Most of the existing designs are very precise, sometimes even to the level of micrometres [32]. This requires either 3D printing or high precision engineering. This constrain usually makes it impossible to realise mass production of metamaterial with low cost, which rather currently limits the application of metamaterial. Moreover, as the structures mentioned above are all artificial, plastic is still the most used material for prototyping.

Therefore, bio-inspired or nature systems are good alternatives to design metamaterials. Different aspects of the natural metamaterial have been investigated. Hierarchical or fractal pattern within biological organisms [33], and bio-inspired metamaterials as artificial materials mimicking natural meta-structure, such as the spider-web inspired hierarchical metamaterial [34] and thermal insulation inspired by polar bear hair [35].

Meanwhile, facing the risks of global warming, many starts to look for eco-friendly sustainable building materials [36], in order to replace petroleum-based plastic foams and carcinogenic vitreous and mineral wool. Commonly studied natural materials include compressed block of biomass [37], straw or reed bale (arranged or random) [38], recycled materials [39], compressed natural fabric [36], vegetations [40].

The acoustic model for these porous media is often empirical, such as the most commonly used Delany & Bazly model [41]. Whereas, more sophisticated models, such as Johnson-Champoux-Allard-Lafarge (JCAL) model [7–10] are less used, unless in the cases of natural fibres [42, 43]. Further study on the subject is therefore needed.

In this manuscript, we will focus on natural metamaterial inspired by straw bale. Straws or more precisely straw-based natural materials, such as wheat, reed or rattan, have been used as building material, or thermal insulation material for thousands of years throughout the world [44]. Some loosely packed straw-bale were tested in laboratory condition for sound transmission losses, along with other civil engineering aspects [45, 46]. In field tests, it has been found out that a timber frame filled with straws can reduce sound level of about 43-60 dB [47, 48].

Moreover, a straw is composed of a stem, which is a cylindrical tube with a fibrous wall, and nodes, which forms the separated segments in the stem [49]. Cross-cut of a straw exposes its inner cavities, also adds gap between them. Contrary to the normal loosely packed natural fibrous material, the straws are normally packed very tightly in a bundle, which leads to a much smaller porosity. Therefore, an idealized straw stack can be seen as an anisotropic porous medium with a highly concentrated periodic arrangement of cylindrical hollow tubes, where the nodes of the straw forms quarter-wavelength resonators. These mentioned features make straw bale a good candidate for the study of acoustic metamaterial for sound absorption.

This manuscript is organised in 3 parts.

In Part I, the basic concepts of the slow sound phenomenon is introduced, through the design of an acoustic metasurface composed of periodic arrangement of slits loaded by quarter-wavelength resonators on one side and saturated by air, see Chapter 1. Then, a similar design with Helmholtz resonators is presented. The critical coupling condition is introduced, along with the associated optimisation techniques. This gives us the basic tool to design optimal absorber with perfect absorption, see Chapter 2.

In Part II, the homogenised problem of a porous medium and its resolution by scale separation are recalled and presented step by step, based on the references [50, 51]. Through the approximation of the JCAL porous material model [7, 10], the frequency independent viscous and thermal parameters are also obtained numerically, see Chapter 3. The theoretical model is further enriched by introducing inner resonances in the homogenised problem [52]. The corresponding dispersion properties are equally studied. The robustness of the theoretical model and numerical computation is tested through impedance tests on various 3D-printed samples, see Chapter 4.

In Part III, we set out to search for optimal configurations of the straw-inspired metamaterial, where a perfect absorption is achieved for a given frequency at normal incidence, see Chapter 5. First, a parametric study on the anisotropic permeable array of solid rigid cylinders is performed. Then, an optimisation process is formulated, which provides several configurations. Impedance tube measurements are performed on 3-D printed samples with controlled parameters to validate the theoretical results. In the end, the anisotropy of this optimal design is studied through different representations of the absorption coefficient in relation to various incident angles and rotational angles of anisotropy, see Chapter 6.

Finally, I conclude and provide further perspectives to the present work.

Part I

Slow Sound based Metasurface

Chapter 1

Slow sound phenomenon

In this first Chapter, we demonstrate the effects of slow sound phenomenon by describing the wave propagation in an impervious periodic structure comprising quarter-wavelength resonators (QWRs), paying attention to the low frequency sound absorption[1]. The array is composed of a periodic arrangement of narrow slits in an imprevious solid block, on one side of which QWRs are drilled in a square lattice. Both modal expansion model and the associated effective parameters are studied. The crucial feature of this structure is the slow sound propagation inside the QWRs-loaded slit. The effects of this phenomenon on the various theoretical components of the physical model are closely studied, which pave the way to the various designs of the following chapters.

Contents

[1]Part of the work described in this Chapter is published in the peer-reviewed article: Groby, J. P., **Huang, W.**, Lardeau, A., and Aurégan, Y. (2015). "*The use of slow waves to design simple sound absorbing materials*". Journal of Applied Physics, 117(12), 124903.

Introduction

Slow wave propagation was first studied in optics, where the light speed was reduced 20 million times to 17 meter per second by introducing an electro-magnetically induced transparency (EIT) band in an ultra-cold gas of sodium atoms [53].

A rapid change transmission profile and associated refractive index are obtained around the resonance frequency of the laser beam. Along with the high density of the ultra-cold sodium gas, the strong dispersion of the system results in extremely slow group velocity of waves whose frequency is centred around a narrow transmission band.

Hereafter, a direct analogy of the EIT band can be realised in acoustics. The phenomenon of acoustic transparency and slow sound propagation was investigated with a pipe loaded with detuned Helmholtz resonators, separated by a sub-wavelength distance [54]. In general, the slow sound phenomenon appears for frequencies below the band gap which is associated with resonator resonance. The inherent dissipation introduced by the loaded resonators gives rise to high dispersion, which results in slow group velocity and high attenuation within the band gap.

Moreover, the slow sound phenomenon opens promising perspective to design sub-wavelength metamaterial that can induce better absorption than conventional sound absorbing material, especially at lower frequencies. That is to say large absorption is achieved for wavelength much larger than four times of the thickness of the rigidly backed structure.

Other similar designs also use tuned or detuned resonators separated by half of the wavelength, giving rise to a coupling between the resonators and the Bragg band-gap [55]. The dissipation effects of the slow sound was discussed by investigating sound propagation in lossy, locally resonant periodic structures by studying an air-filled tube periodically loaded with Helmholtz resonators [56].

It is equally discovered that the slow sound can be achieved by a waveguide in a sonic crystal, a periodic array of solid scatters in a waveguide [57, 58]. In the field of aeroacoustics, it was shown that slow sound can be obtained in low Mach number flow by using reacting liners, reducing sound speed and enhancing the interaction between the acoustic propagation and the mean flow [59, 60].

The objective of this chapter is to demonstrate the various effects brought by the slow sound phenomenon. These effects are then efficiently employed to design an acoustic metamaterial that is capable of strong absorption at low frequencies. Both modal expansion method (MEM) and the associated effective parameters method (EPM) are employed in the process.

1.1 General description

1.1.1 Unit cell description

A unit cell of the 3D scattering problem together with a sketch of one internal face of the narrow slit are shown in Fig. 1.1. Before the addition of the QWRs (QWRs), the unit cell is composed of N identical irregularities of width w and height L occupied by a material M^s modeled as a slit, i.e., the viscous and thermal losses at each lateral boundaries are accounted for.

The left and right flat and mutually parallel boundaries of the structure, whose x_2 coordinates are L and 0, are designated by $\Gamma_{x_2=L}$ and $\Gamma_{x_2=0}$ respectively. The left semi-infinite material M^a, i.e., the ambient fluid that occupies Ω^a, and M^s are in a firm contact at the boundaries $\Gamma^{(n)}_{x_2=L}$, $\forall n \in \mathcal{N}$, meaning that the pressure and normal velocity are continuous across $\Gamma^{(n)}_{x_2=L}$. The thermal losses are neglected on Γ_0 and the end of the QWRs and a Neumann type boundary condition is applied on these boundaries, i.e., the normal velocity vanishes on Γ_0 and the end of the QWRs.

The n-th slit is located at $x_1 = d^{(n)}$, which refers to the slit boundary on which a Neumann type boundary condition is applied, i.e., the interface Γ_N. A periodic set of r in radii QWRs of length l are plugged on one lateral face of the slit with a square lattice of size a in the x_2-x_3 plane, see Fig. 1.1b). The material M^t that occupies each tube Ω^t is modeled as a circular tube and is in firm contact with M^s through Γ_t, i.e., the pressure and normal velocity are continuous across Γ_t.

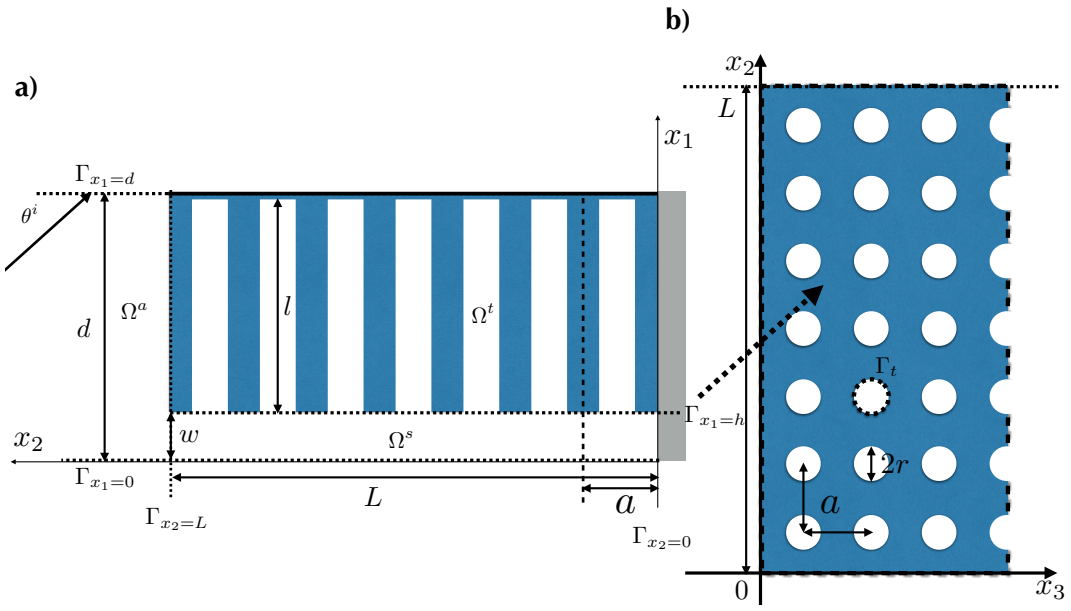

FIGURE 1.1: 2D representation of the unit cell in the periodic structure in $x_1 - x_2$ plane: a) Slit with upper wall loaded with QWRs on the surface $\Gamma_{x_1=h}$, b) Partial view of $\Gamma_{x_1=h}$.

1.1.2 Governing equations

The incident wave propagates in Ω^a and is expressed by $p^i(\mathbf{x}) = A^i e^{\mathrm{i}(k_1^i x_1 - k_2^{ai}(x_2 - L))}$, wherein $k_1^i = -k^a \sin\theta^i$, $k_2^{ai} = k^a \cos\theta^i$ and $A^i = A^i(\omega)$ is the signal spectrum. The system is set in the $e^{\mathrm{i}\omega t}$ time convention.

In each domain Ω^α ($\alpha = a, s, t$), the pressure field fulfils the Helmholtz equation

$$\mathrm{div}\left(\frac{1}{\rho^\alpha}\mathbf{grad} p^\alpha\right) + \frac{(k^\alpha)^2}{\rho^\alpha} p^\alpha = 0, \tag{1.1.1}$$

with the density ρ^α and the wavenumber $k^\alpha = \omega/c^\alpha$, defined as the ratio between the angular frequency ω and the sound speed $c^\alpha = \sqrt{K^\alpha/\rho^\alpha}$.

As the problem is periodic and the excitation is due to a plane wave, each field (X) satisfies the Floquet-Bloch relation

$$X(\mathbf{x} + \mathbf{d}) = X(\mathbf{x}) e^{\mathrm{i}k_1^i d}. \tag{1.1.2}$$

Consequently, it suffices to examine the field in the elementary cell of the material to get the fields, via the Floquet relation, in the other cells.

1.1.3 Viscous-thermal losses

The viscous and thermal losses in the slits $\Omega_1 s$ and the circular tubes Ω^t forming the QWRs are accounted for by considering a plane wave propagation [11, 61].

When only plane waves propagate in a slit of width w , the equivalent complex and frequency-dependent density and bulk modulus are [61]:

$$B^s = \frac{\gamma P_0}{1 + (\gamma - 1)\tanh\left(\frac{w}{2}\sqrt{-\mathrm{i}\rho_0 \mathrm{Pr}\omega/\eta}\right) / \left(\frac{w}{2}\sqrt{-\mathrm{i}\rho_0 \mathrm{Pr}\omega/\eta}\right)}\ , \tag{1.1.3a}$$

$$\rho^s = \frac{\rho_0}{1 - \tanh\left(\frac{w}{2}\sqrt{-\mathrm{i}\rho_0 \omega/\eta}\right) / \left(\frac{w}{2}\sqrt{-\mathrm{i}\rho_0 \omega/\eta}\right)}\ , \tag{1.1.3b}$$

where γ is the specific heat ratio, P_0 the atmospheric pressure, Pr the Prandtl number, η the dynamic viscosity, and ρ_0 the density of the saturating fluid[2].

When only plane waves propagate in a circular tube of radius r, the equivalent complex and frequency depend densities and bulk modulus are [61]:

$$B^t = \frac{\gamma P_0}{1 + 2\,(\gamma - 1) / \sqrt{-\mathrm{i}\rho_0 \mathrm{Pr}\omega/\eta}\, \mathrm{J}_1\left(r\sqrt{-\mathrm{i}\rho_0 \mathrm{Pr}\omega/\eta}\right) / r\mathrm{J}_0\left(r\sqrt{-\mathrm{i}\rho_0 \mathrm{Pr}\omega/\eta}\right)}, \tag{1.1.4a}$$

$$\rho^t = \frac{\rho_0}{1 - 2/\sqrt{-\mathrm{i}\rho_0 \omega/\eta}\, \mathrm{J}_1\left(r\sqrt{-\mathrm{i}\rho_0 \omega/\eta}\right) / r\mathrm{J}_0\left(r\sqrt{-\mathrm{i}\rho_0 \omega/\eta}\right)}\ , \tag{1.1.4b}$$

where J_n is the Bessel function of n-th order.

[2] The numerical values of the constants in use are listed in the Table of constants in the front matter

1.1.4 Surface impedance

The thermal losses are neglected on the end of the QWRs and a Neumann type boundary condition is applied on these boundaries, i.e., the normal velocity vanishes on the end of the QWRs. The first conditions on Γ_t will be reduced to an impedance condition applied on the whole interface $\Gamma_{x_1=h}$ in the following, because the considered wavelength are much larger than the dimensions of Γ_t and the periodicity of this arrangement a inside the slit. This impedance, which already accounts for the material propagation and losses in the tubes, and for the conditions on Γ_t and the end of the QWRs reads as [62]:

$$Z^{\pm} = \pm \mathrm{i} Z^t \mathrm{cotan}\left(k^t l\right)/\phi^t, \tag{1.1.5}$$

wherein $Z^t = \sqrt{\rho^t B^t}$ is the impedance of M^t, k^t is the wavenumber inside the tube, and ϕ^t is the ratio between the area of Γ_t over the one of the unit cell, i.e., a surface porosity $\phi^t = \pi r^2/a^2$. The sign $\pm$ depends on whether the tubes are plugged on the top (+ sign) or bottom (− sign) side of the slit. In what follows, only the positive sign will be used and $Z = Z^+$. The problem therefore reduces to a 2D one. The impedance condition does not account for losses on the rigid portion of $\Gamma_{x_1=h}$, i.e., $\Gamma_{x_1=h} \backslash \Gamma_t$, while use of Eq. (1.1.3) accounts for losses on a fully rigid boundary. The combination of Eq. (1.1.3) and the application of this impedance condition is also valid under the hypothesis of small ϕ^t. This hypothesis is usually accepted when dealing with dissipation in ducts with resonators [56, 63].

1.2 Modal expansion model

1.2.1 Field representations

Separation of variables, radiation conditions, and Floquet theorem lead to the representations:

$$p^a(\mathbf{x}) = \sum_{q\in\mathbb{Z}} \left[A^i e^{-\mathrm{i}k^a_{2q}(x_2-L)}\delta_{0q} + R_q e^{\mathrm{i}k^a_{2q}(x_2-L)} \right] e^{\mathrm{i}k^a_{1q}x_1},\ \forall \mathbf{x}\in\Omega^a\ , \tag{1.2.1}$$

wherein δ_{0q} is the Kronecker symbol, $k^a_{1q} = k^i_1 + \dfrac{2q\pi}{d}$, and $k^a_{2q} = \sqrt{(k^a)^2 - (k^a_{1q})^2}$, with $\mathrm{Re}\left(k^a_{2q}\right) \geq 0$ and $\mathrm{Im}\left(k^a_{2q}\right) \geq 0$. The reflection coefficient of the Bloch wave denoted by the subscripts q is R_q.

According to Ref. [64], the pressure field $p^{s(n)}$, admits the pseudo-modal representation, that already accounts for the boundary conditions on Γ_0, Γ_N and $\Gamma_{x_1=h}$:

$$p^{s(n)} = \sum_{m\in\mathbb{N}} A_n \cos\left(k^s_{1m}\left(x_1 - d^{(n)}\right)\right)\cos\left(k^s_{2m}x_2\right)\forall \mathbf{x}\in\Omega^{s(n)}\ , \tag{1.2.2}$$

wherein A_n are the coefficients of the pseudo modal representation, $k^s_{2m} = \sqrt{(k^s)^2 - (k^s_{1m})^2}$, with $\mathrm{Re}\left(k^s_{2m}\right) \geq 0$ and $\mathrm{Im}\left(k^s_{2m}\right) \geq 0$, and k^s_{1m} is the m-th solution of the dispersion relation and satisfies:

$$k^s_{1m}\tan\left(k^s_{1m}w\right) = \frac{-\mathrm{i}\omega\rho^s}{Z}. \tag{1.2.3}$$

This last equation is solved by use of a Muller's algorithm [65] initiated with the low frequency approximations

$$\tilde{k}^s_{10} = \sqrt{-\mathrm{i}\omega\rho^s w/Z}/w, \text{ and } \tilde{k}^s_{1m} = m\pi\left(1 + \sqrt{1 - 4\mathrm{i}\omega\rho^s w/Z(m\pi)^2}\right)/2w. \tag{1.2.4}$$

These modes are said bi-orthogonal and the bi-orthogonality relation reads as

$$\int_0^w \cos\left(k_{1m}^s x_1\right)\cos\left(k_{1M}^s x_1\right)dx_1 = \delta_{Mm} w\left(1+\operatorname{sinc}\left(2k_{1m}^s h\right)\right)/2 = \delta_{Mm} w N_m. \quad (1.2.5)$$

1.2.2 The linear system for the solution of R_q

The application of the boundary conditions on each interface $\Gamma_{x_2=L}^{(n)}$ lead to two set of coupled equations in terms of $A_m^{(n)}$ and R_q: the continuity of the pressure field is projected on each Bloch mode (making use of the orthogonality of these modes), while the continuity of the normal component of the velocity is projected on the mode of the slit (making use of the bi-orthogonality relation in Eq. (1.2.5)).

The combination of these two set of equations leads to the solution either in terms of R_q or in term of A_m, these two solutions being linked one with each other. In particular, the linear system of equations for the solution for R_q, $\forall q \in \mathbb{Z}$, is

$$R_q - \frac{\mathrm{i}\rho^a}{k_{2q}^a}\sum_{Q\in\mathbb{Z}} R_Q \sum_{n\in\mathcal{N}}\sum_{m\in\mathbb{Z}} \frac{k_{2m}^s \phi^{s(n)}}{\rho^s N_m}\tan\left(k_{2m}^s L\right) I_{mq}^{l/r(n)-} I_{mQ}^{l/r(n)+} =$$
$$A^i\delta_q + A^i \sum_{n\in\mathcal{N}}\sum_{m\in\mathbb{Z}} \frac{\mathrm{i}\rho^a k_{2m}^s \phi^{s(n)}}{k_{2q}^a \rho^s N_m}\tan\left(k_{2m}^s L\right) I_{mq}^{(n)-} I_{mQ}^{(n)+}\ , \quad (1.2.6)$$

where $\phi^{s(n)} = h/d$ is the surface porosity of one slit, such that $\bigcup_{n\in\mathcal{N}} \phi^{s(n)} = \phi^s$ is the global surface porosity of the structure, and

$$I_{mq}^{(n)\pm} = \frac{e^{\pm \mathrm{i}k_{1q}^a\left(d^{(n)}-\frac{w}{2}\right)}}{2}\left[e^{\mathrm{i}k_{1m}^s\frac{w}{2}}\operatorname{sinc}\left(\left(k_{1m}^s \pm k_{1q}^a\right)\frac{w}{2}\right) + e^{-\mathrm{i}k_{1m}^s\frac{w}{2}}\operatorname{sinc}\left(\left(k_{1m}^s \mp k_{1q}^a\right)\frac{w}{2}\right)\right], \quad (1.2.7)$$

when the impedance condition is applied on the right side of the n-th slit and

$$I_{mq}^{(n)\pm} = \frac{e^{\pm \mathrm{i}k_{1q}^a\left(d^{(n)}+\frac{w}{2}\right)}}{2}\left[e^{-\mathrm{i}k_{1m}^s\frac{w}{2}}\operatorname{sinc}\left(\left(k_{1m}^s \pm k_{1q}^a\right)\frac{w}{2}\right) + e^{\mathrm{i}k_{1m}^s\frac{w}{2}}\operatorname{sinc}\left(\left(k_{1m}^s \mp k_{1q}^a\right)\frac{w}{2}\right)\right], \quad (1.2.8)$$

when the impedance condition is applied on the left side of the n-th slit.

The system Eq. (2.5.4) is solved for each q and each m. The absorption coefficient A is then calculated through

$$A = 1 - \sum_{q\in\mathbb{Z}} \frac{\operatorname{Re}\left(k_{2q}^a\right)}{k_2^a}\|R_q\|^2. \quad (1.2.9)$$

1.3 Derivation of the effective parameters model

Assuming the unique propagation of the mode $m = 0$ in the slits and $k_{10}^s w << 1$, $N_0 \approx 1$. The assumption that the frequency is much lower than the Wood anomaly frequency, which corresponds to $k_{1q}^a = k^a$ when $q = \pm 1$, i.e., when only the specularly reflected wave propagates, is not sufficient to derive effective parameters because of the terms $I_{0q}^{(n)\pm}$ in

Eq. (1.2.6). To do so, the condition $\left(k_{10}^s \pm k_{1q}^a\right) w/2 >> 1$, $\forall q \neq 0$ should be imposed.

This condition ensures that only the term $q = 0$ does not vanish and that $I_{00^{(n)\pm}} = 1$. It implicitly means that the position of slits $d^{(n)}$ as well as the side of the slit on which the impedance condition is applied, either on the right or the left of the slit, does not affect the effective parameters. In other words, it means that different structure of different periodicity can have identical effective parameters.

This last condition is more restrictive than the first one, because it also ensures that the higher order Bloch modes, which are only related to the arrangement of the slits, do not contribute to the field, while $q\pi/d$ is always very large. This condition is often forgotten by the porous material community, which mainly focuses on the propagation inside the pores, a few on their arrangement, but never on the possible contribution of evanescent waves.

Effectively, the macroscopic description of the propagation inside the slit is subjected to $k_1^s w << 1$, $k^t r << 1$, and $k_{20}^s a << 1$. The macroscopic description of the propagation inside the material is also subjected to $\left(k_1^s \pm k_{1q}^a\right) w/2 \ll 1$, $\forall q \neq 0$. In the frequency range, where the condition $k_{1q}^a < k^a$ when $q = \pm 1$ is satisfied, but the condition $\left(k_{10}^s \pm k_{1q}^a\right) w/2 \ll 1$, $\forall q \neq 0$ is not satisfied, the higher order Bloch modes do not propagate but can contribute significantly to the field and so to the properties of the material. This is due to the large dispersion of k_{10}^s close to the resonance frequency of the resonators, which shifts the sinc function windowing and could make $I_{0q^{(n)\pm}}$ large for $q \neq 0$. The contribution of these evanescent waves, which are localised close to the interface of the material can nevertheless be accounted for through Drude transition layers [66, 67].

When $\left(k_{10}^s \pm k_{1q}^a\right) w/2 \ll 1$, $\forall q \neq 0$, the system Eq. (1.2.6) reduces to the unique calculation of R_0, which reads as

$$R_0 = A^i \frac{\mathrm{i}\omega\rho^s \cot\left(k_{20}^s L\right)/k_{20}^s\phi^s - Z_0/\sin\theta^i}{\mathrm{i}\omega\rho^s \cot\left(k_{20}^s L\right)/k_{20}^s\phi^s + Z_0/\sin\theta^i}. \tag{1.3.1}$$

A simple identification with the classical formula of the reflection coefficient of a rigidly backed homogeneous slab leads to a surface impedance

$$Z = \mathrm{i}\omega\rho^s \cot\left(k_{20}^s L\right)/k_{20}^s\phi^s. \tag{1.3.2}$$

This impedance does not depend on the angle of incidence. Sound propagation in each slit depends only on the pressure of air above the slit, and the material is a locally reacting material [9]. Another simple identification leads to $Z_{eff} = \omega\rho^s/\tilde{k}_2^s\phi^s$ and $k_{eff} = \tilde{k}_2^s$, where we make use of equations (1.1.5) and (1.2.4), the validity of these expressions being ensured.

The effective density ($\rho_{eff} = Z_{eff}k_{eff}/\omega$) and bulk modulus ($B_{eff} = \omega Z_{eff}/k_{eff}$) of this locally reacting material would read as

$$\rho_{eff} = \rho^s/\phi^s,\ B_{eff} = B^s/\phi^s\left(1 + Z^s\phi^t \tan\left(k^t l\right)/Z^t k^s w\right). \tag{1.3.3}$$

Nevertheless, these formula are derived accounting for the unique porosity of the slit and not for the porosity of the whole structure. Doing so, the effective density and bulk

modulus of this locally reacting material read as

$$\begin{aligned} \rho_{eff} &= \frac{\rho^s \left(1+\phi^t l/w\right)}{\phi^{tot}} \ , \\ B_{eff} &= \frac{B^s \left(1+\phi^t l/w\right)}{\phi^{tot}\left(1+Z^s\phi^t \tan\left(k^t l\right)/Z^t k^s w\right)} \ , \end{aligned} \tag{1.3.4}$$

where ϕ^{tot} is the porosity of the whole structure and $\alpha_\infty = \left(1+\phi^t l/w\right) = \phi^{tot}/\phi^s$ is a tortuosity-like parameter. In this last case, $\lim_{\omega\to 0} B_{eff} = P_0$, which is the usual value limit of the bulk modulus in the classical porous material representation. These effective parameters are independent on wave propagation direction and structure thickness. The effective density and bulk modulus in the slits are $\rho^s_{eff} = \rho_{eff}\phi^{tot} = \rho^s\left(1+\phi^t l/w\right)$ and $B^s_{eff} = B_{eff}\phi^{tot}$, i.e., a unusual tortuosity is introduced and the effective bulk modulus is modified. The addition of the periodic set of resonators acts on the thermal losses and introduces an unusual tortuosity, which acts on the density of the slit and not on a mixture of the densities of the slit and of tubes. To be convinced of the influence of the thermal losses, the assumption $k^t l << 1$ leads to $B^s_{eff} = B^s\left(1+\phi^t l/w\right)/\left(1+\phi^t B^s l/wB^t\right)$, which only depends on the effective bulk modulus in the tube and the slit and so on the thermal losses.

1.4 Dispersion properties

In order to show the slow sound effect in our system, we study various aspects of the dispersion relation of the configuration presented below.

For numerical application, a configuration is set as $h = 2$ mm, $r = 2.5$ mm, $\ell = 40$ mm, $a = 7$ mm, and $d = 42$ mm. That leads to the surface porosity $\phi^t \approx 0.4$, and the resonance frequency of the loading tubes $f_\ell = c_0/4\ell$ at 2144 Hz .

Figure 1.2a) represents the normalised real and imaginary part of the effective bulk modulus as well as their approximation normalised by P_0/ϕ^{tot}. A particular feature of the real part of the effective modulus in the slit is that it becomes negative on the frequencies of the band-gap associated with the resonance of the resonators. This is in accordance with previous results obtained in case of Helmholtz resonators [52, 68].

Figure 1.2b) shows the effective density normalised by ρ_0/ϕ^{tot}. An interesting feature of the real part of the density is its particularly large value, which is due to a particularly large tortuosity-like effect only acting on the density of the slit. Imaginary part of both effective parameters are in accordance with the causality condition [67], with $\mathrm{Im}\left(B_{eff}\right) < 0$ and $\mathrm{Im}\left(\rho_{eff}\right) > 0$.

Figure 1.3 shows the real part of solution of the dispersion relation Eq. (2.5.3) both in lossy and lossless cases, along with the low frequency approximation $\tilde{k}^{(1)}_{10} h \ll 1$, given in Eq. (1.2.4). The real part of the normalised characteristic wavenumber $k^s w$ in Ω^s is also plotted.

In the lossless case, $\rho^s = \rho^t = \rho^a = \rho_0$ and $B^s = B^t = B^a = B_0$, the 1-st order mode possesses a cut-off frequency with an infinite branch when $\mathrm{cotan}(k^t\ell) = \mathrm{cotan}(k^a\ell) \to 0$.

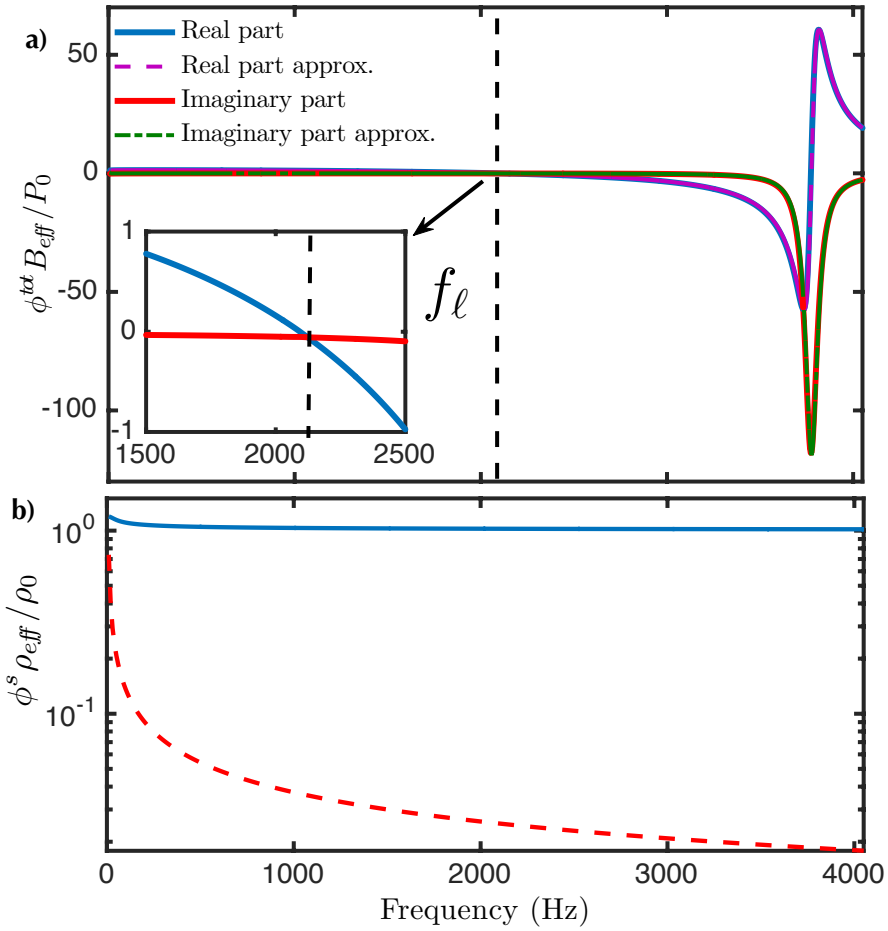

FIGURE 1.2: Effective properties of the structure: a) Normalised real and imaginary part of the effective bulk modulus (solid curves) as well as their approximation (dashed curves) in Eq. (1.3.4). Zoom-in view around the tube resonance frequency f_l (black dashed line); b) Normalised real (in blue) and imaginary (in red) part of the effective density.

Meanwhile in the lossy case, and for small values of w, only the fundamental mode $\tilde{k}^s_{10}$ leads to propagative waves. This mode is close to a propagative plane mode, as $\tilde{k}^s_{10} h \ll \pi$. This fact together with the small value of ϕ^t ensure the validity of the combination of Eq. (1.1.3) with the application of the impedance condition.

The structure possesses a band-gap associated with the resonance of the QWRs. Because of the losses, the band-gap definition and bounds are not clear here. Nevertheless, it corresponds to $\tilde{k}^s_{10} = k^s$, i.e., $\tan k^t l = -k^s h Z^t / Z^s \phi^t$.

To determine the low and high frequency bounds of the band-gap. First, we assume that all properties of the materials are frequency independent and real. Thus, the low frequency bound corresponds to the first sign change of $\tan(k^t \ell)$, i.e., $f_\ell \approx c^t/4\ell$. And the high frequency bound corresponds to $\tan(k^t \ell) \approx k^t \ell - \pi$, i.e., $f_h = 1/\left(2(\ell/c^t + h Z^t / c^{(1)} Z^s \phi^t)\right)$.

Now, we reconsider that the material properties are frequency dependent. The two frequency bounds can be determined by the intersection of the real part of $\tan(k^t \ell)$ with frequency axe, i.e., $\mathrm{Re}[\tan(k^t \ell)] = 0$. This leads to $f_\ell \approx 2080$ Hz and $f_h \approx 3890$ Hz,

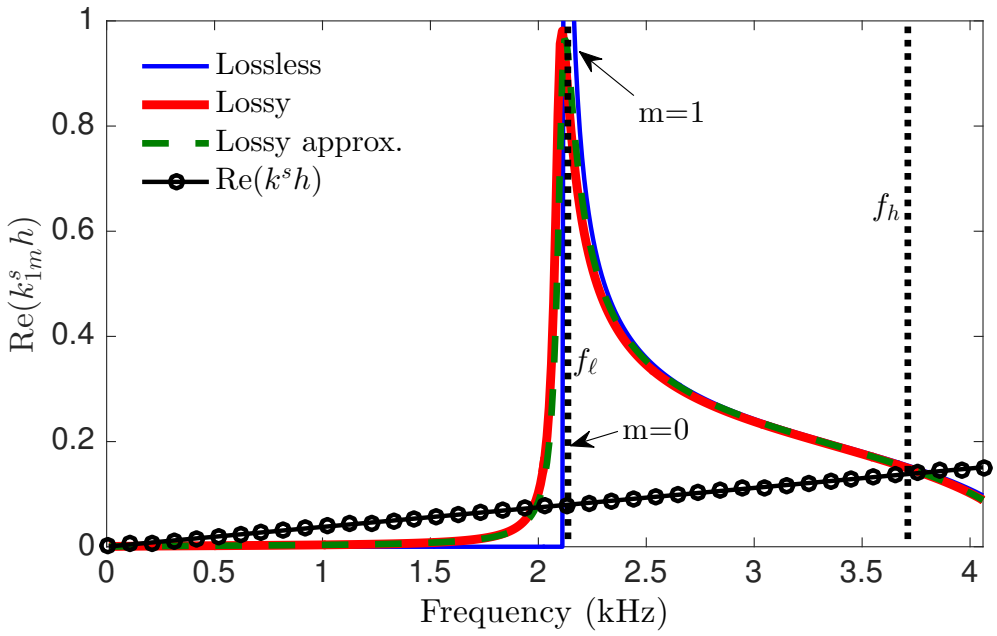

FIGURE 1.3: Real part of the wavenumbers in Ω^s: $k^{(1)}_{1m} w$, without and with losses, as well as $\tilde{k}^s_{10} w$, characteristic wavenumber $k^s w$, along with the position of both bounds of the band-gap f_l and f_h.

whose value highlight the difficult determination of the band-gap bounds in the lossy case and with dispersion.

While f_ℓ corresponds to the quarter-wavelength frequency of the tubes, f_h also depends on various parameters among which the dimensions and mechanical parameters of the slit. This explains why f_h is that affected when compared to f_ℓ by the flow in duct experiments for example [59].

Figure 1.4 gives out real and imaginary part of k^s_2 in the slit along the x_2 direction, parallel to $\Gamma_{x_1=h}$, normalised respectively.

The normalised imaginary part of k^s_{20} corresponds to the attenuation factor inside Ω^s. It has a huge peak within the band gap $[f_l, f_h]$. which represents high attenuation within the band-gap inside the slit.

The relation between dimensions of the structure and the attenuation is shown by the low frequency limit of $\mathrm{Im}(k^s_{20})$, which is obtained by the asymptotic expansion of the wavenumber derived from Eq. (1.3.4) at $k^t \ell \ll 1$:

$$\lim_{k^t \ell \ll 1} \mathrm{Im}\left(\tilde{k}^s_{20}\right) = \mathrm{Im}\left(k^s \sqrt{1 + \phi^t \ell Z^s c^s / h Z^t c^t}\right), \tag{1.4.1}$$

which clearly show that the attenuation increases with the ratio $\phi^t l/h$. To ensure high attenuation, the ratio $\phi^t \ell/h$ should be large.

Also, the slope of the curve for $\mathrm{Re}(k^s_2)$ is smaller than that of the case without QWRs and that of the ambient air case before f_l. Inside the band-gap, the value of the slope tends to zero. All in all, this implies that the wave propagates in the slits with a sound

speed much lower than $c^s \leq c^a$.

Four zones are exhibited:

1. At frequency close to 0, sound speed vanishes because of the viscous regime;
2. Below f_ℓ, the sound speed is much smaller than the speed of sound in the air and in the slit in absence of tubes, i.e., subsonic regime;
3. Inside the band-gap $[f_\ell, f_h]$, the real part of the sound speed vanishes;
4. Above f_h, the sound speed is higher than the air speed of sound, i.e., supersonic regime.

Notice that again the band-gap does not seem to have the same bounds as before, because of the losses and dispersion.

Furthermore, Figure 1.5 depicts the real part of the sound speed of the wave traveling in the slit, $\mathrm{Re}(\omega/k_{20}^{(1)})$, and the sound speed of air c^a, and the effective sound speed in the slit without QWRs, $\mathrm{Re}\,(c^s) = \mathrm{Re}(\sqrt{B^s/\rho^s})$.

Below f_ℓ, the sound speed possesses a plateau at low frequency and slowly decreases to a value close to zero at f_l. The value of this plateau can be approximated ($k^t\ell \ll 1$) by the low frequency limit of c_2^s, shown in Fig. 1.5,

$$\lim_{k^t\ell \ll 1} c_2^s = \mathrm{Re}\left(c^s / \sqrt{1 + \frac{Z^s c^s}{Z^t c^t} \cdot \frac{\phi^t \ell}{h}} \right), \tag{1.4.2}$$

which clearly shows that the speed of sound in the slit is always smaller than the ambient sound speed c^a and decreases when the ratio $\phi^t\ell/h$ increases.

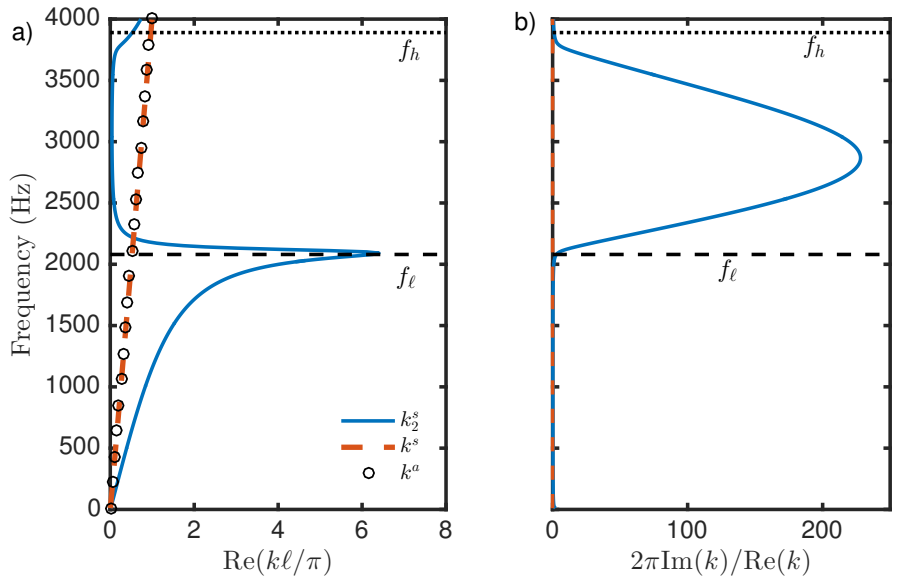

FIGURE 1.4: Wavenumber in x_2 direction: a) Real part of k_2^s (—), k^s (−−) and $k^a = k_0$ (o) normalised by π/ℓ; b) Imaginary part of k_2^s (—), k^s (−−), normalised by its respective real part $\mathrm{Re}(k)/2\pi$ (f_l: black dashed), f_h: black dotted).

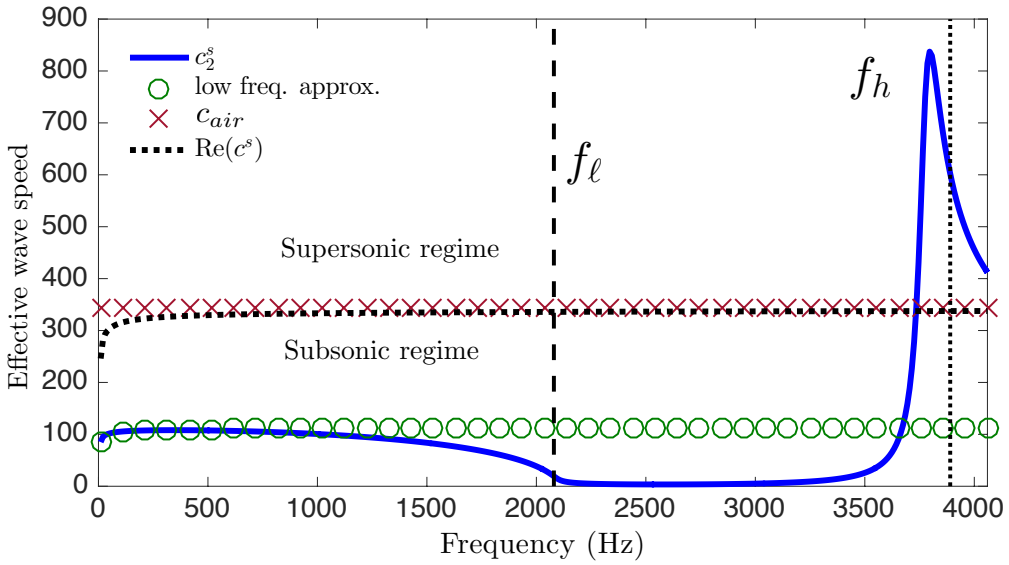

FIGURE 1.5: Effective wave speed: Real part of the effective sound speed in x_2 direction, $\mathrm{Re}(c_2^s)$ (—), as well as the ambient sound speed c_{air} (×) and $\mathrm{Re}\,(c^s)$ (· · ·). The asymptotic low frequency limit of c_2^s is also plotted (O). And band gap bounds f_ℓ (black dashed line), f_h (black dotted line)

The supersonic regime was already noticed in Ref. [52] over a small frequency range just after Helmholtz resonance. Meanwhile the subsonic regime seems normal for an effective porous medium. As the sound propagation goes through a porous media, the value of the acoustic wave speed is always smaller than that of the air [9]. But the extreme low wave speed cannot be explained simply by the porous material theory, but by the slow sound phenomenon. Without losses, the limit in Eq. (1.4.2) reduces to $c^a/\sqrt{1+\phi^t\ell/h}$, which clearly shows that the speed of sound in the slit is always smaller than c^a and decreases when the ratio $\phi^t\ell/h$ increases.

1.5 Results and discussion

The infinite sums in the linear system Eq. (1.2.6) are truncated at M and Q. The goal is to design a material that achieve high absorption at low frequency. Low frequency means: for a wavelength in the air larger than four times the thickness of the structure, where only one reflected Bloch wave is propagating. The high frequency bound can be approximated by the frequency where the Wood's anomaly happens [69].

In this case, the high absorption is only associated with the quarter-wavelength resonance of the slits. Contrary to the one usually encountered for regular porous material and associated with interference phenomena, this quarter-wavelength resonance is a real resonance of the slits.

For fixed ratio $\phi l/w$, Figure 1.5 shows that the sound speed decreases from a plateau, while the attenuation $\mathrm{Im}\,(k_2^s)$ increases with frequency below the bandgap. This means that the structure possesses an optimum in terms of attenuation-thickness of the structure at the quarter-wavelength resonance of the slit when the frequency of the end of the plateau f_{opt} equals $c_2^s/4L$.

For the dimensions considered in section 1.4, $f_{opt} \approx 550$ Hz, which leads to $L \approx 45$ mm. In practice, this length can be smaller. Figure 1.6(a) depicts the absorption coefficient for $d = 84$ mm, $L = 42$ mm, $N = 2$, with $d^{(1)} = d^{(2)} = 42$ mm (the other dimensions are those of section 1.4), with the QWRs plugged on the left for the first slit and on the right for the second slit, when $M = 2$ and $Q\pm = 0$, $Q^{\pm} = 22$ as well as the calculation ran with the equivalent parameters derived in section 1.3 at normal incidence.

It should be noticed that in this case, the equivalent parameters being independent of the slit position and side of the slit on which the impedance condition is applied, the effective parameters reduce to those of $N = 1$ and $d' = 42$ mm. Their validity is ensured till the quarter-wavelength resonance. The calculation performed with the help of the effective parameters are identical (as expected) with the calculation performed when only the terms $Q = 0$ is dominant. While the calculation derived with the effective parameters constitutes a good approximation, the effect of the Drude transition layers [66] are clearly visible around this bound, f_l.

Effectively, the required number of Bloch modes is very large at the lower bound of the bangap. This is explained by the large dispersion of the waves inside the slits around this frequency. The absorption coefficient vanishes inside the bandgap because all the energy is reflected. The structure response possesses absorption peaks which all correspond to resonances of the slits.

The high absorption obtained at 590 Hz is of particular interest. It should be noticed that this peak is not associated with the resonance of the resonators but to a resonance

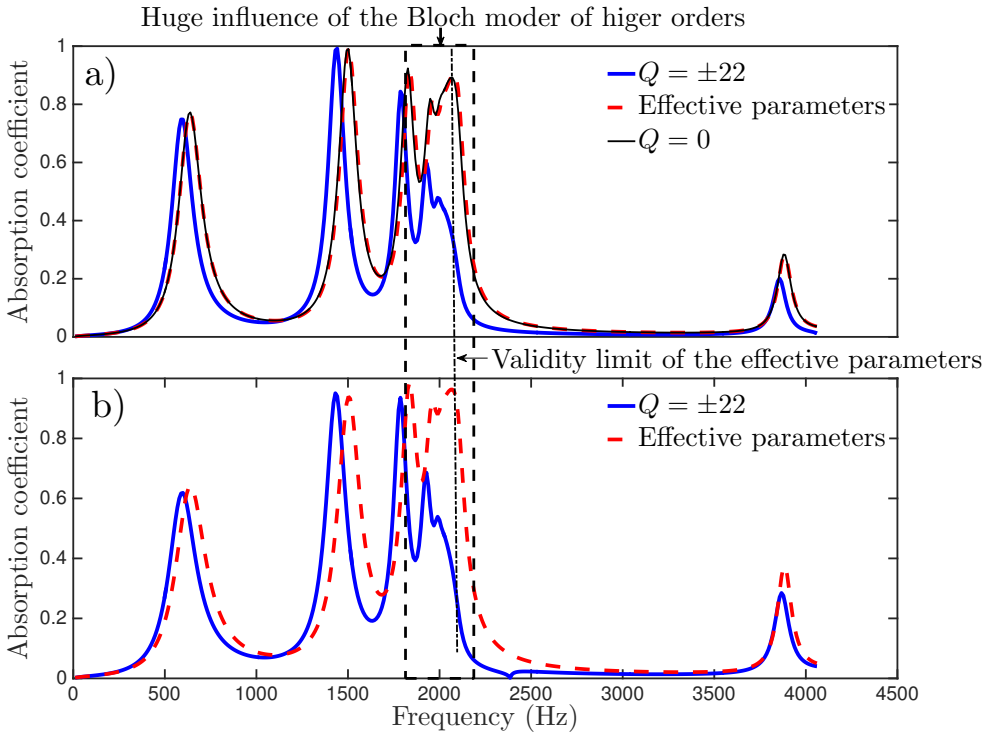

FIGURE 1.6: Absorption coefficient for $L = 42$ mm, $N = 2$, with $d = 42$ mm, with the QWRs plugged on the left for the first slit and on the right for the second slit, when $M = 2$ and $Q = 0$, $Q^{=}22$ as well as the calculation ran with the equivalent parameters, (a) normal incidence, and (b) $\theta^i = \pi/4$.

of the slit with a sound velocity reduced because of the presence of the side resonators. In first approximation, the sound speed is reduced by a factor $\sqrt{1+\phi^t l/w} = \sqrt{\alpha_\infty} \approx 3$.

Thus, this material will be efficient at a frequency 3 times smaller than a classical one. This frequency corresponds in practice to a wavelength in the air $\lambda^a = 579.6$ mm, which is 14 times bigger than the thickness of the structure. The higher order quarter-wavelength resonances lead to high absorption peak, which concentrates around f_l because the speed of sound is rapidly decreasing around this value. The measurement of this resonances could be used to analyse back the speed of sound inside the slits.

Figure 1.6b) illustrates the absorption of the same configuration at $\theta^i = \pi/4$, when 3 modes are accounted for in the slits and $Q^{\pm} = 22$ as well as the calculation ran with equivalent parameters derived in section 1.3. The band-gap frequency range and the position of the absorption peaks are identical, because the band-gap is due to quarter-wavelength resonance of the tubes, and because the high absorption peaks correspond to resonances of the slits. In practice, the calculation performed with the use of the effective parameters are in good agreement below the band-gap till grazing incidence despite the first Wood anomaly (which appears around 2100 Hz, Figure 1.6b)).

The amplitude and frequency of the first absorption peak can further be improved with the help of the ratio $w/\phi^t l$, as explained in Sec. 1.3. This validates the previously effective parameters below the band-gap and proves the efficiency of the structure as sound absorbing metamaterial.

1.6 Experimental validation

The samples were composed of an aluminum block of $40 \times 42 \times 42$ mm^3. Sample 1 is composed of a solid metal block that was drilled from side to side along the 40 mm thick direction with circular holes of $r = 2.5$ mm equally spaced of 7 mm as shown in Fig. 1.7. As for Sample 2, an aluminum plate of 1 mm thick was glued on one side of Sample 1 to close the holes.

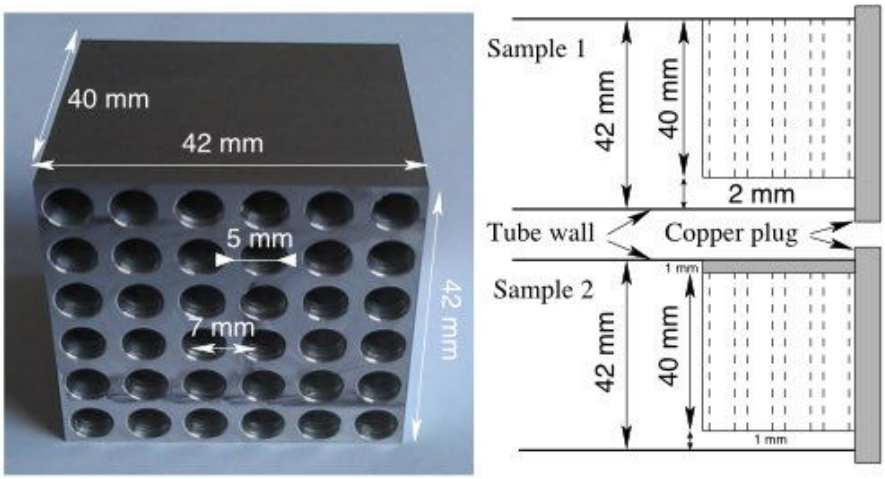

FIGURE 1.7: Picture of Sample 1, along with the experimental set-ups for Sample 1 and 2; Impedance tube cross-section 4.2 cm × 4.2 cm with the cut-off frequency at 4200 Hz.

1.6.1 Experimental set-up

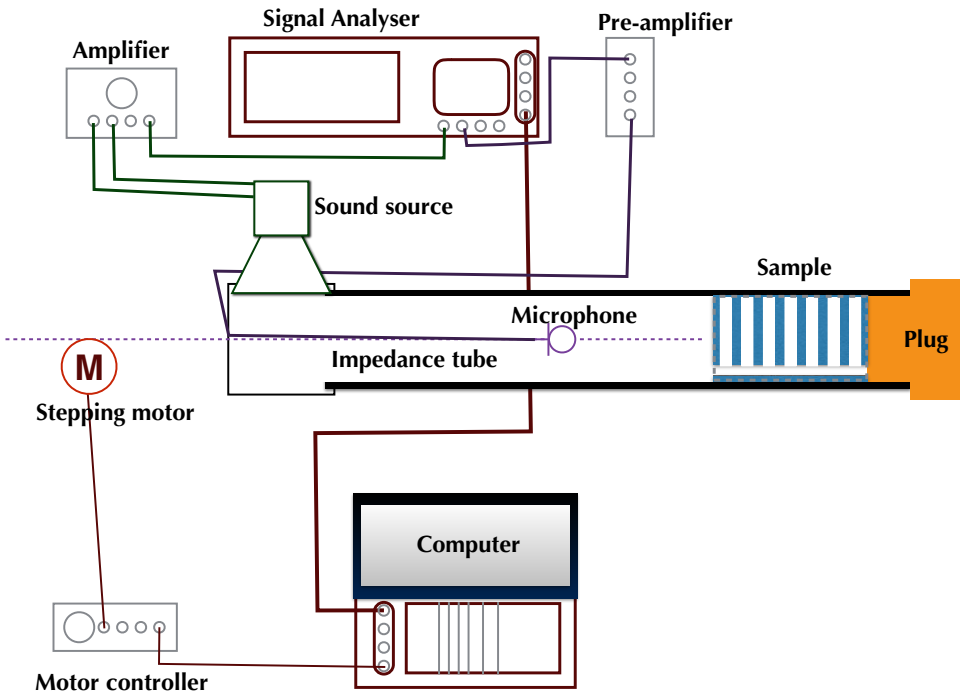

FIGURE 1.8: Schematic of the experimental set-up.

The absorption coefficient of the sample is measured in an impedance tube of square cross section (42 mm by 42 mm) with a cut-off frequency (4200 Hz). By assuming that only plane waves propagate below the cut-off frequency, the infinitely rigid boundary conditions of the tube act like perfect mirrors and create a periodicity pattern in the x_1 and x_3 directions, shown in Figs. 1.8 and 1.9 . This technique was previously used in various articles [24, 70] and allows to determine experimentally the absorption coefficient

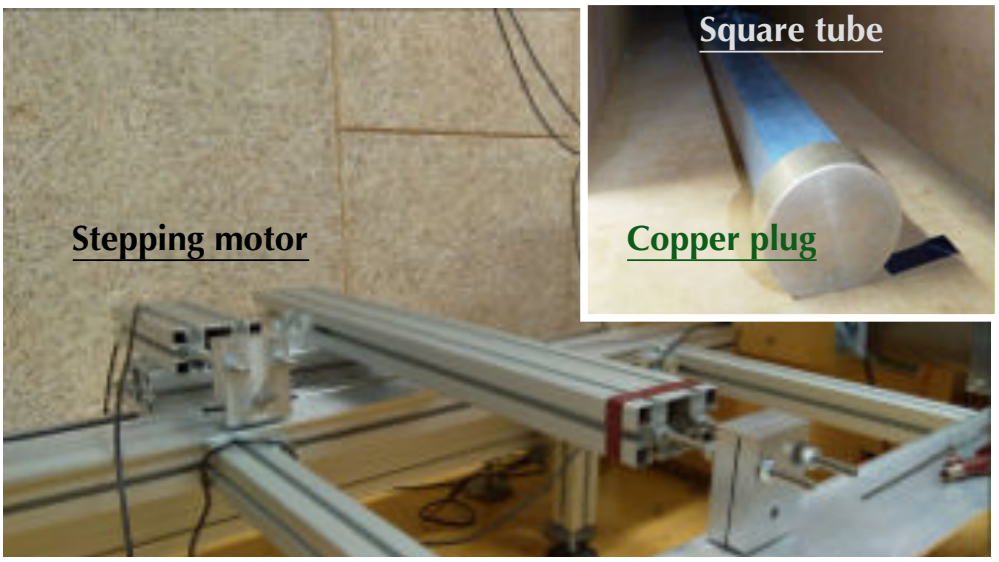

FIGURE 1.9: Photo of the stepping motor and the square cross-section impedance tube with the copper plug.

at normal incidence of a quasi-infinite 2D periodic structure just with half or a quarter of the unit cell.

Samples are placed at the end of the tube against a copper plug that closes the tube and acts as a rigid backing boundary, therefore creating a periodicity along the x_1 direction of 8.4 cm with slit width $w = 2$ mm and $w = 1$ mm respectively, shown in Fig. 1.7.

A one-microphone method is applied here. The microphone is mounted at the end of a thin stick, placed in the middle of the impedance tube. The source used emits a repeated chirp signal from 50 to 4200 Hz.

The microphone along with the stick is towed by a stepping motor to measure sound pressure of various positions in x_1 direction, as shown in Fig. 1.8. The first measurement position is 5 cm to the surface of the sample in order to uphold the plane wave assumption. The transfer functions between the microphone and the output source from multiple positions are measured by the signal analyser and recorded by a computer. The whole operation is synchronised by the same computer.

The reflection coefficient is calculated. The experiment is performed at two different levels of excitation, with identical results, ensuring the repeatability of the tests and the linearity of the response.

1.6.2 Absorption coefficients

Figure 1.10 depicts the experimental absorption coefficient of Sample 1, the calculated one in the corresponding case, i.e., the one studied in Sec. 1.5, and its approximation with the effective parameters. All the three curves match well below the bandgap. As explained in Sec. 1.3, only the fully calculated absorption coefficient is valid inside the bandgap. Inside the latter, the experimental absorption coefficient is very low and is also difficult to measure, explaining the oscillations of the experimental curve.

Figure 1.11 depicts the same curves for Sample 2, i.e., in the case $w = 1$ mm. Once again the curves match well. A small disagreement is noticed around f_l. This can be explained by several things related to the manufacturing and the misplacement of the sample, but more surely by the use of the impedance model. Effectively, the wavelength ($\mathrm{Re}(c_2^s/f)$) is very small (while on the other hand the imaginary part $\mathrm{Im}(c_2^s/f)$ is very large) and can be comparable to a around f_l, making improper the impedance model around this frequency.

In both cases, the absorption for frequency higher than f_h are not well measured because the absorption is very low, but also because this frequency is very close from the cut-off frequency of the tube. These two experiments validate the previous method of calculation, as well as the derived effective parameters.

Of particular interest is the absorption coefficient of Sample 2, which exhibits a total absorption peak at 480 Hz, which corresponds to a wavelength in the air medium 17 times larger than the structure thickness.

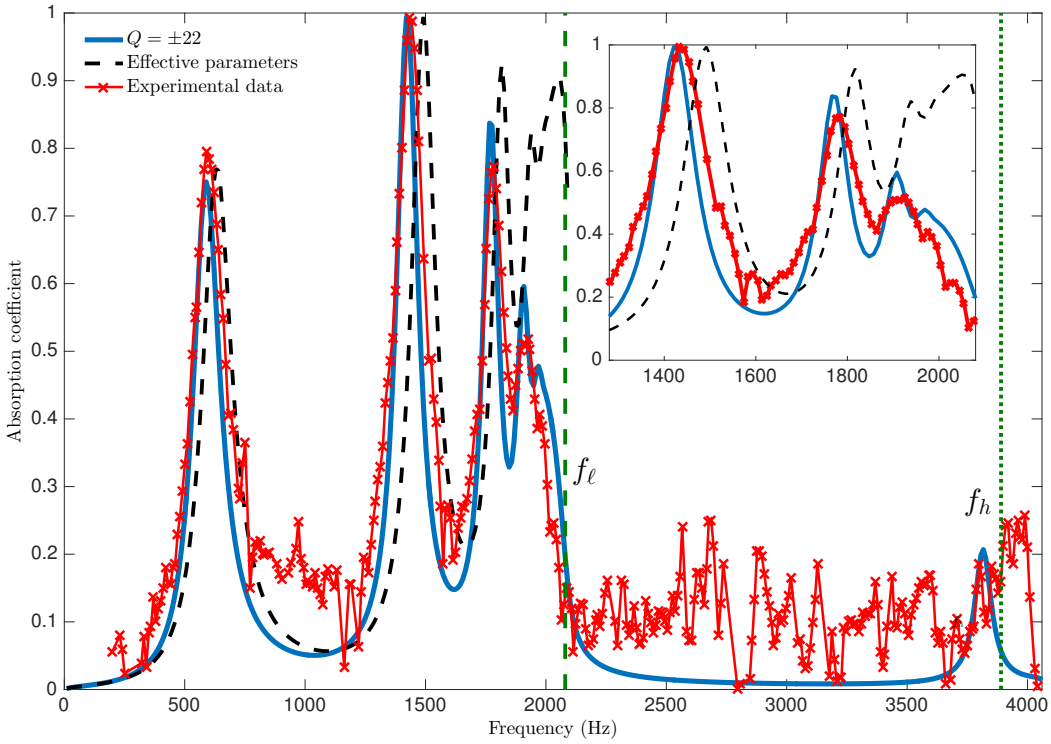

FIGURE 1.10: Absorption coefficients: Sample 1 measured and simulated with the full model and with the effective parameters (f_l and f_h in green).

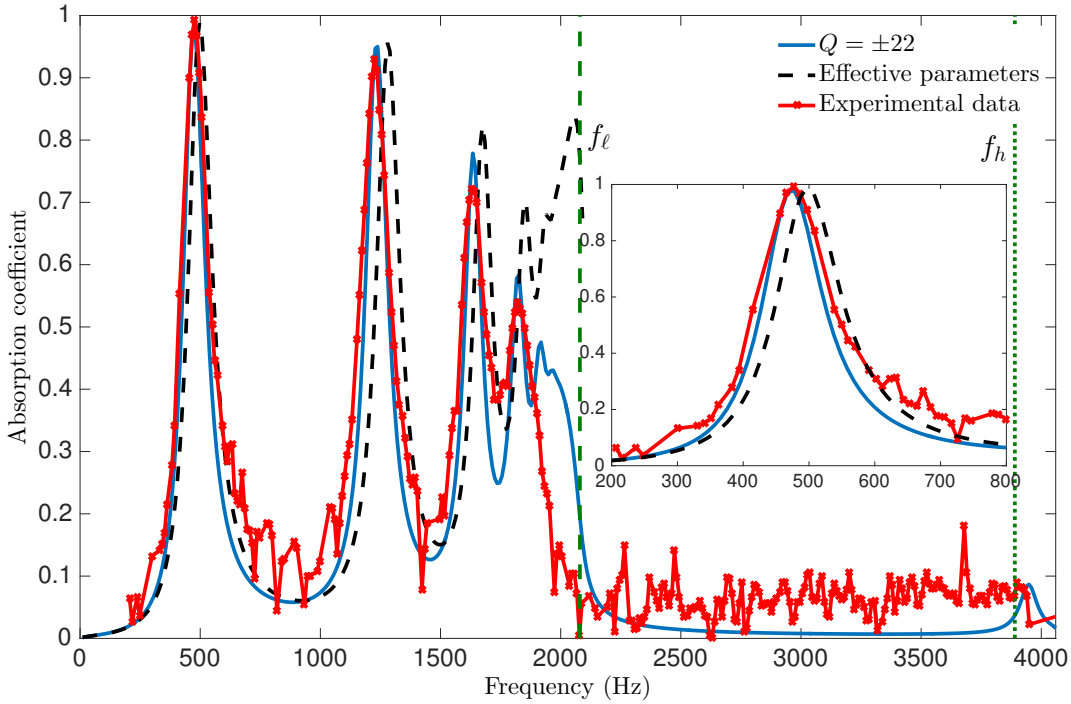

FIGURE 1.11: Absorption coefficients: Sample 2 measured and simulated with the full model and with the effective parameters (f_l and f_h in green).

Conclusion

The acoustic properties of a periodic arrangement of narrow slits with QWRs loaded on one of the slit walls has been studied here. The QWRs are arranged in a square lattice whose periodicity is smaller than the analysed wavelength.

In general, it is shown that the wave propagating in such slit possesses the specific features of slow sound propagation over a quite large frequency band with a phase (and/or group) velocity much smaller than the one of air and the one of the wave propagating in the slit in the absence of the QWRs, for all frequencies below the resonance of the resonators.

The associated dissipation is also analysed, showing strong dependence with regards to the dimensions of the structure, especially the surface porosity, length of resonators and width of the slit. The slowing of the wave speed, related to dispersion, shifts the slits resonances towards lower frequency below band-gap. Moreover high attenuation is found within the band-gap, due to the negative bulk modulus induced by the loaded QWRs, affecting the surface impedance of the slit wall.

The effective parameters are equally derived, both for the modelling of the sound propagation in a single slit, exhibiting negative bulk modulus within the band-gap, and for the modelling of the whole structure. Of particular interest is the frequency limit of these effective parameters which are clearly identified, pointing to the interest of the use the Drude transition layers. These effective parameters also clearly show that the reduction of the sound speed in the slit is only due to a modified bulk modulus and not to a tortuosity effect. Otherwise there would have found translation only on the effective density.

Both the reduced sound speed and the hightened dissipation (dispersion and attenuation) are then used to design sound absorbing metamaterials, which exhibit a low frequency prefectxs absorption peak for wavelength much larger than four times the thickness of the structure.

These results are validated experimentally, showing a lowest frequency total absorption peak at 480 Hz, for a wavelength 17 times larger the thickness of the structure. And a band-gap is found starting at the QWR's resonance frequency.

This paves the way to the design of more complex sound absorbing structures, involving resonators of different nature in the following chapters, using the slow sound phenomenon. Also, the mechanism of the total absorption will be explained in the next chapter.

Chapter 2

Critical coupling condition

This Chapter focuses on using the concepts of slow sound and critical coupling condition to design an ultra-thin acoustic metamaterial panel for total and quasi-omnidirectional absorption[1]. The system geometry is similar to the one used in the previous chapter but the wall of the slit is loaded by Helmholtz resonators (HRs) instead of QWRs, as HRs possess much lower resonance frequency and have more tuneable dimensions. By tuning the geometry of the configuration, the energy leakage of the resonating system can be perfectly compensated by the intrinsic visco-thermal losses arising in both the resonators and the slits. Thus the critical coupling condition is fulfilled and leads to the total absorption of sound in a large range of incidence angles due to the deep sub-wavelength behaviour.

Contents

[1]The work in this Chapter is published in the peer-reviewed article and the corresponding supplementary materials: Jiménez, N., **Huang, W.**, Romero-García, V., Pagneux, V., & Groby, J. P. (2016). "*Ultra-thin metamaterial for perfect and quasi-omnidirectional sound absorption.* Applied Physics Letters, 109(12), 121902.

Introduction

The ability to perfectly absorb an incoming wave field in a sub-wavelength material is advantageous for several applications in wave physics as energy conversion [26], time reversal technology [25], coherent perfect absorbers [27] or soundproofing [18], etc. The solution of this challenge requires to solve a complex problem: reducing the geometric dimensions of the structure while increasing the density of states at low frequencies and finding the good conditions to match the impedance to the ambient medium.

A successful approach for increasing the density of states at low frequencies with reduced dimensions is the use of metamaterials. Recently, several possibilities based on these systems have been proposed to design sound absorbing structures which can present simultaneously sub-wavelength dimensions and strong acoustic absorption [71]. One strategy to design these sub-wavelength systems consists of using space-coiling structures [20, 21]. Another way is to use sub-wavelength resonators as membranes [18, 72] or Helmholtz resonators (HRs) [73, 74].

Moreover, sub-wavelength metamaterials based on the concept of slow sound propagation have been used to the same purpose [75], see Chapter 1. This last type of metamaterials [75–77] makes use of its strong dispersion for generating slow-sound conditions inside the material, therefore, drastically decreasing frequency of the absorption peaks. However, all of these structures, while they bring potential solutions to reduce the geometric dimensions, face the challenge of impedance mismatch to the ambient medium.

Many researches study the interaction of an incoming wave with a lossy open resonant structure, in particular searching for the impedance matching with the background field in the field of wave physics [25–27]. One of the solutions is the critical coupling technique [28]. These open systems, at the resonant frequency, are characterised by both the leakage rate of energy (i.e., the coupling of the resonant elements with the propagating medium), and the intrinsic losses of the resonator. The balance between the leakage and the losses activates the condition of critical coupling, trapping the energy around the resonant elements and generating a maximum of energy absorption [28–30].

In this Chapter, using the concepts of slow sound and critical coupling, we theoretically and experimentally report a prefect and quasi-omnidirectional absorbing metamaterial panel with deep sub-wavelength thickness. The system consists of a thin panel perforated with a periodic arrangement of slits. The upper wall of the slit is loaded by identical HRs of square cross-section, arranged in a square array.

Several different theoretical models are used to analyse the structure. Through these methods, we analyse the dispersion properties, inside the slit in order to inspect the slow sound behaviour. By modifying the geometry, the intrinsic losses of the system can be efficiently tuned. Thus critical coupling condition can be fulfilled to solve the impedance matching to the exterior medium. Through an optimisation process, one configuration of the deepest sub-wavelength absorber is 3D-printed and tested in the impedance tube.

2.1 General description

The system consists of a thin panel perforated with a periodic arrangement of closed slits, of thickness h, along the x_1 direction with periodicity d, as shown in Fig. 2.1b) and Fig. 2.2. The upper wall of the slit is loaded by N identical Helmholtz resonators (HRs) in a square array of side a.

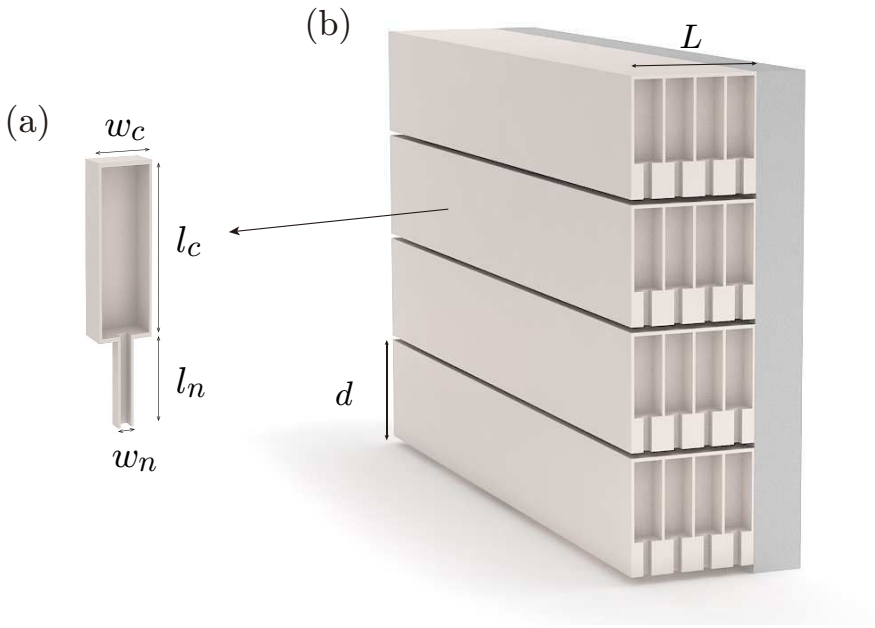

FIGURE 2.1: (a) Square cross-section Helmholtz resonator (HRs). (b) Conceptual view of the metamaterial panel placed on a rigid wall with $N = 4$ layers of HRs.

At the boundaries $\Gamma_{x_1=nh}$ and $\Gamma_{x_1=nh+d}, n = 0, 1, 2...$, the periodic boundary conditions are assumed. In a similar way as Chapter 1, the effect of the resonators is modeled by a impedance condition $Z_{\text{wall}} = Z_{\text{HR}}/\phi^n$.

We use HR with square cross-section, characterised by a neck and cavity of width w_n, and w_c and length ℓ_n and ℓ_c respectively, see Fig. 2.1a). The visco-thermal losses in the system are considered both in the resonators and in the slit by using its effective complex and frequency dependent parameters [61].

The incident wave propagates in Ω^a and is expressed by $p^i(\mathbf{x}) = A^i e^{\mathrm{i}(k_1^i x_1 - k_2^{ai}(x_2 - L))}$, wherein $k_1^i = -k^a \sin\theta^i$, $k_2^{ai} = k^a \cos\theta^i$ and $A^i = A^i(\omega)$ is the signal spectrum. As the problem is periodic and the excitation is due to a plane wave, each field (X) satisfies the Floquet-Bloch relation,

$$X(\mathbf{x} + \mathbf{d}) = X(\mathbf{x}) e^{\mathrm{i}k_1^i d}. \tag{2.1.1}$$

Consequently, it suffices to examine the field in the elementary cell of the material to get the fields, via the Floquet relation, in the other cells.

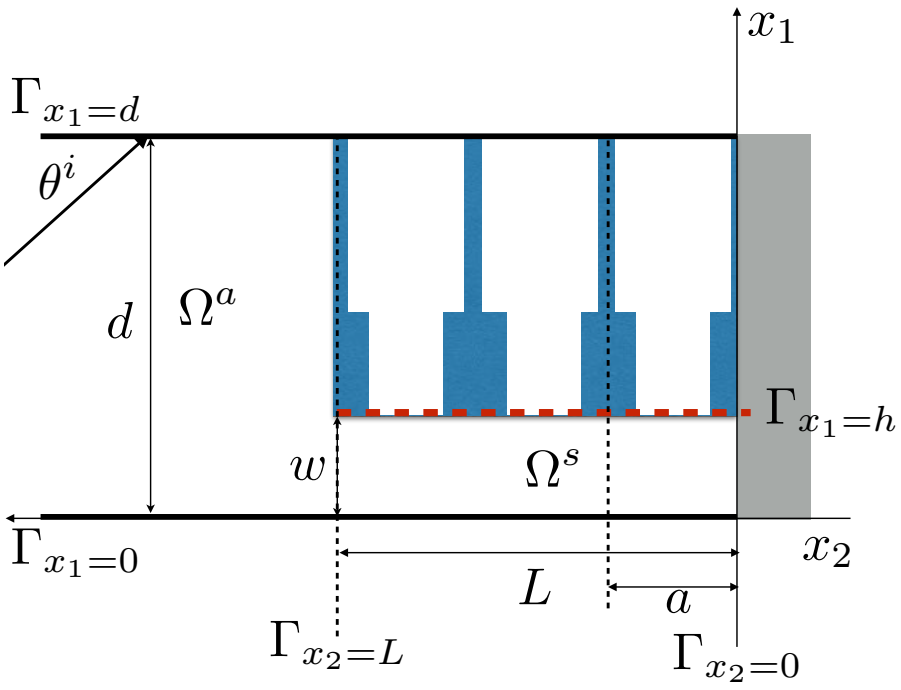

FIGURE 2.2: Scheme of the unit cell of the panel composed of a set of N Helmholtz resonators. Periodic boundary conditions are applied at boundaries $\Gamma_{x_1=d}$ and $\Gamma_{x_1=0}$, which reduces to symmetric (rigid) boundary conditions for normal incidence.

2.2 Visco-thermal losses model in the structure

Similar to that of Eq.(1.1.4), the effective parameters in the slit, considering that only plane waves propagate inside, are expressed as:

$$\rho^s = \rho_0 \left[1 - \frac{\tanh\left(\frac{h}{2}G_\rho\right)}{\frac{h}{2}G_\rho} \right]^{-1}, \tag{2.2.1a}$$

$$B^s = B_0 \left[1 + (\gamma - 1)\frac{\tanh\left(\frac{h}{2}G_\kappa\right)}{\frac{h}{2}G_\kappa} \right]^{-1}, \tag{2.2.1b}$$

with $G_\rho = \sqrt{\mathrm{i}\omega\rho_0/\eta}$ and $G_\kappa = \sqrt{\mathrm{i}\omega \mathrm{Pr}\rho_0/\eta}$, and where γ is the specific heat ratio of air, P_0 is the atmospheric pressure, Pr is the Prandtl number, η the dynamic viscosity, ρ_0 the air density and $B_0 = \gamma P_0$ the air bulk modulus. Also, $Z^s = \sqrt{\rho^s B^s}$ is the characteristic impedance of the slit, and $k^s = \omega\sqrt{B^s/\rho^s}$ and is the characteristic wavenumber of the slit.

In addition, the propagation in a rectangular cross-section tube can be described by its complex and frequency dependent density and bulk modulus, and considering that plane waves propagate inside, can be expressed as [61]:

$$\rho^t = -\frac{\rho_0 \ell_x^2 \ell_y^2}{4G_\rho^2 \sum_{k\in\mathbb{N}}\sum_{m\in\mathbb{N}} \left[\alpha_k^2\beta_m^2\left(\alpha_k^2 + \beta_m^2 - G_\rho^2\right)\right]^{-1}}, \tag{2.2.2a}$$

$$B^t = \frac{B_0}{\gamma + \frac{4(\gamma-1)G_\kappa^2}{\ell_x^2\ell_y^2}\sum_{k\in\mathbb{N}}\sum_{m\in\mathbb{N}} \left[\alpha_k^2\beta_m^2\left(\alpha_k^2 + \beta_m^2 - G_\kappa^2\right)\right]^{-1}}, \tag{2.2.2b}$$

where the superscript $t = n, c$ represents respectively the neck or the cavity, with the constants $\alpha_k = 2(k + 1/2)\pi/a$ and $\beta_m = 2(m + 1/2)\pi/b$, and the dimensions of the duct ℓ_x and ℓ_y being either the neck, $\ell_x = \ell_y = w_n$, or the cavity, $\ell_x = \ell_y = w_c$ of the Helmholtz resonators as we consider only square cross-section ducts $\ell_x = \ell_y$.

Moreover, $Z^n = \sqrt{\rho^n B^n}$ and $Z^c = \sqrt{\rho^c B^c}$ are receptively the characteristic impedance of the neck and the cavity, also $k^n = \omega\sqrt{B^n/\rho^n}$ and $k^c = \omega\sqrt{B^c/\rho^c}$ are receptively the characteristic wavenumber of the neck and the cavity.

2.3 Surface impedance

Using the above effective parameters for the neck and cavity elements of a Helmholtz resonator, its impedance can be written as

$$Z_{\mathrm{HR}} = \mathrm{i}Z^n \frac{\mathcal{Z}^{nc} - \tan(k^n\ell_n)\tan(k^c\ell_c)}{\mathcal{Z}^{nc}\tan(k^n\ell_n) + \tan(k^c\ell_c)}, \tag{2.3.1a}$$

$$\text{with } \mathcal{Z}^{nc} = \frac{S_n}{S_c}\frac{Z^n}{Z^c}, \tag{2.3.1b}$$

where $\mathcal{Z}^{nc}$ is the normalised surface impedance at the interface of the neck and the cavity, with the respective cross-section surface of the neck and cavity $S_n = w_n^2$ and $S_c = w_c^2$.

In the low frequency regime, where the corresponding wavelength is much longer than the neck and the cavity's dimensions , as $|k^n\ell_n| \ll 1$ and $|k^c\ell_c| \ll 1$, the asymptotic expansion of Z_{HR} writes as

$$\tilde{Z}_{\mathrm{HR}} = \lim_{|k^n\ell_n|\ll 1, |k^c\ell_c|\ll 1} Z_{\mathrm{HR}} = \mathrm{i}\frac{Z^n}{\phi^n}\cdot\frac{\mathcal{Z}^{nc} - k^n\ell_n k^c\ell_c}{\mathcal{Z}^{nc}k^n\ell_n + k^c\ell_c}, \tag{2.3.2}$$

where $\phi^n = S_n/a^2$ is the surface porosity of the resonator array.

In the lossless case, the impedances ratio becomes $\tilde{\mathcal{Z}}^{nc} = \dfrac{S_n}{S_c}$, as $Z^n = Z^c$. The wavenumbers $k^n = k^c = k_0 = \dfrac{\omega}{c_0}$. Thus, Eq.(2.3.2) reduces to :

$$\tilde{Z}_{\mathrm{HR}} = \mathrm{i}\frac{Z^n}{\phi^n}\frac{\tilde{\mathcal{Z}^{nc}} - \ell_n\ell_c k_0^2}{\tilde{\mathcal{Z}^{nc}}\, k_0(\ell_n + \ell_c)} = \mathrm{i}\frac{Z^n}{\phi^n}\frac{1 - V_c\ell_c k_0^2/S_n}{k_0(\ell_n + \ell_c)}, \tag{2.3.3}$$

where $V_c = \ell_c S_c$ is the volume of the cavity.

So, $\tilde{Z}_{\mathrm{HR}}$ turns to zero, when $k_0^2 = S_n/(V_c L_n)$. From this, the usual resonance frequency of HR without losses is found via,

$$\frac{\partial\tilde{Z}_{\mathrm{HR}}}{\partial k_0} = \frac{\dfrac{S_n/S_c}{k_0^2} - \ell_n\ell_c}{(S_n/S_c)\ell_n + \ell_c} = 0\ , \tag{2.3.4}$$

$$\Rightarrow \qquad f_{\mathrm{HR}} = \frac{c_0}{2\pi}\sqrt{\frac{S_n}{V_c\ell_n}}. \tag{2.3.5}$$

2.4 End correction

It is worth noting here that the expression of the surface impedance in Eq.(2.3.1a) is not exact. The end correction due to the radiation should be included in the equation.

The characteristic impedance accounting for the neck radiation can be expressed as [78]:

$$Z_{\mathrm{HR}} = -\mathrm{i}\frac{1 - Z^n k^n \Delta l \tan(k^c \ell_c)/Z^c - Z^n \tan(k^n \ell_n)\tan(k^c \ell_c)/Z^c}{\tan(k^n \ell_n)/Z^n - k^n \Delta l \tan(k^n \ell_n)\tan(k^c \ell_c)/Z^c + \tan(k^c \ell_c)/Z^c}\,, \tag{2.4.1}$$

where the correction length is deduced from the addition of two correction lengths $\Delta l = \Delta l_1 + \Delta l_2$ as

$$\Delta l_1 = 0.82\left[1 - 1.35\frac{r_n}{r_c} + 0.31\left(\frac{r_n}{r_c}\right)^3\right] r_n\,, \tag{2.4.2a}$$

$$\Delta l_2 = 0.82\left[1 - 0.235\frac{r_n}{r_s} - 1.32\left(\frac{r_n}{r_t}\right)^2 + 1.54\left(\frac{r_n}{r_t}\right)^3 - 0.86\left(\frac{r_n}{r_t}\right)^4\right] r_n, \tag{2.4.2b}$$

where $r_x = \sqrt{S_x/\pi}, x = n, c, s, t$ is the effective radius of the cross-section of the neck, the cavity, the slit and the unit-cell. The first length correction, Δl_1, is due to pressure radiation at the discontinuity from the neck duct to the cavity of the Helmholtz resonator [79], while the second Δl_2 comes from the radiation at the discontinuity from the neck to the principal waveguide [80].

In the original works [79, 80], the resonator is of circular cross-section, here we approximate the formulas with the effective radius of the square cross-section re-sonators. This correction only depends on the radius of the waveguides, so it becomes important when the duct length is comparable to the radius, i.e., for small neck lengths and for frequencies where $kr_n \ll 1$.

2.5 Modal expansion method (MEM)

As sketched in Fig. 2.2, the full space is divided into two sub-domains, the free air, Ω^a, and the interior of the slit, Ω^s.

In a similar way as in Chapter 1, separation of variables, radiation conditions, and Floquet theorem lead to the representations:

$$p^a(\mathbf{x}) = \sum_{q\in\mathbb{Z}}\left[A^i e^{-\mathrm{i}k^a_{2q}(x_2-L)}\delta_{0q} + R_q e^{\mathrm{i}k^a_{2q}(x_2-L)}\right] e^{\mathrm{i}k^a_{1q}x_1},\ \forall \mathbf{x}\in\Omega^a\,, \tag{2.5.1}$$

wherein δ_{0q} is the Kronecker symbol, $k^a_{1q} = k^i_1 + \dfrac{2q\pi}{d}$, and $k^a_{2q} = \sqrt{(k^a)^2 - (k^a_{1q})^2}$, with $\mathrm{Re}\left(k^a_{2q}\right) \geq 0$ and $\mathrm{Im}\left(k^a_{2q}\right) \geq 0$. The reflection coefficient of the Bloch wave denoted by the subscripts q is R_q. The pressure field p^s, admits the pseudo-modal representation, that already accounts for the boundary conditions on $\Gamma_{x_1=0}$ and $\Gamma_{x_1=h}$:

$$p^s = \sum_{m\in\mathbb{N}} A_n \cos\left(k^s_{1m}x_1\right)\cos\left(k^s_{2m}x_2\right)\forall \mathbf{x}\in\Omega^s\,, \tag{2.5.2}$$

wherein A_n are the coefficients of the pseudo modal representation, $k^s_{2m} = \sqrt{(k^s)^2 - (k^s_{1m})^2}$, with $\mathrm{Re}\,(k^s_{2m}) \geq 0$ and $\mathrm{Im}\,(k^s_{2m}) \geq 0$, and k^s_{1m} is the m-th solution of the dispersion relation and satisfies [62]:

$$k^s_{1m}\tan\left(k^s_{1m}w\right) = \frac{-\mathrm{i}\omega\rho^s}{Z_{HR}}. \tag{2.5.3}$$

The solution of the problem is similar to what is described in Chapter 1 and reduces to the system 1.2.6, where the impedance boundary condition is replaced by Z_{HR}. Once solved, the absorption coefficient A is then calculated through

$$A = 1 - \sum_{q\in\mathbb{Z}} \frac{\mathrm{Re}\left(k^a_{2q}\right)}{k^a_2}\|R_q\|^2. \tag{2.5.4}$$

2.6 Effective parameter method (EPM)

The resonant scattering problem analysed here can be characterised by the reflection coefficient. A simpler way to obtain this reflection coefficient consists of using the effective bulk modulus, K_{eff}, and effective density, ρ_{eff} of the system [81]. The reflection coefficient reads as

$$R_{\mathit{eff}}(\theta) = \frac{iZ'_{\mathit{eff}}\cot(k_{\mathit{eff}}L) - i\omega\Delta l_{\mathrm{slit}}/\phi^t c_0 - 1/\cos(\theta)}{iZ'_{\mathit{eff}}\cot(k_{\mathit{eff}}L) - i\omega\Delta l_{\mathrm{slit}}/\phi^t c_0 + 1/\cos(\theta)}, \tag{2.6.1}$$

where the normalised effective impedance is $Z'_{\mathit{eff}} = \sqrt{\rho_{\mathit{eff}}K_{\mathit{eff}}/\rho_0 K_0}$, with ρ_0 and K_0 are the density and bulk modulus of the ambient air, $k_{\mathit{eff}} = \omega\sqrt{\rho_{\mathit{eff}}/K_{\mathit{eff}}}$ is the effective wavenumber , Δl_{slit} is the end correction of the slit accounting for the radiation from the slit to the free space, $\phi^t = h/d$ is the total porosity of the metamaterial, ω is the angular frequency, c_0 the sound speed of air and θ the angle of incidence.

The effective parameters can be obtained in the low frequency approximation of the MEM as

$$K_{\mathit{eff}} = \frac{B^s}{\phi^t}\left[1 + \frac{B^s\phi\left(V_c B^n + V_n B^c\right)}{B^n h\left(S_n B^c - V_c\rho^n\ell_n\omega^2\right)}\right]^{-1}, \tag{2.6.2}$$

$$\rho_{\mathit{eff}} = \frac{\rho^s}{\phi^t}, \tag{2.6.3}$$

where $V_n = S_n\ell_n$ is the volume of the neck in HR.

Here, the end correction Δl_{slit} comes from the radiation from the slits to the free air. The radiation correction for a periodic distribution of slits can be expressed as [81]:

$$\Delta l_{\mathrm{slit}} = h\phi^t\sum_{n=1}^{\infty}\frac{\sin^2\left(n\pi\phi^t\right)}{(n\pi\phi^t)^3}. \tag{2.6.4}$$

Note for $0.1 \leq \phi^t \leq 0.7$ this expression reduces to $\Delta l_{\mathrm{slit}} \approx -\sqrt{2}\ln\left[\sin\left(\pi\phi^t/2\right)\right]/\pi$.

Although Eq. (2.6.4) is appropriate for a periodic array of slits, it is not exact for slits loaded with HRs. Therefore, we can evaluate a more realistic value for the end correction by reconstructing an equivalent impedance, $\tilde{Z}$, from the reflection coefficient of the 0-th order Bloch mode calculated with the full model and comparing it as [77]:

$$\tilde{Z} - \mathrm{i}Z_{\mathit{eff}}\mathrm{cotan}(k_{\mathit{eff}}L) = -i\omega\frac{\rho_0}{\phi^t}\Delta l_{\mathrm{slit}} \tag{2.6.5}$$

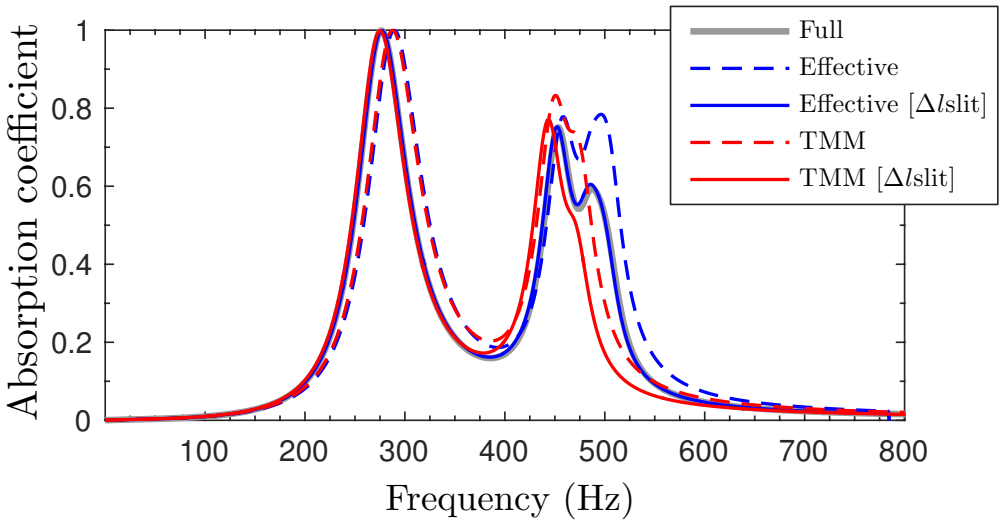

FIGURE 2.3: Absorption of a panel calculated with and without including the end correction of the slit for a panel of $N = 3$ resonators.

The end correction using this last approach gives a value that depends on the geometry of the HRs and for the present examples is around 1.5 times the one using Eq.(2.6.4).

To test the validity of the end correction of the slit, a configuration with total absorption is chosen. The absorption is calculated through EPM and TMM[2] with and without Δl_{silt}. The results are compared with the one calculated through the full MEM. For numerical application, the dimensions of the configuration used in here are as followed: $h = 1.2$ mm, $a = 12$ mm, $w_n = a/6$, $w_c = a/2$, $d = 70$ mm, $\ell_n = d/3$, $\ell_c = d - h - \ell_n$, and $N = 3$.

Figure 2.3 shows the absorption of the system using Eq.(2.6.5) and without any end correction. Perfect agreement between the full modal calculation and using the effective parameters can be obtained using the proper end correction. On the other hand, using the same length correction used in the TMM calculations, a perfect agreement is observed for the low frequency peaks of absorption curve.

2.7 Dispersion properties

We start by analysing the dispersion properties, along the dimension x_2, inside the slit in order to inspect the slow sound behaviour. The dispersion relation represented in Eq.(2.5.3) are studied with the configuration used in Sec. 2.6.

Figure 2.4a, b) shows the real and imaginary part of the solution of Eq.(2.5.3). The solution is in the form of the wavenumber k in the slit along x_2 direction, normalised by π/L. The results are calculated by all three methods, in both lossless and lossy cases.

The lossless cases give out infinite branch at the resonant frequency of the HRs, f_{HR}, by MEM and EPM. Though the TMM gives only a clear-cut top-end at f_{HR}, due to the fact that the method only accounts for discrete and finite number of resonators, as $N = 3$ in this case, while MEM and the associated EPM account for an infinite number

[2]Detail on resolution of transfer matrix method (TMM) is shown in Appendix A.

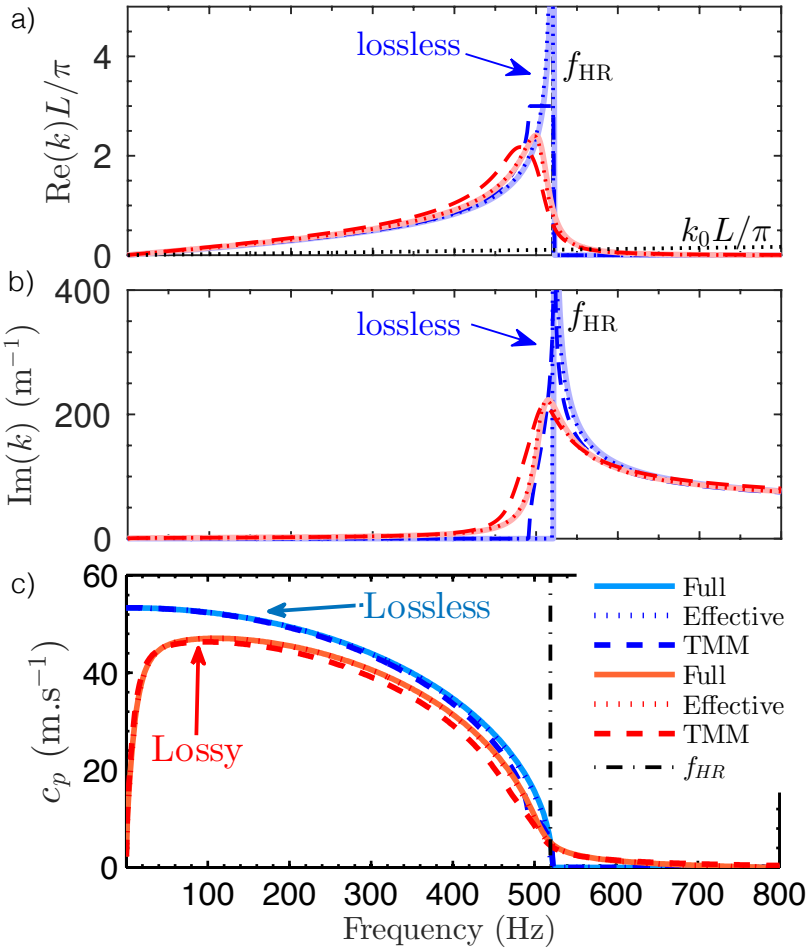

FIGURE 2.4: Wavenumber in slit in x_2 direction, for a panel of $N = 3$ resonators calculated by full MEM (continuous gray), EPM (dotted) and TMM (dashed) for the lossless case (blue) and lossy case (red): a) Real part of wavenumber normalised by π/L; b) Imaginary part; c) Effective sound speed in slit.

of resonators in the unit cell.

Nevertheless, a band gap can be clearly observed above f_{HR} for both lossy and lossless cases, where the slope of the real part becomes extremely steep, indicating a small wave speed, and the imaginary part takes large value after f_{HR}, indicating a huge attenuation within the band gap, similar to the ones described in Fig. 1.4. It is worth noting that the maximum wavenumber inside the slit is limited by the discreteness to the value $k_{\max} = \pi N/L$, as shown by the TMM calculations (dashed blue curve in Fig. 2.4b)).

Figure 2.4c) shows the corresponding real part of the phase velocity in the slit, calculated both in the lossless and lossy cases. Due to the presence of the band gap, slow sound propagation conditions are achieved in the dispersive band below f_{HR}.

In the lossless case, zero phase velocity can be observed at f_{HR}. In the lossy case, the sound speed below f_{HR} is much lower than the speed of sound in air. It has a local maximal plateau at 48 m.s^{-1}.

Compared with lossless case, the losses limit the minimum value of group velocity

[56], but in this system slow sound velocity can also be achieved in the dispersive band below f_{HR}. Therefore, the collective resonances produced by the array of HRs will be in the deep sub-wavelength regime compared with L the length of the slit.

For usual slit open to semi-infinite rigid-backed space, the resonance frequency of the slit is that of the quarter-wavelength resonator, as $f_{slit} = c^a/4L = 2382$ Hz in lossless case. Here as the effective sound speed is reduced in the slit, $f_{slit} = c^s/4L$. As $c^s \leq 48$ m.s^{-1}, $f_{slit} \leq 333$ Hz. This leads to the sub-wavelength ratio $\lambda/L \geq 28.6$.

2.8 Optimal configuration

2.8.1 Critical coupling

As mentioned in the Introduction of this Chapter, the critical coupling condition is achieved for an open, lossy and resonant system, when the energy leakage of the resonant elements is perfectly balanced by the inherent losses of the inner cavities [30, 82].

In the case of transmission systems, degenerate critically coupled resonators with symmetric and antisymmetric resonances can be used to perfectly absorb the incoming energy by trapping the energy in the resonant element, i.e. without reflection nor transmission [83, 84]. In the case of purely reflecting system, only symmetric resonances that are critically coupled can be used to obtain perfect absorption of energy by a perfect trapping of energy [19, 85].

Hereby, we use a visualisation of the eigenvalues of the scattering matrix, which in the reflection problem, i.e., the reflection coefficient in the complex frequency plane, which gives a general overview of the physical behaviour of the system. It is evaluated in the complex frequency plane, by substituting the frequency with complex frequency as $F = F_{Re} + \mathrm{i}F_{Im}$ in the wavenumber.

In the lossless case, one finds pairs of poles at complex frequency F_{pole} and zeros at complex conjugate of $F_{zero} = F^*_{pole}$ symmetrically distributed on both sides of the real frequency axis. The zeros (poles) are in the positive (negative) half imaginary frequency plane in the $\exp(-\imath\omega t)$ sign convention [86]. The imaginary part of the complex frequency of the poles of the reflection coefficient represents the energy leakage of the system into the free space [82].

When the intrinsic losses are considered, the zeros and the poles are down-shifted. In the case where the zero is located on the real frequency axis as $F_{zero} = F_{pole} + \mathrm{i}0$, and $R(F_{zero}) = 0$. Thus, the critical coupling condition is fulfilled and the perfect absorption is obtained [85].

As an example, the theoretical results of the configuration defined in previous sections are shown in Fig. 2.5. In Fig. 2.5a), the complex plane of $\log|\ R\ |^2$ is shown against real and imaginary frequencies. The lower frequency zero is located on the real axis, where the critical coupling condition is fulfilled as the geometry of the system has been tuned to introduce the exact amount of intrinsic losses that exactly compensates the energy leakage of the system. This leads to perfect absorption at 275 Hz for a thickness of $L = 3a$, where the sub-wavelength ratio $\lambda/L = 34.5$.

Figure 2.5b) shows the corresponding absorption predicted by the different models. In addition, as there are $N = 3$ resonators in the layer, other two secondary peaks of absorption are observed at higher frequencies 442 Hz and 471 Hz. Their corresponding zeros are located close to the real axis and, although the critical coupling condition is not exactly fulfilled, high absorption values still can be observed at these frequencies.

The differences between the different models of solution observed in the absorption coefficient are due to the fact that the effect of the discreteness is not captured by neither the MEM nor the associated EPM. MEM leads to an infinite number of zeros and poles close to the resonance, producing the artificial increase of the absorption observed near f_{HR}, see Fig. 2.5b) .
Consequently, the prediction of absorption by MEM is accurate only if these zeros do not interact with the real axis or if the number of resonators is considerably increased. The TMM captures this discreteness effect and shows good results in this range of frequencies (400-500 Hz).

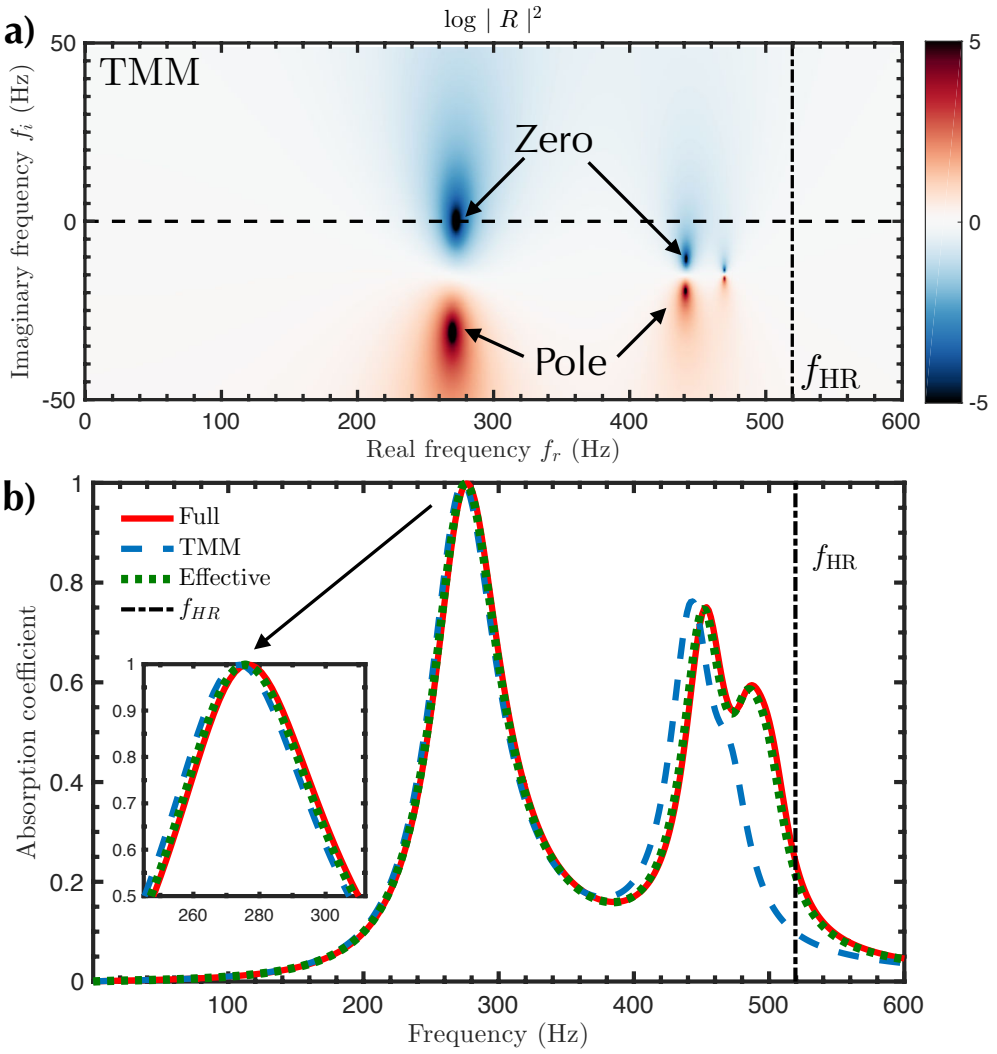

FIGURE 2.5: a) Complex-frequency planes of the reflection coefficient calculated by TMM where f_r and f_i is the real and imaginary part of the complex frequency; b) Absorption of the panel. The dashed-dotted line marks the resonant frequency of the HRs and the shaded area corresponds to the band-gap.

2.8.2 Optimisation

Using an optimisation algorithm (sequential quadratic programming (SQP) method as in [87]), the geometry of the system can be tuned in order to minimise the thickness of the material, providing structures with perfect absorption for normal incidence and deep sub-wavelength dimensions. The TMM was employed in the optimisation to consider the discreteness effects on the reflection coefficient.

Here, the constraint conditions of the manufacturing, material rigidity and the measurement system are all taken into consideration. The resulting structure from the optimisation procedure is shown in Fig. 2.6: a sample with a single layer of resonators, $N = 1$ with $h = 2.63$ mm, $d = 14.9$ cm, $a = L = d/13 = 1.1$ cm, $w_n = 2.25$ mm, $w_c = 4.98$ mm, $\ell_n = 2.31$ cm, $\ell_c = 12.33$ cm. The width of the impedance tube used for measurements, d, allows to fit 13 resonators in the transversal dimension as shown Fig. 2.6.

In particular, this optimal design has only one layer of HR, as the periodicity of the array of HRs is not a necessary condition for these perfect absorbing panels. Because the slow sound propagation is caused by the local resonance of the HRs. However, considering periodicity allows us to design and tune the system using the present analytical methods.

The sample was built using stereolithography techniques using a photosensitive epoxy polymer (Accura 60®, 3D Systems Corporation, Rock Hill, SC 29730, USA), where the acoustic properties of the solid phase are $\rho_0 = 1210$ kg/m^3, $c_0 = [1570, 1690]$ m.s^{-1}.

The experiment is carried out in an impedance tube of square cross-section (15 cm by 15 cm) with a cut-off frequency 1500 Hz. Similarly to the method presented in Section 1.6.1, the reflection coefficient is measured with a single microphone method from 50 to 750 Hz.

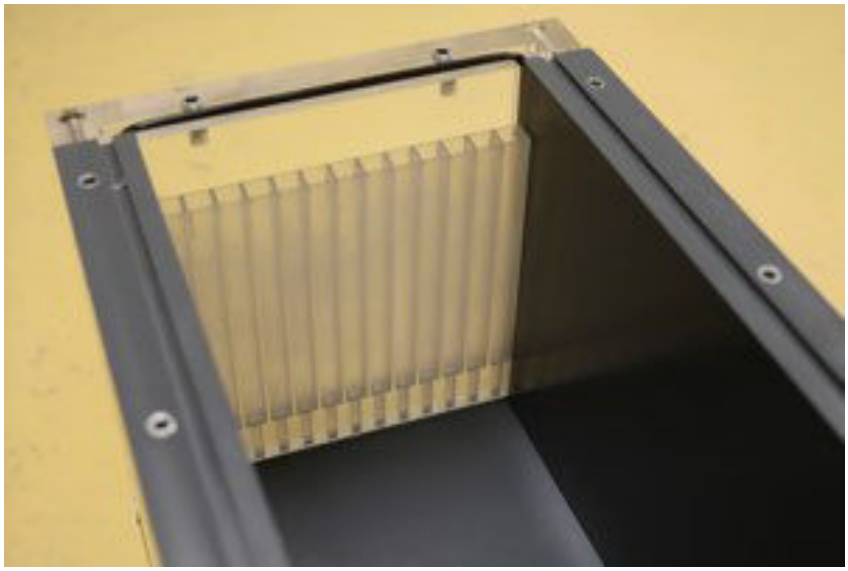

FIGURE 2.6: Photograph of the experimental setup: The optimal sample with vertical unit cells, $N = 1$, in the interior of the impedance tube. The translucent resin allows to see the array of HRs. Picture shows the tube open, but it was closed for the experiments.

2.8.3 Results and analysis

Figure. 2.7a) shows the reflection coefficient in the complex frequency plane calculated with MEM, along with the trajectories of the zero of $\mid R \mid^2$ of during the tuning of the geometry of the unit cell. The colour map corresponds to the case in which the critical coupling condition is fulfilled, i.e., the zero of the reflection coefficient is exactly located on the real frequency axis.

As the intrinsic losses depend on the geometry of the resonators and the thickness of the slits, each trajectory of the zero corresponds to the movement of the zero when only one of the dimensions of the resonator is being modified, with the rest of the dimensions

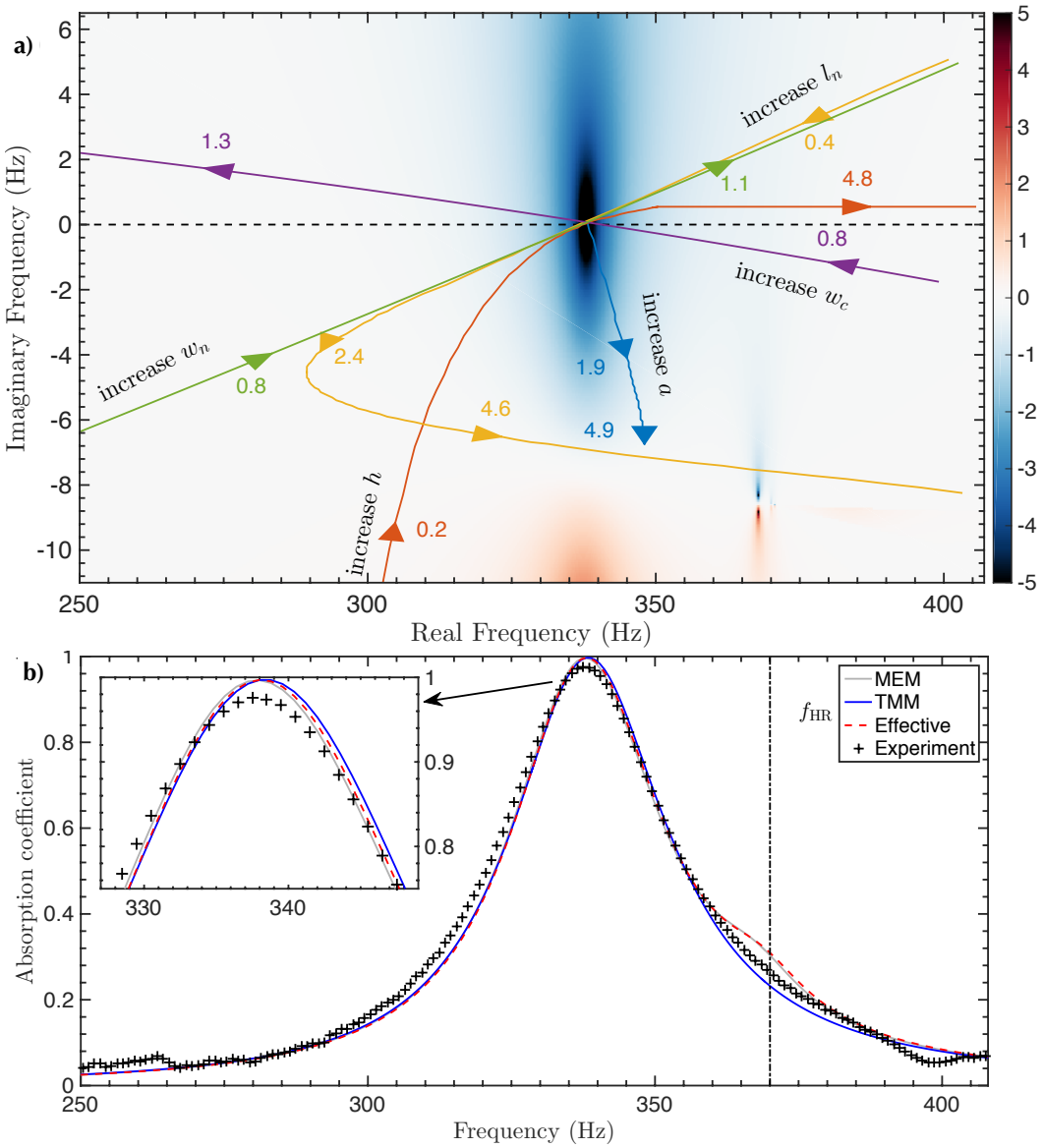

FIGURE 2.7: a) Representation of the reflection coefficient in the complex frequency plane for the optimised sample. Coloured lines: the trajectories of the zero by changing only one of the geometry parameters; b) Absorption of the system measured experimentally (crosses), calculated by the full modal expansion (thick continuous grey), effective parameters (dashed red), transfer matrix method (continuous blue) and finite element method (circles).

being fixed. The crossing of the trajectories with the real frequency axis implies that perfect absorption can be theoretically achieved with this system configuration, at this particular frequency.

Although, in this study the optimisation is automated by the algorithm of the SQP method, the tuning process is less important in the sense of finding the optimal design. The tuning trajectories still reveals details of the internal mechanism of absorption, with regards to each different dimension of the configuration. This may help to find other optimal designs, for more customised situations, where frequency band and/or material layer thickness could be constraint.

Figure 2.7b) shows the absorption coefficient of the optimal configuration, at normal incidence, calculated with the different semi-analytical methods, predicted numerically by FEM and measured experimentally.

At $f = 338.5$ Hz, perfect absorption can be observed. The maximum absorption measured experimentally was $\alpha = 0.97$, as shown in the inset of Fig. 2.7b). This small discrepancy between the measurements and the models can be caused by experimental reasons including the non perfect fitting of the slit on the impedance tube and the excitation of plate modes of the solid medium that composes the metamaterial.

The structure presents a peak of perfect absorption at $f = 338.5$ Hz (different than that of the HR, $f_{\mathrm{HR}} = 370$ Hz) with a thickness L equals to 88 times of the corresponding wavelength. Theoretically, this ratio of sub-wavelength given by the optimisation algorithm could be as high as 99, but in that case all the effects brought by the critical coupling are masked by the elastic resonances of the structure, as the building material of the absorber cannot be considered as perfectly rigid at extremely low frequency.

2.9 Absorption in diffuse field

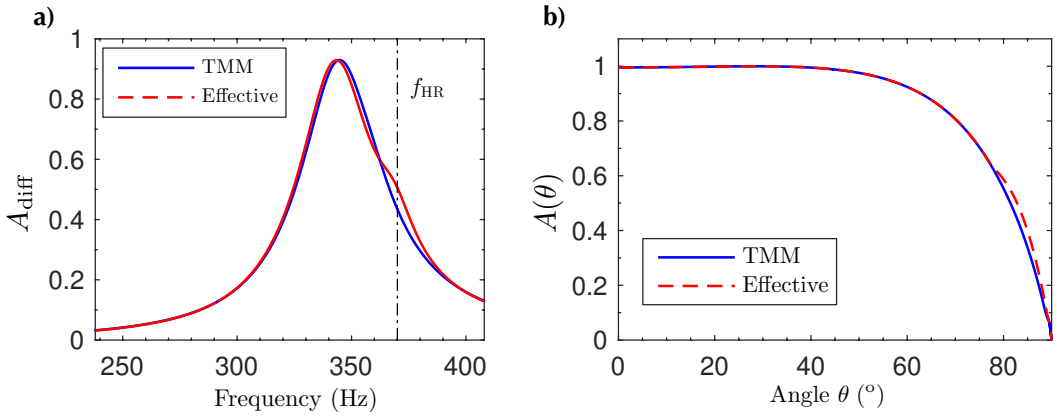

FIGURE 2.8: a) Absorption peak as a function of the angle of incidence calculated by the effective parameters (dashed red), transfer matrix method (continuous blue); b) Absorption coefficient in diffuse field as a function of frequency.

Now, we consider an oblique plane wave incidence facing the optimal design, with incidence angle θ, as the effective material could be considered as anisotropic. The reflection and absorption coefficients of the effective material layer are calculated with TMM

and EPM, with which the actual shape of the structure can be ignored [75].

Figure. 2.8a) shows the absorption in diffuse field [88] calculated as

$$A_{\text{diff}}(f) = 2\int_0^{\pi/2} A(\theta, f)\cos(\theta)\sin(\theta)\mathrm{d}\theta, \tag{2.9.1}$$

where at the working frequency it reaches a value of $\alpha_{\text{diff}} = 0.93$, showing the quasi-omnidirectional behavior of the absorption in this sub-wavelength structure.

Figure. 2.8b) shows the absorption of the metamaterial panel as a function of the angle of incidence at 338.5 Hz. It can be observed that almost perfect absorption is obtained for a broad range of angles, being $\alpha > 0.90$ for incident waves with $\theta < 60°$.

Conclusion

In this Chapter, an impervious array of square-periodic Helmholtz resonators of square cross-section is studied. Several theoretical approaches, such as modal expansion model, the corresponding effective parameters model, the transfer matrix method and the finite element method are used to derive the characteristics of dispersion, attenuation and absorption of this proposed structure.

Designs of panel for perfect sound absorption with sub-wavelength size are conceived by considering slow sound propagation and the critical coupling technique. Moreover, an optimal design with a minimal material thickness has been given by an optimisation algorithm. The perfect absorption of sound brought by this design is experimentally verified, being at 338.5 Hz with a panel thickness of $L = \lambda/88 = 1.1$ cm.

Furthermore, the tuning trajectories related to various geometrical elements are visualised in the complex frequency plane. It opens a gateway to better understand the internal mechanism of reflection, absorption of acoustic material [89]. And this can be a very useful and intuitive tool in the designing of perfect absorption metamaterial with strong dissipations [90].

In addition, several theoretical approaches have been presented and validated experimentally, where their limits of validity are discussed. In order to provide accurate models, we have presented the design with standard Helmholtz resonators. However, the thickness of the structure can be even reduced by engineering the geometry using coiled-up channels or embedding the neck into the cavity of the HRs [21, 77].

It is also worth noting here that the total panel size in the vertical dimension x_1 is also sub-wavelength $d = \lambda/6.5 = 14.5$ cm. The sub-wavelength feature of the presented structure provides perfect absorption for a wide range of incident angles. This quasi-omnidirectional sound absorber can be employed in realistic scenarios where the omnidirectional feature is mandatory, such as sound diffusers [91].

These promising results give us very useful tools and methodologies, which open the possibilities to study different configurations based on these metamaterials and to extend the results to broadband and/or omnidirectional perfect absorption with deep subwavelength structures, such as the idealized straw stack which consists of tightly packed three-dimensional periodic arrangement of straight hollow cylindrical tubes.

Part II

Anisotropic Acoustic Metamaterial for Sound Absorption

Chapter 3

Homogenisation of the anisotropic porous medium

In this Chapter, the effective fluid properties of rigid-framed porous material are studied. A homogenisation procedure on the macro- and micro-scale field in the porous medium is recalled and presented step by step. The properties of effective viscous and thermal permeabilities are analysed, and the semi-phenomenological JCAL model is recalled.

Contents

Introduction

The theoretical model for the acoustic analysis of the porous materials has been developed since Darcy's work on a fluid flow through a porous medium during his engineering career in the city of Dijon, France [92].

Since then, several models have been proposed. The acoustic porous material model based on the hypothesis of rigid skeleton started in the 20th century, first by Zwikker & Kosten [11]. In 1956, Biot went one step further and proposed a vibro-acoustic biphasic model consisting of a porous elastic skeleton saturated by a compressible viscous fluid [12, 13]. In 1987, Johnson *et al.* proposed a semi-phenomenological model to describe the complex density of an acoustic porous material with a perfectly-rigid (motionless) skeleton with arbitrary pore shapes [7]. In 1991, Champoux and Allard introduced the dynamic bulk modulus for the same kind of porous material [8]. Then, Lafarge *et al.* introduced a new parameter, the static thermal permeability, in order to better describe the low-frequency behaviour of thermal effects [10]. This model is called Johnson-Champoux-Allard-Lafarge (JCAL) model.

In parallel, the homogenisation method for periodic structures was introduced by Sanchez-Palencia for scaled flow problem in heterogenous complex media in elasticity, heat conduction, electromagnetism, and acoustics [50]. This method gives the possibility to describe an equivalent macro-scale continuous phenomenon from the fundamental principles applied at the microstructural scale.

In acoustics, many researchers have contributed to the study of acoustic porous materials through homogenisation of periodic media. Auriault, together with Sanchez-Palencia first studied the saturated deformable porous media in 1977 [51, 93]. Asymptotic limit of the dynamic viscous permeability tensor was also studied by Auriault in 1985 [94]. Auriault *et al.* were also the first to perform experiments on the dynamic complex-valued frequency-dependent visco-inertial permeability in 1985 [94], followed by Sheng in 1989 [95], although their high-frequency limit was not accurately described.

Furthermore, Boutin *et al.* investigated the rigid porous media with inner resonators both saturated by the same gas, both theoretically and experimentally [52, 96] in simplified configurations. More recently, the theory and concept of permeo-elasticity was developed by Venegas & Boutin [97].

In this Chapter, the homogenisation of an anisotropic porous acoustic material is recalled. The approach to this permeable array relies on the homogenisation of the idealised periodic arrangement of Representative Elementary Volume (REV) [51]. An analogy is established between the homogenised model [51] and classic porous material model [9] on the definition of dynamic viscous and thermal permeabilities.

The characteristic frequency-independent static parameters are accordingly extracted, to approximate the effective behaviour of this anisotropic penetrable array in different configurations, following the numerical resolution of the homogenised cell problem [7, 10].

3.1 Unit cell problem

We begin the homogenisation process by defining the problem at hand, see Fig. 3.1. In the fluid domain Ω_f of the unit cell Ω with the rigid surface Γ, the governing equations are:

- Mass conservation equation:
$$\operatorname{div} \boldsymbol{v} = \mathrm{i}\omega \frac{\rho}{\rho_0}. \tag{3.1.1}$$
- Heat transfer equation for perfect gas:
$$\operatorname{div}(\lambda \mathbf{grad} \tau) = -\mathrm{i}\omega(\rho_0 c_p \tau - p). \tag{3.1.2}$$
- State equation for perfect gas:
$$\frac{p}{P_0} = \frac{\rho}{\rho_0} + \frac{\tau}{T_0}. \tag{3.1.3}$$
- Dynamic equilibrium of stress:
$$\operatorname{div} \boldsymbol{\sigma} = -\mathrm{i}\omega\rho_0 \boldsymbol{v}. \tag{3.1.4}$$
- Rheological relation for Newtonian fluid:
$$\boldsymbol{\sigma} = -p\boldsymbol{I} + 2\eta \boldsymbol{D}(\boldsymbol{v}). \tag{3.1.5}$$

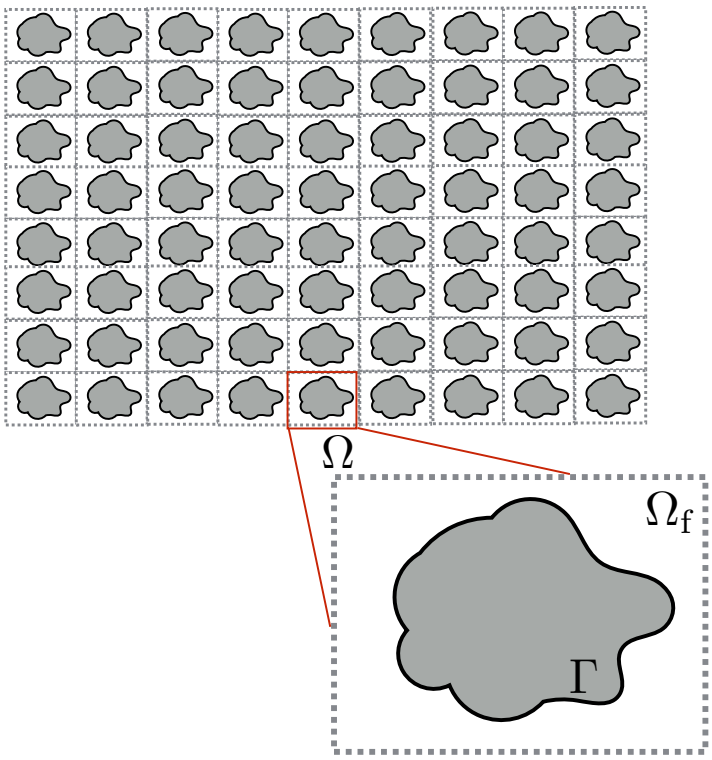

FIGURE 3.1: General schematic of the porous medium: periodic arrangement of the unit cell Ω.

In previous equations, p is the excess pressure field; τ is excess temperature; ρ is the excess density; v is the particle velocity; $\boldsymbol{D}(\boldsymbol{v})$ is the strain rate, with $\boldsymbol{D} = (\mathbf{grad} + {}^{T}\mathbf{grad})/2$; and $\boldsymbol{I}$ is the identity tensor.

The following relation stemming from the state equation of perfect gas is also noted for later use,

$$\frac{P_0}{T_0} = \rho_0 c_p (1 - 1/\gamma). \tag{3.1.6}$$

The following boundary conditions are applied at the solid front Γ (normal $\boldsymbol{n}$ directed at fluid):

$$\text{no-slip condition (adherence): } \boldsymbol{v} = \mathbf{0} \qquad \text{on } \Gamma, \tag{3.1.7a}$$

$$\text{no thermal transfer: } \tau = 0 \qquad \text{on } \Gamma. \tag{3.1.7b}$$

Local periodicity conditions are applied to the boundaries of Ω, as we will discuss in the following section.

3.2 Scale separation and two-scale description

Homogenisation process relies on the separation of the micro and macro scales. The whole problem, including the cell problem and the operators, are now re-described in two scales.

3.2.1 Scaled variables

The problem is studied by assuming that a scale separation is satisfied, whereby the wavelength is much larger than the characteristic size ℓ of REV Ω. That is quantified by the scale parameter:

$$\epsilon = \frac{\ell\omega}{c} \ll 1. \tag{3.2.1}$$

That introduces two scales in the system:

- the microscopic scale with the characteristic length ℓ, related to the micro-structure;
- the macroscopic scale with the characteristic length $L \gg \ell$, related to the wave propagation.

To describe the system at both scales, the usual space variable $\boldsymbol{X}$ is normalised by either length:

$$\boldsymbol{x}^* = \boldsymbol{X}/L \quad ; \qquad \boldsymbol{y}^* = \boldsymbol{X}/\ell. \tag{3.2.2}$$

That provides the two space variables:

$$\boldsymbol{x} = L\boldsymbol{x}^* \quad ; \qquad \boldsymbol{y} = L\boldsymbol{y}^* = \epsilon^{-1}\boldsymbol{x}. \tag{3.2.3}$$

The fields are set to depend on both space variables:

$$p(\boldsymbol{x}, \boldsymbol{y}) \quad ; \quad \boldsymbol{v}(\boldsymbol{x}, \boldsymbol{y}) \quad ; \quad \tau(\boldsymbol{x}, \boldsymbol{y}) \quad ; \quad \rho(\boldsymbol{x}, \boldsymbol{y}), \tag{3.2.4}$$

where the fields are Ω-periodicity with respect to $\boldsymbol{y}$.

The use of the two space variables leads to modify the differential operators as:

$$\begin{aligned}
&\mathrm{div}() = \mathrm{div}_x() + \epsilon^{-1}\mathrm{div}_y(),\\
&\mathbf{grad}() = \mathbf{grad}_x() + \epsilon^{-1}\mathbf{grad}_y(),\\
&\boldsymbol{D}() = \boldsymbol{D}_x() + \epsilon^{-1}\boldsymbol{D}_y(),
\end{aligned}$$

where div_x is the divergence with respect to $\boldsymbol{x}$ and div_y is the divergence with respect to $\boldsymbol{y}$, and likewise for **grad** and $\boldsymbol{D}$.

3.2.2 Scaled equations

Situations are considered where viscous and thermal phenomena occur at the microscopic scale. That leads to rescale the governing equations in the framework of the two-scale description, with the thermal conductivity and the viscosity equally rescaled as,

$$\lambda = \epsilon^2\lambda^{(2)} \quad ; \qquad \eta = \epsilon^2\eta^{(2)}. \tag{3.2.5}$$

The rescaled governing equations are

- Mass conservation equation:

$$\left\{\mathrm{div}_x + \epsilon^{-1}\mathrm{div}_y\right\}\boldsymbol{v}(\boldsymbol{x},\boldsymbol{y}) = \mathrm{i}\omega\frac{\rho(\boldsymbol{x},\boldsymbol{y})}{\rho_0}. \tag{3.2.6}$$

- Heat transfer equation for perfect gas:

$$\begin{aligned}
\epsilon^2\lambda^{(2)}\left\{\mathrm{div}_x + \epsilon^{-1}\mathrm{div}_y\right\}\left\{\mathbf{grad}_x + \epsilon^{-1}\mathbf{grad}_y\right\}\tau(\boldsymbol{x},\boldsymbol{y})\\
= -\mathrm{i}\omega(\rho_0 c_p\tau(\boldsymbol{x},\boldsymbol{y}) - p(\boldsymbol{x},\boldsymbol{y})).
\end{aligned} \tag{3.2.7}$$

- State equation for perfect gas:

$$\frac{p(\boldsymbol{x},\boldsymbol{y})}{P_0} = \frac{\rho(\boldsymbol{x},\boldsymbol{y})}{\rho_0} + \frac{\tau(\boldsymbol{x},\boldsymbol{y})}{T_0}. \tag{3.2.8}$$

- Dynamic equilibrium of stress:

$$\left\{\mathrm{div}_x + \epsilon^{-1}\mathrm{div}_y\right\}\boldsymbol{\sigma}(\boldsymbol{x},\boldsymbol{y}) = -\mathrm{i}\omega\rho_0\boldsymbol{v}(\boldsymbol{x},\boldsymbol{y}). \tag{3.2.9}$$

- Rheological relation for Newtonian fluid:

$$\boldsymbol{\sigma}(\boldsymbol{x},\boldsymbol{y}) = -p(\boldsymbol{x},\boldsymbol{y})\boldsymbol{I} + 2\epsilon^2\eta^{(2)}\left\{\boldsymbol{D}_x + \epsilon^{-1}\boldsymbol{D}_y\right\}(\boldsymbol{v}(\boldsymbol{x},\boldsymbol{y})). \tag{3.2.10}$$

3.2.3 Asymptotic expansions

Due to the presence of ϵ in the governing equations, all the variables are expanded asymptotically in powers of ϵ:

$$\begin{aligned}
p(\boldsymbol{x},\boldsymbol{y}) &= p^{(0)}(\boldsymbol{x},\boldsymbol{y}) + \epsilon p^{(1)}(\boldsymbol{x},\boldsymbol{y}) + \epsilon^2 p^{(2)}(\boldsymbol{x},\boldsymbol{y}) + \cdots,\\
\boldsymbol{v}(\boldsymbol{x},\boldsymbol{y}) &= \boldsymbol{v}^{(0)}(\boldsymbol{x},\boldsymbol{y}) + \epsilon\boldsymbol{v}^{(1)}(\boldsymbol{x},\boldsymbol{y}) + \epsilon^2\boldsymbol{v}^{(2)}(\boldsymbol{x},\boldsymbol{y}) + \cdots,\\
\tau(\boldsymbol{x},\boldsymbol{y}) &= \tau^{(0)}(\boldsymbol{x},\boldsymbol{y}) + \epsilon\tau^{(1)}(\boldsymbol{x},\boldsymbol{y}) + \epsilon^2\tau^{(2)}(\boldsymbol{x},\boldsymbol{y}) + \cdots,\\
\rho(\boldsymbol{x},\boldsymbol{y}) &= \rho^{(0)}(\boldsymbol{x},\boldsymbol{y}) + \epsilon\rho^{(1)}(\boldsymbol{x},\boldsymbol{y}) + \epsilon^2\rho^{(2)}(\boldsymbol{x},\boldsymbol{y}) + \cdots.
\end{aligned}$$

The bracketed superscript $^{(*)}$ represents the order of the terms in the asymptotic expansions.

Substituting these expansions in the re-scaled governing equations, the following asymptotic equations are obtained for leading order 0 and 1. Terms of equal power of ϵ are collected to describe the following asymptotic problems:

- Mass conservation equation:

$$\mathrm{div}_y \boldsymbol{v}^{(0)} = 0 \,, \tag{3.2.11a}$$
$$\mathrm{div}_x \boldsymbol{v}^{(0)} + \mathrm{div}_y \boldsymbol{v}^{(1)} = \mathrm{i}\omega \rho^{(0)}/\rho_0. \tag{3.2.11b}$$

- Heat transfer equation:

$$\mathrm{div}_y(\lambda^{(2)} \mathbf{grad}_y \tau^{(0)}) \;\; = \;\; -\mathrm{i}\omega(\rho_0 c_p \tau^{(0)} - p^{(0)}). \tag{3.2.12}$$

- State equation for perfect gas:

$$\frac{p^{(0)}}{P_0} = \frac{\rho^{(0)}}{\rho_0} + \frac{\tau^{(0)}}{T_0}. \tag{3.2.13}$$

- Dynamic equilibrium of stress:

$$\mathrm{div}_y \boldsymbol{\sigma}^{(0)} = 0 \,, \tag{3.2.14a}$$
$$\mathrm{div}_x \boldsymbol{\sigma}^{(0)} + \mathrm{div}_y \boldsymbol{\sigma}^{(1)} = -\mathrm{i}\omega \rho_0 \boldsymbol{v}^{(0)}. \tag{3.2.14b}$$

- Rheological relation:

$$\boldsymbol{\sigma}^{(0)} = -p^{(0)} \boldsymbol{I} \,, \tag{3.2.15a}$$
$$\boldsymbol{\sigma}^{(1)} = -p^{(1)} \boldsymbol{I} + 2\eta^{(2)} \boldsymbol{D}_y(\boldsymbol{v}^{(0)}). \tag{3.2.15b}$$

3.3 Resolution at the leading order

In this section, the problem is solved up to the leading order for the effective macroscopic description. Divergence theorem and partial integrations are used and each are formulated for local problems.

3.3.1 Macro-scale pressure

Now, we look for the macro-scale pressure $p^{(0)}$, by considering Eqs. (3.2.14a) and (3.2.15a):

$$\mathrm{div}_y \boldsymbol{\sigma}^{(0)} = 0, \quad , \boldsymbol{\sigma}^{(0)} = -p^{(0)} \boldsymbol{I}.$$

These equations show that at the local scale and at the leading order, the fluid equilibrium is quasi-static while the stress is only driven by the pressure $p^{(0)}$. Combining these equations yields:

$$\mathbf{grad}_y p^{(0)}(\boldsymbol{x}, \boldsymbol{y}) = 0, \tag{3.3.1}$$

which shows that the pressure $p^{(0)}$ is independent from the micro-variable $\boldsymbol{y}$.

It means that $p^{(0)}$ is purely macroscopic and is uniform over the cell Ω:

$$p^{(0)}(\boldsymbol{x},\boldsymbol{y}) = p^{(0)}(\boldsymbol{x}). \tag{3.3.2}$$

3.3.2 Thermal problem

Equation. (3.2.12) for the temperature field $\tau^{(0)}(\boldsymbol{x},\boldsymbol{y})$ is given by:

$$\begin{cases} \lambda \operatorname{div}_y \mathbf{grad}_y \tau^{(0)}(\boldsymbol{x},\boldsymbol{y}) + \mathrm{i}\omega\rho_0 c_p \tau^{(0)}(\boldsymbol{x},\boldsymbol{y}) = \mathrm{i}\omega p^{(0)}(\boldsymbol{x}), & \text{(3.3.3a)} \\ \tau^{(0)} = 0, \text{ at } \Gamma, & \text{(3.3.3b)} \\ \tau^{(0)} : \ \Omega\text{-periodic with } y. & \text{(3.3.3c)} \end{cases}$$

This is a thermal diffusion problem. To show that it is well-posed, and justify the existence and uniqueness of the field $\tau^{(0)}(\boldsymbol{x},\boldsymbol{y})$, a weak formulation of the problem with $\hat{\tau}$ is considered as the thermally-admissible test-field.

To do so, Eq. (3.2.12) is multiplied by $\hat{\tau}$ and integrated over the fluid volume Ω_f, which yields:

$$\begin{aligned} \frac{1}{|\Omega|_y}\left(\lambda^{(2)}\int_{\Omega_f}\hat{\tau}\operatorname{div}_y\mathbf{grad}_y\tau^{(0)}d\Omega_y\right) + \frac{1}{|\Omega|_y}\left(\mathrm{i}\omega\rho_0 c_p\int_{\Omega_f}\hat{\tau}\tau^{(0)}d\Omega_y\right) \\ = \frac{1}{|\Omega|_y}\left(\mathrm{i}\omega\int_{\Omega_f}\hat{\tau}p^{(0)}(\boldsymbol{x})d\Omega_y\right). \end{aligned} \tag{3.3.4}$$

Accounting for the boundary and periodicity conditions and the fact that $p^{(0)}$ is independent from $\boldsymbol{y}$, Eq. (3.3.4) is transformed, using differential identity, by applying the divergence theorem:

$$\int_{\Omega_f}\mathbf{grad}_y\hat{\tau}\cdot\mathbf{grad}_y\tau^{(0)}d\Omega_y - \frac{\mathrm{i}\omega\rho_0 c_p}{\lambda^{(2)}}\int_{\Omega_f}\hat{\tau}\tau^{(0)}d\Omega_y = -\frac{\mathrm{i}\omega p^{(0)}(\boldsymbol{x})}{\lambda^{(2)}}\left(\int_{\Omega_f}\hat{\tau}d\Omega_y\right). \tag{3.3.5}$$

Using the Lax-Milgram theorem [98], there exists one and only one field $\tau^{(0)}(\boldsymbol{x},\boldsymbol{y})$. Since it is linearly driven by $-\mathrm{i}\omega p^{(0)}(x)/\lambda$, it can be written in the following form:

$$\tau^{(0)}(\boldsymbol{x},\boldsymbol{y}) = \frac{-\mathrm{i}\omega p^{(0)}(\boldsymbol{x})}{\lambda^{(2)}}\theta^{(2)}(\boldsymbol{y}), \tag{3.3.6}$$

where the field $\theta^{(2)}(\boldsymbol{y})$ is the particular solution of the following cell problem:

$$\frac{1}{|\Omega|_y}\int_{\Omega_f}\mathbf{grad}_y\theta^{(2)}\cdot\mathbf{grad}_y\hat{\tau}d\Omega_y - \frac{1}{|\Omega|_y}\frac{\mathrm{i}\omega\rho_0 c_p}{\lambda^{(2)}}\int_{\Omega_f}\theta^{(2)}\hat{\tau}d\Omega_y = \frac{1}{|\Omega|_y}\int_{\Omega_f}\hat{\tau}d\Omega_y\,. \tag{3.3.7}$$

This last equation can be reformulated in the following system (strong formulation):

$$\begin{cases} \operatorname{div}_y\mathbf{grad}_y\theta^{(2)} + \dfrac{\mathrm{i}\omega\rho_0 c_p}{\lambda^{(2)}}\theta^{(2)} = -1, & \text{(3.3.8a)} \\ \theta^{(2)} = 0 \text{ on } \Gamma, & \text{(3.3.8b)} \\ \theta^{(2)}, \ \Omega\text{ -periodic.} & \text{(3.3.8c)} \end{cases}$$

The solution of this equation by numerical methods gives out the frequency-dependent dynamic thermal permeability, as discussed later in Sec. 3.3.4.

3.3.3 Macroscopic law of mass conservation

Recalling Eq. (3.2.11b):

$$\mathrm{div}_x \boldsymbol{v}^{(0)} + \mathrm{div}_y \boldsymbol{v}^{(1)} \quad = \quad \mathrm{i}\omega \rho^{(0)}/\rho_0,$$

this shows that the excess density is driven by particle velocity at both the macro-scale on leading order and at micro-scale on first order.

Then, taking on volume average, the equation writes as,

$$\frac{1}{|\Omega|}\int_{\Omega_f} \mathrm{div}_x \boldsymbol{v}^{(0)} d\Omega_y + \frac{1}{|\Omega|}\int_{\Omega_f} \mathrm{div}_y \boldsymbol{v}^{(1)} d\Omega_y = \mathrm{i}\omega \frac{1}{|\Omega|}\int_{\Omega_f} \frac{\rho^{(0)}}{\rho_0} d\Omega_y \,. \tag{3.3.9}$$

As determined by periodicity and boundary conditions,

$$\frac{1}{|\Omega|}\int_{\Omega_f} \mathrm{div}_y \boldsymbol{v}^{(1)} d\Omega_y = \frac{1}{|\Omega|}\int_{\partial\Omega_f} \boldsymbol{v}^{(1)} \cdot \boldsymbol{n}_y d\Gamma_y = 0 \,.$$

Permuting $y-$integral with $x-$divergence, the macroscopic law of mass conservation takes the form:

$$\mathrm{div}_{\boldsymbol{x}} \langle \boldsymbol{v}^{(0)} \rangle = \mathrm{i}\omega \frac{\langle \rho^{(0)} \rangle}{\rho_0}, \tag{3.3.10}$$

where $\langle * \rangle = \dfrac{1}{|\Omega|_y} \int_{\Omega_f} * \, d\Omega_y$.

3.3.4 Effective compressiblity

Consider now the state equation of perfect gas Eq. (3.1.3):

$$\frac{p^{(0)}}{P_0} = \frac{\rho^{(0)}}{\rho_0} + \frac{\tau^{(0)}}{T_0}.$$

Averaging over the fluid volume provides :

$$\frac{\langle \rho^{(0)} \rangle}{\rho_0} = \frac{\phi p^{(0)}}{P_0} - \frac{\langle \tau^{(0)} \rangle}{T_0}, \tag{3.3.11}$$

as $p^{(0)}$ is independent from $\boldsymbol{y}$.

Reshaping Eq. (3.3.6) correspondingly, the mean value of the excess temperature reads as:

$$\langle \tau^{(0)} \rangle = \frac{-\mathrm{i}\omega p^{(0)}(\boldsymbol{x})}{\lambda^{(2)}} \Theta^{(2)}, \tag{3.3.12}$$

where Θ is the thermal permeability, and it is given by averaging θ over the REV:

$$\Theta^{(2)} = \frac{1}{|\Omega|}\int_{\Omega_f} \theta^{(2)} d\Omega_y \,. \tag{3.3.13}$$

Substituting Eq. (3.3.12) into (3.3.11) leads to the relation:

$$\frac{\langle \rho^{(0)} \rangle}{\rho_0} = \phi \beta_f \frac{p^{(0)}}{\gamma P_0}, \tag{3.3.14}$$

where β is the effective dynamic compressibility factor of Ω_f and reads:

$$\beta = \frac{B_0}{B} = \gamma + \mathrm{i}\omega \frac{\rho_0 c_p}{\lambda}(\gamma - 1)\Theta^{(2)}. \tag{3.3.15}$$

3.3.5 Viscous problem

Then, we recall Eqs.(3.2.14a) to (3.2.15b) at the leading order,

$$\begin{cases} \mathrm{div}_y \boldsymbol{v}^{(0)} = 0, & \text{(3.3.16a)} \\ \mathrm{div}_x \boldsymbol{\sigma}^{(0)} + \mathrm{div}_y \boldsymbol{\sigma}^{(1)} = -\mathrm{i}\omega\rho_0 \boldsymbol{v}^{(0)}, & \text{(3.3.16b)} \\ \boldsymbol{\sigma}^{(0)} = -p^{(0)} \boldsymbol{I}, & \text{(3.3.16c)} \\ \boldsymbol{\sigma}^{(1)} = -p^{(1)} \boldsymbol{I} + 2\eta^{(2)} \boldsymbol{D}_y(\boldsymbol{v}^{(0)}), & \text{(3.3.16d)} \\ \boldsymbol{v}^{(0)} = 0, \text{ at } \Gamma, & \text{(3.3.16e)} \\ v^{(0)} : \Omega\text{-periodic with } y. & \text{(3.3.16f)} \end{cases}$$

Combining Eq. (3.2.14b) and Eq. (3.2.15a) provides the following problem of incompressible Stokes-flow through REV Ω:

$$\begin{cases} \mathrm{div}_y \boldsymbol{v}^{(0)} = 0, & \text{(3.3.17a)} \\ -\mathrm{i}\omega\rho_0 \boldsymbol{v}^{(0)} = -\mathbf{grad}_x p^{(0)} - \mathbf{grad}_y p^{(1)} + \mathrm{div}_y \left[2\eta^{(2)} \boldsymbol{D}_y(\boldsymbol{v}^{(0)}) \right], & \text{(3.3.17b)} \\ \boldsymbol{v}^{(0)} = 0, \text{ at } \Gamma, & \text{(3.3.17c)} \\ v^{(0)} : \Omega\text{-periodic with } y. & \text{(3.3.17d)} \end{cases}$$

The weak formulation of this equation sets the requirement for a kinematically-admissible test-field $\hat{\boldsymbol{w}}$, that

$$\hat{\boldsymbol{w}} \quad \Omega\text{-periodic} \quad ; \quad \mathrm{div}_y \hat{\boldsymbol{w}} = 0 \text{ and } \hat{\boldsymbol{w}} = 0 \text{ on } \Gamma. \tag{3.3.18}$$

Here, $\hat{\boldsymbol{w}}$ is multiplied to Eq. (3.3.17a), the integration of the equation over Ω_f gives:

$$\begin{aligned} \frac{1}{|\Omega|_y} \left(\int_{\Omega_f} \hat{\boldsymbol{w}} \, \mathrm{div}_y \boldsymbol{\sigma}^{(1)} d\Omega_y \right) + \frac{1}{|\Omega|_y} \left(\mathrm{i}\omega\rho_0 \int_{\Omega_f} \hat{\boldsymbol{w}} \cdot \boldsymbol{v}^{(0)} d\Omega_y \right) \\ = \frac{1}{|\Omega|_y} \left[\left(\int_{\Omega_f} \hat{\boldsymbol{w}} d\Omega_y \right) \cdot \mathbf{grad}_x p^{(0)} \right]. \end{aligned} \tag{3.3.19}$$

Using the divergence theorem, the first term of Eq. (3.3.19) turns to

$$\int_{\Omega_f} \hat{\boldsymbol{w}} \, \mathrm{div}_y \boldsymbol{\sigma}^{(1)} d\Omega_y = \int_{\partial\Omega_f} \hat{\boldsymbol{w}} \cdot (\boldsymbol{\sigma}^1 \cdot \boldsymbol{n}) dS_y - \int_{\Omega_f} \mathbf{grad}_y \hat{\boldsymbol{w}} : \boldsymbol{\sigma}^1 d\Omega_y. \tag{3.3.20}$$

The boundary conditions and periodicity determine that $\hat{\boldsymbol{w}} \cdot (\boldsymbol{\sigma}^1 \cdot \boldsymbol{n}) = 0$, which sets

$$\int_{\Omega_f} \hat{\boldsymbol{w}} \, \mathrm{div}_y \boldsymbol{\sigma}^1 d\Omega_y = -\int_{\Omega_f} \mathbf{grad}_y \hat{\boldsymbol{w}} : \boldsymbol{\sigma}^1 d\Omega_y. \tag{3.3.21}$$

Substituting Eq. (3.2.15b) to Eq (3.3.21), taking into consideration of the symmetry in $\boldsymbol{\sigma}^{(1)}$

$$\int_{\Omega_f} \mathrm{div}_y \hat{\boldsymbol{w}} : \boldsymbol{\sigma}^1 d\Omega_y = -\int_{\Omega_f} p^1 \mathrm{div}_y \hat{\boldsymbol{w}} d\Omega_y + 2\eta^{(2)} \int_{\Omega_f} \boldsymbol{D}_y(\boldsymbol{v}^{(0)}) : \boldsymbol{D}_y(\hat{\boldsymbol{w}}) d\Omega_y. \tag{3.3.22}$$

As indicated in Eq. (3.3.18), $\mathrm{div}_y \hat{\boldsymbol{w}} = 0$,

$$\int_{\Omega_f} \hat{\boldsymbol{w}} \, \mathrm{div}_y \boldsymbol{\sigma}^1 d\Omega_y = -2\eta^{(2)} \int_{\Omega_f} \boldsymbol{D}_y(\boldsymbol{v}^{(0)}) : \boldsymbol{D}_y(\hat{\boldsymbol{w}}) d\Omega_y. \tag{3.3.23}$$

Finally, Eq. (3.3.19) yields:

$$\begin{aligned} \frac{1}{|\Omega|_y} \left(2 \int_{\Omega_f} \boldsymbol{D}_y(\boldsymbol{v}^{(0)}) : \boldsymbol{D}_y(\hat{\boldsymbol{w}}) d\Omega_y \right) - \frac{1}{|\Omega|_y} \left(\frac{\mathrm{i}\omega\rho_0}{\eta^{(2)}} \int_{\Omega_f} \hat{\boldsymbol{w}} \cdot \boldsymbol{v}^{(0)} d\Omega_y \right) \\ = \frac{1}{|\Omega|_y} \left[- \left(\int_{\Omega_f} \hat{\boldsymbol{w}} d\Omega_y \right) \cdot \frac{\mathbf{grad}_x p^{(0)}}{\eta^{(2)}} \right]. \end{aligned} \tag{3.3.24}$$

Using the Lax-Milgram theorem [98], there exists one and only one field $\boldsymbol{v}^{(0)}$ that is linearly driven by each component of $\mathbf{grad}_x p^{(0)}$, which takes the form:

$$\boldsymbol{v}^{(0)}(\boldsymbol{x}, \boldsymbol{y}) = -\frac{\left[\boldsymbol{k}^{(2)}(\boldsymbol{y})\right]}{\eta^{(2)}} \mathbf{grad}_x p^{(0)}(\boldsymbol{x}), \tag{3.3.25}$$

where the j-th column vectors $\boldsymbol{k}_j^{(2)} = \left[\boldsymbol{k}^{(2)}(y)\right] \boldsymbol{e}_j$ of the the tensor $\left[\boldsymbol{k}^{(2)}(y)\right]$ is the particular solution of Eq. (3.3.24) when Eq. (3.3.25) is substituted, for the pressure gradient $\mathbf{grad}_x p^{(0)} = -\eta^{(2)} \boldsymbol{e}_j$.

The effective velocity is given by the following generalised Darcy's Law:

$$\langle \boldsymbol{v}^{(0)} \rangle = -\frac{[\boldsymbol{K}^{(2)}]}{\eta^{(2)}} \mathbf{grad}\, p^{(0)}, \tag{3.3.26}$$

where $[\boldsymbol{K}^{(2)}]$ is the complex frequency-dependent tensor of dynamic viscous integral permeability reads:

$$[\boldsymbol{K}^{(2)}] = \frac{1}{|\Omega|_y} \int_{\Omega_f} [\boldsymbol{k}^{(2)}] d\Omega_y. \tag{3.3.27}$$

Taking into account of the solution form in Eq. (3.3.25), with the excitation $\boldsymbol{e}_j$, the viscous cell problem Eq. (3.3.16) in strong formulation, rewrites as,

$$\begin{cases} \mathrm{div}_y(\boldsymbol{k}_j^{(2)}) = 0, & \text{(3.3.28a)} \\ \mathrm{div}_y \mathbf{grad}_y \boldsymbol{k}_j^{(2)} + \dfrac{\mathrm{i}\omega\rho_0}{\eta^{(2)}} \boldsymbol{k}_j^{(2)} = \mathbf{grad}_y(\alpha_j^{(1)}) - \boldsymbol{e}_j, & \text{(3.3.28b)} \\ \boldsymbol{k}_j^{(2)} = 0, \text{ on } \Gamma, & \text{(3.3.28c)} \\ \langle \alpha_j^{(1)} \rangle = 0, \text{ on } \Gamma, & \text{(3.3.28d)} \\ (\boldsymbol{k}_j^{(2)}, \alpha_j), \ \Omega \text{ -periodic}, & \text{(3.3.28e)} \end{cases}$$

where α_j is the scalar "pressure" associated to the vector $\boldsymbol{k}_j$. The vector $\boldsymbol{\alpha} = \sum \alpha_j \boldsymbol{e}_j$ is related to pressure field $p^{(1)}$ as the following relation shows,

$$p^{(1)} = -\boldsymbol{\alpha}^{(1)} \cdot \mathbf{grad}_x p^{(0)}. \tag{3.3.29}$$

The solution of Eq. (3.3.28) by numerical methods gives out the frequency-dependent dynamic viscous permeability $[\boldsymbol{K}^{(2)}]$, as described by Eq. (3.3.29).

3.3.6 Rescaled equations and homogenised description

To summarise all the theory shown in this section, we present the rescaled solution at the dominant order (0). The physical constants are rescaled, as $\lambda = \epsilon^2 \lambda^{(2)}$ and $\eta = \epsilon^2 \eta^{(2)}$. We define the macroscopic fields from their value at the micro-scale:

- the pressure field $P = p^{(0)}$ which is quasi-uniform over the REV;
- the particle velocity $\boldsymbol{V} = \langle \boldsymbol{v}^{(0)} \rangle$, which is the average of the particle velocity over the fluid in the REV;
- the excess density $\langle \rho \rangle = \langle \rho^{(0)} \rangle$ which is the average of the excess density over the fluid in the REV.

We define the equations governing the macro-fields:

- The macroscopic law of mass conservation, which takes the same form as the law of mass conservation at the local scale:

$$\mathrm{div} \boldsymbol{V} = \mathrm{i}\omega \frac{\langle \rho \rangle}{\rho_0}. \tag{3.3.30}$$

- The relation of dynamic compressibility:

$$\frac{\langle \rho \rangle}{\rho_0} = \phi\beta \frac{p}{\gamma P_0} \quad \text{where} \quad \beta = \gamma + \mathrm{i}\omega \frac{\rho_0 c_p}{\lambda}(\gamma - 1)\Theta, \tag{3.3.31}$$

  where β is the effective dynamic compressibility factor and Θ the dynamic thermal permeability;

- The generalised Darcy's Law (which is fundamentally different from the Navier-Stokes equation that holds at the local scale):

$$\boldsymbol{V} = -\frac{[\boldsymbol{K}]}{\eta} \mathbf{grad}\, p, \tag{3.3.32}$$

  where $[\boldsymbol{K}]$ is the tensor of dynamic viscous-inertial permeability.

We define the effective constitutive parameters Θ and $[\mathbf{K}]$ from cell problem, see Sec. 3.3.3 and Sec. 3.3.5.

Eliminating the excess density from the equations, the macroscopic equilibrium is governed by:

$$\operatorname{div} V = \frac{\mathrm{i}\omega\phi}{B_0/\beta}\, p \quad \text{and } V = -\frac{[\boldsymbol{K}]}{\eta}\, \mathbf{grad}\ p. \tag{3.3.33}$$

Finally, the tensor of effective density $[\boldsymbol{\rho}]$ is defined as,

$$-\mathrm{i}\omega\,[\boldsymbol{\rho}]\,\boldsymbol{V} = \mathbf{grad}\, p, \text{ with } [\boldsymbol{\rho}] = \frac{\eta}{-\mathrm{i}\omega}[\boldsymbol{K}]^{-1}. \tag{3.3.34}$$

Note that analogous density tensors have been described in the framework of mechanical metamaterials with complex effective density matrices, becoming apparently negative in the presence of inner resonance [99].

Next, certain steps and assumptions are formulated to calculate frequency-dependence of the viscous and thermal permeabilities Θ and $[\boldsymbol{K}]$ respectively.

3.4 General properties of Thermal permeability

Here the system of equations for thermal problem is recalled as in Eq. (3.3.8), where the superscript (2) is dropped out for θ

$$\begin{cases} \operatorname{div}_y \mathbf{grad}_y \theta + \dfrac{\mathrm{i}\omega\rho_0 c_p}{\lambda^{(2)}}\theta = -1, & \text{(3.4.1a)} \\ \theta = 0 \text{ on } \Gamma, & \text{(3.4.1b)} \\ \theta,\ \Omega\text{-periodic.} & \text{(3.4.1c)} \end{cases}$$

Averaging Eq. (3.4.1a) on the fluid volume Ω_f gives out the following equation [100]:

$$\langle \mathbf{grad}_y \theta \cdot \mathbf{grad}_y \hat{\tau} \rangle - \frac{\mathrm{i}\omega\rho_0 c_p}{\lambda^{(2)}} \langle \theta\hat{\tau} \rangle = \langle \hat{\tau} \rangle\,. \tag{3.4.2}$$

Taking the complex conjugate θ^* as the test-field in the weak formulation in Eq. (3.3.7), Eq. (3.4.2) gives out

$$\Theta^* = \langle \mathbf{grad}_y \theta \cdot \mathbf{grad}_y \theta^* \rangle - \frac{\mathrm{i}\omega\rho_0 c_p}{\lambda^{(2)}} \langle \theta\theta^* \rangle, \tag{3.4.3a}$$

$$\Rightarrow \Theta = \langle \mathbf{grad}_y \theta \cdot \mathbf{grad}_y \theta^* \rangle + \frac{\mathrm{i}\omega\rho_0 c_p}{\lambda^{(2)}} \langle \theta\theta^* \rangle, \tag{3.4.3b}$$

where the real and imaginary parts of the solution Θ has the following feature:

$$\mathrm{Re}(\Theta) = \langle \mathbf{grad}_y \theta \cdot \mathbf{grad}_y \theta^* \rangle \in \mathbb{R}^+, \tag{3.4.4a}$$

$$\mathrm{Im}(\Theta) = \frac{\omega\rho_0 c_p}{\lambda^{(2)}} \langle \theta\theta^* \rangle \in \mathbb{R}^+. \tag{3.4.4b}$$

Then the low and high frequency limits and expansions of the problem is discussed in the following sections[1], with the regard to the boundary conditions.

[1] In this section, the superscripts 0 and ∞ represent only the respective low or high frequency approximation, if not otherwise specified.

3.4.1 Low and high frequency limits of permeability

In the static regime $\omega = 0$, heat conduction is dominant, while the inertial-thermal regime is neglected. Thus, the thermal cell problem in Eq. (3.4.1a) with $\theta(\omega = 0) = \theta^0$, reduces to the diffusion equation,

$$\mathrm{div}_y \mathbf{grad}_y \theta^0 = -1,\ \theta^0 = 0 \,\mathrm{on}\, \Gamma,\ \theta^0\ \Omega - \text{periodic}. \tag{3.4.5}$$

Here, the whole cell problem and solution become purely real, as defined in Eq. (3.4.4a). The rough low frequency limit of Θ is given as,

$$\Theta^0 = \Theta(\omega = 0) = \langle \mathbf{grad}_y \theta^0 \cdot \mathbf{grad}_y \theta^{0*} \rangle \in \mathbb{R}^+. \tag{3.4.6}$$

At the high frequency limit, the thermal inertia is dominant, while the heat conduction can be neglected. So the problem with $\theta^\infty = \theta(\Omega \to \infty)$ reduces to

$$\frac{\mathrm{i}\omega\rho_0 c_p}{\lambda^{(2)}}\theta = -1. \tag{3.4.7}$$

The equation has a constant solution which is purely imaginary,

$$\Theta^\infty(\omega) = \langle \theta^\infty \rangle = \frac{\phi\lambda^{(2)}}{-\mathrm{i}\omega\rho_0 c_p}, \tag{3.4.8}$$

with the porosity $\phi = \langle 1 \rangle = |\Omega_f|/|\Omega|$. This solution does not comply with the global boundary condition as in Eq. (3.4.1b) ($\theta = 0, \mathrm{on}\, \Gamma$). In fact, the transition form θ^∞ to θ^0 at Γ is made within a thermal boundary layer [8].

We can define the characteristic thermal frequency ω_t as the transitional frequency between the low and high frequency limits of the thermal permeability,

$$\omega_t = \frac{\phi\lambda}{\rho_0 c_p \Theta^0}, \tag{3.4.9}$$

when $|\Theta^\infty(\omega)| = |\Theta^0(\omega)|$.

So, the effective dynamic compressibility β rewrites accordingly as,

$$\beta = \gamma + \frac{\mathrm{i}\omega}{\omega_t}(\gamma - 1)\frac{\Theta}{\Theta^0}. \tag{3.4.10}$$

Its low and high frequency limits are as follows:

- at low frequency $\omega \to 0$, $\beta = \gamma$, the effective bulk modulus $B_{eff} = \dfrac{B_0}{\phi\gamma} = \dfrac{P_0}{\phi}$. This corresponds to the isothermal regime;
- at high frequency $\omega \to \infty$, $\beta = 1$, the effective bulk modulus $B_{eff} = \dfrac{B_0}{\phi} = \dfrac{\gamma P_0}{\phi}$. This corresponds to the adiabatic regime.

3.4.2 Low and high frequency asymptotics

Now, the dynamic thermal permeability is expanded asymptotically at low and high frequency limits.

For $\omega/\omega_t \ll 1$, the limit writes as,

$$\Theta(\omega \to 0) = \Theta^0 \left(1 + \frac{\mathrm{i}\omega}{\omega_t}\zeta^0\right), \tag{3.4.11}$$

where $\zeta^0 = \phi\dfrac{\langle\theta^0\theta^{0*}\rangle}{\langle\theta^0\rangle^2}$ is the characteristic equator to the heat capacity. This is defined by taking θ^0 as the test-field in the weak formulation as in Eq. (3.4.3b).

At high frequency, the predominant regime becomes adiabatic. More precisely, the high frequency approximation $\theta^\infty \neq 0$ does not comply with the initial boundary condition of no heat-transfer. The high frequency asymptotic expansion is calculated to account for the locally plane thermal boundary layer.

Thus, the asymptotic high frequency limit of the thermal permeability reads as [8]

$$\Theta(\omega \to \infty) = \frac{\phi\lambda^{(2)}}{-\mathrm{i}\omega\rho_0 c_p}\left(1 - \mathrm{i}\frac{\omega}{\omega_t}\frac{\delta_t}{\Lambda_t}\right), \tag{3.4.12}$$

with the thermal skin depth $\delta_t = \sqrt{2\lambda^{(2)}/(\rho_0 c_p \omega)}$.

Also the thermal characteristic length Λ_t can be obtained by [8, 10],

$$\Lambda_t = 2\frac{\int_{\Omega_f}(\theta^\infty)^2\, d\Omega_y}{\int_\Gamma (\theta^\infty)^2\, d\Gamma_y} = 2\frac{|\Omega|}{|\Gamma|} = \mathcal{O}(\ell), \tag{3.4.13}$$

So Λ_t is the volume-to-surface ratio of REV, which only depends on the geometry of the unit-cell Ω.

Further steps take Eq. (3.4.12) to the alternative form as:

$$\Theta(\omega \to \infty) = \Theta^0\frac{\omega_t}{-\mathrm{i}\omega}\left(1 - \mathrm{i}\frac{\omega}{\omega_t}\frac{\delta_t}{\Lambda_t}\right) = \Theta^0\frac{\omega_t}{-\mathrm{i}\omega}\left(1 - \mathrm{i}\sqrt{\frac{\omega}{\omega_t}\frac{1}{2}\frac{M'}{2}}\right), \tag{3.4.14}$$

where $M' = \dfrac{8\Theta^0}{\phi\Lambda_t^2}$ is the dimensionless shape factor.

And for $\omega/\omega_t \gg 1$, further approximation as the Taylor expansion of Eq. (3.4.14) gives out,

$$\Theta(\omega \to \infty) = \Theta^0\frac{\omega_t}{-\mathrm{i}\omega}\left(1 - \mathrm{i}\sqrt{\frac{\omega}{\omega_t}\frac{1}{2}\frac{M'}{2}}\right) \approx \frac{\Theta^0}{\sqrt{-\mathrm{i}\dfrac{\omega}{\omega_t}\cdot\dfrac{M'}{2}} - \mathrm{i}\dfrac{\omega}{\omega_t}}. \tag{3.4.15}$$

To satisfy the high frequency asymptotic expansions in Eq. (3.4.15) and the value of θ^0 at $\Omega = 0$, the following approximation was proposed [7, 8]:

$$\Theta(\omega) = \frac{\Theta^0}{\sqrt{1 - \mathrm{i}\dfrac{\omega}{\omega_t}\cdot\dfrac{M'}{2}} - \mathrm{i}\dfrac{\omega}{\omega_t}}. \tag{3.4.16}$$

This approximation between the JCAL and the homogenisation models is mathematically sound and physically causal.

3.5 General properties of Viscous permeabilities

The same analogy can be used on the viscous cell problem. But it is more complicated, due to the additional tortuosity parameter and the vectorial nature of the problem.

First, the viscous cell problem in Eqs.(3.3.16) is recalled as,

$$\begin{cases} \mathrm{div}_y(\boldsymbol{k}_j) = 0, & \text{(3.5.1a)} \\ \mathrm{div}_y \mathbf{grad}_y \boldsymbol{k}_j + \dfrac{\mathrm{i}\omega\rho_0}{\eta^{(2)}} \boldsymbol{k}_j = \mathbf{grad}_y(\alpha_j) - \boldsymbol{e}_j, & \text{(3.5.1b)} \\ \boldsymbol{k}_j = 0 \text{ on } \Gamma, & \text{(3.5.1c)} \\ \langle \alpha_j \rangle = 0, & \text{(3.5.1d)} \\ (\boldsymbol{k}_j, \alpha_j),\ \Omega\text{-periodic.} & \text{(3.5.1e)} \end{cases}$$

Similar to the thermal case, the test-field of the weak formulation takes form of its own complex conjugate. Then Eq. (3.3.24) rewrites as,

$$K^*_{ij} = 2\langle \boldsymbol{D}(\boldsymbol{k}_i) : \boldsymbol{D}(\boldsymbol{k}^*_j) \rangle - \frac{\mathrm{i}\omega\rho_0}{\eta^{(2)}} \langle \boldsymbol{k}_i \boldsymbol{k}^*_j \rangle, \tag{3.5.2a}$$

$$\Rightarrow K_{ij} = 2\langle \boldsymbol{D}(\boldsymbol{k}_i) : \boldsymbol{D}(\boldsymbol{k}^*_j) \rangle + \frac{\mathrm{i}\omega\rho_0}{\eta^{(2)}} \langle \boldsymbol{k}_i \boldsymbol{k}^*_j \rangle, \tag{3.5.2b}$$

where the real and imaginary parts of the solution K_{ii} has the following feature:

$$\mathrm{Re}(K_{ij}) = 2\langle \boldsymbol{D}(\boldsymbol{k}_i) : \boldsymbol{D}(\boldsymbol{k}^*_j) \rangle \in \mathbb{R}^+, \tag{3.5.3a}$$

$$\mathrm{Im}(K_{ij}) = \frac{\omega\rho_0}{\eta^{(2)}} \langle \boldsymbol{k}_i \boldsymbol{k}^*_j \rangle \in \mathbb{R}^+. \tag{3.5.3b}$$

3.5.1 Low and high frequency limit of permeability

Same as in Eq. (3.3.27), $\boldsymbol{K}_j = \langle \boldsymbol{k}_j \rangle$, the low and high frequency asymptotic expansions give out the following statements.

At low frequency where $\omega = 0$, the couple $(\boldsymbol{k}^0_j, \alpha^0_j)$ gives out $\boldsymbol{K}^0_j$. The system is reduced to

$$\begin{cases} \mathrm{div}_y(\boldsymbol{k}^0_j) = 0, & \text{(3.5.4a)} \\ \mathrm{div}_y \mathbf{grad}_y \boldsymbol{k}^0_j = \mathbf{grad}_y(\alpha^0_j) - \boldsymbol{e}_j, & \text{(3.5.4b)} \\ \langle \alpha^0 \rangle = 0, \text{ on } \Gamma. & \text{(3.5.4c)} \end{cases}$$

Then, this cell problem here and its solutions become purely real, the low frequency approximation writes as

$$\boldsymbol{K}^0_j = 2\langle \boldsymbol{D}(\boldsymbol{k}^0_j) : \boldsymbol{D}(\boldsymbol{k}^{0*}_j) \rangle = \langle \boldsymbol{k}^0_j \rangle. \tag{3.5.5}$$

It is related to a creeping flow problem in static regime.

At high frequency where $\omega \to \infty$, the couple $(\boldsymbol{k}_j^\infty, \alpha_j^\infty)$ gives out $\boldsymbol{K}_j^\infty$. The system reduces to

$$\begin{cases} \mathrm{div}_y(\boldsymbol{k}_j^\infty) = 0, & \text{(3.5.6a)} \\ \dfrac{\mathrm{i}\omega\rho_0}{\eta^{(2)}}\boldsymbol{k}_j^\infty = \mathbf{grad}_y(\alpha_j^\infty) - \boldsymbol{e}_j. & \text{(3.5.6b)} \end{cases}$$

All components $(\boldsymbol{k}_j, \alpha_j)$ still comply with the boundary and periodicity conditions set in Eq. (3.3.28), with the additional consideration of a viscous boundary layer at higher frequencies.

Denoting $\boldsymbol{\alpha}^\infty = \alpha^\infty \boldsymbol{e}_j$ the high frequency limit of $\boldsymbol{\alpha}$, the high frequency cell problem gives out the solution in the following forms,

$$[\boldsymbol{k}^\infty] = \boldsymbol{k}_j \otimes \boldsymbol{e}_j = \frac{\eta^{(2)}}{-\mathrm{i}\omega\rho_0}\left[\boldsymbol{I} -^T \mathbf{grad}\alpha^\infty\right], \tag{3.5.7}$$

and taking the averaged value,

$$[\boldsymbol{K}^\infty] = \frac{\eta^{(2)}}{-\mathrm{i}\omega\rho_0}\langle \boldsymbol{I} -^T \mathbf{grad}\alpha^\infty\rangle = \frac{\phi_f\eta^{(2)}}{-\mathrm{i}\omega\rho_0}\left[\boldsymbol{\tau}^\infty\right]^{-1}, \tag{3.5.8a}$$

$$\text{with } [\boldsymbol{\tau}^\infty] = \phi\langle \boldsymbol{I} -^T \mathbf{grad}\alpha^\infty\rangle^{-1}, \tag{3.5.8b}$$

where τ^∞ is the high frequency limit of the dynamic tortuosity.

In one principal direction, $\boldsymbol{k}_j = k_j\boldsymbol{e}_j$, and the associated characteristic frequency for this principal direction is $\omega_j = \dfrac{\phi\eta^{(2)}}{\rho_0 K_j^0}$.

For frequency $\omega \ll \omega_j$, the problem is in the viscous regime. It can be described by a diffusion equation. For frequency $\omega \gg \omega_j$, the problem goes in an inertial regime. It is one degree of differential, completely different to the diffusion problem, as it becomes propagative.

3.5.2 Low and high frequency asymptotics

Similarly as the thermal case, the high frequency asymptotic expansion writes as [7],

$$K_j(\omega \to \infty) = \frac{\eta^{(2)}}{-\mathrm{i}\omega\rho_0}\left(1 - \frac{\mathrm{i}\omega}{\omega^j}\frac{\delta_v^j}{\Lambda^j}\right) = K_j^0\frac{\omega_j}{-\mathrm{i}\omega}\left(1 - \mathrm{i}\sqrt{\frac{\omega}{\omega_j}\frac{1}{2}\frac{M}{2}}\right), \tag{3.5.9}$$

where $M_j = \dfrac{8K^{j0}\tau^{j0}}{\phi(\Lambda^j)^2}$ is the dimensionless viscous shape factor, with the viscous skin depth $\delta_v(\omega) = \sqrt{\dfrac{\eta}{\rho_0\omega}}$.

For $\omega/\omega_t \gg 1$, further approximation as the Taylor expansion of Eq. (3.5.9) gives out,

$$K_j(\omega \to \infty) = K_j^0\frac{\omega_j}{-\mathrm{i}\omega}\left(-\mathrm{i}\sqrt{\frac{\omega}{\omega_j}\frac{1}{2}\frac{M}{2}}\right) \approx \frac{K^{j0}}{\sqrt{\mathrm{i}\dfrac{\omega}{\omega_j}\cdot\dfrac{M_j}{2}} - \dfrac{\mathrm{i}\omega}{\omega_j}}. \tag{3.5.10}$$

Also, the characteristic viscous length Λ_f^i in the principal direction $\boldsymbol{e}_i$ of the Darcy permeability tensor is defined by [51]:

$$\Lambda^j = 2\frac{\int_{\Omega_f} k_j^\infty \cdot k_j^\infty \, d\Omega_y}{\int_\Gamma k_j^\infty \cdot k_j^\infty \, d\Gamma_y}. \tag{3.5.11}$$

To match K_j^0 at $\omega = 0$ and satisfy the high frequency asymptotic in Eq. (3.5.10), the approximation of dynamic viscous permeability reads as [7, 8]:

$$K_j(\omega) = \frac{K^{j0}}{\sqrt{1 - \mathrm{i}\frac{\omega}{\omega_j} \cdot \frac{M_j}{2}} - \frac{\mathrm{i}\omega}{\omega_j}}. \tag{3.5.12}$$

Conclusion

In this Chapter, the propagation of small acoustic perturbation through a anisotropic porous medium has been studied. The medium is a periodic arrangement of solid scatterers inside REV saturated in ambient air.

The two-scale asymptotic homogenisation procedure is recalled, where the macro-scale behaviour of the porous material is described by the micro-scale field. Then the governing equations of macro-scale are given as the generalised Darcy's law and the mass conservation. The resolution of the micro-scale cell problems also gives rise to the effective behaviours of the porous material. They are represented by the frequency-dependent effective viscous and thermal permeabilities.

Through analysing the properties of the permeabilities, the analogy between JCAL and homogenisation models has been established. The frequency-independent viscous and thermal parameters were approximated in accordance with the JCAL model. Two thermal parameters and three viscous parameters for each principal direction are used to describe the frequency-dependent complex valued permeabilities.

The viscous parameters for each principal direction $\boldsymbol{e}_i, i = \mathrm{I}, \mathrm{II}, \mathrm{III}$ of a fluid domain Ω_f are

- Static viscous permeability K_f^{i0},
- High-frequency limit of the dynamic tortuosity $\tau_f^{i\infty}$,
- Viscous characteristic length Λ_f^i,

with the viscous characteristic frequency ω_f^i.

The thermal parameters are

- Static thermal permeability Θ_f^0,
- Thermal characteristic length Λ_f',

with the thermal characteristic frequency ω_f'.

A numerical resolution based on the homogenisation procedures is then conceived using FEM software to compute the mentioned dynamic permeabilities and frequency-independent parameters, based on the homogenisation procedure. The results are used in the following Chapter to study the permeable array of resonators.

Chapter 4

Anisotropic acoustic metamaterial based on array of hollow tubes

In this Chapter, an anisotropic acoustic metamaterial is theoretically and experimentally studied for sound absorption. The design of this metamaterial is based on the homogenisation of an idealised periodic arrangement of hollow tubes coupled to the exterior medium and the hollow tubes acting as acoustic resonators. The physical model of this anisotropic porous media, discussed in the previous chapters, is enriched in the current one by tailoring inner resonances. Impedance tube measurements are performed on 3-D printed samples with controlled parameters to validate the theoretical results [1].

Contents

[1] Part of the work in this Chapter is published in the peer-reviewed conference proceeding: **Huang, W.**, Schwan, L., Romero-García, V., Genevaux, J.-M., & Groby, J.-P. (2017, August). "*3D-printed straw-inspired metamaterial for sound absorption*". Engineered Materials Platforms for Novel Wave Phenomena (Metamaterials), 2017 11th International Congress on (pp. 157-159). IEEE.

Introduction

Homogenisation is a versatile tool when dealing with multi-physics problems. Based on the study of double porosity media [101–103], Boutin *et al.* investigated heterogeneous porous media saturated by the same gas where inner resonance occurs. The investigation was conducted both theoretically and experimentally [52, 96]. It provides a means of modelling of acoustic waves propagating through a rigid frame porous medium with embedded resonators in simplified configurations. The slow sound phenomenon is also noticed in this situation.

Chevillotte *et al.* used the approach to predict the sound absorption predictions of perforated closed-cell metallic foams [104]. Glé *et al.* studied the properties of recycled material composed of vegetable particles with multi-scales of porosity [105]. It is found out that adding porous hemp particles into concrete, the material has better sound absorption than before. Double porosity granular material are also investigated for low-frequency sound absorption [106]. Also, a double porosity granular material absorbs more at reduced weight compared to its solid grain counterparts [106].

Some phononic crystal designs also use a periodic arrangement of solid cylindrical, or spherical micro-scatters to focus, guide sound wave in ultrasonic range [107, 108]. Some use the crystal to create elastic band gaps for surface waves [109]. Some sonic crystal design utilises arranged bamboo rods with inner cavities drilled as resonators to improve transmission losses in audible regime [110]. Others also deal with broadband transmission loss using the overlap of resonances by square-rod rigid scatterers incorporating a periodic arrangement of quarter-wavelength resonators [111]. Also, sound barriers made of recycled materials consists of the periodic arrangements of perforated metal cylinders filled with rubber crumb, having good performance of the transmission loss [112].

In this Chapter, the design of sound absorbing materials with inner resonances is further investigated. In particular, this metamaterial design is based on an idealised periodic arrangement of hollow tubes. The approach to this structured material design relies on the homogenisation of this arrangement [51, 52], where the outer matrix and the inner resonators are seen as two different acoustic fields co-existing and interacting at the scale of the unit cell period, where macro wavelength phenomenon and local resonance occur simultaneously.

In this Chapter, we start by recalling the homogenised model with inner resonance, accounting for the geometry of the periodic arrangement of hollow tubes. The dispersion properties are discussed, to reveal the slow sound aspects of this configuration.

Then, a calculation of the reflection of a rigidly backed layer of anisotropic material is proposed, which also accounts for oblique incidence. The absorption of this metamaterial design is then obtained theoretically.

Finally, impedance tube measurements are performed on 3-D printed samples with controlled parameters to test the validity and robustness of the developped theoretical model and the numerical computation of the JCAL parameters.

4.1 General description

The anisotropic acoustic metamaterial consists of the three-dimensional Ω-periodic arrangement of straight hollow tubes, with a single tube per period, as shown in Fig. 4.1.

Here, the unit cell Ω is a rectangular cube with the dimensions $\ell_{\mathrm{I}} \times \ell_{\mathrm{II}} \times \ell_{\mathrm{III}}$ in the directions of the Cartesian coordinate system $(\boldsymbol{e}_{\mathrm{I}}, \boldsymbol{e}_{\mathrm{II}}, \boldsymbol{e}_{\mathrm{III}})$. The hollow tube in the unit cell Ω has the outer radius R_x, the finite length $\ell_x \leq \ell_{\mathrm{I}}$, and its axis oriented along $\boldsymbol{e}_{\mathrm{I}}$. The air domain outside the tube is denoted Ω_{m}.

The inside of the tube is splited into two cylindrical ducts Ω_1 and Ω_2 by a rigid wall. Each has the length h_1 or h_2 and the outside apertures Σ_1 and Σ_2 with the unit normal vectors $\boldsymbol{n}_1 = -\boldsymbol{e}_{\mathrm{I}}$ and $\boldsymbol{n}_2 = \boldsymbol{e}_{\mathrm{I}}$ directed towards the outside of the ducts. The two ducts have the same inner radius R_i, the value of which is limited as $R_i < R_x$.

The filling fractions $\phi_{\mathrm{m}} = |\Omega_{\mathrm{m}}|/|\Omega|$, and $\phi_j = |\Omega_j|/|\Omega|$ with $j \in \{1, 2\}$ are defined, where the volume of the domains Ω, Ω_{m}, and Ω_j read as:

$$|\Omega| = \ell_{\mathrm{I}}\ell_{\mathrm{II}}\ell_{\mathrm{III}}, \quad |\Omega_{\mathrm{m}}| = |\Omega| - \pi R_x^2 \ell_x, \quad |\Omega_j| = \pi R_i^2 h_j. \tag{4.1.1}$$

The total porosity of the medium is $\phi = \phi_{\mathrm{m}} + \phi_1 + \phi_2 < 1$. In this system, the propagation of air-borne acoustic waves is studied under ambient conditions in the linear harmonic regime at frequencies ω (time convention $e^{-\mathrm{i}\omega t}$).

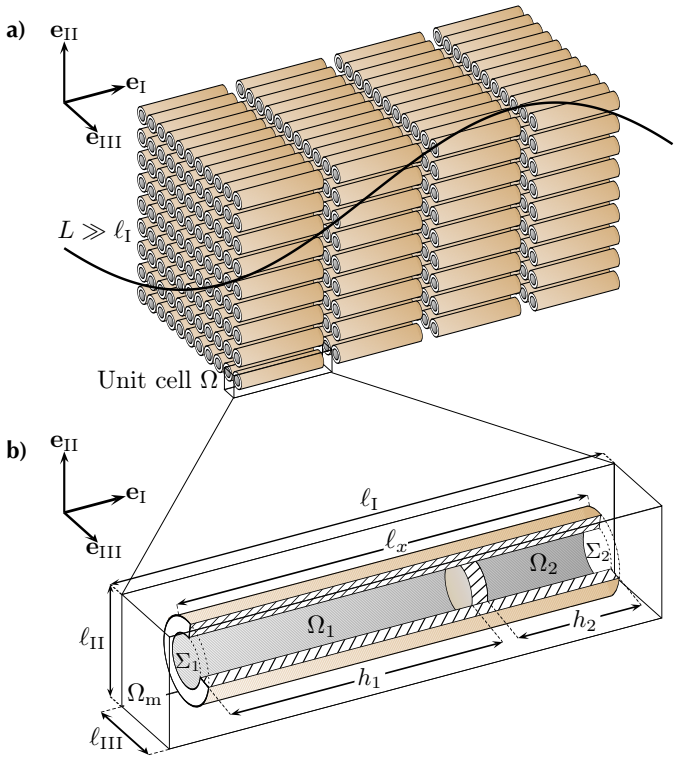

FIGURE 4.1: Material description: a)Effective material sketch-up; b) Unit cell Ω Configuration: resonators' inner space in orange and green, solid tube walls in blue.

4.2 Homogenised model with inner resonators

The periodic arrangement of QWRs is studied in the long-wavelength approximation, assuming that the condition of scale separation $\epsilon = \ell_1/L \ll 1$ is satisfied, where $L = c_0/\omega$ is the characteristic length of the sound wave. The scale separation and the Ω-periodicity of the array allow using the two-scale asymptotic homogenisation method to derive the effective behaviour of the metamaterial, see Chapter 3. The procedure is similar to that applied to porous materials with embedded Helmholtz resonators [51, 52].

Diverting from the homogenisation process without considering the inner resonators, Eq. (3.3.9) writes here as,

$$\frac{1}{|\Omega|}\int_{\Omega_\mathrm{m}} \mathrm{div}_x \boldsymbol{v}^{(0)} d\Omega_y + \frac{1}{|\Omega|}\int_{\Omega_\mathrm{m}} \mathrm{div}_y \boldsymbol{v}^{(1)} d\Omega_y = \mathrm{i}\omega \frac{1}{|\Omega|}\int_{\Omega_\mathrm{m}} \frac{\rho^0}{\rho_0} d\Omega_y \,. \tag{4.2.1}$$

Applying the divergence theorem, now the additional flux from the aperture is also taken into consideration,

$$\begin{aligned} \frac{1}{|\Omega|}\int_{\Omega_\mathrm{m}} \mathrm{div}_x \boldsymbol{v}^{(1)} d\Omega_y &= \frac{1}{|\Omega|}\int_{\partial\Omega_\mathrm{m}} \boldsymbol{v}^{(1)} \cdot \boldsymbol{n_y} d\Gamma_y \\ &= \frac{1}{|\Omega|}\int_{\Gamma} \boldsymbol{v}^{(1)} \cdot \boldsymbol{n_y} d\Gamma_y + \sum_{j=1,2} \frac{1}{|\Omega|}\int_{\Sigma_j} \boldsymbol{v}^{(1)} \cdot \boldsymbol{n_j} d\Sigma_j \,, \end{aligned} \tag{4.2.2}$$

because $\partial\Omega_\mathrm{m} = \Gamma + \Sigma_1 + \Sigma_2$. Also considering periodicity and boundary conditions, the air-solid surface Γ of Ω_m determines that

$$\frac{1}{|\Omega|}\int_{\Gamma} \boldsymbol{v}^{(1)} \cdot \boldsymbol{n_y} d\Gamma_y = 0. \tag{4.2.3}$$

Thus, the macroscopic mass conservation rewrites as:

$$\mathrm{div}\, \boldsymbol{V} - \frac{Q_1 + Q_2}{|\,\Omega\,|} = \mathrm{i}\omega \frac{\langle\rho\rangle_\mathrm{m}}{\rho_0} \,, \tag{4.2.4}$$

where the added inner resonators are theorised by the flux emitted from the duct aperture Σ_j inside unit-cell Ω,

$$Q_j = \int_{\Sigma_j} \boldsymbol{v}^{(1)} \cdot \boldsymbol{n}_j \, d\Sigma. \tag{4.2.5}$$

Also, the flux emitted from the duct aperture Q_j in Eq. (4.2.4) is the response to the pressure P acting on it. Independently of the homogenisation approach, the duct Ω_j is regarded as a quarter-wavelength resonator, which results in:

$$Q_j = \frac{\mathrm{i}\omega|\Omega_j|}{B^*} \frac{\tan\left(k^* h_j\right)}{k^* h_j} P, \quad \text{with} \quad k^* = \omega\sqrt{\rho^*/B^*}, \tag{4.2.6}$$

where $\rho^*(R_i)$ and $B^*(R_i)$ are the effective density and bulk modulus of air in a cylindrical tube with a circular cross section [11, 61], details given in Chapter 1.

Substitution of Eq. (4.2.6) into Eq. (4.2.4) results in the following equation:

$$\mathrm{div}\, \boldsymbol{V} = \frac{\mathrm{i}\omega P}{B_0/\beta}, \tag{4.2.7}$$

where the effective compressibility β reads as the series association of the compressibility β_{m} of the medium outside the tubes and apparent compressibility β_j induced by the resonator Ω_j:

$$\beta = \phi_{\mathrm{m}}\beta_{\mathrm{m}} + \sum_j \phi_j \beta_j, \quad \text{with } \beta_j = \frac{B_0}{B^*}\frac{\tan\left(k^* h_j\right)}{k^* h_j}. \tag{4.2.8}$$

At low frequencies, $\omega \to 0$, the resonator-induced compressibility β_j tends to the adiabatic constant γ, and the limit of the overall compressibility $\beta \to \phi\gamma$ bears testament to the isothermal regime in the metamaterial.

At higher frequencies, the compressibility β_j, experiences a resonance at a frequency close to the quarter-wavelength eigenfrequency

$$\omega_j = \pi c_0/(2h_j), \text{ with } j = 1, 2.... \tag{4.2.9}$$

Neglecting visco-thermal effects in the tubes, the compressibility β_j is real-valued and becomes negative, which can cause the real part of the overall compressibility β to be negative for frequencies around ω_1. That offers the possibility to open non-propagative band-gaps [32, 75] as illustrated in Chapter 1 and 2.

To summarise, the governing equations for a layer of the proposed metamaterial are the effective mass conservation and the generalised Darcy law in the metamaterial:

$$\operatorname{div} \boldsymbol{V} = \frac{\mathrm{i}\omega P}{B_0/\beta}, \tag{4.2.10a}$$

$$\boldsymbol{V} = -\frac{\boldsymbol{K}_{\mathrm{m}}}{\eta}\,\mathbf{grad}\, P. \tag{4.2.10b}$$

Here, $\boldsymbol{V}$ is the effective particle velocity, P is the macroscopic pressure, β_{m} and $\boldsymbol{K}_{\mathrm{m}}$ are the effective compressibility (scalar) and Darcy permeability (tensor) of air in the domain Ω_{m} outside the tubes, while Q_j is the flux pulsed out from the aperture Σ_j of the duct Ω_j.

Equation (4.2.10) via β shows that the duct apertures act as secondary sources in the mass conservation. They radiate the flux $Q_1 + Q_2$ in the effective porous medium formed by the array of tubes as these latter modifies the air flow path.

Particularly, the symmetric tensor $\boldsymbol{K}_{\mathrm{m}}$ of generalised Darcy permeability characterises the dynamic visco-inertial diffusion of air in the porous medium. It is anisotropic due to symmetries in the unit cell. Besides, the effective compressibility β_{m} accounts for thermo-acoustic effects in Ω_{m}. Their properties have been described in Chapter 3.

4.3 Dispersion relation

The main feature of such porous medium with inner resonances is the possibility of the effective compressibility β to become negative at frequencies so that $\beta_r \leq -\beta_m\phi_m/\phi_r$.

To illustrate this effect, a configuration with the following dimensions is adopted: $\ell_{\mathrm{II}} = \ell_{\mathrm{III}} = 6$ mm, $\ell_{\mathrm{I}} = 42$ mm, $R_x = 2.9$ mm, $R_i = 1.9$ mm, $\ell_x = 40$ mm, $h_1 = 39$ mm, $h_2 = 0$ mm. This leads to the filling fractions $\phi_m \approx 0.3$ and $\phi_r \approx 0.29$, and QWR's

natural frequency $\omega_1/2\pi \approx 2.2$ kHz.

The numerical solution of the cell problem yields JCAL viscous and thermal parameters as below:

- static viscous permeabilities: $K_{\mathrm{m}}^{\mathrm{I}0} \approx 615\ \mu\mathrm{m}^2$, $K_{\mathrm{m}}^{\mathrm{II}0} \approx 185\ \mu\mathrm{m}^2$;
- high frequency limit of the dynamic tortuosities:$\tau_{\mathrm{m}}^{\mathrm{I}\infty} \approx 1.11$, $\tau_{\mathrm{m}}^{\mathrm{II}\infty} \approx 2.09$;
- viscous characteristic lengths $\Lambda_{\mathrm{m}}^{\mathrm{I}} \approx 1.052$ mm, $\Lambda_{\mathrm{m}}^{\mathrm{II}} \approx 488\ \mu$m ;
- static thermal permeability $\Theta_{\mathrm{m}}^{0} \approx 7.51\ \mu\mathrm{m}^2$ and characteristic thermal length $\Lambda'_{\mathrm{m}} \approx 978\ \mu$m.

Wave propagation in the transverse direction $\boldsymbol{e}_{\mathrm{II}}$ is studied with the wavenumber $k = \omega/\sqrt{B/\rho_{\mathrm{II}}}$ where $B = \gamma P_0/\beta$ is the effective bulk modulus and $\rho_{\mathrm{II}} = \mathrm{i}\eta/\omega K_{\mathrm{m}}^{\mathrm{II}0}$ is the effective density in the transverse direction. The results for the hollow tubes are compared with those for the solid cylinder array ($R_i = h_1 = h_2 = 0$) which produce no inner resonance ($\beta_r = 0$).

It is worth noting that the resonance frequency $\omega_0/2\pi$ is much higher than the viscous characteristic frequency $\omega_{\mathrm{m}}^{\mathrm{II}}/2\pi = \phi_m\eta/[2\pi\rho_0\tau_{\mathrm{m}}^{\mathrm{II}\infty}K_{\mathrm{m}}^{\mathrm{II}0}] \approx 17$ Hz and the thermal characteristic frequency $\omega'_{\mathrm{m}}/2\pi = \phi_m\lambda/[2\pi\rho_0 c_p\Theta_{\mathrm{m}}^{0}] \approx 14$ Hz, which indicates that the porous medium is in the quasi adiabatic inertial regime with $\beta_m \approx 1$ and $\rho_{\mathrm{II}} \approx \rho_0\tau_{\mathrm{m}}^{\mathrm{II}\infty}/\phi_m$, close to the resonance of the tubes .

The real and imaginary parts of the normalised bulk modulus $B/\gamma P_0 = 1/\beta$ is shown in Fig. 4.2. It can be observed that with the added QWRs, the real part of the effective bulk modulus B becomes negative in a broadband frequency range from ω_1 to 2.714 kHz, see shaded area in Fig. 4.2. The imaginary part has a negative peak at 2.714 kHz. Particularly, around the QWR's resonance frequency 2.2 kHz, both the real and imaginary parts are negative, which can lead to a broad pseudo-band-gap.

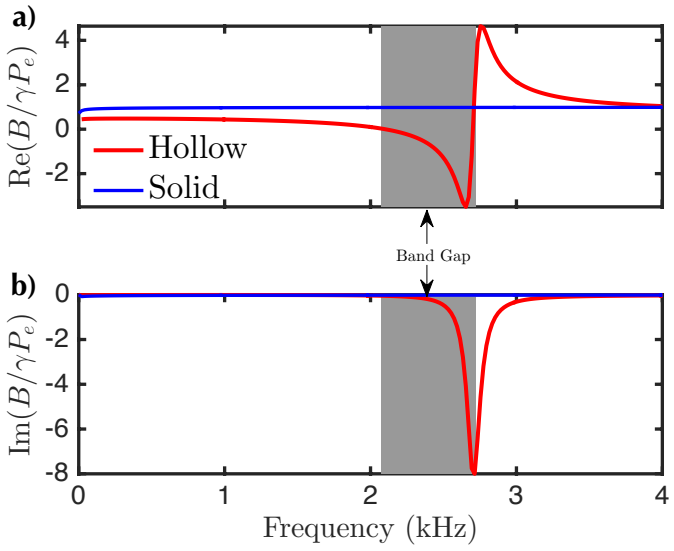

FIGURE 4.2: Normalised bulk modulus: a) Real and b) imaginary part: Hollow tube array in red, Solid cylinder array in blue.

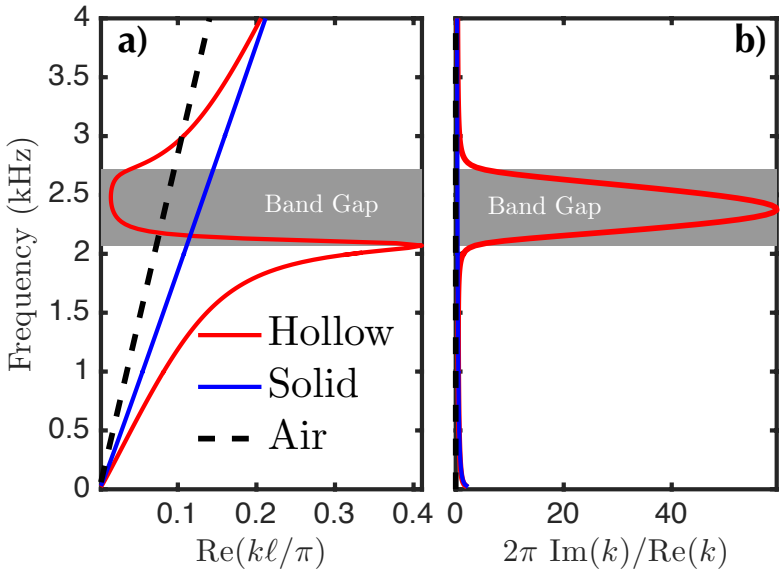

FIGURE 4.3: a) Real part of the normalised wavenumber $\mathrm{Re}(k\ell_{\mathrm{II}}/\pi)$; b) Attenuation factor $2\pi\mathrm{Im}(k)/\mathrm{Re}(k)$: Hollow tube array in red, Solid cylinder array in blue and ambiant air in black dashed line.

The wavenumber k in the medium is shown against the frequency in Fig. 4.3. The real part of k is shown, normalised by π/ℓ_{II}. The imaginary part is shown in the form of the attenuation factor $2\pi\mathrm{Im}(k)/\mathrm{Re}(k)$.

At almost all frequencies, the slope of the dispersion curve $k(\omega)$ of the hollow tube array is lower than that for the solid cylinder array or the ambient air line, indicating a lower sound groupe velocity inside the array. Conversely, a quasi non-propagative band gap as $\mathrm{Re}(k) \to 0$ is found above the QWR resonance frequency 2.2 kHz where the effective bulk modulus B is negative. Along with the slow sound speed, a highly-attenuated mode also appears shown in Fig. 4.3b), where the wavelength $2\pi/\mathrm{Re}(k)$ up to 60 times of the characteristic attenuation length $1/\mathrm{Im}(k)$.

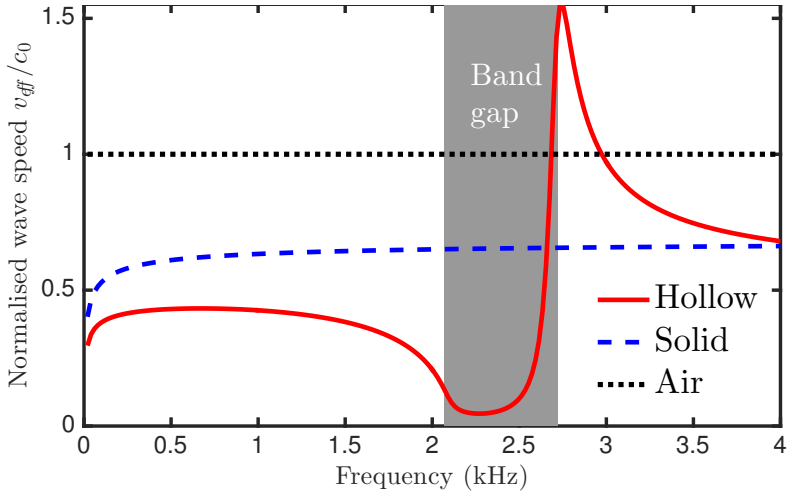

FIGURE 4.4: Normalised wave speed : Hollow tube array in red, Solid cylinder array in blue and ambiant air in black dotted line.

Likewise, the effective sound speed $v_{eff} = \mathrm{Re}(\sqrt{B/\rho_{\mathrm{II}}})$ is normalised by sound speed in air, as shown in Fig. 4.4. It further confirms that the sound speed inside an array of hollow tubes is lower than that in the solid cylinder array, also presenting almost half of the value of sound speed in air. Moreover, inside the pseudo-band-gap, the sound speed drops to near zero, whereby the slope $d\omega/d\mathrm{Re}(k)$ of the real dispersion curve tends to zero. This phenomenon will eventually induce absorption at lower frequency range, similar as shown in Part I.

4.4 Reflection of a plane wave incidence

The reflection from a rigidly backed layer of the metamaterial is calculated under a plane wave incidence. The studied space is divided in two: the upper semi-infinite medium Ω_0 of ambient air ($x_3 > D$), the lower medium Ω_1 occupied by the rigidly backed anisotropic material layer ($0 < x_3 < D$), see Fig. 4.5.

The ambient air medium Ω_0 is defined by the following governing equation at $x_3 > D$,

$$\mathrm{div}\boldsymbol{v}_0 = \frac{i\omega}{B_0} p_0, \quad i\omega\rho_0\boldsymbol{v}_0 = \mathbf{grad}\, p_0, \tag{4.4.1}$$

with $c_0 = \sqrt{B_0/\rho_0}$ and $k_0 = \omega/c_0$.

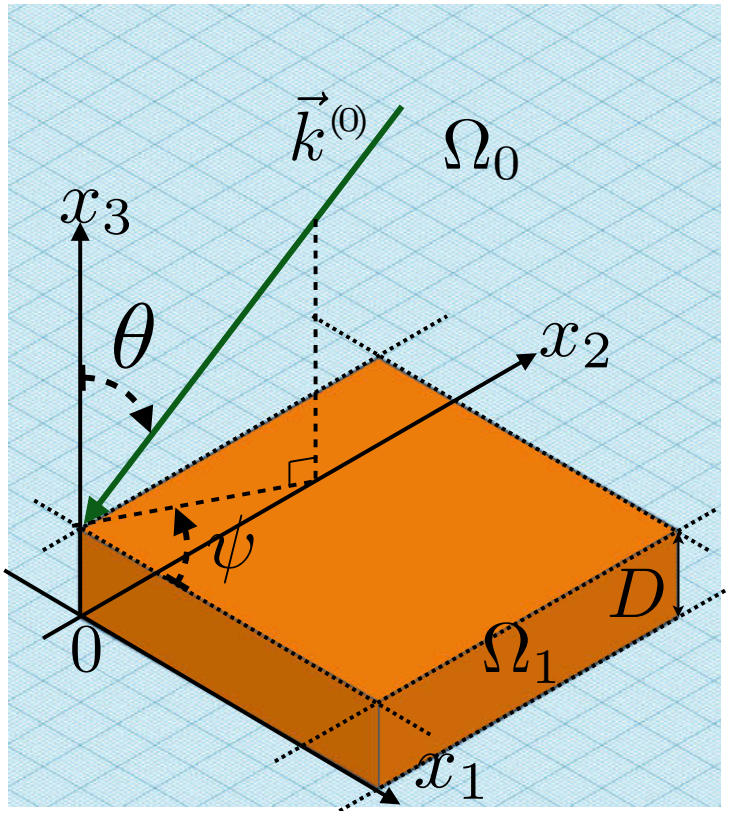

FIGURE 4.5: Incidence plane at oblique angles into a rigid-backed slab of the material

.

From medium Ω_0, a plain wave incidence is considered. In the incidence plane $\mathcal{P}_\psi(\boldsymbol{k}_\Gamma, \psi)$, the wavenumber vector $\boldsymbol{k}^{(0)} = (\boldsymbol{k}_\Gamma, k_3^{(0)})$ with $\boldsymbol{k}_\Gamma = (k_1^{(0)}, k_2^{(0)})$ in plane $x_\Gamma(x_1, x_2)$,

$$p_0 = \left(Re^{\mathrm{i}k_3^{(0)}(x_3 - D)} + e^{-\mathrm{i}k_3^{(0)}(x_3 - D)} \right) e^{i\boldsymbol{k}_\Gamma \cdot \boldsymbol{x}_\Gamma}, \tag{4.4.2a}$$

$$\boldsymbol{v}_0.\boldsymbol{e}_3 = \frac{k_3^{(0)}}{\omega \rho_0} \left(Re^{\mathrm{i}k_3^{(0)}(x_3 - D)} - e^{-ik_3^{(0)}(x_3 - D)} \right) e^{i\boldsymbol{k}_\Gamma \cdot \boldsymbol{x}_\Gamma}. \tag{4.4.2b}$$

with $k_1^{(0)} = k_0 \sin(\theta)\cos(\psi),\ k_2^{(0)} = k_0 \sin(\theta)\sin(\psi),\ k_3^{(0)} = k_0 \cos(\theta)$.

In the anisotropic porous medium Ω_1 at $0 < x_3 < D$, the governing equations in Eq. (4.2.10) give out the dispersion relation as

$$\boldsymbol{k} \cdot (\boldsymbol{H}.\boldsymbol{k}) = \frac{\omega^2}{B}, \tag{4.4.3}$$

where the tensor $\boldsymbol{H} = \boldsymbol{\rho}^{-1}$ is symmetric, and full for most cases, with the wave vector $\boldsymbol{k} = (k_1, k_2, k_3)$, and $k_1 = k_1^{(0)},\ k_2 = k_2^{(0)}$.

In full expansion, Equation (4.4.3) develops into the following form:

$$H_{33}k_3^2 + 2\left(H_{13}k_1 + H_{23}k_2\right)k_3 + \left(-\frac{\omega^2}{B} + H_{11}k_1^2 + H_{22}k_2^2 + 2H_{12}k_1k_2 \right) = 0. \tag{4.4.4}$$

The solution for this equation of k_3 in the most general case is,

$$k_3^{\pm} = -\frac{H_{13}k_1 + H_{23}k_2}{H_{33}} \pm \kappa, \tag{4.4.5a}$$

$$\text{with } \kappa = \sqrt{\frac{\left(H_{13}k_1 + H_{23}k_2\right)^2}{(H_{33})^2} - \frac{1}{H_{33}} \left(-\frac{\omega^2}{\tilde{B}} + H_{11}k_1^2 + H_{22}k_2^2 + 2H_{12}k_1k_2 \right)}. \tag{4.4.5b}$$

As the tensor $\boldsymbol{H}$ is symmetric and full. It is pertinent to normalise the tensor by H_{33}, which is the more important element of the tensor as the main incident direction is $\boldsymbol{e}_3$. Moreover, H_{33} should be non-zero for the studied case to be meaningful.

This rewrites $\boldsymbol{H}$ in the block form as followed,

$$\boldsymbol{H} = H_{33} \left[\begin{array}{c|c} H^* & \boldsymbol{\mathcal{C}} \\ \hline \boldsymbol{\mathcal{C}}^T & 1 \end{array} \right], \tag{4.4.6}$$

where $\mathcal{C}_i = H_{i3}/H_{33}\boldsymbol{e}_i$ and $H_{ij}^* = H_{ij}/H_{33}$, with $(i, j) \in (1, 2)$.

Accordingly, the dispersion relation Eq. (6.2.3) rewrites as

$$k_3^2 + 2(\boldsymbol{\mathcal{C}}.\boldsymbol{k}_\Gamma)k_3 + \boldsymbol{k}_\Gamma^T \cdot (\boldsymbol{H}^*.\boldsymbol{k}_\Gamma) - \frac{\omega^2}{BH_{33}} = 0. \tag{4.4.7}$$

Then, the solution of the equation is given as,

$$k_3^{\pm} = -(\boldsymbol{\mathcal{C}}.\boldsymbol{k}_\Gamma) \pm \kappa, \tag{4.4.8a}$$

$$\text{with } \kappa = \left[\frac{\omega^2}{BH_{33}} + (\boldsymbol{\mathcal{C}}.\boldsymbol{k}_\Gamma)^2 - \boldsymbol{k}_\Gamma^T \cdot (\boldsymbol{H}^*.\boldsymbol{k}_\Gamma)\right]^{1/2}. \tag{4.4.8b}$$

The expressions of solution in medium Ω_1 are:

$$P = (P^+ e^{ik_3^+ x_3} + P^- e^{ik_3^- x_3}) e^{i\boldsymbol{k}_\Gamma \cdot \boldsymbol{x}_\Gamma}, \tag{4.4.9a}$$

$$\boldsymbol{V}.\boldsymbol{e}_3 = \frac{H_{33}\kappa}{\omega}(P^+ e^{ik_3^+ x_3} - P^- e^{ik_3^- x_3}) e^{i\boldsymbol{k}_\Gamma \cdot \boldsymbol{x}_\Gamma}. \tag{4.4.9b}$$

The boundary conditions applied at both interfaces are:

- continuity of pressure: $p_0(x_3 = D) = P(x_3 = D)$;
- continuity of normal particle velocity: $\boldsymbol{v}_0(x_3 = D) \cdot \boldsymbol{e}_3 = \boldsymbol{V}(x_3 = D) \cdot \boldsymbol{e}_3$;
- rigid backing condition: $\boldsymbol{V}(x_3 = 0) \cdot \boldsymbol{e}_3 = 0$.

Thus, the linear system of equations is as below:

$$P^+ e^{ik_3^+ D} + P^- e^{ik_3^- D} = R + 1, \tag{4.4.10a}$$

$$\frac{H_{33}\kappa}{\omega}(P^+ e^{ik_3^+ D} - P^- e^{ik_3^- D}) = \frac{k_3^{(0)}}{\omega\rho_0}(R - 1), \tag{4.4.10b}$$

$$\frac{H_{33}\kappa}{\omega}(P^+ - P^-) = 0. \tag{4.4.10c}$$

The final solutions are

$$R = \frac{\cos(\kappa D) + i\sigma \sin(\kappa D)}{\cos(\kappa D) - i\sigma \sin(\kappa D)}, \tag{4.4.11a}$$

$$P^+ = P^- = \frac{1}{\cos(\kappa D) - i\sigma \sin(\kappa D)}, \tag{4.4.11b}$$

$$\text{with } \sigma = \rho_0 H_{33}\kappa / k_3^{(0)}. \tag{4.4.11c}$$

Finally, the absorption coefficient can be obtained from $A = 1 - \mid R \mid^2$. All calculation related to reflection of a plane wave incidence in the later sections are done in the way described here.

4.5 Experimental validation

The unit cell Ω used here is a rectangular cube with the dimensions $\ell_{\mathrm{I}} \times \ell_{\mathrm{II}} \times \ell_{\mathrm{III}}$ in the directions of the Cartesian coordinate system $(\boldsymbol{e}_{\mathrm{I}}, \boldsymbol{e}_{\mathrm{II}}, \boldsymbol{e}_{\mathrm{III}})$. The tube in the unit cell Ω has the outer radius R_x, the finite length $\ell_x \leq \ell_{\mathrm{I}}$, and its axis oriented along $\boldsymbol{e}_{\mathrm{I}}$. The air domain outside the tube is denoted Ω_{m}. The JCAL viscous and thermal parameters used in this section are listed in Appendix B.

To validate theoretical model, configurations which consist of 7 by 7 square periodic arrangements of straight cylinders fixed onto a single plate or between double plates are tested. Several samples of different configurations are 3D printed, see Fig. 4.6 for details

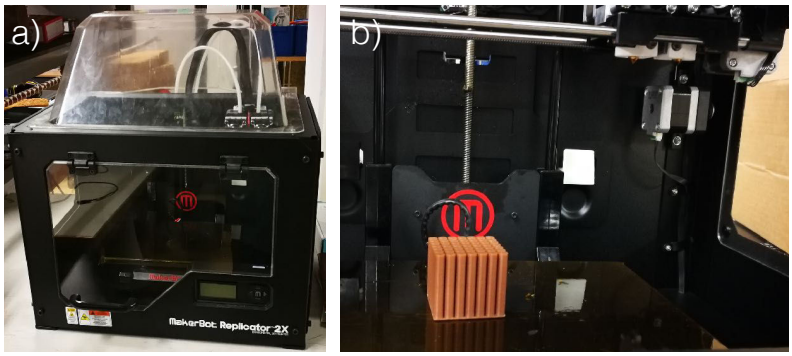

FIGURE 4.6: Photos: a) 3D printer: MakerBot®, Replicator™ 2X; b) Printing process: Fused Deposition Modelling(FDM).

about the 3D printer.

Two identical samples are made for each configuration and each sample are tested twice for reproducibility and repeatability. The absorption coefficient of the sample is measured in an impedance tube with a square cross section 4.2 cm by 4.2 cm, see Fig. 4.8c,d). The tube cut-off frequency is 4200 Hz. By assuming that plane waves propagate below the cut-off frequency, the infinitely rigid boundary conditions of the tube act like perfect mirrors in low frequency regime and create a periodicity pattern in the $\boldsymbol{e}_1$ and $\boldsymbol{e}_2$ directions.

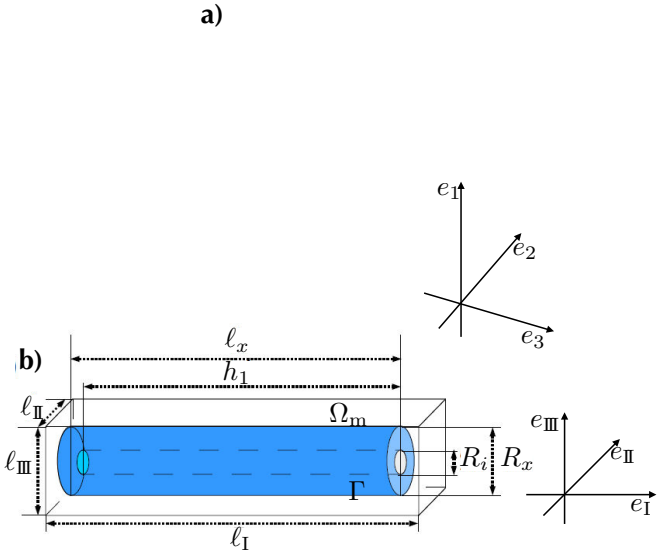

FIGURE 4.7: Test sample system description: a) Test sample in impedance tube; b) Representative Elementary Volume (REV) Ω. In Ω, the fluid volume outside resonators is Ω_{m}, the air/solid interface is Γ.

The printed samples are placed at the end of the tube against a copper plug that closes the tube and acts as a perfectly rigid boundary, therefore creating a periodicity along the $\boldsymbol{e}_3$ direction. Thus, we define two types of tests: $\boldsymbol{e}_{\text{I}}$ test where the unit cell vector $\boldsymbol{e}_{\text{I}}$ is parallel to $\boldsymbol{e}_3$ the axis of the impedance tube, and $\boldsymbol{e}_{\text{II}}$ test where the unit cell vector $\boldsymbol{e}_{\text{II}}$ is parallel to $\boldsymbol{e}_3$

This technique allows us to determine experimentally the absorption coefficient at normal incidence of a quasi-infinite 2D periodic structure. The reflection coefficient is measured with a single microphone method. For more details, see Sec. 1.6.1.

4.5.1 Solid cylinder Samples: non-resonant acoustic metamaterial

First, the configurations composed of solid cylinders are tested, therefore without inner resonator length, i.e., $h_1 = h_2 = 0$ and the resonator aperture $R_i = 0$. Pictures of the printed samples are shown in Fig. 4.8. Their dimensions are shown in Tab. 4.1.

Config.n°	R_x (mm)	ℓ_{II} (mm)	ℓ_x (mm)	ℓ_{I} (mm)	Info
1	2.9	6	40	40	double plate, $\boldsymbol{e}_{\text{II}}$ test
2	2.9	6	41	41	single plate, $\boldsymbol{e}_{\text{I}}$ test
3	2.9	6	37	41	single plate, $\boldsymbol{e}_{\text{II}}$ test
4	2.9	6	39	41	single plate, $\boldsymbol{e}_{\text{II}}$ test
5	2.9	6	40	41	single plate, $\boldsymbol{e}_{\text{II}}$ test

TABLE 4.1: Dimensions of configurations n°1 to 5, with a global thickness D in $\boldsymbol{e}_3$ equals to 42 mm.

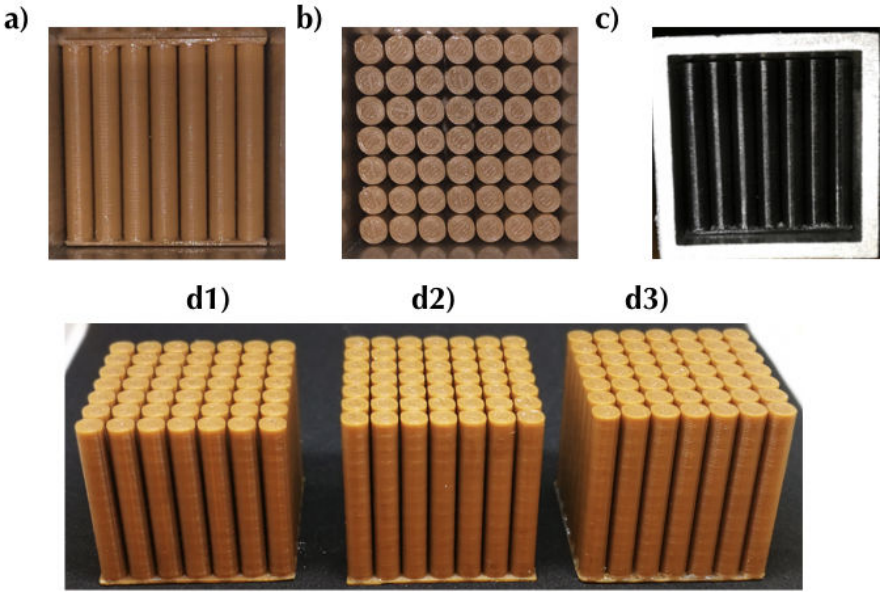

FIGURE 4.8: Pictures of the samples: a) Config.n°1: double plate, $\boldsymbol{e}_{\text{II}}$ test; b) Config.n°2: single plate, $\boldsymbol{e}_{\text{I}}$ test; c) Config.n°3: single plate, $\boldsymbol{e}_{\text{II}}$ test; d1)-d3): Confign°3 to n°5.

The absorption coefficients of the effective material in normal incidence into $\boldsymbol{e}_{\text{I}}$ and $\boldsymbol{e}_{\text{II}}$ directions are shown in Fig. 4.9 for Config.n°1 (Fig. 4.8a) and n°2 (Fig. 4.8c). Both results show good agreement between theoretical predictions and experimental results in terms of peak frequencies and absorption amplitude. Though, both test results are influenced by noise, causing numerous small variation, especially in low absorption level area and higher frequencies.

The absorption coefficients of the solid array at normal incidence into $\boldsymbol{e}_{\text{II}}$ direction are shown in Fig. 4.10 for Config.n°3 to n°5. Config.n°3 to n°5 bear the same R_x, ℓ_{I} and ℓ_{II},

but different ℓ_x, meaning that the total porosity of the three configuration are different. Also a small "gap" is formed between the impedance tube wall and the extremity of the solid cylinders as $\ell_x < \ell_{\mathrm{I}}$, which resembles a "slit" similar to the ones in Chapter 1 and 2, see Fig. 4.8b).

Seemingly, the spaces between cylinders resemble the added resonators in Chapter 1 and 2. Nevertheless, it should be clearly pointed out that the unit-cell here is completely different than those of Chapter 1 and 2. The main difference is that the array is now permeable, all fluid inside the unit cell interacts accounting for the bulk effective behaviour of the whole medium, whether in the "slit" or between cylinders.

All three tests show very good agreement with theoretical prediction up to 2.5 kHz. The predictions on the peak frequencies and amplitudes are accurate. For frequencies higher than the absorption peaks where the experimental curves are closely followed by the theoretical ones, the theoretical model still gives out good predictions.

Here the global thickness $D = 42$ mm. For lossless cases, the resonance frequency of the rigid-backed layer is $c_0/4D \approx 2$ kHz. Though in the lossy case, as the effective sound speed of this porous medium of solid cylinder array is around 0.65, shown in Fig. 4.4. The theoretical prediction locates the resonance frequency $v_{eff}/4D$ around 1.35 kHz $\approx 0.65 c_0/4D$.

Also, it is clear that Config.n°4 and n°5 are very similar in dimensions, only 1 mm difference on ℓ_x, thus they give out very similar theoretical predictions and experimental results. The experimental results confirm that the theoretical model is not very sensitive to small changes in h_1.

4.5.2 Hollow tube samples: resonant acoustic metamaterial

Then, a series of tests are performed with configurations of hollow tube array. To facilitate the fabrication, only sided hollow tube array are built ($h_2 = 0$ mm). The configuration tested consists of a 7 by 7 square periodic arrangement of straight hollow tubes fixed onto a single plate, see Fig. 4.11. The end of QWR is the backing plate, thus making $\ell_x = h_1$. The experiments are carried out in the same manner as those conducted during the solid cylinder tests. Pictures of the printed samples are shown in Fig. 4.11. Their dimensions are shown in Tab. 4.2:

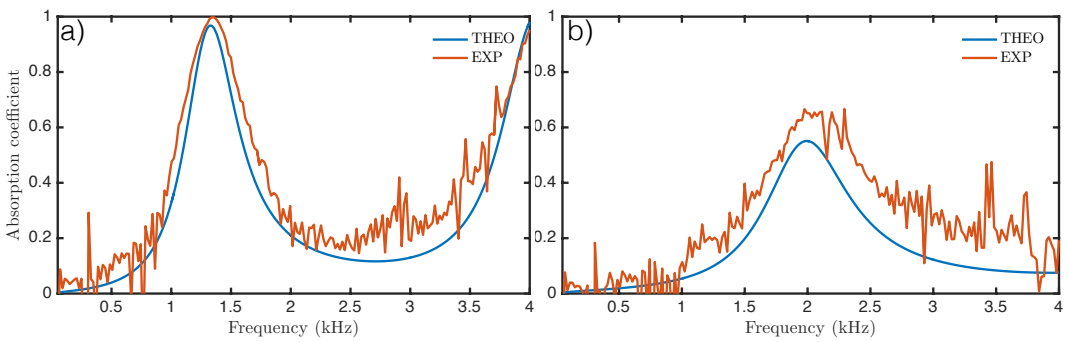

FIGURE 4.9: Absorption coefficients against frequency: a) Config.n° 1: $\boldsymbol{e}_{\mathrm{II}}$ test ; b) for Config.n° 2: $\boldsymbol{e}_{\mathrm{I}}$ test.

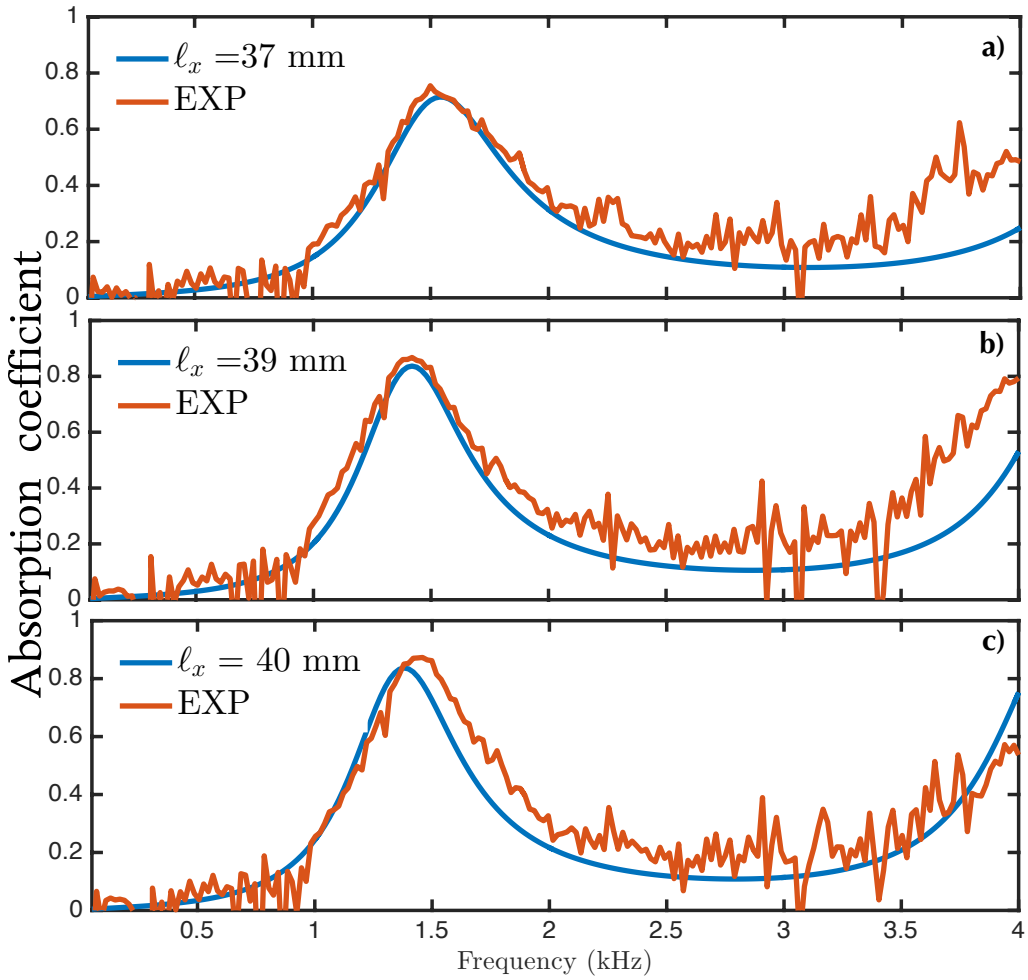

FIGURE 4.10: Absorption coefficients against frequency of $\boldsymbol{e}_{\mathrm{II}}$ test: a) Config.n°3: ℓ_x = 37 mm; b) for Config.n°4: $\ell_x = 39$ mm; c) Configuration n°5: $\ell_x = 40$ mm.

In Fig. 4.12, all three tests show good agreement with theoretical prediction up to the QWR resonance frequencies ω_1, both qualitatively and quantitatively, despite the discrepancies in the frequencies of the absorption peaks at lower frequencies.

These small discrepancies can be due to compressible effects occurring at the scale of the unit cell since the micro-to-macro scale parameters $\epsilon_{\mathrm{II}} = \ell_{\mathrm{II}}\omega/c_0 \approx 0.3$ and $\epsilon_{\mathrm{I}} = \ell_{\mathrm{I}}\omega/c_0 \approx 2$ at frequencies around 2.5 kHz indicate a poor scale separation and question the long-wavelength approximation. They can be due to the fact that the theoretical model considers an infinite periodicity in the effective metamaterial layer, which accumulates infinite amount of Fabry-Pérot interference together at the tube resonance. However in reality, there exists only 7 rows of resonator in the tested samples, so the

Config.n°	R_x (mm)	R_i (mm)	ℓ_{II} (mm)	ℓ_{I} (mm)	ℓ_x (mm)	h_1 (mm)
6	2.9	1.9	6	41	37	37
7	2.9	1.9	6	41	39	39
8	2.9	1.9	6	41	40	40

TABLE 4.2: Dimensions of Config.n°6 to 8.

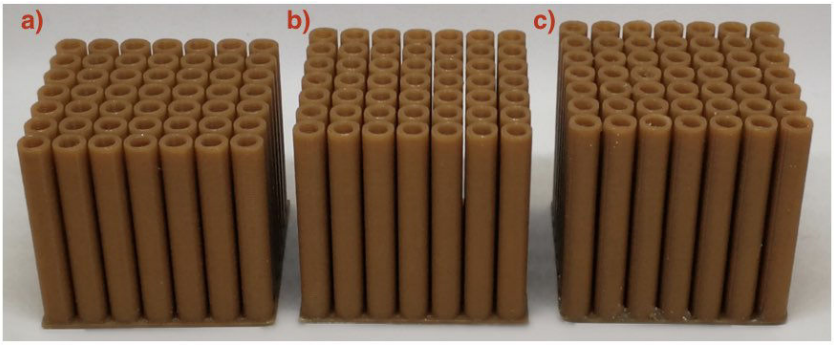

FIGURE 4.11: Picture of samples : a) Config.n°6: $\ell_x = 37$ mm, $h_1 = 37$ mm; b) Config.n°7: $\ell_x = 39$ mm, $h_1 = 39$ mm; c) Config.n°8: $\ell_x = 40$ mm, $h_1 = 40$ mm.

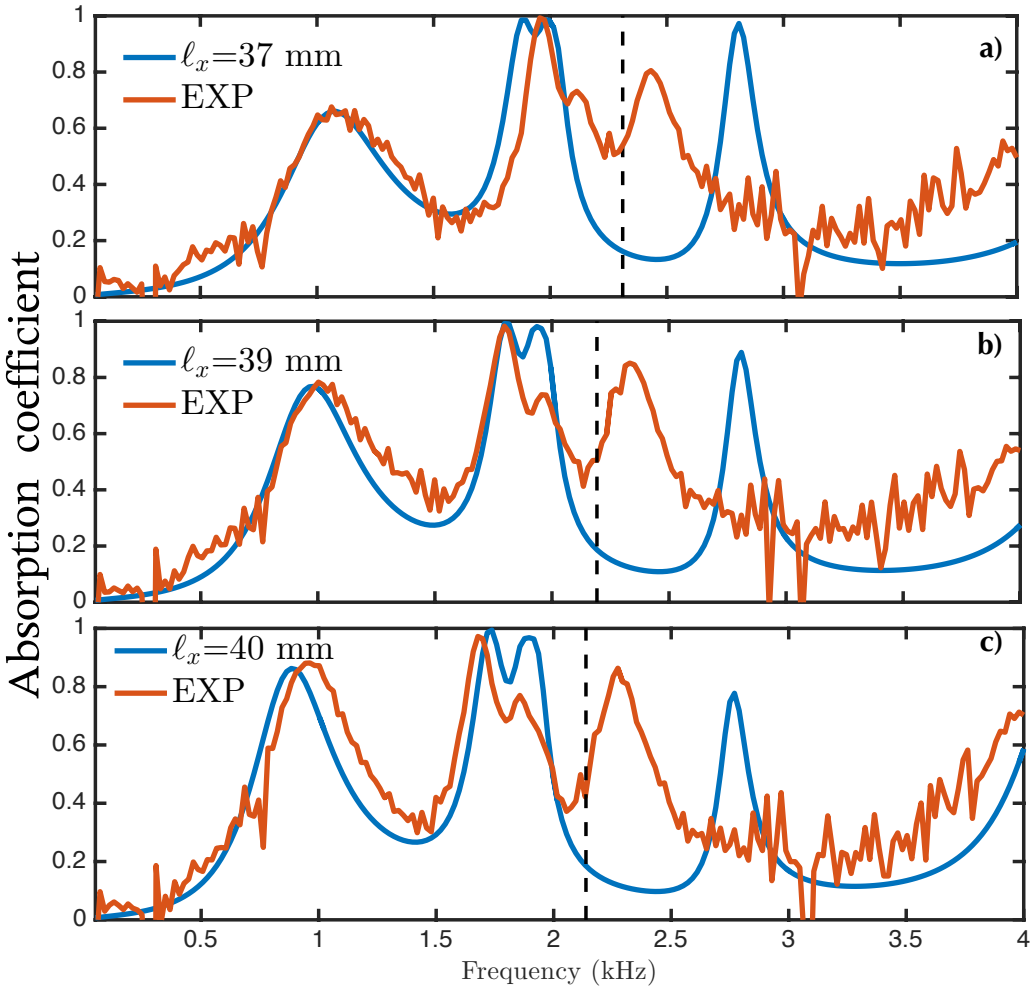

FIGURE 4.12: Absorption coefficients against frequency of $\boldsymbol{e}_{\mathrm{II}}$ test with the respective tube resonance frequency in dashed line: a) Config.n°6; b) for Config.n°7: c) Config.n°8.

experimental amplitude of the peak at f_R is much smaller than theoretically expected.

Due to manufacture limitation of the 3D printer, the outer and inner radii of the hollow tubes are not exactly those imposed theoretically. This indicates that the physic model is very sensitive on small dimension changes in R_x, R_i and $\ell_{\mathrm{II}}(\ell_{\mathrm{III}})$. Nevertheless, the results bear testament to the robustness of the physical phenomena at stake.

Conclusion

In this Chapter, an anisotropic acoustic metamaterial based on a square-periodic arrangement of hollow cylindrical tubes is studied. The physical model relies on the homogenisation procedure of the solid cylinder array, while tailoring the added inner resonance. The added QWRs in the cylindrical tubes are modelled by the flux radiating from the apertures of the resonators Σ_j into fluid domain Ω_{m}. These apertures act as secondary sources in the mass conservation.

The dispersion properties of the hollow tubes array are studied and compared with the solid cylinder counterparts. A negative compressibility is found with the hollow case. This leads to the slow sound effect before the tube resonance frequency. A pseudo-band gap is found around the tube resonance frequency, which is represented by a huge attenuation within the frequency band.

Various samples of the solid and hollow tube configurations are manufactured through 3D printing. Impedance tube tests are conducted to measure the reflection and absorption coefficient of the samples in different principal direction. A general good agreement between the theoretical model and experimental results are obtained for all tests.

The solid tube tests validate the theoretical model of homogenisation without inner resonance and the numerically obtained JCAL parameters in different principal directions for anisotropic material. The hollow tube tests further validate the homogenised model with inner resonators.

As the accuracy of the whole theoretical model is clearly demonstrated, optimisation procedure on the metamaterial can be carried out in the next part of this PhD thesis.

Part III

Straw-inspired Metamaterial

Chapter 5

Perfect absorption design

In this Chapter, the straw-inspired acoustic metamaterial is theoretically and experimentally studied for perfect sound absorption. A parametric study on the porous medium consisting of the periodic repetition of the unit cell with embedded rigid cylinder is performed first. It gives out the variation patterns of various parameters according to different dimensions. A design is proposed for perfect absorption by a sub-wavelength absorber based on critical coupling condition. Impedance tube tests are finally performed on the 3D-printed samples of the optimal configuration.

Contents

Introduction

Natural or bio-inspired materials have been recently shown as good candidates to control waves in both acoustics and optics. For example, in acoustics straw has been used as building material for thousands of years. On one hand, acoustic insulation tests in lab and in real condition have revealed that wood-framed non-arranged loosely packed straw bales have a good ability for sound absorption and present a transmission loss of 35-46 dB [47, 48]. On the other hand, natural structures which possess specific properties of metamaterial have also been found in the field of optics and electromagnetism [31].

Inspired by these recent developments, we propose here a straw-inspired metamaterial constituted of a periodic arrangement of hollow tubes, which mimics straws cut in between nodes. The metamaterial is considered anisotropic, which is ideal for strong dispersion and angle-selective absorption, like the butterfly wings in Ref. [31].

Furthermore, optimisation is done based on the critical coupling theory [30] to increase the sound absorption of the metamaterial, as presented in Chap 2. When the leakage of energy out of a resonant system and its inherent losses are perfectly balanced, the critical coupling condition is thus fulfilled. Then, a perfect destructive interference between the transmitted (or reflected) and the internal fields leads to maximum absorption at the resonance frequency of the effective layer [29, 30].

We study the trajectories of the zero and pole of the absorption coefficient in the complex frequency plane, by tuning the system dimensions. The zero appears at a complex frequency the real part of which is related to the resonance frequency while the imaginary part is related to the leakage rate of the system. The cross-section of the complex plane on the purely real frequency line is related to the reflection coefficient result that can be measured in reality. So, the total absorption can be achieved when the zero is exactly located on the purely real frequency line [82, 85].

In this Chapter, we look for a configuration at normal incidence and orthotropic orientation, based on the critical coupling theory.

First, a parametric study is performed on the air domain of the unit cell, considering only the solid cylinder inside the unit cell. In doing so, the variation patterns of the JCAL visco-thermal parameters in relation to the dimensions of the unit cell are revealed to facilitate the tuning of the exterior of the tube in the unit cell. Based on the knowledge of the parametric study, we design a configuration which has a total absorption peak in the sub-wavelength regime, by tuning the various dimensions.

Impedance tube tests are carried out of 3D-printed samples of one of the designs with perfect absorption.

5.1 General description

The straw-inspired metamaterial consists of closely packed three-dimensional Ω-periodic arrangement of straight hollow tubes with a single tube per period. The general configuration of the unit cell and periodic arrangement is the same as shown in Fig. reflfig:Figure1.

Here, the unit cell Ω is a rectangular cube with the dimensions $\ell_{\mathrm{I}} \times \ell_{\mathrm{II}} \times \ell_{\mathrm{III}}$ in the directions of the Cartesian coordinate system $(\boldsymbol{e}_{\mathrm{I}}, \boldsymbol{e}_{\mathrm{II}}, \boldsymbol{e}_{\mathrm{III}})$. The hollow tube in the unit cell Ω has the outer radius R_x, the inner radius $R_i < R_x$, the finite length $\ell_x \leq \ell_{\mathrm{I}}$, and its axis oriented along $\boldsymbol{e}_{\mathrm{I}}$. The air domain outside the tube is denoted Ω_{m}.

The inner part of the tube is split into two cylindrical ducts Ω_1 and Ω_2 by a rigid wall. Each has the length h_1 or h_2 and the outside apertures Σ_1 and Σ_2 with the unit normal vectors $\boldsymbol{n}_1 = -\boldsymbol{e}_{\mathrm{I}}$ and $\boldsymbol{n}_2 = \boldsymbol{e}_{\mathrm{I}}$ directed towards the outside of the ducts. The filling fractions $\phi_{\mathrm{m}} = |\Omega_{\mathrm{m}}|/|\Omega|$, and $\phi_j = |\Omega_j|/|\Omega|$ with $j \in \{1, 2\}$ are defined, where the volume of the domains Ω, Ω_{m}, and Ω_j read: $|\Omega| = \ell_{\mathrm{I}}\ell_{\mathrm{II}}\ell_{\mathrm{III}}$, $|\Omega_{\mathrm{m}}| = |\Omega| - \pi R_x^2 \ell_x$, $|\Omega_j| = \pi R_i^2 h_j$. The total porosity of the medium is $\phi = \phi_{\mathrm{m}} + \phi_1 + \phi_2 < 1$.

The straw-inspired metamaterial is studied in the long-wavelength approximation, assuming that the condition of scale separation $\epsilon = \ell_{\mathrm{I}}/L \ll 1$ is satisfied, where $L = c_0/\omega$ is the characteristic length of the sound wave. The scale separation and the Ω-periodicity of the array allow using the two-scale asymptotic homogenisation method [51, 52] to derive the effective behaviour of the metamaterial, as explained in Chapter 4.

The effective mass conservation and the generalised Darcy law in the metamaterial are recalled here:

$$\operatorname{div} \boldsymbol{V} = \frac{\mathrm{i}\omega P}{B_0/\beta}, \quad \boldsymbol{V} = -\frac{\boldsymbol{K}_{\mathrm{m}}}{\eta} \operatorname{\mathbf{grad}} P, \tag{5.1.1}$$

where the effective compressibility β reads as the series association of the compressibility β_{m} of the medium outside the tubes and apparent compressibility β_j induced by the resonator Ω_j:

$$\beta = \phi_{\mathrm{m}}\beta_{\mathrm{m}} + \sum_j \phi_j \beta_j, \quad \text{with } \beta_j = \frac{B_0}{B^*} \frac{\tan(k^* h_j)}{k^* h_j}, \quad \text{with } k^* = \omega\sqrt{\rho^*/B^*}, \tag{5.1.2}$$

where ρ^* and B^* are the effective density and bulk modulus of air in a cylindrical tube with a circular cross section [61].

5.2 Parametric analysis

First, we look to the relations between the viscous and thermal parameters of JCAL model and the dimensions of the unit-cell. The array consists of the three-dimensional Ω-periodic arrangement of straight rigid solid cylinders ($h_1 = h_2 = 0$), with a single tube per period, see Fig. 5.1.

In this parametric analysis, 245 different unit-cell configurations are calculated with *COMSOL Multiphysics* ®, varying in all dimensions. In order to save computation time, ℓ_{III} is still set equal to ℓ_{II}. Their viscous and thermal parameters are extracted, interpolated and normalised accordingly, see Chapter 3. These frequency-independent viscous and thermal parameters are shown against the normalised dimensions: the transversal

porosity $\phi_t = 1 - \pi R_x^2/\ell_{\mathrm{II}}^2$, the relative cylinder length ℓ_x/ℓ_{I} and the relative unit-cell size $\ell_{\mathrm{I}}/\ell_{\mathrm{II}}$, see Fig. 5.2 to 5.4. We notice that for high values of porosity, these viscous and thermal parameters have analytical approximated solutions as shown in Ref. [43], where the current model becomes 2D equivalent, as $\ell_x = \ell_{\mathrm{I}}$ and $\phi = \phi_t$.

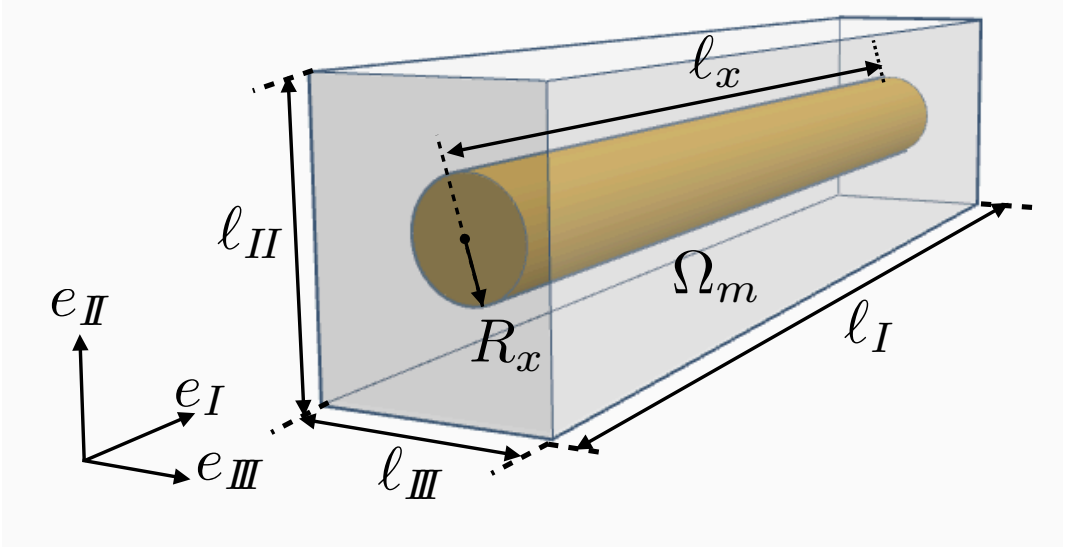

FIGURE 5.1: Solid tube array as $R_i = 0$.

5.2.1 Viscous parameters

In Fig. 5.2 and 5.3, the sub-figures of different parameters in relation to different variables are presented and arranged in the following way ($i = \mathrm{I}, \mathrm{II}$):

- Row.1: Normalised viscous static permeability $K_{\mathrm{m}}^{i0}/R_x^2$;
- Row.2: High frequency limit of dynamic tortuosity $\tau_{\mathrm{m}}^{i\infty}$;
- Row.3: Normalised viscous characteristic length $\Lambda_{\mathrm{m}}^{i}/R_x$;
- Col.1: Parameters in relation to ϕ_t when $\ell_{\mathrm{I}}/\ell_{\mathrm{II}} = 8.4$, $\ell_x/\ell_{\mathrm{II}} = 0.12, 0.26, 0.57, 0.98$;
- Col.2: Parameters in relation to ℓ_x/ℓ_{I} when $\ell_{\mathrm{I}}/\ell_{\mathrm{II}} = 8.4$, $\phi_t = 0.25, 0.5, 0.95$;
- Col.3: Parameters in relation to ϕ_t when $\ell_x/\ell_{\mathrm{I}} = 0.95$, $\ell_{\mathrm{I}}/\ell_{\mathrm{II}} = 14, 6, 3$.

Along the $\boldsymbol{e}_{\mathrm{I}}$ principal direction, the viscous parameters are shown in Fig. 5.2, where the axis solid cylinder is parallel to the principal direction $\boldsymbol{e}_{\mathrm{I}}$.

Most of the relations shown in Fig. 5.2 are monotonic, except for those with tortuosity. The high frequency limit of dynamic tortuosity, often simply called tortuosity has its maximal value here at 1.6, when the relative cylinder length ℓ_x/ℓ_{I} equals to 0.5. It also decreases as the transversal porosity increases. The value of the tortuosity tends to 1, when ϕ_t approaches 1.

Meanwhile, the normalised static viscous permeability $K_{\mathrm{m}}^{\mathrm{I}0}/R_x^2$ and the normalised viscous characteristic length $\Lambda_{\mathrm{m}}^{\mathrm{I}}/R_x$ increase when the transversal porosity becomes bigger. But they decrease in value as the the relative cylinder length ℓ_x/ℓ_{I} becomes larger. The small dynamic of variation demonstrates that ℓ_x/ℓ_{I} has very small influence on this

principal direction, see Fig. 5.2, Col.2) Row.1,3).

Along the $\boldsymbol{e}_{\mathrm{II}}$ principal direction, the parameters are shown in Fig. 5.3, where the solid cylinder is perpendicular to the principal direction $\boldsymbol{e}_{\mathrm{II}}$. $K_{\mathrm{m}}^{\mathrm{I}0}/R_x^2$ and $\Lambda_{\mathrm{m}}^{\mathrm{I}}$ increase as the transversal porosity decreases, while decrease as the the relative cylinder length increases. They also vary in a synchronicity. But the dynamic of the variation is smaller than in the previous cases. In the case of 2D equivalent geometry as $\ell_{\mathrm{I}} = \ell_x$, most of data converges to the 2D value [43], with discrepancies found on Col 2) of relation to the relative cylinder length.

Similarly, tortuosity decreases as the transversal porosity increases. As ϕ_t tends towards its geometrical limit $1-\pi/4$, the peak value of the tortuosity shown here is around 2.5, which is obtained at extremely low porosity where $R_x \to \ell_{\mathrm{II}}/2$ and relative cylinder length close to 1.

The value of the tortuosity of the 3D model is clearly different with respect to he one of the 2D limit, where the model becomes 2D equivalent as $\ell_x \to \ell_{\mathrm{I}}$. This shows that a simple 2D calculation is not sufficiently precise, even when only a small "gap" is added to the unit-cell, especially in the $\boldsymbol{e}_{\mathrm{II}}$ principal direction [43].

Theoretically, the maximal tortuosity could be as high as 3, where the distance between the cylinders are in micrometer level. This is made possible, especially because of the 3D nature of the unit cell.

Now, comparing the parameters of the two principal directions, it becomes evident that all parameters in the parallel direction are smaller than those of the $\boldsymbol{e}_{\mathrm{II}}$ direction of the same dimension configurations, and the variations of the tortuosity are often in opposite tendency to the rest of the parameters.

These observations are consistent with the conventional consensus, that smaller total porosity creates bigger obstacles for the flow as in the case of $\phi_{\mathrm{m}} \to 1-\pi/4$ and $\ell_x/\ell_{\mathrm{I}} \to 1$. Numerically, $K_{\mathrm{m}}^{i0}/R_x^2$ and $\Lambda_{\mathrm{m}}^{i}/R_x$ becomes smaller and tortuosity becomes bigger. Eventually this is translated into much more losses in the medium. If, only a non-dispersive medium is considered, this highly lossy medium can induce extraordinary high absorption with a large thickness of medium [113].

The variation of $K_{\mathrm{m}}^{i0}/R_x^2$ and $\Lambda_{\mathrm{m}}^{i}/R_x$ is synchronised in all cases, because they are both related to the frequency-independent shape factor M_{m}^{i}.

Also, it can be concluded that the relative unit-cell size has little influence on all parameters in both principal directions. Meanwhile, the relative cylinder length has a greater influence than other variables, especially on the tortuosity. This reminds us again that the consideration of total porosity ϕ_{m} is essential in this full 3D model.

5.2.2 Thermal parameters

As thermal effects are scalar in nature, only one set of parameters is obtained from the numerical computations. The thermal parameters are shown in Fig. 5.4. The sub-figures of different parameters in relation to different variables are presented and arranged in the following way:

- Row.1: Normalised thermal static permeability $\Theta^0_{\mathrm{m}}/R^2_x$;
- Row.2: Normalised thermal characteristic length $\Lambda'_{\mathrm{m}}/R_x$;
- Col.1: Parameters in relation to ϕ_t when $\ell_{\mathrm{I}}/\ell_{\mathrm{II}} = 8.4$, $\ell_x/\ell_{\mathrm{II}} = 0.12, 0.26, 0.57, 0.98$;
- Col.2: Parameters in relation to ℓ_x/ℓ_{I} when $\ell_{\mathrm{I}}/\ell_{\mathrm{II}} = 8.4$, $\phi_t = 0.25, 0.5, 0.95$;
- Col.3: Parameters in relation to ϕ_t when $\ell_x/\ell_{\mathrm{I}} = 0.95$, $\ell_{\mathrm{I}}/\ell_{\mathrm{II}} = 14, 8.4, 6, \frac{14}{3}$.

Similarly to the viscous cases, the two thermal parameters are in monotone to all three geometry dimensions. The permeability $\Theta^0_{\mathrm{m}}/R^2_x$ and the characteristic length Λ'_{m} increase as the transversal porosity increase, while decreases as the the relative cylinder length increases, and their variations are in a synchronicity.

Their values are bigger than those of their viscous counterparts, which the fact is in line with the conventional consensus [10]. When transiting to the 2D equivalent geometry, all data converge to the 2D value.

Nevertheless discrepancies are found for normalised thermal characteristic length at the limit of the 2D equivalent configuration. The crossing of the curves are not admissible. The reason of this is mainly due to human error during the naming of different dimension configuration.

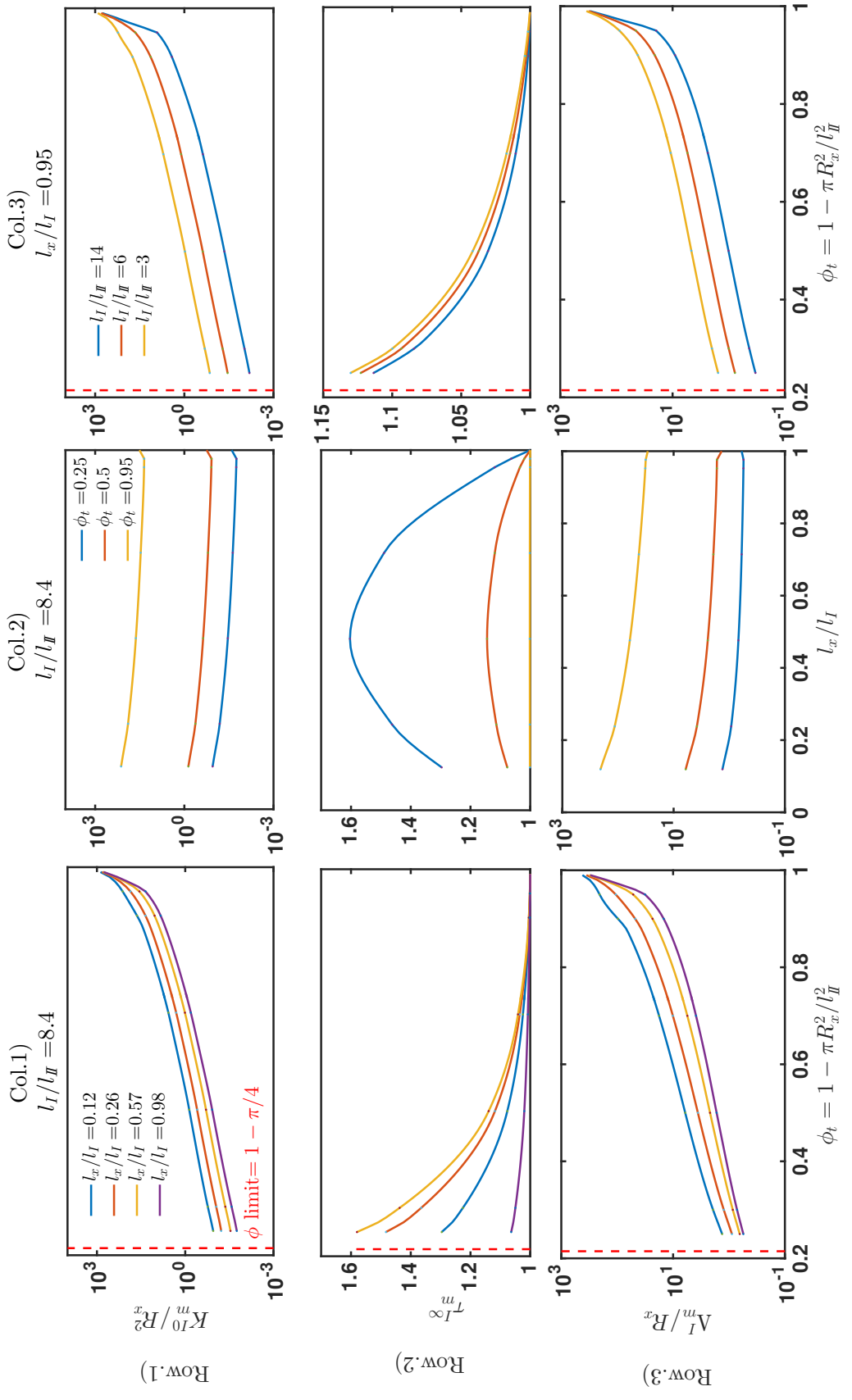

FIGURE 5.2: Normalised viscous parameters in principal direction $\mathbf{e}_\mathrm{I}$. .

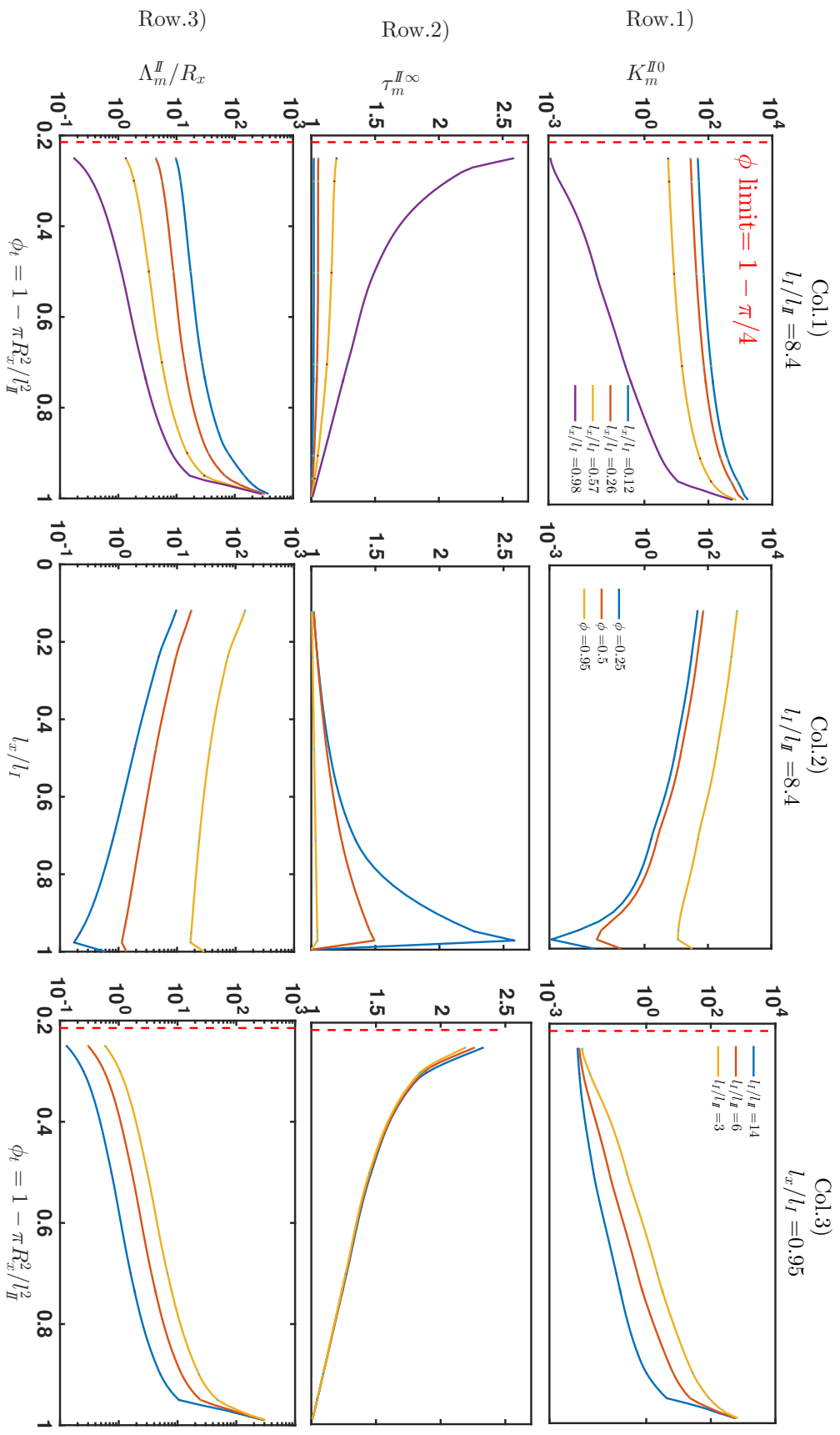

FIGURE 5.3: Normalised viscous parameters in principal direction $\boldsymbol{e}_{II}$. .

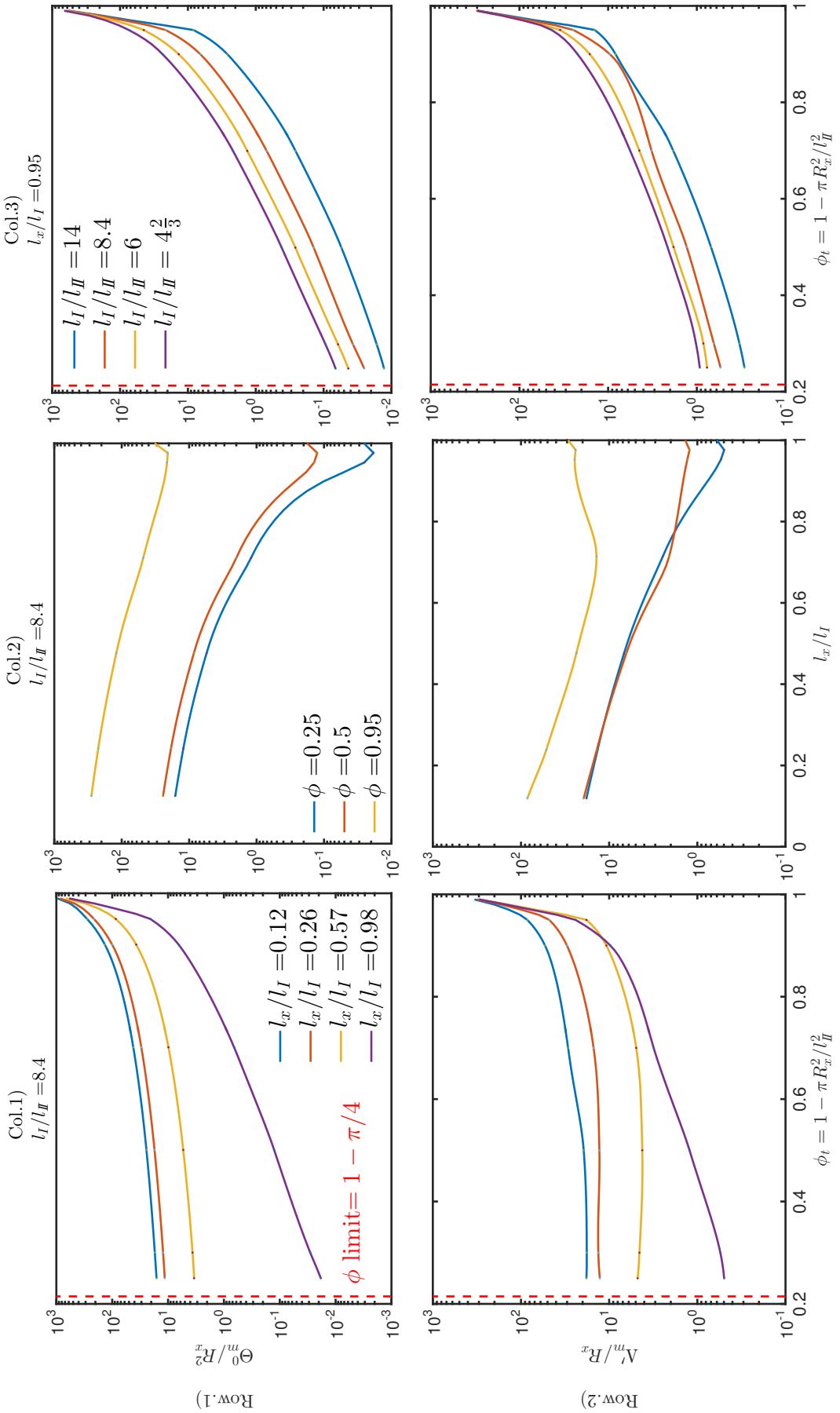

FIGURE 5.4: Normalised thermal parameters.

5.3 Dispersion relation

The dispersion properties of the design shown in Tab. 5.1 is studied, for principal directions $\boldsymbol{e}_{\mathrm{I}}$ and $\boldsymbol{e}_{\mathrm{II}}$, compared with their solid tube array counterparts. The quarter-wavelength resonance frequencies of the larger inner resonator is designated as $f_{\mathrm{R}} = \omega_1/(2\pi)$.

We start by analysing the effective properties of the material made of solid and hollow tubes. Figure 5.5 shows the real and imaginary parts of the normalised bulk modulus $B/\gamma P_e = 1/\beta$ of the straw-inspired metamaterial (Hollow case) against the normalized frequency. They are compared with the Solid case where the unit cell configuration stays the same but $R_i = 0$.

It is shown that the real part of the effective bulk modulus remains negative till $1.127 f_R$. The imaginary part of the effective bulk modulus B becomes negative from f_R till $1.3 f_R$ in the pseudo-bandgap characterised by $\mathrm{Re}(k_n) \to 0$.

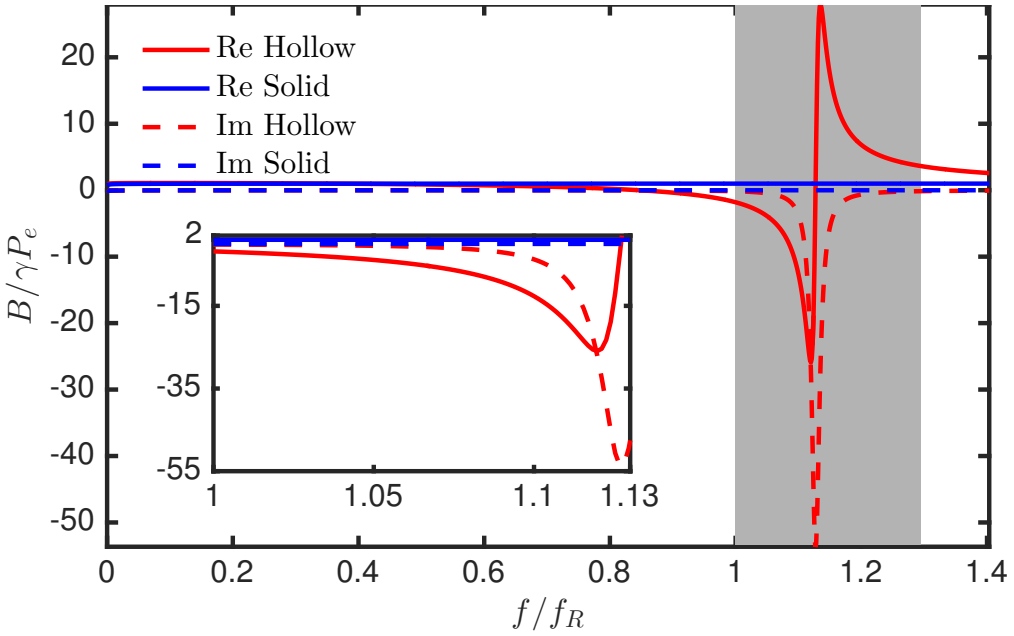

FIGURE 5.5: Normalised bulk modulus $B/\gamma P_e$ of the straw-inspired metamaterial: Real part (solid line), imaginary part (in dashed line): Hollow case in red, Solid case array in blue.

Here, the propagation of the plane wave $P = e^{\mathrm{i}k_i \boldsymbol{e}_i \cdot \boldsymbol{x}}$ in the principal direction $\boldsymbol{e}_i$ is studied, where k_i is the wavenumber in the direction $\boldsymbol{e}_i$ such that $\mathrm{Re}(k_i) \geq 0$, and $\boldsymbol{x}$ is the position vector. Substituting $P = e^{\mathrm{i}k_i \boldsymbol{e}_i \cdot \boldsymbol{x}}$ in the governing equations (5.1.1), the dispersion relation is derived in the form:

$$k_i = \sqrt{\frac{\mathrm{i}\omega}{B_0/\beta} \frac{\eta}{K_i}}, \quad \text{with } \mathrm{Re}(k_i) \geq 0. \tag{5.3.1}$$

The results are also compared between different principal directions $\boldsymbol{e}_{\mathrm{I}}$ and $\boldsymbol{e}_{\mathrm{II}}$.

In Fig. 5.6a), the effective wavenumbers $\mathrm{Re}(k(\omega))$ normalised by π/ℓ_{II} is shown against the normalised frequency, for hollow and solid tube array in the principal directions $\boldsymbol{e}_{\mathrm{I}}$

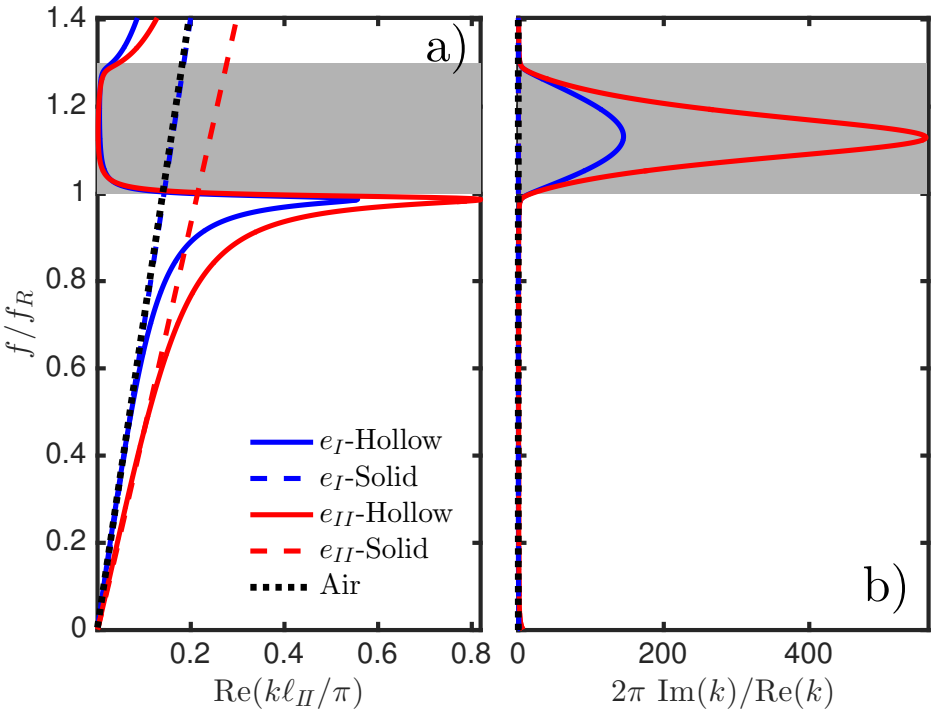

FIGURE 5.6: Normalised wavenumber for hollow tube array: a) Real parts of the normalized wavenumber ; b) Imaginary parts of the normalized wavenumber: Air characteristic wavenumber or sound speed (in black dash-dotted line), direction $\boldsymbol{e}_{\mathrm{I}}$ in blue and direction $\boldsymbol{e}_{\mathrm{II}}$ in red.

and $\boldsymbol{e}_{\mathrm{II}}$.

The slope of effective wavenumber Re($k(\omega)$) in the principal direction $\boldsymbol{e}_{\mathrm{II}}$ for the hollow tubes is smaller than that of the air and that of the solid tubes at all frequencies till around $1.3f_R$, indicating a slower wave speed in presence of hollow tubes array than that in the ambient conditions. This pseudo-band-gap is shown in grey. Its counterpart in $\boldsymbol{e}_{\mathrm{I}}$ has a slope almost identical to that of the ambient air, indicating a similar sound speed in this direction.

Meanwhile, an highly-attenuated mode, shown in Fig. 5.6b) appears above f_R, with the wavelength $2\pi/\mathrm{Re}(k)$ up to 145 times (in direction $\boldsymbol{e}_{\mathrm{I}}$) or 560 times (in direction $\boldsymbol{e}_{\mathrm{II}}$) of the characteristic attenuation length $1/\mathrm{Im}(k)$. The corresponding characteristic attenuation lengths are 3.2 mm for $\boldsymbol{e}_{\mathrm{II}}$, and 4.8 mm for $\boldsymbol{e}_{\mathrm{I}}$. They are both smaller than the dimensions of the unit cell, indicating a large attenuation.

Thus, the effective wave speed $v_{\mathrm{eff}} = \mathrm{Re}(\sqrt{B/\rho_n})/c_0$ is shown against normalised frequency in Fig. 5.7. The slow sound regime is observed at frequencies from 0 to $1.3f_R$. The effective wave speed reaches its minimum around f_R, which equals only 6.5% for $\boldsymbol{e}_{\mathrm{II}}$ or 11% for $\boldsymbol{e}_{\mathrm{I}}$ of the sound speed c_0 in ambient condition. This demonstrates a quasi non-propagative band from f_R to $1.3f_R$.

Also it is worth noting that the sound speed profiles of the solid tube array are similar to those of the hollow tube array in both principal directions, for frequencies below $0.6f_R$. This observation in the critically coupled case is different than those in the non-critical cases, shown in Sec. 4.3, where the sound speed of the hollow tube array is much lower

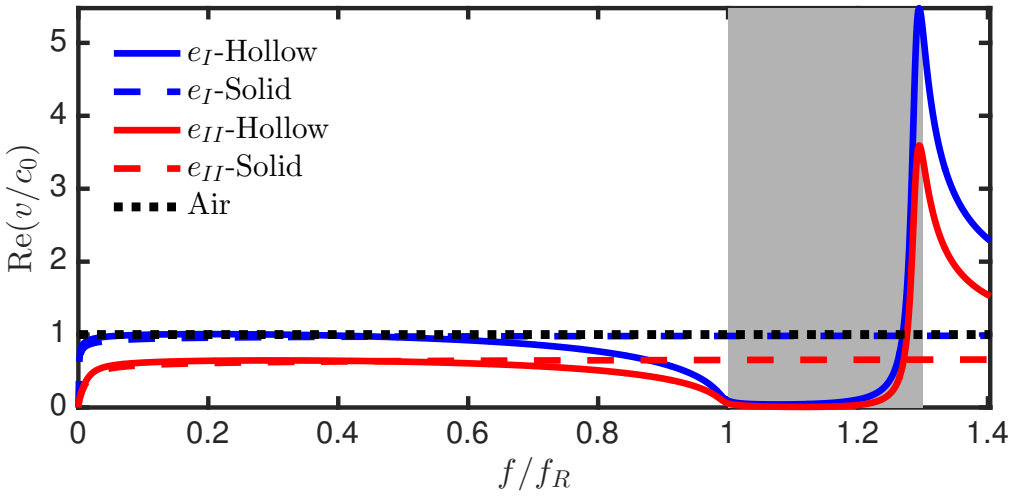

FIGURE 5.7: Effective wave speed, normalised by the sound speed c_0, Air sound speed in black dotted line, Direction $\boldsymbol{e}_{\mathrm{I}}$ in blue Direction $\boldsymbol{e}_{\mathrm{II}}$ in red.

than the one of the solid tube array. This may be due to the fact that the solid tube array is already tuned to a near-critical coupled state, the adding of QWRs has less effect than it has for the non-critical cases.

When comparing results of $\boldsymbol{e}_{\mathrm{I}}$ and $\boldsymbol{e}_{\mathrm{II}}$ directions, it is clear that the straw-inspired material induces more attenuation and lower wave speed in $\boldsymbol{e}_{\mathrm{II}}$ direction, of which the fact agrees with the FEM results of Johnson-Lafarge model parameters where the tortuosity plays a major role in defining losses in the periodic array [9].

The speed profiles shown in Fig. 5.7 have their local maxima at frequencies below f_R. For the principal direction $\boldsymbol{e}_{\mathrm{II}}$, this local maxima is at 64.5% of ambient sound speed c_0. Meanwhile, for the principal direction $\boldsymbol{e}_{\mathrm{I}}$, the local maxima reaches c_0. This may help to induce a surface wave propagation for a grazing incidence at the material surface.

Moreover, effects of the apparent tube resonance stands out in both directions as it affects dispersion in both directions through its association with the air-matrix bulk modulus, and plays a major role in generating slow-sound regime at lower frequencies.

To summarise, the unit cell configuration with two QWRs can efficiently induce a negative compressibility, causing high attenuation at resonance frequency, which manifests in slower effective wave speed than sound speed in air.

5.4 Design process of finite size samples for perfect absorption

In this Section, we look for total absorption at the first resonance of the Fabry-Pérot of a structure made of N by M unit cells at low frequency, when the incident wave impinges the structure at normal incidence along the $\boldsymbol{e}_{\mathrm{II}}$ direction of the unit cell. In other words, the unit cell is placed such a way that the material is orthotropic with $\boldsymbol{e}_{\mathrm{I}} = \boldsymbol{e}_1$, $\boldsymbol{e}_{\mathrm{II}} = \boldsymbol{e}_2$ and $\boldsymbol{e}_{\mathrm{III}} = \boldsymbol{e}_3$. The design is done through tuning the various dimensions of the effective material and the unit cell configuration.

5.4.1 Global thickness

To locate the first resonance in low frequency regime, we start with basic rigid-backed material resonance frequencies, as $c_0/4D$. Although, the effective sound velocity is already reduced because of slow sound effects. For frequencies below f_{R}, it still requires that the finite slab has a larger global thickness D, because the sound speed profile usually has its local maxima at frequencies below f_{R} [32, 75]. Accordingly, in the complex plane, increasing global thickness translates into the fact that the zero moves towards lower frequency, see Fig. 5.8, cyan trace, for a fixed unit cell configuration with QWR.

Generally speaking, as the inherent losses are introduced in the system, the zeros and the poles are down-shifted [85]. Thus, the zero also move downward to negative imaginary frequencies, as bigger the losses are, brought by larger width of material introduced in the resonant system. As the zero approaches the real frequency axis, the material absorbs a larger proportion of the energy, thus radiates less toward the ambient medium. A critical coupling can be achieved simply by using a large thickness of the material [113].

Additionally, the global thickness D is a discrete quantity as $D = N\ell_{\mathrm{II}}$. It is possible that a suitable material thickness D does not correspond to any discrete quantity $N\ell_{\mathrm{II}}$. This restricts the flexibility of the design.

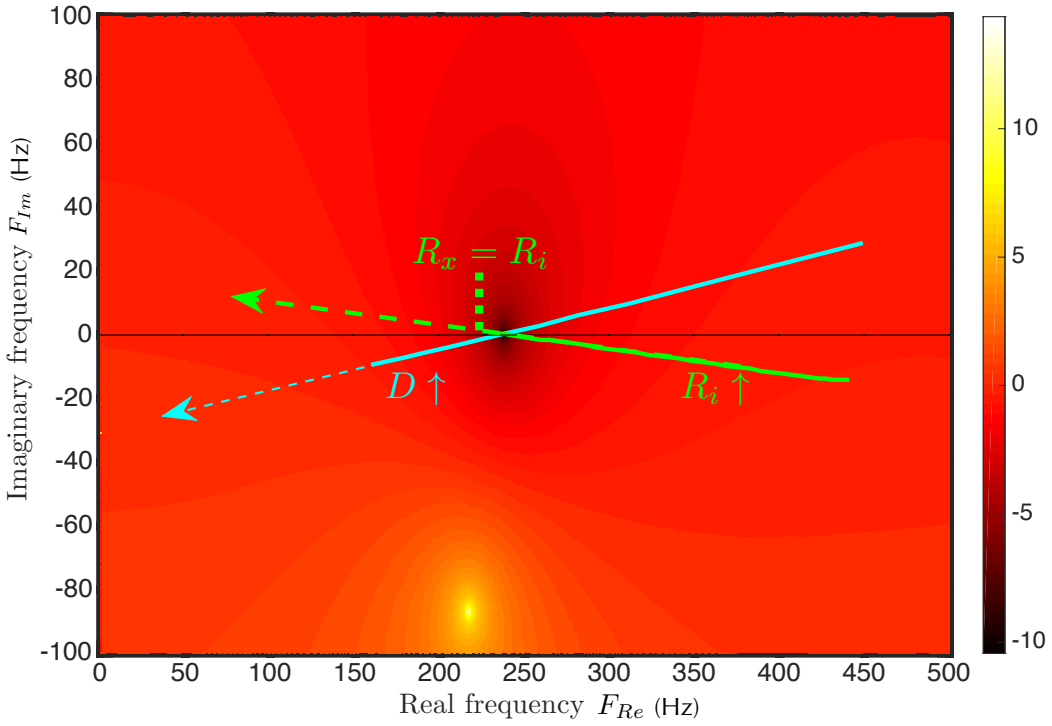

FIGURE 5.8: Tuning trajectories on the complex frequency plane: $\log(|\ R\ |^2)$ against real frequency F_{Re} and imaginary frequency F_{Im} of the first layer resonance: $\ell_{\mathrm{I}} = 41.2$ mm, $\ell_{\mathrm{II}} = \ell_{\mathrm{III}} = 8.4$ mm, $\ell_x = 40.2$ mm, $R_x = 4$ mm, $R_i = 3.8$ mm, $h_1 = 30$ mm and $h_2 = 10$ mm.

5.4.2 Inner resonators

Due to the presence of the inner resonators, there are two main effects in the finite size samples. On one hand, the addition of losses due to the visco-thermal effect in the tube, allows us to improve the absorption of the system. This means that the zero of the resonant mode moves to the real frequency axis. On the other hand, the slow sound induced in the material due to the resonances produces a shift of the resonant mode to lower frequency range, when compared to the case of solid tubes. Visually, it means that the zero moves to smaller values of the real frequency axis, see Fig. 5.8, green trace.

The resonator also has geometrical limit as inner radius has to be smaller than the outer one $R_i < R_x$. This limits the effective range of the QWRs and further restricts the flexibility of the design. Additionally, the current 3D-printing technology available to us cannot make the tube wall thin and rigid at the same time. This adds another restriction on the optimisation.

5.4.3 Resonator external configuration

Looking at the unit cell configuration, we concluded from the parametric study that the most decisive dimensions are the resonator external length ℓ_x and the transversal porosity. For the direction $\boldsymbol{e}_{\mathrm{II}}$ considered in this case, the relative cylinder length ℓ_x/ℓ_{I} has monotonic relation to all visco-thermal parameters. The value of ℓ_x/ℓ_{I} should be as close to 1 as possible, bringing bigger tortuosity. If not, the system energy leakage is much higher, creating a zero far above the real frequency line, see Fig. 5.9c).

As for the transversal porosity, the choice is more delicate. If the tube matrix is too coarsely packed ($\phi_m > 0.3$), the zero of the system is far above real frequency line, as

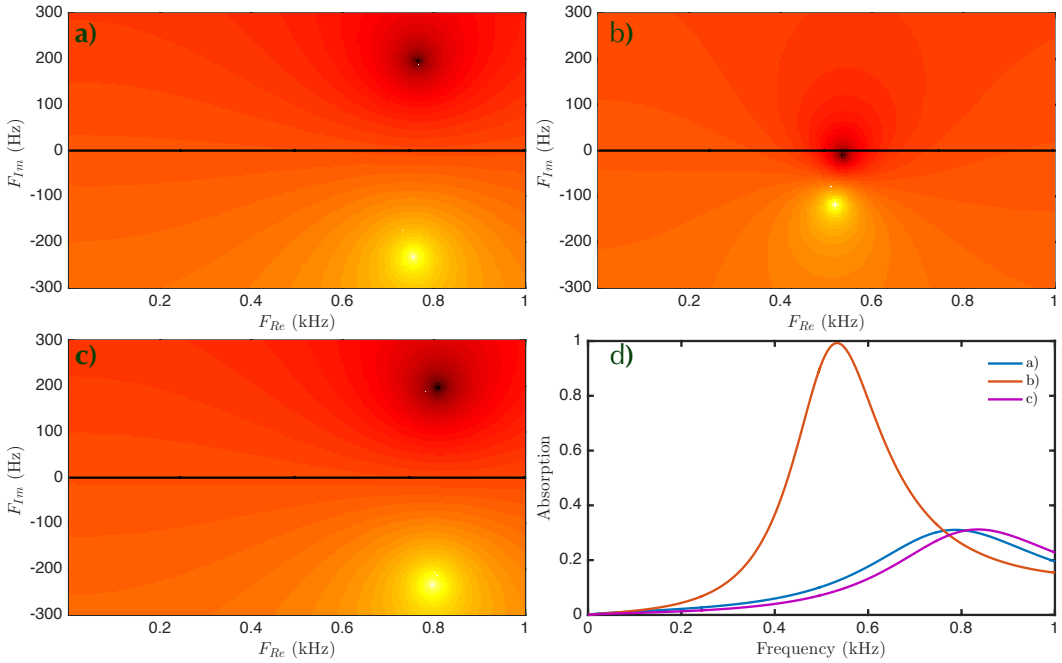

FIGURE 5.9: Complex frequency plane for unit cell configuration without QWRs of $\ell_{\mathrm{I}} = 42$ mm, $\ell_{\mathrm{II}} = \ell_{\mathrm{III}} = 9$ mm, with different R_x and ℓ_x: a) $R_x = 3.6$ mm and $\ell_x = 41$ mm; b) $R_x = 4.4$ mm and $\ell_x = 41$ mm; c) $R_x = 4.4$ mm and $\ell_x = 30$ mm; d) The respective absorption coefficients .

$F_{Im} \gg 0$, see Fig. 5.9a). It will take considerable global thickness D for zero to drop near or under zero. Thus, the feature of sub-wavelength absorber is no longer pertinent. Also, in extreme cases, the first resonance peak may appear at frequency lower than the characteristic frequency, where our theoretical model is no longer valid in the purely viscous regime.

In acoustics, it has been demonstrated that lowering the crystal filling fraction increases the wave interaction time and is responsible for the enhancement of intrinsic material dissipation, making the system more absorptive with less material [113]. So, the hollow tubes should be more closely packed. But, if the tube matrix is too densely packed ($\phi_m \sim 1-\pi/4$), it introduces a much greater resonant leakage of the tube matrix. It could be impossible for the resonators to compensate the system leakage within its geometrical limit ($R_i < R_x$). Even if the resonator radius is equal to tube external radius, the zero is still at $F_{Im} \ll 0$.

5.4.4 Perfect absorption design

Based on the observations made in this section, we propose a optimisation process that comprehensively takes all dimensions into consideration, to design a sub-wavelength absorber with low frequency perfect absorption. The process can be summarised in three steps:

1. Chose a suitable unit cell configuration without QWR, as mentioned in the last subsection;
2. Tune the global thickness of the slab D so that the zero is located closely under the real frequency line (approximately $-5 < F_{Im} < 0$), see Fig. 5.9b);
3. Add resonators with a suitable inner radius, so that this zero is lifted to the real frequency line $F_{Im} = 0$.

In a case of near-critical coupling (quasi-total absorption $0.95 < A < 1$), the design process can also be summarised in three steps:

1. Chose a less suitable unit cell configuration without QWR;
2. Tune the the global thickness of the slab D so that the zero is located closely above the real frequency line (approximately $0 < F_{Im} < 5$), without involving QWRs;
3. Add resonators with a suitable inner radius, so that the zero is shifted to lower frequencies, making use of slow sound.

Compared to the optimisation procedure completely with generic algorithm as in Chapter 2, this proposal is a more tangible solution for a discretised system as the straw-inspired metamaterial. It also reduces time for try-and-error, as the FEM computation time is quite considerable to calculate the JCAL parameters for each unit cell configuration.

In the end, this comprehensive process provides multiple theoretical perfect absorption designs. One of the optimal designs which is easier for manufacturing is chosen to be tested.

The dimensions of the chosen perfect absorption configuration are presented in Tab. 5.1. It leads to the filling fractions $\phi_{\mathrm{m}} \approx 0.3$, $\phi_1 \approx 0.16$ and $\phi_2 \approx 0.47$, the total porosity

$\phi = 0.93$, and the quarter-wavelength resonance frequencies of the larger inner resonator $f_{\mathrm{R}} = \omega_1/(2\pi) \approx 2.85\,\mathrm{kHz}$ and $\omega_2/(2\pi) \approx 8.55\,\mathrm{kHz}$ for the ducts Ω_1 and Ω_2.

Material	ℓ_{I}	ℓ_{II}	D
Dimension (mm)	41.2	8.4	109.2
Tube exterior	R_x	ℓ_x	
Dimension (mm)	4.0	40.2	
Resonators	R_i	h_1	h_2
Dimension (mm)	3.9	30	10

TABLE 5.1: Dimensions of the chosen perfect absorption configuration.

Using the Finite Element Method (FEM), the precise viscous and thermal JCAL parameters for this configuration are computed. Their values are provided along with those for the characteristic frequencies ω_{m}^i and ω_{m}' in the following list.

- Static viscous permeability: $K_{\mathrm{m}}^{\mathrm{I}0} \approx 137\ \mathrm{mm}^2$, $K_{\mathrm{m}}^{\mathrm{II}0} \approx 3.2\ \mu\mathrm{m}^2$;
- High frequency limit of the dynamic tortuosity:$\tau_{\mathrm{m}}^{\mathrm{I}\infty} \approx 1.06$, $\tau_{\mathrm{m}}^{\mathrm{II}\infty} \approx 2.08$;
- Viscous characteristic length $\Lambda_{\mathrm{m}}^{\mathrm{I}} \approx 1.6$ mm, $\Lambda_{\mathrm{m}}^{\mathrm{II}} \approx 0.35$ mm ;
- Static thermal permeability $\Theta_{\mathrm{m}}^0 \approx 139\ \mathrm{mm}^2$ and characteristic thermal length $\Lambda_{\mathrm{m}}' \approx 1.2\,;\mathrm{mm}$
- Characteristic frequencies $\omega_{\mathrm{m}}^{\mathrm{I}}/2\pi = 5.07$ Hz, $\omega_{\mathrm{m}}^{\mathrm{II}}/2\pi = 110$ Hz, and $\omega_{\mathrm{m}}'/2\pi = 7.45$ Hz.

5.5 Results and discussion

With this design procedure in place, a series of perfect absorption designs are found with different hollow tube dimensions. While taking into consideration the manufacture and measurement condition available, one of the optimal designs is chosen to be made into experimental samples. Its dimension are provided as in Tab. 5.1.

The sample is made of 5 by 13 periodic hollow tube array. A sample with solid tubes of the same outer dimensions is also made to serve as the control group. The two samples of the configuration are manufactured by 3D printer (MakersBot *Replicator 2X*), following the optimal design, see Fig. 5.10. The samples are made of the Acrylonitrile butadiene styrene (ABS)[1].

The measurement of the printed samples' dimensions shows a small system error from 3D-printing process: The outer radius $R_x = 4.1$ mm and the inner radius $R_i = 3.9$ mm. Additional numerical simulation is performed to adjust the visco-thermal parameters with the exact measurement. Using the Finite Element Method (FEM), the precise viscous and thermal JCAL parameters for this configuration are computed.

Their values are provided along with those for the characteristic frequencies ω_{m}^i and ω_{m}' in the following list.

[1]The material mechanic properties are not specified by the supplier. Though statistics show that the average number for its density at 1.05 g/mL, Young's modulus at 2.07 GPa, Poisson's ratio at 0.3.

- Static viscous permeability: $K_{\mathrm{m}}^{\mathrm{I}0} \approx 108$ mm^2, $K_{\mathrm{m}}^{\mathrm{II}0} \approx 3.9$ μm^2;
- High frequency limit of the dynamic tortuosity:$\tau_{\mathrm{m}}^{\mathrm{I}\infty} \approx 1$, $\tau_{\mathrm{m}}^{\mathrm{II}\infty} \approx 2.10$;
- Viscous characteristic length $\Lambda_{\mathrm{m}}^{\mathrm{I}} \approx 1.3$ mm, $\Lambda_{\mathrm{m}}^{\mathrm{II}} \approx 0.4$ mm ;
- Static thermal permeability $\Theta_{\mathrm{m}}^{0} \approx 160$ mm^2 and characteristic thermal length $\Lambda'_{\mathrm{m}} \approx 1.7$ mm;
- Characteristic frequencies $\omega_{\mathrm{m}}^{\mathrm{I}}/2\pi = 4.48$ Hz, $\omega_{\mathrm{m}}^{\mathrm{II}}/2\pi = 79.5$ Hz, and $\omega'_{\mathrm{m}}/2\pi = 5.72$ Hz;
- Porosity $\phi_{\mathrm{m}} = 0.270$, $\phi_1 = 0.493$, $\phi_2 = 0.165$, total porosity $\phi = 0.927$.

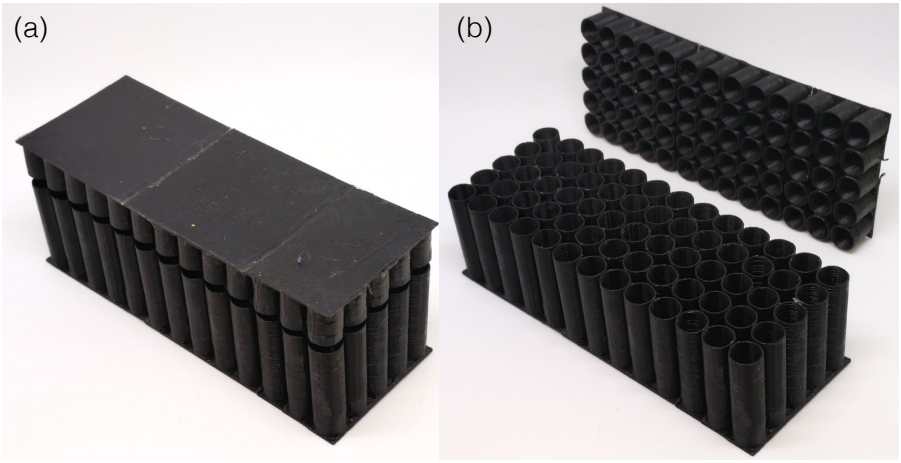

FIGURE 5.10: 3D Printed optimal experimental sample: (a) assembled test block; (b) test block parts.

As the theoretical model for the Q_j accounts for only the interaction between the Ω_j and Ω_m, but not between Ω_j, a similar end correction as in Chap 1 and 2 is added to Q_j. Then, the corrected apparent compressibility $\hat{\beta}_j$ rewrites :

$$\hat{\beta}_j = \left(\beta_j^{-1} - \frac{\omega^2}{c_0^2}\ell_{corr}h_j\right)^{-1}, \tag{5.5.1}$$

where ℓ_{corr} is obtained with the same method as in Sec. 2.5 [78, 80]. For numerical application $\ell_{corr} \approx \sqrt{2}R_i$.

Reflection and absorption coefficients for a normal incidence are calculated with the same method as in Sec.3.6. The experimental measurements are carried out in the same process presented in Sec.3.7, with 3D-printed samples, illustrated in Fig. 5.10. Theoretical and experimental results are presented as: first, theoretical prediction in complex frequency plane, then, the reflection coefficient expressed in both amplitude and phase, and finally the absorption coefficient, in Figs. 5.11 and 5.12.

The theoretical predictions of a sample of solid cylinder array are compared with the experimental data In Fig. 5.11. A typical porous material slab absorption pattern appears. The experimental results are in a very good agreement with the simulations for all frequencies considered. This validates the numerical calculation of the JCAL parameters.

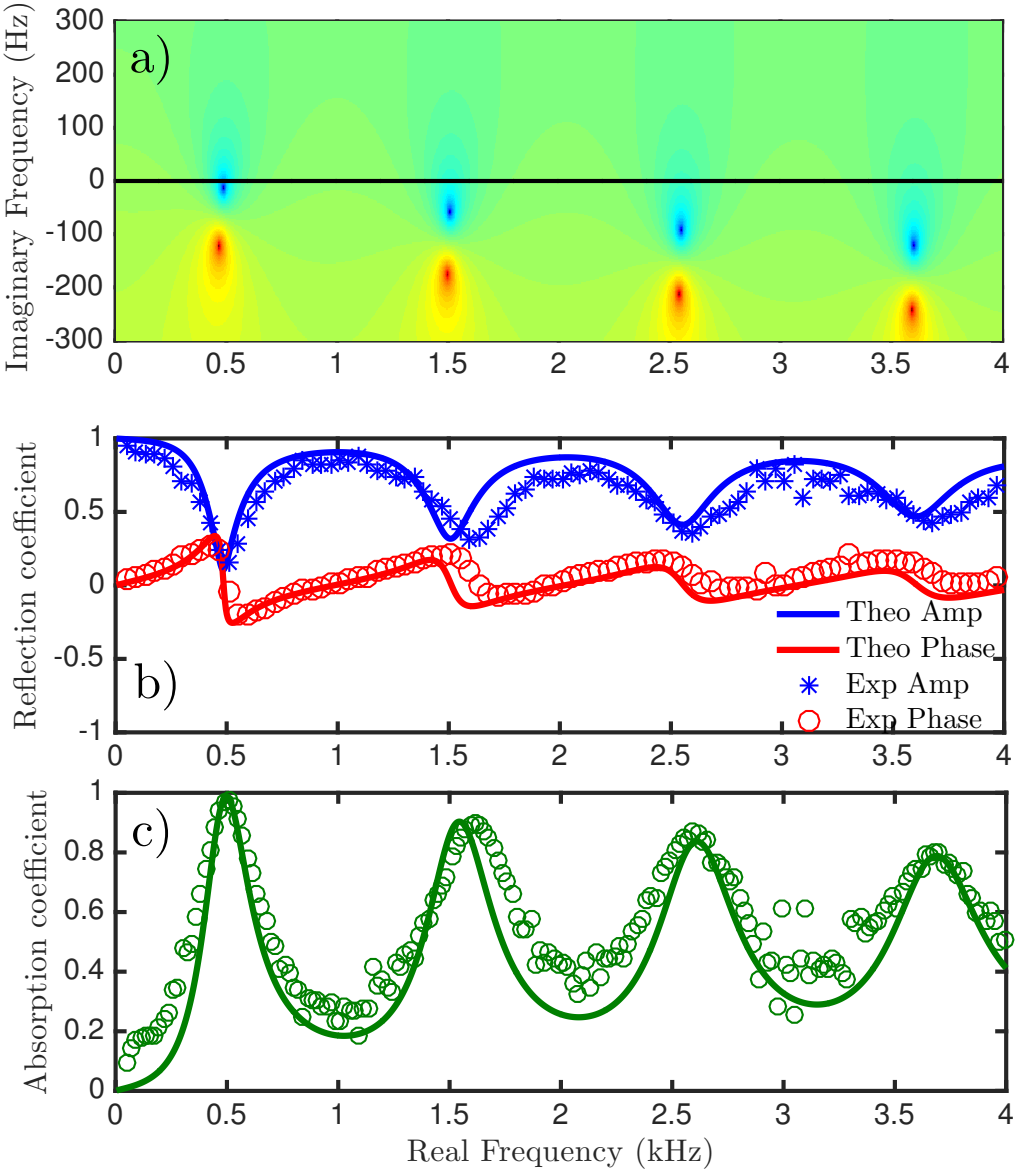

FIGURE 5.11: Theoretical and experimental results for solid configuration $R_i = 0$: a) Complex plane ; b) Reflection coefficient; c) Absorption coefficient: experimental result in green circle, theoretical in green solid line.

Notably, a near-perfect absorption (97.4%) is observed experimentally on the first peak at 509 Hz while the corresponding theoretical zero is predicted at coordinates $(0.49, -4.69)$ on the complex frequency plane. This agrees with the predetermined design procedure in Sec. 5.4.4, so that the structure leakage can be compensated by adding QWRs into the solid cylinder in the unit-cell.

Moreover, a series of secondary high absorption peaks ($A > 0.8$) are observed at 1.6 kHz, 2.6 kHz, and 3.6 kHz, which correspond to secondary metamaterial layer resonances, i.e. Fabry-Pérot ones. These peaks are equally spaced on frequency, as the medium is non-dispersive without QWRs.

The theoretical predictions for the absorption coefficient of a sample of hollow tube array are compared with the experimental data in Fig. 5.12. A good agreement between

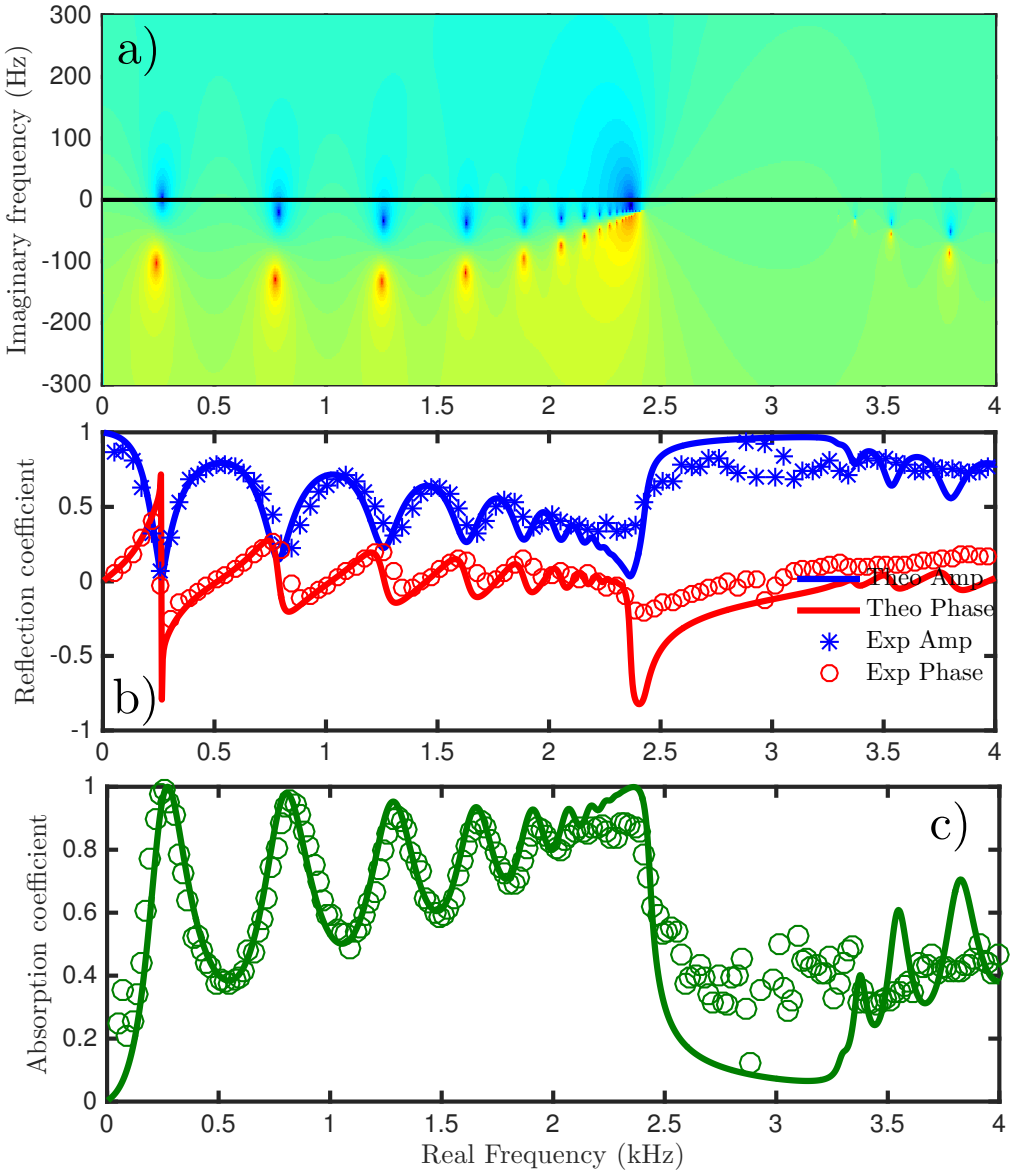

FIGURE 5.12: Absorption coefficients against frequency for hollow configuration $R_i = 0$: a) Complex plane ; b)Reflection coefficient ; c) Absorption coefficient: experimental result in green circle, theoretical in green solid line.

the experimental and theoretical results before the tube resonance frequency $f_R = 2.4$ kHz is observed.

At the first resonance peak, it is consistent with the slow sound effect brought by QWRs, moving the first peak from 500 Hz to 272 kHz, based on the theoretical model. More importantly, we observe a total absorption at the first peak (experimentally $A = 0.996$ at 258 Hz), where the corresponding wavelength of this peak equals to 13 times of the effective slab thickness D. This is effectively a sub-wavelength absorber.

Furthermore, adding of resonators brings forward on frequency a series of secondary resonant regimes before f_R. Four secondary absorption peaks can be clearly distinguished, with a 5th larger one around f_R, due to the Fabry-Pérot resonances of the metamaterial. All these peaks have high absorption peak value more than 95%, which yields a board

band high absorption in the frequencies lower than f_R. Additionally, the peaks here are no longer equi-spaced, as the medium has become dispersive with the adding of QWRs.

A semi-stop band can be clearly spotted at f_R, but with some discrepancies. This is mainly due to the homogenisation scale separation, characterised by its factor $\epsilon = k\ell = \ell\omega/c_0$, supposedly much smaller than 1. While the unit cell used in the model sets ϵ_{II} for 2.4 kHz at 0.38, which is not ideal for sufficient scale separation. But for the first absorption at frequency low as 0.27 kHz ($\epsilon_{\text{II}} \approx 0.04$) , the theoretical result gives out excellent fit to the experiment.

The other discrepancy appears at frequencies just before the resonance frequency. Here, the simulation stacks a infinite number of the resonant regimes together, forming a seemingly prefect absorption. Compared to the experiment, it can be noted that as the effective slab is penetrable in all directions, and the effective slab has only 13 rows of hollow tubes in the tested $\boldsymbol{e}_{\text{II}}$ direction, a infinite sum of peaks is not possible in reality.

Conclusion

In this Chapter, an anisotropic square-periodic arrangement of hollow cylindrical tubes is reported for slow sound effects and perfect absorption in the low-frequency range.

The physical model relies on the homogenisation procedure of the solid cylinder array while tailoring the added inner resonance. The added QWRs in the cylindrical tubes are modelled by the flux radiating from the apertures of the resonators Σ_j into fluid domain Ω_{m}. These apertures act as secondary sources in the mass conservation.

Based on the physical model validated in previous chapters, a parametric study is performed. It shows the relationship between the different dimension of the unit cell configuration and the JCAL viscous and thermal parameters. In essence, the variation pattern of the porous model parameters can help to prepare the basic building blocks towards an optimal straw-inspired metamaterial design consisted of the permeable array of hollow tubes.

Design process is then rationalised, considering all aspect of the material and unit cell configuration for obtaining perfect absorption samples. The process eventually yields multiple solutions. One of the optimal designs, which is more suitable for manufacture and measurement is 3D-printed into the experimental sample.

A solid cylinder array of the exact same exterior dimensions ($R_i = 0$) is also made as a control group sample, in order to demonstrate the mechanisms behind the design process. The two samples are tested in the impedance tube as in Chap. 1 and 4. The experimental results have a good agreement with the theoretical prediction.

The perfect absorption design gives out a perfect absorption peak at 258 Hz, of which the wavelength corresponds to 13 times of the slab thickness D. A board band absorption plateau composed of secondary absorption peaks is observed before the resonance frequency. All results point out that the straw-inspired metamaterial design is a sub-wavelength absorber that can achieve perfect absorption at the very low-frequency range.

Moreover, the validation of the inner resonance model gives more motivation to look into the anisotropic aspect of this straw-inspired metamaterial. Its performances facing oblique incidence in non-orthotropic orientations will be under examination in the next chapter.

Chapter 6

Absorption in oblique incidence: effect of anisotropy

This Chapter investigates the anisotropic aspects of the straw-inspired metamaterial, while facing oblique incidence, with different unit cell orientations. The symmetry of the system is studied at oblique incidence. Special attention is also paid to critical coupling condition at grazing incidence, to investigate the high absorption at large incident angles. The positions of zero and pole determine whether it fulfils the critical coupling condition. The absorption in diffuse field is also calculated to reveal the omnidirectional functionality and the anisotropy of the metamaterial design.

Contents

Introduction

Conventional acoustic materials for absorption and insulation, such as plastic foams or glass wool, are often considered homogenous and isotropic [9]. The anisotropic design of acoustic material, although it has been studied for wave control [114, 115]. It has been applied for acoustic absorption [113].

In mechanics, anisotropic acoustic pentamode metamaterial has been realised to modify elasticity [116]. In the field of electromagnetic and optics, Cui *et al.* studied the omnidirectional high and total absorption of the infrared wave by a sawtoothed anisotropic absorber [117]. The single-wall carbon nanotube has been found having a good quality of depolarised absorption of the visible optical wave, due to its anisotropic geometry [118].

Here, the straw-inspired metamaterial of the periodic arrangement of cuboid unit cells with embedded scatterer is again studied. The physics of the medium relies on the homogenisation of the unit cell problem previously studied and validated in Chapter 3 and 4. Based on those results, the porous medium is considered statistically homogenous, but anisotropic in nature, due to the geometry of the scatterer and the dimension of the unit cell, represented by an anisotropic generalised Darcy's permeability tensor.

The anisotropy of the analysed system mainly resides within the air-matrix formed by the array of solid cylinders. Reflection and absorption of the straw-inspired metamaterial are calculated for various oblique incidences and different rotations of the unit cell in order to describe its anisotropic properties.

Different representations of the absorption coefficient are shown for a various oblique incident plane and different unit-cell orientations. The symmetry of the system is studied by varying the incident angle and the incident plane angle. Its absorption in diffuse field is also calculated to reveal the array's omnidirectional functionality.

We argue that an anisotropic design of acoustic material can present a better absorption at oblique incident angles and especially at grazing incident angles, and therefore possessing a diffusion field absorption larger than an isotropic one.

6.1 General description

The unit cell Ω is a rectangular cube with the dimensions $\ell_{\mathrm{I}} \times \ell_{\mathrm{II}} \times \ell_{\mathrm{III}}$ in the directions of the Cartesian coordinate system $\mathcal{R} = (\boldsymbol{e}_{\mathrm{I}}, \boldsymbol{e}_{\mathrm{II}}, \boldsymbol{e}_{\mathrm{III}})$, see Fig. 6.1b). The solid tube in the unit cell Ω has the outer radius R_x, the finite length $\ell_x \leq \ell_{\mathrm{I}}$, and its axis oriented along $\boldsymbol{e}_{\mathrm{I}}$. Three rotational angles α_i are defined as rotation around the respective axis $\boldsymbol{e}_i$, with $i = \mathrm{I}, \mathrm{II}, \mathrm{III}$.

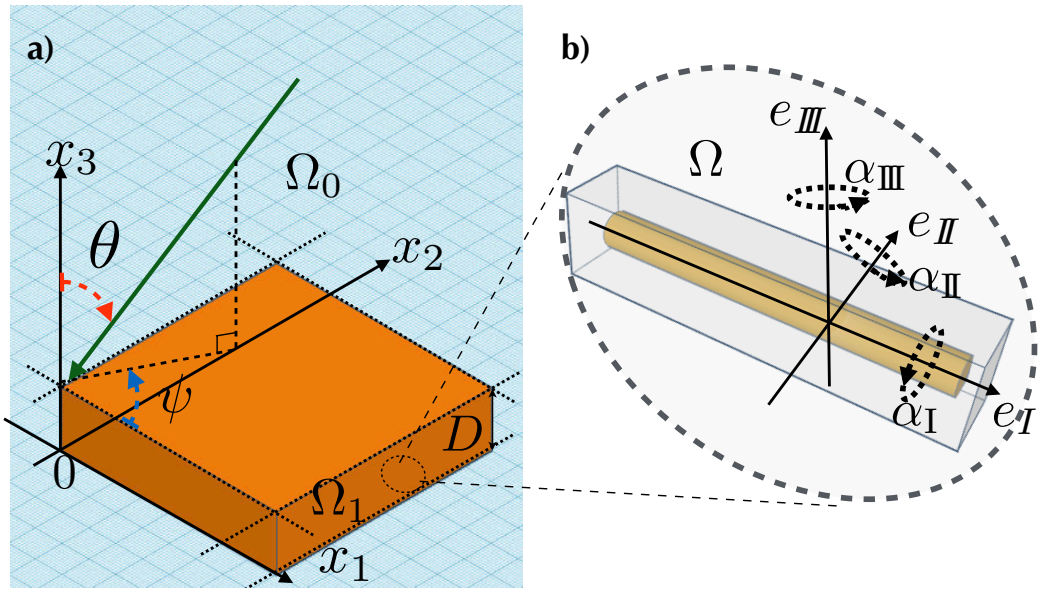

FIGURE 6.1: Incidence plane and effective layer: oblique incident vector $k(\alpha, \psi)$, Zoom-in view: Unit cell with orientation vector $\boldsymbol{\alpha}(\alpha_{\mathrm{I}}, \alpha_{\mathrm{II}}, \alpha_{\mathrm{III}})$.

Firstly, only the configuration with solid cylinders is considered. As the anisotropy of the straw-inspired metamaterial resides only in its viscous part, adding inner resonators which modifies only the thermal part of the problem may mask the effect of anisotropy. Thus, a periodic arrangement of cuboid unit cells with only solid cylinder is studied here, similar to the one used in Sec. 5.3.

The ambient air medium Ω_0 occupies the semi-infinite space $x_3 > D$, see Fig. 6.1a). From medium Ω_0, a plain wave incidence is considered in Cartesian coordinate system (x_1, x_2, x_3). In the incidence plane, the incident wave $\mathcal{P}_\psi(\boldsymbol{k}_\Gamma, \psi)$ is defined by the in-plane incident angle θ, and incidence plane angle ψ. The corresponding wavenumber vector is $\boldsymbol{k} = (\boldsymbol{k}_\Gamma, k_3)$ with $\boldsymbol{k}_\Gamma = (k_1, k_2)$ in plane $x_\Gamma(x_1, x_2)$. The components of the incident wavenumber are:

$$k_1 = k_0 \sin(\theta)\cos(\psi),\ k_2 = k_0 \sin(\theta)\sin(\psi),\ k_3 = k_0 \cos(\theta). \tag{6.1.1}$$

The effective material layer has a thickness D, which occupies medium Ω_1 $0 < x_3 < D$. The associated wavenumber system is specified in the later subsections. Theoretical description of the anisotropy of the considered material is presented in the following.

6.1.1 Coordinate Systems

The equivalent medium Ω_1 has its own coordinates (e_1, e_2, e_3) with the wavenumber (k_1, k_2, k_3). Equally, the unit-cell domain Ω has its own coordinates $(e_{\mathrm{I}}, e_{\mathrm{II}}, e_{\mathrm{III}})$. So, we name the two coordinate systems respectively,

- the Unspecified Coordinate System (UCS) based on Ω_1, subjected to the material layer whereas the unit cell orientation in this system is unspecified;
- the Principal Coordinate System (PCS) based on Ω, subjected to the unit cell: the unit cell is in its own principal direction, as $\boldsymbol{e}_i$ parallel to $\boldsymbol{e}_j, i = \mathrm{I}, \mathrm{II}, \mathrm{III}, j = 1, 2, 3$;

Accordingly, the naming convention for all associated variables and operators are listed in Tab. 6.1.

Variables & Operators	UCS	PCS
Basis	$\mathcal{R} = (e_1, e_2, e_3)$	$\tilde{\mathcal{R}} = (e_{\mathrm{I}}, e_{\mathrm{II}}, e_{\mathrm{III}})$
Position vector	$\boldsymbol{x} = (x_1, x_2, x_3)$	$\tilde{\boldsymbol{x}} = (x_{\mathrm{I}}, x_{\mathrm{II}}, x_{\mathrm{III}})$
E Wavenumber	$\boldsymbol{k} = (k_1, k_2, k_3)$	$\tilde{\boldsymbol{k}} = (k_{\mathrm{I}}, k_{\mathrm{II}}, k_{\mathrm{III}})$
Particular velocity	v	$\tilde{v}$
Density matrix	$\boldsymbol{\rho}$	$\tilde{\boldsymbol{\rho}} = \mathrm{diag}(\rho_i),\ i = \mathrm{I}, \mathrm{II}, \mathrm{III}$
Tortuosity matrix	$H = \boldsymbol{\rho}^{-1}$	$\tilde{H} = \tilde{\boldsymbol{\rho}}^{-1}$
Operators	div_x, $\mathbf{grad}_x$	$\mathrm{div}_{\tilde{x}}$, $\mathbf{grad}_{\tilde{x}}$

TABLE 6.1: List of variables & operators in the Unspecified Coordinates System(UCS) and Principal Coordinates System(PCS).

Note that the density tensor for the UCS, $\boldsymbol{\rho}$, is a 3 by 3 square matrix. In our case, it is considered non-zero, full, and symmetrical.

As thermal effects are scalar in nature, the bulk modulus does not change between systems. It is simply written as B. The pressure is also a scalar field, it is noted as p. So, the governing equations for the PCS and the UCS are rewritten as listed in Tab. 6.2.

Equations	UCS	PCS
Mass conservation	$\mathrm{div}_x\, \boldsymbol{v} = \frac{\mathrm{i}\omega}{B} p$	$\mathrm{div}_{\tilde{x}}\, \tilde{\boldsymbol{v}} = \frac{\mathrm{i}\omega}{B} p$
Momentum conservation	$\mathrm{i}\omega\boldsymbol{\rho}\boldsymbol{v} = \mathbf{grad}_x p$	$\mathrm{i}\omega\tilde{\boldsymbol{\rho}}\tilde{\boldsymbol{v}} = \mathbf{grad}_{\tilde{x}} p$

TABLE 6.2: Governing equations in different coordinates systems.

Variables & Equations	UCS→PCS	PCS→UCS
Transfert matrix	$\boldsymbol{R} = \tilde{\mathcal{R}}\mathcal{R}^{-1}$	$\boldsymbol{R}^{-1} = \mathcal{R}\tilde{\mathcal{R}}^{-1}$
Position vector	$x = \boldsymbol{R}\tilde{x}$	$\tilde{x} = \boldsymbol{R}^{-1} x$
Wavenumber	$k = \boldsymbol{R}\tilde{k}$	$\tilde{k} = \boldsymbol{R}^{-1} k$
Particular velocity	$v = \boldsymbol{R}\tilde{v}$	$\tilde{v} = \boldsymbol{R}^{-1} v$
Density matrix	$\boldsymbol{\rho} = \boldsymbol{R}\tilde{\rho}\boldsymbol{R}^{-1}$	$\tilde{\boldsymbol{\rho}} = \boldsymbol{R}^{-1}\rho\boldsymbol{R}$
Normalized tortuosity	$H = \boldsymbol{R}\tilde{H}\boldsymbol{R}^{-1}$	$\tilde{H} = \boldsymbol{R}^{-1} H \boldsymbol{R}$

TABLE 6.3: Transitions of variables and equations between UCS and PCS.

Finally, the transitions between the PCS and UCS are also listed in Tab. 6.3. The transfer matrix $\boldsymbol{R}$ between PCS and UCS can be expressed as the rotational matrix. It is specified in the next subsection.

6.1.2 Rotational matrix

The general rotational matrix $\boldsymbol{R}(\boldsymbol{\alpha})$, where the rotation angle vector $\boldsymbol{\alpha} = (\alpha_1, \alpha_2, \alpha_3)$ with the rotation angle α_i is defined here in a the Euler's rotational system, with $i = \mathrm{III}, \mathrm{II}, \mathrm{I}$, shown in Fig. 6.1.

In particular, the Euler's rotation angles system used here is also called the aviation angles. The three rotational angles are defined in a Roll-Yaw-Pitch convention, explained in the following list.

- α_I, also called **Roll** angle, is the angle which the unit-cell rotates around axe x_I by:

$$\boldsymbol{R}_\mathrm{I}(\alpha_\mathrm{I}) = \begin{bmatrix} 1 & 0 & 0 \\ 0 & \cos(\alpha_\mathrm{I}) & \sin(\alpha_\mathrm{I}) \\ 0 & -\sin(\alpha_\mathrm{I}) & \cos(\alpha_\mathrm{I}) \end{bmatrix}. \tag{6.1.2}$$

- α_II, also called **Pitch** angle, is the angle which the unit-cell rotates around axe x_II by:

$$\boldsymbol{R}_\mathrm{II}(\alpha_\mathrm{II}) = \begin{bmatrix} \cos(\alpha_\mathrm{II}) & 0 & -\sin(\alpha_\mathrm{II}) \\ 0 & 1 & 0 \\ \sin(\alpha_\mathrm{II}) & 0 & \cos(\alpha_\mathrm{II}) \end{bmatrix}. \tag{6.1.3}$$

- α_III, also called **Yaw** angle, is the angle which the unit-cell rotates around axe x_III by:

$$\boldsymbol{R}_\mathrm{III}(\alpha_\mathrm{III}) = \begin{bmatrix} \cos(\alpha_\mathrm{III}) & \sin(\alpha_\mathrm{III}) & 0 \\ -\sin(\alpha_\mathrm{III}) & \cos(\alpha_\mathrm{III}) & 0 \\ 0 & 0 & 1 \end{bmatrix}. \tag{6.1.4}$$

Thus the general rotational matrix $\boldsymbol{R}(\boldsymbol{\alpha})$ writes as,

$$\boldsymbol{R}(\boldsymbol{\alpha}) = \boldsymbol{R}_\mathrm{III}(\alpha_\mathrm{III}) \cdot \boldsymbol{R}_\mathrm{II}(\alpha_\mathrm{II}) \cdot \boldsymbol{R}_\mathrm{I}(\alpha_\mathrm{I}) = \begin{bmatrix} c_2c_3 & c_3s_1s_2 + c_1s_3 & s_1s_3 - c_1c_3s_2 \\ -c_2s_3 & c_1c_3 - s_1s_2s_3 & c_3s_1 + c_1s_2s_3 \\ s_2 & -c_2s_1 & c_1c_2 \end{bmatrix}, \tag{6.1.5}$$

where $c_i = \cos(\alpha_j)$ and $s_i = \sin(\alpha_j)$, with $i = 1, 2, 3, j = \mathrm{I}, \mathrm{II}, \mathrm{III}$. Note all the rotational matrices, including $\boldsymbol{R}(\boldsymbol{\alpha})$, are orthogonal matrices, which means $\boldsymbol{R}_i^T = \boldsymbol{R}_i^{-1}$ and $\det(\boldsymbol{R}_i) = 1$.

6.2 Dispersion relations

In PCS, $\tilde{\mathcal{R}} = (e_\mathrm{I}, e_\mathrm{II}, e_\mathrm{III})$, the governing equations are:

$$\mathrm{div}_{\tilde{x}}\, \tilde{\boldsymbol{v}} = \frac{\mathrm{i}\omega}{\tilde{B}}\tilde{p}, \quad \mathrm{i}\omega\tilde{\boldsymbol{\rho}}\tilde{\boldsymbol{v}} = \mathbf{grad}_{\tilde{x}}\tilde{p}, \tag{6.2.1}$$

where $\tilde{p}$ is the excess pressure field, $\tilde{\boldsymbol{v}}$ is the particule velocity, with the anisotropic density tensor $\tilde{\boldsymbol{\rho}} = \tilde{H}^{-1} = \mathbf{diag}(\rho_i)$, $i = \mathrm{I}, \mathrm{II}, \mathrm{III}$ in its principal directions $(e_\mathrm{I}, e_\mathrm{II}, e_\mathrm{III})$.

Equation (6.2.1) gives out the dispersion relation as,

$$\mathrm{div}_{\tilde{x}}\left(\tilde{\boldsymbol{H}}\mathbf{grad}_x p\right)+\frac{\omega^2}{B}p=0, \tag{6.2.2}$$

$$\frac{(k_{\mathrm{I}})^2}{\rho_{\mathrm{I}}}+\frac{(k_{\mathrm{II}})^2}{\rho_{\mathrm{II}}}+\frac{(k_{\mathrm{III}})^2}{\rho_{\mathrm{III}}}=\frac{\omega^2}{B}. \tag{6.2.3}$$

The solution k_{III} is,

$$k_{\mathrm{III}}=\sqrt{\rho_{\mathrm{III}}\left(\frac{\omega^2}{B}-\frac{(k_{\mathrm{I}})^2}{\rho_{\mathrm{I}}}-\frac{(k_{\mathrm{II}})^2}{\rho_{\mathrm{II}}}\right)}. \tag{6.2.4}$$

In UCS, $\mathcal{R}=(e_1,e_2,e_3)$, the governing equations are:

$$\mathrm{div}_x\,\boldsymbol{v}=\frac{\mathrm{i}\omega}{B}p,\quad \mathrm{i}\omega\boldsymbol{\rho}\boldsymbol{v}=\mathbf{grad}_x p, \tag{6.2.5}$$

where p is the excess pressure field, $\boldsymbol{v}$ is the wave velocity, with the tilted effective density tensor $\boldsymbol{\rho}=\boldsymbol{H}^{-1}=\boldsymbol{R}\cdot\mathbf{diag}(\rho_i)\cdot\boldsymbol{R}^{-1}$, $i=\mathrm{I},\mathrm{II},\mathrm{III}$, with $\boldsymbol{R}$ the rotational matrix.

Overall, the tensor $\boldsymbol{\rho}$ and $\boldsymbol{H}$ are symmetric for any orientation and full in the most cases. So Eq. (6.2.5) gives out the dispersion relation:

$$\boldsymbol{k}\cdot(\boldsymbol{H}.\boldsymbol{k})=\frac{\omega^2}{B}, \tag{6.2.6}$$

where the boundary condition at the interface of the effective material layer dictates that $k_1=k_0\sin\theta\cos\psi$, $k_2=k_0\sin\theta\sin\psi$. To have a meaningful case, H_{33} should be non-zero. Then, the solution k_3 is in the tensorial form as,

$$k_3^{\pm}=-(\boldsymbol{\mathcal{C}}.\boldsymbol{k}_\Gamma)\pm\kappa, \tag{6.2.7a}$$

$$\text{with }\kappa=\left[\frac{\omega^2}{BH_{33}}+(\boldsymbol{\mathcal{C}}.\boldsymbol{k}_\Gamma)^2-\boldsymbol{k}_\Gamma^T\cdot(\boldsymbol{H}^*.\boldsymbol{k}_\Gamma)\right]^{1/2}, \tag{6.2.7b}$$

where $\boldsymbol{k}_\Gamma=(k_1,k_2)$ is the in-plane incidence vector. For detailed calculation, see Sec.4.4.

In the case where the unit cell only rotates in plane (x_1,x_2), $\alpha_{\mathrm{I}}=\alpha_{\mathrm{II}}=0$, $H_{13}=H_{23}=0$, thus $\boldsymbol{\mathcal{C}}=0$. So, Eq. (6.2.7) can be simplified as

$$k_3^{\pm}=\pm\kappa=\pm\left[\frac{\omega^2}{BH_{33}}-\boldsymbol{k}_\Gamma^T\cdot(\boldsymbol{H}^*.\boldsymbol{k}_\Gamma)\right]^{1/2} \tag{6.2.8a}$$

$$=\pm\left\{\frac{\omega^2}{BH_{33}}-k_0^2\sin^2(\theta)\left[H_{11}^*\cos^2(\psi)+H_{22}^*\sin^2(\psi)+H_{12}^*\sin(2\psi)\right]\right\}^{1/2}. \tag{6.2.8b}$$

Moreover, if $\psi=0$, $k_2=0$, Eq. (6.2.8) can be written as $k_3^{\pm}=\pm\kappa=\pm nk_0$ where the refractive index $n(\omega,\theta)$ is as followed,

$$n(\omega,\theta)=\frac{\kappa}{k_0}=\frac{c_0}{c_{\mathit{eff}}}=\sqrt{\frac{c_0^2}{c_{33}^2}-H_{11}^*\sin^2(\theta)}\,,\text{with }c_{33}=\sqrt{BH_{33}}. \tag{6.2.9}$$

In the case of normal incidence $\boldsymbol{k}_\Gamma=0$, the system is reduced to a 1D isotropic model, where $k_3^{\pm}=\pm\omega/c_{33}$, which has been discussed in Chapter 5.

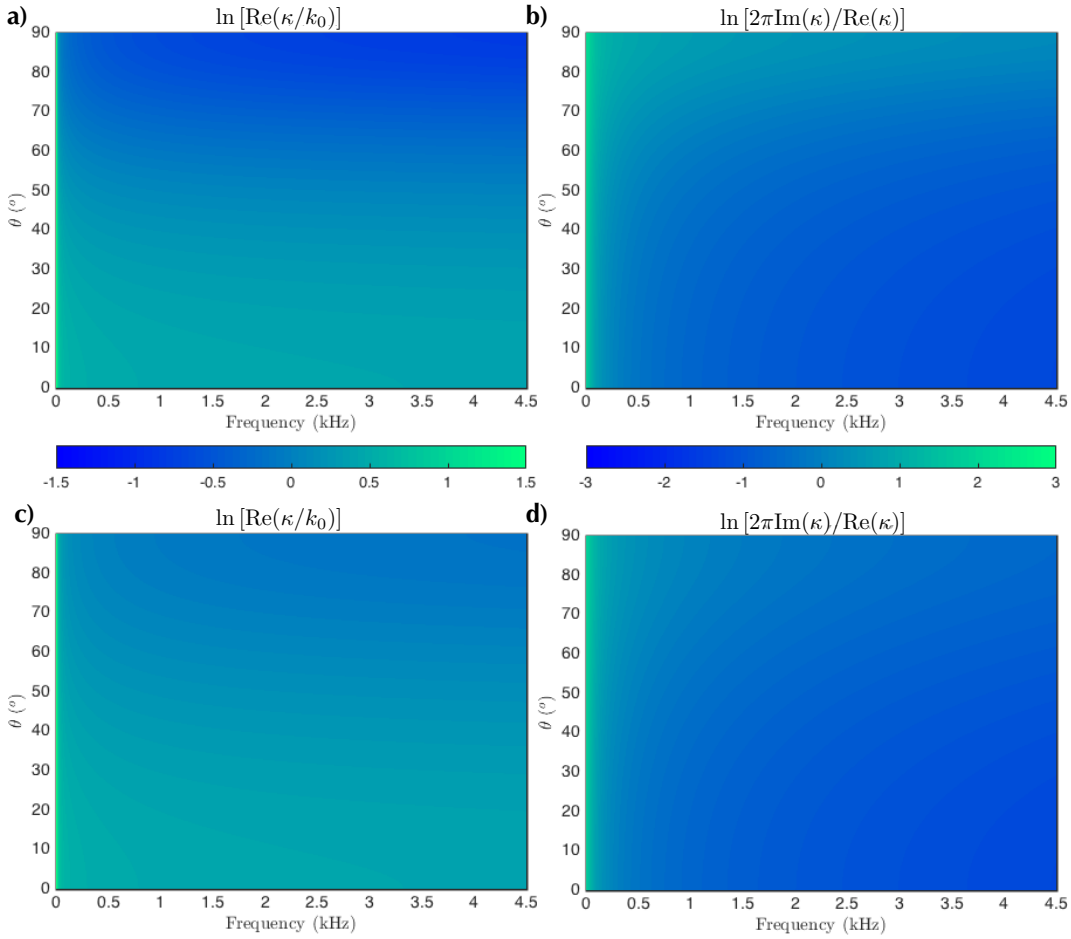

FIGURE 6.2: Dispersion properties of cases where $\boldsymbol{\alpha} = (0, 0, 0)$: a,b) for $\psi = 0$; c,d) for $\psi = \pi/4$. (a) and c), b) and d) share the same colorbars).

For numerical application, a configuration similar to the one described in Sec. 4.2 is used here with the solid cylinders as $\ell_{\mathrm{I}} = 41.2$ mm and $\ell_{\mathrm{II}} = \ell_{\mathrm{III}} = 8.4$ mm, $R_x = 4.1$ mm, $h = 40.2$ mm. The real and imaginary parts of the wavenumber for the cases of $\boldsymbol{\alpha} = (0, 0, 0)$ while $\psi = 0, \pi/4$ are shown in their respective normalised form in Fig. 6.2. The real part is normalised by k_0, giving rise to the refractive index $n(\omega, \theta)$, and the imaginary part is given in the form of the attenuation factor.

Comparing results in Fig. 6.2, it seems that the real part increases its value with larger ψ, and the attenuation does not change visibly in the same manner. The imaginary part increases its value when both the angle and the frequency increase. From these results, the effect of anisotropy is evidenced. To evidence the anisotropy, it seems better to look at the reflection and absorption pattern in relation to incidence (θ, ψ) and frequency.

6.3 Symmetry

Here, a layer of material made of periodic arrangement of unit cell set in a PCS position is solicited by a plane wave with oblique incidence. The thickness of the material layer D is set to be 110 mm. More precisely, $\boldsymbol{\alpha} = (0, 0, 0)$, which means $\boldsymbol{e}_{\mathrm{I}}$ parallel to $\boldsymbol{e}_1$, $\boldsymbol{e}_{\mathrm{II}}$ parallel to $\boldsymbol{e}_2$, and $\boldsymbol{e}_{\mathrm{III}}$ parallel to $\boldsymbol{e}_3$. The reflection and absorption coefficients are calculated with the method used in Sec. 4.4. Nevertheless, the absorption coefficient A

depends on f, ψ and θ. It is impossible to show the effects of all three variables at the same time, so we analyse the results by taking on two variables each time.

Firstly, the incident angle θ varies from $[-\pi/2, \pi/2]$, while the incidence plane is fixed in the plane $(x_3, 0, x_1)$ with $\psi = 0$. And the frequency $f = [0, 2.5]$ kHz.

The reflection coefficient is shown in the form of $\ln(\mid R \mid^2) = \ln(1 - A)$ against frequency f and incident angle θ in Fig. 6.3a). A zoom-in view of Fig. 6.3a) presents the result from $f = [1.4, 2.4]$ and $\theta = [80^o, 90^o]$ in Fig. 6.3d) . To understand the colormaps here, darker colour corresponds to higher absorption and vice versa.

So, it is clearly noted in Fig. 6.3a) that the system bears a symmetry in θ, around the normal direction $\boldsymbol{e}_3$. Two curves of high absorption of "quasi-periodic" shape are observed, due to the resonances of the material layer. Meanwhile two high absorption areas are found for large oblique angles $[82^o, 88^o]$, around $f = [1.4, 2.2]$ kHz. The first high absorption curve is partially presented in Fig. 6.3c), as the absorption in relation to θ at 477 Hz. The absorption is higher than 0.5 between $[-40^o, 40^o]$, with a quasi-total absorption plateau between $[-20^o, 20^o]$.

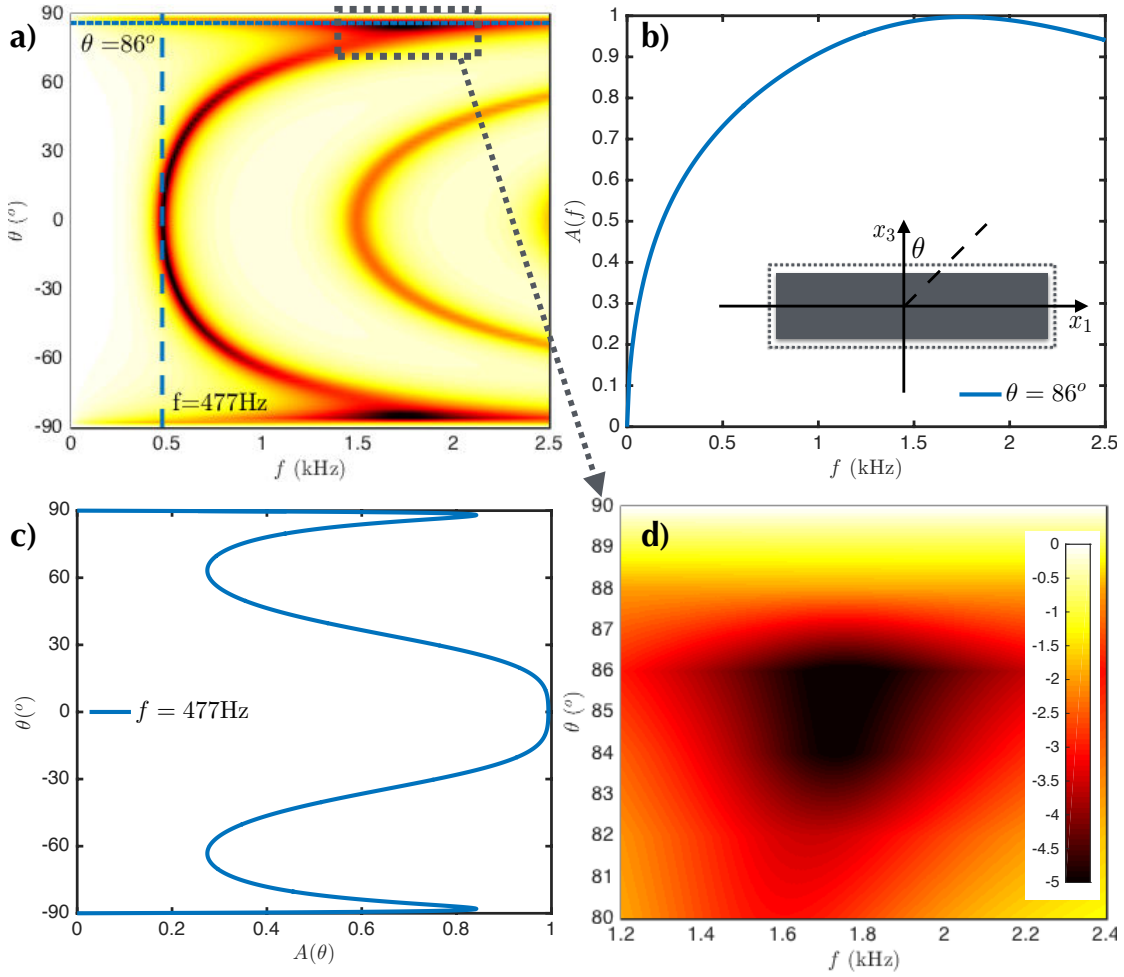

FIGURE 6.3: a) Frequency-incidence diagram of $\ln(R^2)$ at $\psi = 0$ $\boldsymbol{\alpha} = (0, 0, 0)$; b) Absorption coefficient against frequency at incident angle $\theta = 86^o$; c) Absorption coefficient against incident angle θ at frequency $f = 477$ Hz; d) Zoom-in view of a) at $f = [1.4, 2.4]$ kHz and $\theta = [80^o, 90^o]$.

A drastic change in absorption value is observed at around 65° in Fig. 6.3c). In order to see its evolution, we plot $A(f)$ at $\theta = 86°$. The whole curve presents high absorption while a total absorption peak is found around 1750 Hz.

The area that corresponds to high absorption for large oblique incidence is located between the two layer resonances. It does not seem to correspond to either of the two resonances of the material layer. With a quasi-grazing incident angle, it may be related to surface wave propagation. This point will be investigated later.

Now, consider the incident angle θ from $[-\frac{\pi}{2}, \frac{\pi}{2}]$, while the incident plane angle ψ varies from $[-\pi, \pi]$. We analyse into the frequencies at which maximal absorption has been previously shown, i.e., at 477 Hz and 1750 Hz.

Figure 6.4 shows the reflection coefficients as function of ψ and θ of the same anisotropic composition as $\boldsymbol{\alpha} = (0, 0, 0)$. A clear symmetry can be observed at $\psi = 0$ and π, which conforms with the theoretical model as the incidence plane vector $\boldsymbol{k}_\Gamma = (k_1, k_2)$ is related to both $\sin(\psi)$ and $\cos(\psi)$.

As shown in Fig. 6.4a), the absorption pattern is omnidirectional in ψ and quasi-total for θ up to 30° at 477 Hz. Furthermore, 4 more high absorption points at large oblique angle are found in Fig. 6.4b), at $\psi = \pm\frac{\pi}{4}, \pm\frac{3}{4}\pi$, different to the ones at $\psi = 0, \pm\pi$.

Taking into account the symmetries both in ψ and θ, later calculations only consider $(\psi, \theta) \in [0, \frac{\pi}{2}]$. Now, we present the unit cell set in two of the PCS positions $\boldsymbol{\alpha}_1 = (0, 0, 0)$ and $\boldsymbol{\alpha}_2 = (0, 0, \pi/2)$ in oblique incidence of θ and various incidence plane angles $\psi = 0, \pi/6, \pi/3, \pi/2$ in Fig. 6.5.

Firstly, a general observation of Fig. 6.5 gives out the general effect of changing the incidence plane angle, that larger ψ makes the absorption strips curve towards higher

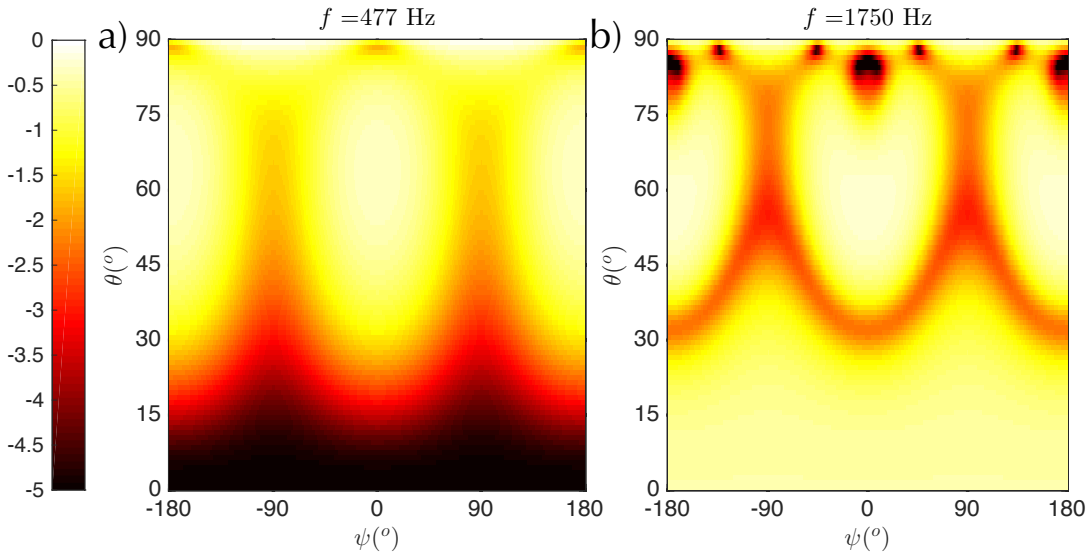

FIGURE 6.4: Simulation results of $\ln(|\ R\ |^2)$ against incidence plane angle ψ and incident angle θ at $\boldsymbol{\alpha} = (0, 0, 0)$ for a) $f = 477$ Hz, b) $f = 1750$ Hz.

frequencies at bigger incident angles ($\pi/6 < \theta < \pi/3$), while its effect is nearly unidentifiable in small incident angles ($\theta < \pi/6$). This is also confirmed by the observation in Fig. 6.4. In other way, more curving towards higher frequencies can also be translated into better absorptions at $\pi/6 < \theta < \pi/3$.

Secondly, the sub-figures of Fig. 6.5 are identical in pairs. Subfigure a1) and b4) are identical, so do a2) and b3), a3) and b2). This symmetry is due to the symmetry of the unit cell, whereas the cylinder is placed at the centre of the cuboid and $\ell_{\mathrm{II}} = \ell_{\mathrm{III}}$. In this case, the yaw of the unit cell around $\boldsymbol{e}_{\mathrm{II}}$ is equivalent to the variation of incident angle θ. This leads to isotropic behaviour when the incidence plane is in plane with cross-section of the unit cell.

With regards to the absorption at $\theta \approx \pi/2$, the frequencies where the high absorption appears, are multiple of 1.3 kHz in Fig. 6.5 a4,b1), and multiple of 1.5 kHz in Fig. 6.5 a3,b2). This clearly indicates a non-dispersive resonance regime.

But larger ψ does not result in uniform changes with $\boldsymbol{\alpha}_1$ and $\boldsymbol{\alpha}_2$. In the case of $\boldsymbol{\alpha}_2$,

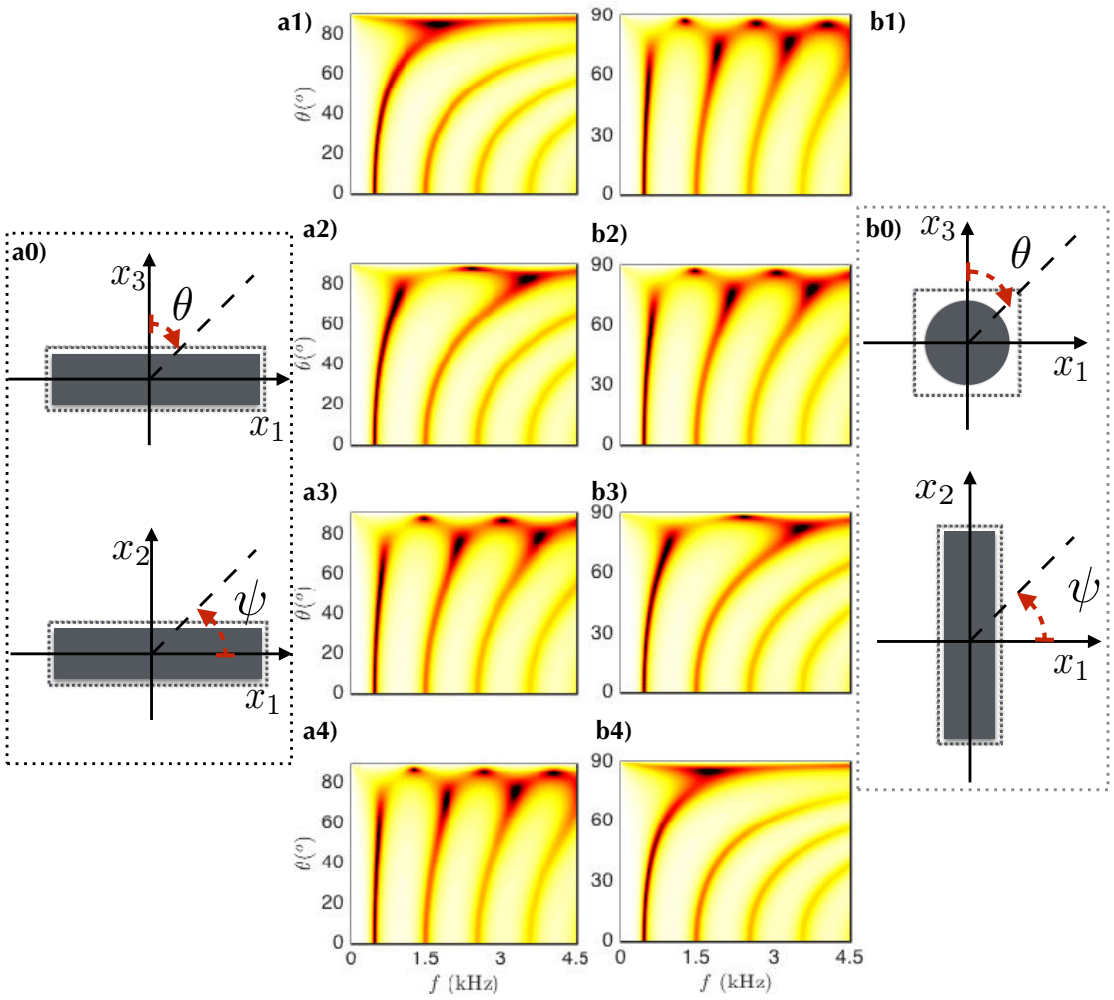

FIGURE 6.5: Frequency-incidence diagram of $\ln(|\ R\ |^2)$: Column a) $\boldsymbol{\alpha}_1 = (0, 0, 0)$; Column b) $\boldsymbol{\alpha}_2 = (0, 0, \pi/2)$; Row 1-4), at $\psi = 0, \pi/6, \pi/3, \pi/2$. Colour map is the same as in Fig. 6.4.

the black areas reduce in number with more ψ considered, resembling a shift to high frequency, in contrary to the case of $\boldsymbol{\alpha}_1$. This may be due to the fact that the symmetry of surface wave regime is centred at $\alpha_{\mathrm{II}} = \pi/2$. The more the incidence plane is approaching the symmetry axis, the more the high absorption areas will surface in lower frequency range. Conversely, it means that more drastically difference between different components of the anisotropy brings out better absorption.

Apart from the regime changes observed in Fig. 6.5a1, b4), a third transitional regime is observed in Fig. 6.5a2,a3) and b2,b3) for second and third resonance, around $\theta = 75^{\mathrm{o}}$.

6.4 Critical coupling

In order to better understand the mechanism behind the high or total absorptions at oblique incidence, we investigate the state of coupling in relation to the incident angle θ. The PCS configuration with $\boldsymbol{\alpha} = (0, 0, \pi/2)$ and $\ell_{\mathrm{II}} = \ell_{\mathrm{III}}$ is chosen for this study, as it has more high absorption at grazing angle, see Fig. 6.5. The absorption of the layer is visualised in the complex plane.

In Fig. 6.6, the complex plane of $\ln|\ R\ |^2$ while $\psi = 0, \theta = 75^{\mathrm{o}}$ is shown along with the trajectories of zeros and poles of the reflection coefficient on the complex frequency plane. Each corresponds to a Fabry-Pérot interference. Their corresponding positions on the frequency-incidence diagram are shown in Fig. 6.7. The precise results of the zero trajectories are listed in Tab. 6.4.

First, the zero trajectory of N-th resonance moves slightly towards higher frequency from 0^{o} to 75^{o} closely above the real frequency line, which creates an omnidirectional absorption in this angular range. Later, it rises up until 82^{o}, then jumps about 500 Hz toward higher frequency within only 1^{o} of incident angle change to 83^{o}. Afterwards, the zero continues to move towards real frequency line, crossing the real frequency axis at around 87^{o}, which creates the total absorption peak at grazing incidence, shown in Fig. 6.7. At last, it joins position with the pole from $(N+1)$-th resonance. We also notice that between 82^{o} and 83^{o}, the change of $A(f)$ is very rapid.

The zero of the reflection coefficient corresponds to the zeros of the following function,

$$F(\omega, \theta) = \tan(\kappa D) - \mathrm{i}\frac{k_0 \cos(\theta)}{\rho_0 H_{33} \kappa}. \tag{6.4.1}$$

In our case where $\alpha_{\mathrm{I}} = \alpha_{\mathrm{II}} = 0$, $H_{11} = H_{33}$, and $\psi = 0$, the complex function reduces to

$$F(\omega, \theta \to \pi/2) = \tan(n k_0(\omega) D) - \mathrm{i}\frac{\cos(\theta)}{\rho_0 H_{33} n}, \text{with } n(\omega) = \sqrt{c_0^2/c_{33}^2 - \sin^2\theta}\,. \tag{6.4.2}$$

For every angle of incidence considered, there are multiple complex solutions which correspond to the respective order of Fabry-Pérot interferences.

The pole of the N-th resonance moves slightly towards higher frequencies from 0^{o} to 75^{o} closely under the real frequency line, following the zero in parallel. Then, it diverts towards negative imaginary frequency at about 75^{o}. A jump of about 500 Hz also occurs at the very same angular range from 82^{o} to 83^{o}, but this time towards lower real frequency. In the end, the pole goes toward the real frequency line, joins with the zero

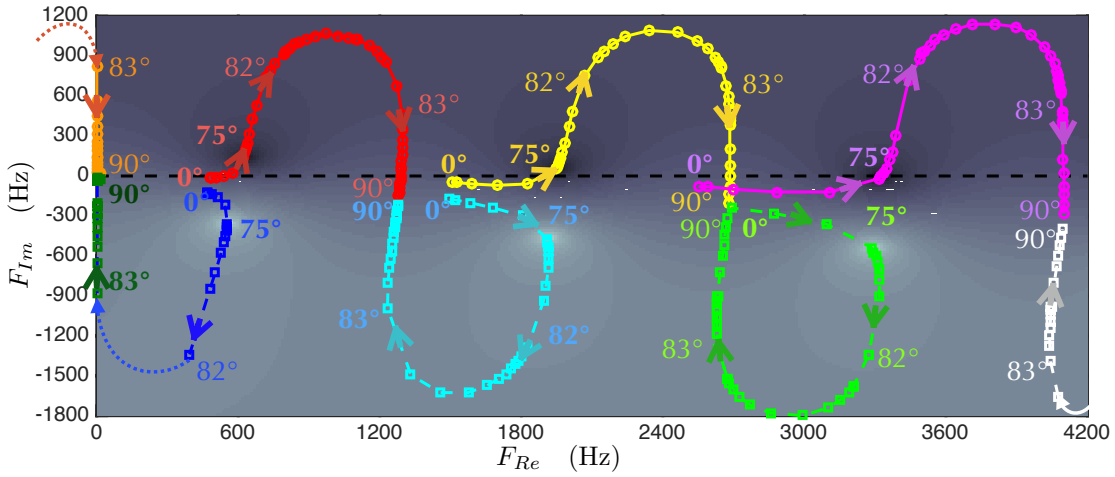

Figure 6.6: Complex frequency plane of ln| R |^2,while $\psi = 0, \theta = 75^o$: Zero point trajectories in orange, red, yellow and purple solid lines (circles for exact zero found in simulation), Pole point trajectories in green, blue, cyan, neon green and grey dashed lines (square for exact pole found in simulation).

Tracjectory	Colour	F_R range (Hz)	Critical point 1	Critical point 2
Zero 1	Orange	0-17	None	None
Zero 2	Red	538-1290	50^o, 550 Hz	87^o, 1289 Hz
Zero 3	Yellow	1496-2685	72^o, 1923 Hz	86^o, 2683 Hz
Zero 4	Purple	2551-4103	76^o, 3326 Hz	85^o, 4098 Hz

Table 6.4: Zero trajectories in relation to θ at $\phi = 0$.

point of $(N-1)$-th resonance.

Furthermore, although common knowledge suggests that the zero and pole of the same resonance always appear simultaneously in pairs at normal incidence condition. But, here at large incidence angle, or grazing incidence angle, the zero and pole of the same resonance moves extraordinarily far away from each other and the real frequency line, and eventually pairing with the zeros and poles from other resonances at $\theta = \pi/2$.

The pattern of trajectories repeats itself at almost all Fabry-Pérot interferences, except for 1st zero trajectory (in orange line) and 1st and 2nd pole trajectories (in green and blue lines). Though the pattern should repeat itself at the 1st and 2nd pole trajectories as the blue dotted arrow in Fig. 6.6a), there is not any evident pole found between the crucial 82^o to 83^o angular range. Thus this trajectory becomes discontinuous. Meanwhile, the 1st zero trajectory seems to jump out from under 0 Hz of the real frequency (orange dotted arrow), which can not be explained by the Fabry-Pérot resonance theory.

Finally, for all trajectories, zero (or pole) with incidence angle bigger than 75^o occupies the most portion of the trajectory. This high absorption at large incidence angle and sudden change in zero trajectory points to a potential change of regime from Fabry-Pérot regime of the metamaterial layer to a surface wave regime of the air-material interface. As energy is diverted to the surface wave, it no longer propagates, or more precisely it is not reflected into the ambient air medium, seemingly causes an absence of reflection, which translates to a high absorption. The associated critical angle for surface propagation is

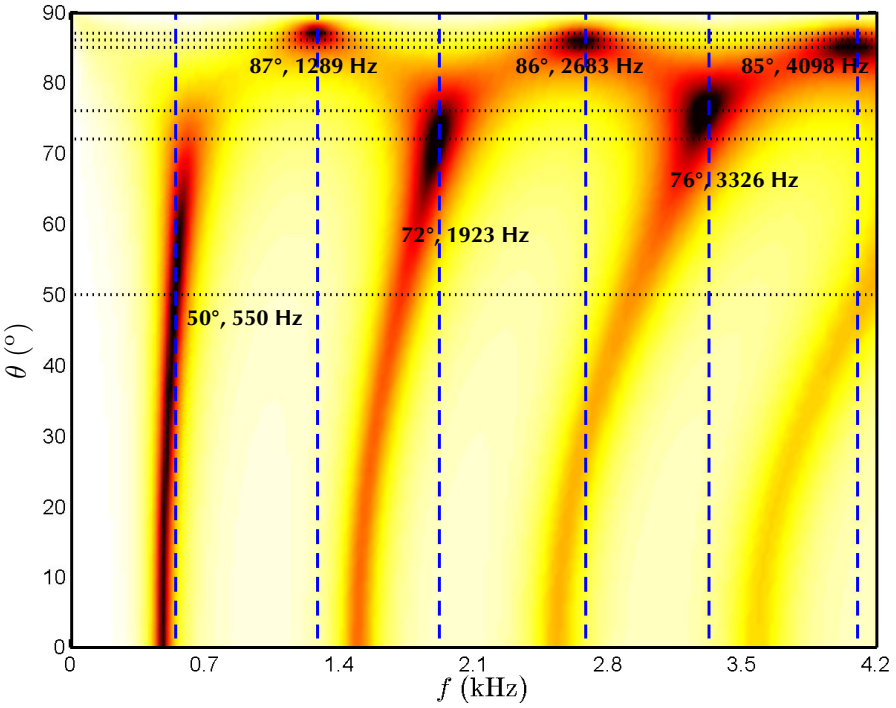

FIGURE 6.7: Frequency-incidence diagram of $\ln(R^2)$ at $\phi = 0$.

found as 82°.

It is much worthwhile to investigate further into the dispersion relation in grazing incidence at extremely low frequency, see Appendix C.

6.5 Diffuse field

As shown in Chapter 5, the metamaterial bears multiple high absorption peak, which can form a broad band absorption plateau. It is worthwhile to look into the absorption in diffuse field, similar as the one in Section 2.7. The simple absorption coefficient A for a certain unit cell configuration of rotation $\boldsymbol{\alpha}$ is calculated for any incidence (θ, ψ) and frequencies from 0 to 2.5 kHz.

First, the absorption in diffuse field is calculated with consideration of θ. The averaged value of absorption in diffuse field with consideration of ψ is also formulated for a certain unit cell rotation [119],

$$A_{diff}(\psi, f) = 2\int_0^{\frac{\pi}{2}} A(\psi, \theta, f)\sin(\theta)\cos(\theta)d\theta \; ; \tag{6.5.1a}$$

$$A_{diff}(f) = \frac{1}{\pi}\int_0^{\pi} A_{diff}(\psi, f)d\psi \; . \tag{6.5.1b}$$

Here, unit cell configuration of the last section in rotation $\boldsymbol{\alpha}_2 = (0, 0, \pi/2)$ is used. The corresponding absorptions in diffuse field are shown in Fig. 6.8.

Figure 6.8a) shows the absorption coefficient in diffuse field in the representation of $[1 - A_{diff}(\psi, f)]$, against $\psi \in [0, \pi/2]$ and $f \in [0, 2.5]$ kHz, where darker colour represents higher absorption. It can be seen that the high absorption corresponding to the first

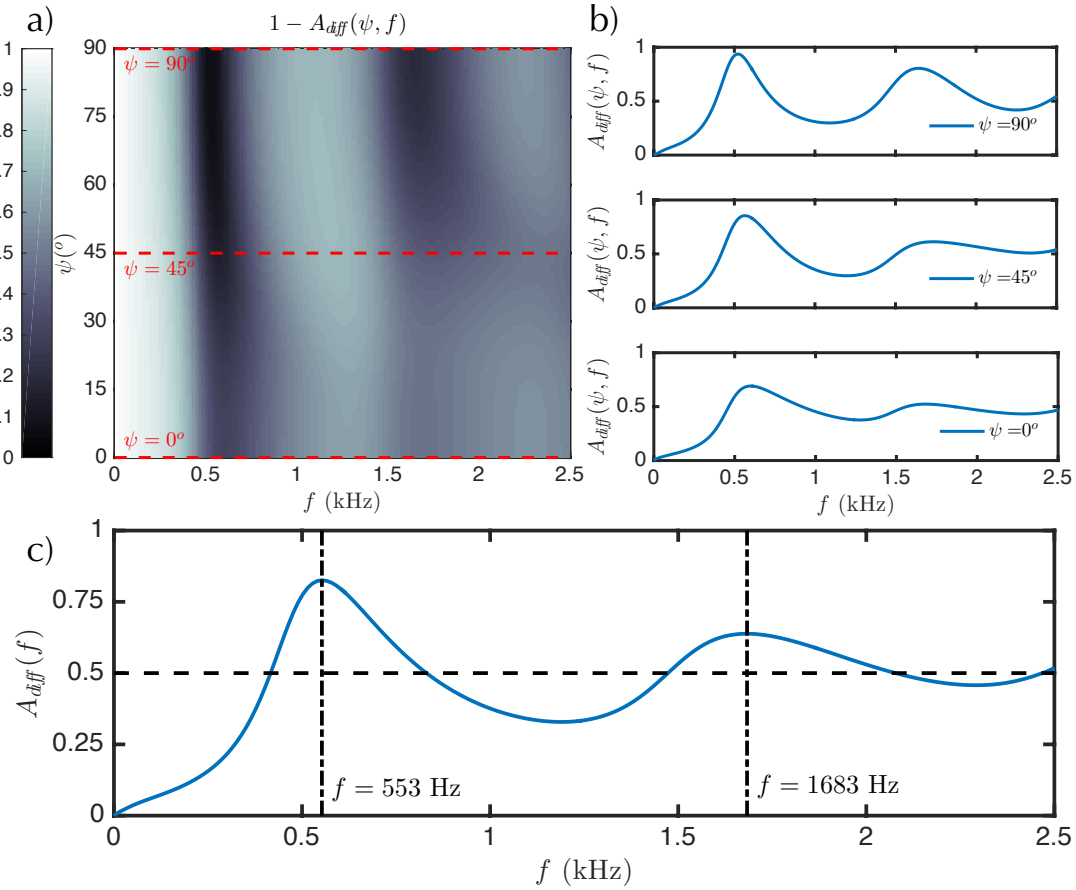

FIGURE 6.8: Absorption coefficient in diffuse field: a) The θ-averaged absorption as in Eq. (6.5.1a) in form of $1 - A_{diff}(\psi, f)$; b) The θ-averaged absorption $A_{diff}(\psi, f)$ against f, for $\psi = 0, \pi/4, \pi/2$; c) The (θ, ψ)-averaged absorption $A_{diff}(f)$ in Eq. (6.5.1b).

layer resonance regime is slightly shifted towards lower frequency around 500 Hz, with the increase of ψ. The second high absorption zone around 1700 Hz follows the same pattern with smaller absorption.

Figure 6.8c) shows the absorption coefficient in diffuse field A_{diff}, averaged on θ and ψ, against frequency f. The averaged absorption is higher than 0.5 from 410 Hz, with a high absorption peak in low frequency range around 553 Hz and a second one around 1683 Hz. The material can be generally considered as a quasi-omnidirectional absorber in both ψ and θ directions.

The absorption of the material layer is not only related to incidence, but also the anisotropy. The simple absorption coefficient should be written as $A(\boldsymbol{\alpha}, \theta, \psi, f)$. But the unit-cell is symmetric for $\ell_{\mathrm{II}} = \ell_{\mathrm{III}}$, α_{I} only rotates the unit cell in $(\ell_{\mathrm{II}}, \ell_{\mathrm{III}})$ plane. This renders rotation in this direction no influence at all. So the rotation angle α_{I} is not considered for anisotropy in this case. It is set to be 0.

Considering the findings on symmetry of the system in Sec.6.3, the effect of a varying α_{III} is equivalent to a varying ψ. And the calculation of $A_{diff}(f)$ already accounts for all $\psi \in [0, \pi]$. There is no need to consider α_{III} for anisotropy in this case either. Then it is set to be $\pi/2$ as in the previous case.

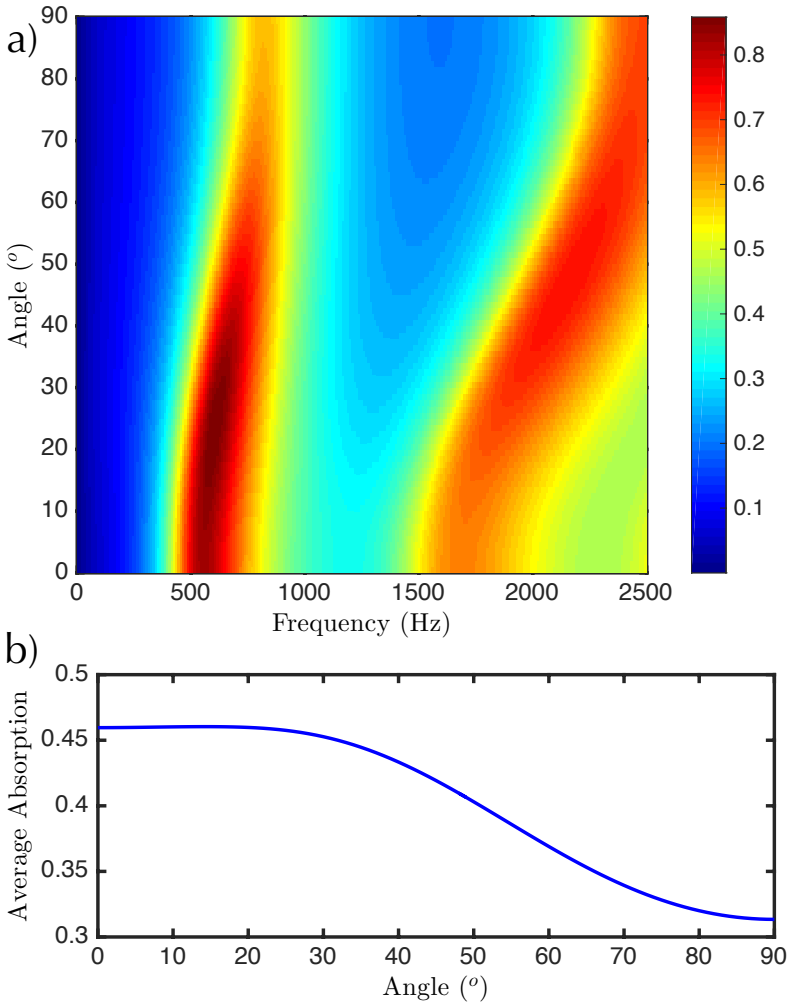

FIGURE 6.9: a) Absorption in diffuse field $A_{diff}(f, \alpha_{\text{II}})$; b) Average absorption in diffuse field $\bar{A}$ against rotation angle α_{II} .

Thus, the only remaining rotation angle is α_{II}, which defines the angle between $\boldsymbol{e}_{\text{I}}$ and $\boldsymbol{e}_1$. Also recalling the theoretical and experimental results in Sec. 4.4, the absorption in parallel and perpendicular directions are drastically different, see Fig. 4.9. Thus α_{II} should be considered the decisive factor in this study of general anisotropy.

Now, in order to take into account the effects of the anisotropy, we define the average absorption in diffuse field for a certain anisotropy $\boldsymbol{\alpha}$, normalised by the bandwidth F as follows:

$$\bar{A}(\boldsymbol{\alpha}) = \frac{1}{F}\int_F^0 A_{diff}(f, \boldsymbol{\alpha})df, \tag{6.5.2}$$

with $A_{diff}(f, \boldsymbol{\alpha})$ defined in Eq. (6.5.1b).

A series of calculations of $\bar{A}(\boldsymbol{\alpha})$ is launched where $\boldsymbol{\alpha} = (0, \alpha_{\text{II}}, \pi/2)$. And the rotation α_{II} varies from 0 to 90°. The results are represented in Fig. 6.9.

Similar to the absorption in diffuse field $A_{diff}(f)$ in Fig. 6.8c), two resonances are clearly identified in Fig. 6.9a). The first absorption peak slightly shifts towards higher frequencies by adding α_{II}. The second absorption peak is lower than the first and shifts much more towards higher frequencies by increasing α_{II}. A closer look determines the

maximum value of each peak. For the first resonance, the maximum value appears at 23° with an absorption of 0.86 at 602 Hz. As for the second one, the maximum value appears at 46° with an absorption of 0.74 at 2149 Hz.

More generally, the average absorption $\bar{A}$ wraps all effects of incidence and anisotropy into a single deciding factor. It is shown in Fig. 6.9b). The value of different anisotropy varies only slightly from around 0.45 for a small angle to around 0.31 at 90°. A closer look finds out that the average absorption is above 0.45 from 0 to 32°, with a maximum value found at 14° with an absorption of 0.46.

6.6 Performance of Hollow tubes array

The same analyses on incidence and anisotropy as in the above sections are performed on the hollow tube array with the same dimensions as the optimal design in Chapter 5. For numerical application, the dimensions are $\ell_{\mathrm{I}} = 41.2$ mm and $\ell_{\mathrm{II}} = \ell_{\mathrm{III}} = 8.4$ mm, $R_x = 4.1$ mm, $R_i = 3.9$ mm, $h = 40.2$ mm, with $h_1 = 30$ mm and $h_2 = 10$ mm.

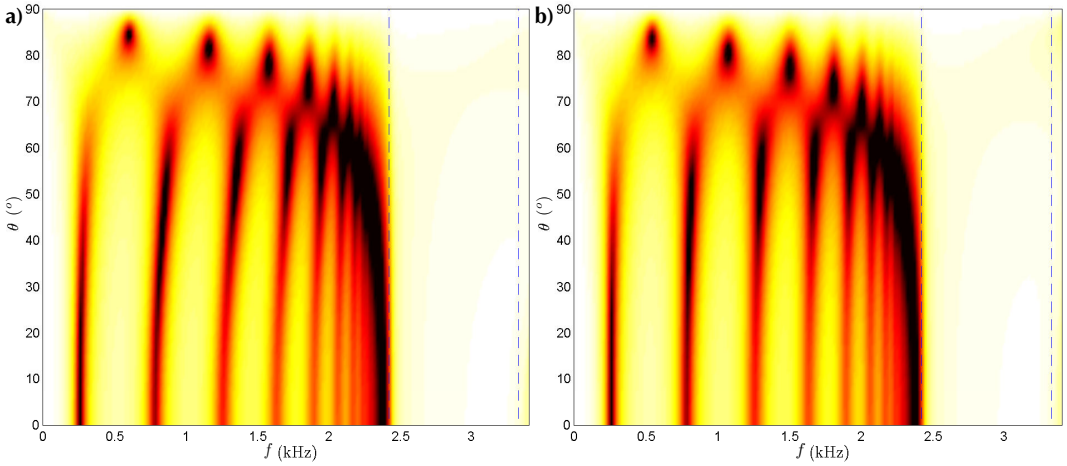

FIGURE 6.10: Frequency-incidence diagram of $\ln(R^2)$ at $\psi = 0$: a) $\boldsymbol{\alpha} = (0, 0, 0)$; b) $\boldsymbol{\alpha} = (0, \pi/2, 0)$.

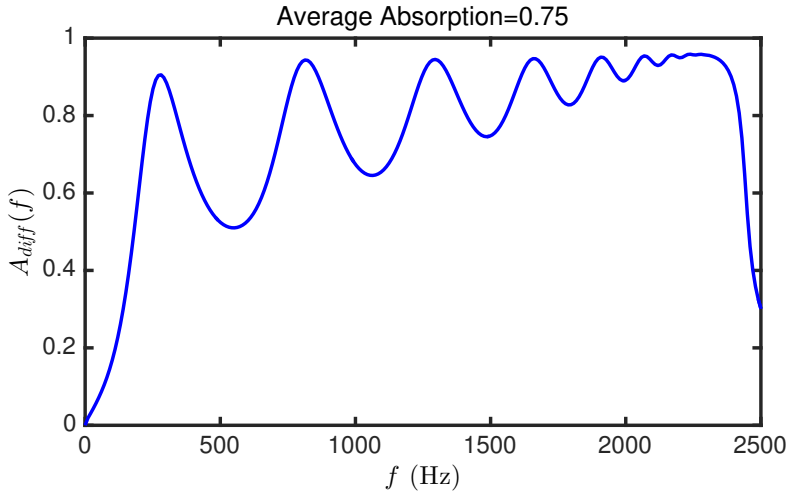

FIGURE 6.11: The (θ, ψ)-averaged absorption $A_{diff}(f)$, with $\boldsymbol{\alpha} = (0, 0, \pi/2)$.

Figure 6.10 shows the reflection coefficient in the form of $\ln(\mid R \mid^2) = \ln(1 - A)$ against frequency f and incident angle θ. The effects of slow sound compress all the peaks towards lower frequencies. And the accumulation of resonances appears at the tube resonance frequency ω_1, forming a high absorption zone before 2.5 kHz. These two features together makes the difference between the results from two different anisotropic compostions visually undistinguishable.

The band-gap is very clear for all incidences and anisotropies, as its effects are scalar in nature. So, it can be concluded that the anisotropic effects are masked in the hollow tube cases, and are less important than the solid cases. Also there will be no need to perform the symmetry tests on ψ.

The trajectories of the zeros and poles are much more difficult to calculate, since the space between each interference is much smaller than for the solid case. A rational sepeculation should suggest that the two kinds of trajectories still follow the same patterns as before, though more of them are superposed at the limited frequency-range from 0 to 2.5 kHz. Towards higher frequencies, it will be impossible to distinguish zeros and poles from different interferences, as they all converge towards the real frequency line around 2.5 kHz.

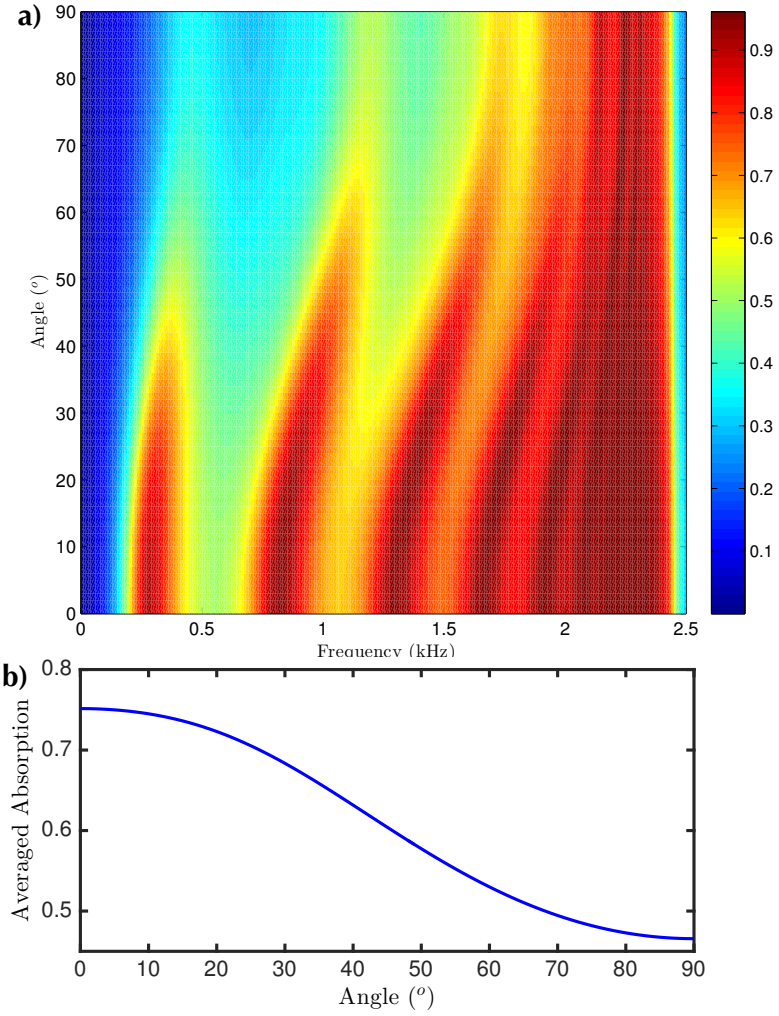

FIGURE 6.12: a) Absorption in diffuse field $A_{diff}(f, \alpha_{\text{II}})$; b) Average absorption in diffuse field $\bar{A}$ against rotation angle α_{II} .

Furthermore, Figure 6.11 shows the diffuse field absorption coefficient A_{diff} calculated as in Eq. (6.5.1b). Its value is averaged on θ and ψ, compiling information from all incidences into a simple absorption spectrum. Compared to the solid results in Fig. 6.9, a much boarder absorption spectrum is found, forming a high absorption plateau in the low-frequency range. The average value of absorption for 0 to 2.5 kHz is at 75%.

Moreover, a calculation of $\bar{A}(\boldsymbol{\alpha})$ as in Eq. (6.5.2) for the hollow case is launched where $\boldsymbol{\alpha} = (0, \alpha_{\mathrm{II}}, \pi/2)$. The rotation α_{II} varies from 0 to 90°. The results are represented in Fig. 6.12a). The absorption peaks slightly shifts towards higher frequencies with adding α_{II}. All secondary absorption peaks are unified towards the tube resonance frequency.

In Fig. 6.12b), the average absorption taking into account all factors is presented. The curve is monotone in nature. The best absorption performance is found at $\alpha_{\mathrm{II}} = 0$. No evident optimal angle is found for the hollow tube case.

Conclusion

The straw-inspired metamaterial is reported in this Chapter for absorption at oblique incidence while considering its anisotropic composition.

Using the optimal configuration without QWRs of the previous chapter, the sample with a thickness of 110 mm is studied for absorption under oblique incidence, defined by the in-plane incident angle θ and incident plane angle ψ. Various compositions of the frequency-incidence diagram are applied for different studies.

First, the symmetry study reveals that facing a fixed orthotropic configuration of the unit cell, the system bears a symmetry in θ, around the normal direction $\boldsymbol{e}_3$, and symmetry in ψ around 0 and $\pi/2$. Also, high absorption areas are found at large oblique incident angles.

Later, a study of the trajectories of the zeros and poles shows that for each Fabry-Pérot resonance, the zero trajectory crosses the real frequency line twice when the incident angle θ varies from 0 to $\pi/2$. Thus, the critical coupling condition is fulfilled twice. The first time happens at the small incident angle (normal incidence for the first peak). The second time at large incident angles. This explains the high absorption areas around this angular range.

Furthermore, absorption in diffuse field is calculated, while considering the anisotropic composition. The absorption is related to the incidence, represented by the incidence angles ψ and θ, and also the anisotropy, represented by the unit cell rotation angles $\boldsymbol{\alpha}$. The absorption coefficient can be averaged on all of these variables. The final results on the averaged absorption coefficient reveals that the optimal rotation angle around $\boldsymbol{e}_{\text{II}}$ is 14^{o} for the tested configuration.

Lastly, the same methods of study used in the previous sections are applied to the optimal configuration with QWRs. This gives a clear picture that the hollow tube array is a low-frequency broad-band absorber with high absorption level.

Conclusion & Perspectives

In this Thesis, the straw-inspired metamaterial has been theoretically and experimentally reported for sound absorption. The metamaterial mimics the composition of a straw bale which consists of tightly packed three-dimensional periodic arrangement of straight hollow cylindrical tubes, with a single tube per period. Therefore, an idealized straw stack can be seen as a highly concentrated anisotropic porous medium with resonances.

First, the acoustic properties of a periodic arrangement of narrow slits with QWRs loaded on one of the slit walls has been studied, which only mimics the resonator part of the proposed metamaterial. It has been shown that the wave propagating in such slit possesses the specific features of slow sound propagation over a quite large frequency band with a phase (and/or group) velocity much smaller than the one of the ambiant air. The effective parameters are derived, which show that the reduction of the sound speed in the slit is only due to a negative bulk modulus within the band-gap, not due to a tortuosity effect.

Based on these findings, an impervious array of square-periodic Helmholtz resonators of square cross-section has been studied with several theoretical approaches. Designs of panel for perfect sound absorption with sub-wavelength size are conceived by considering slow sound propagation and the critical coupling technique. The tuning trajectories related to various geometrical elements are visualised in the complex frequency plane. It opens a gateway to better understand the internal mechanism of reflection, absorption of acoustic material. It has also given as a very useful and intuitive tool in the design of perfect absorption metamaterial with strong dissipations

These promising results have given us very useful tools and knowledge, to study the the idealized straw stack which consists of tightly packed periodic arrangement of resonators.

The periodic arrangement of resonators has been studied in the long-wavelength approximation, assuming a satisfactory condition of scale separation, where the characteristic length of the sound wave is much larger than the unit cell dimension. The scale separation and the periodicity of the array allow us to use the two-scale asymptotic homogenisation method to derive the effective behaviour of the metamaterial.

The approach to this straw-inspired metamaterial relies on the homogenization of the idealized periodic arrangement of straw-like hollow tubes [51, 52], where the outer matrix and the inner resonators are seen as two different acoustic fields co-existing and interacting at the scale of the unit cell period, where macro wavelength phenomenon and local resonance occur simultaneously.

The outer matrix has been studied through homogenization of the idealized periodic arrangement of solid cylinders. The effective medium is characterised by frequency-dependent Darcy permeabilities in different principal directions and thermal permeability

[94]. Through approximation of the JCAL porous material model [7, 10], the frequency independent viscous and thermal parameters have been obtained numerically by Finite Element Method.

The inner resonator is considered as a secondary single point-source radiating throughout the outer matrix inside the unit cell, which can be characterised as a negative apparent admittance that combines in a porosity-weighted series with the effective compressibility of the outer matrix [52], analytically modelled by the theory of Zwikker & Kosten [11, 61].

Nevertheless, a series of impedance tube test on 3D-printed samples of hollow and solid samples have been performed, which validated the theoretical model and the numerical computation of the JCAL parameters. The slow sound phenomenon is found by studying the dispersion properties of the unit cell. A negative compressibility is found with the hollow tube case. This leads to the slow sound propagation before the tube resonance frequency. A pseudo-band-gap is found around the tube resonance frequency, which is characterised by huge attenuation within the frequency band.

This porous resonant system behaves like an open and lossy resonator, therefore the critical coupling condition is used to find configurations with total absorption. When the critical coupling condition is satisfied, the leakage of the resonating system is perfectly compensated by the added intrinsic visco-thermal losses [28–30], by tuning the dimensions of the configuration, thus, leading to a total absorption [82, 85].

An optimisation process has been performed based on the observations during the parametric study and the visualisation of the trajectories of the zeros of the reflection coefficient on the complex frequency plane. The process gave out multiple possibilities of optimal configuration for perfect absorption. One of them which is more suitable for manufacturing and testing has been 3D-printed and tested in the impedance tube. The optimal design gave out a total absorption peak at 272 Hz, and experimentally 99.6% absorption at 258 Hz, the wavelength of which corresponds to 13 times of the metamaterial slab thickness. A broad band secondary absorption peaks have been found before the tube resonance frequency, due to the Fabry-Pérot regime of the metamaterial. All results point out that the straw-inspired metamaterial design is a sub-wavelength absorber that can achieve total absorption at a very low-frequency range.

Furthermore, the metamaterial configuration without inner resonators has been studied for absorption at oblique incidence, while different anisotropic compositions of the unit cell are considered equally. The results show the symmetry of the configuration in terms of incidence and anisotropy. Also, the critical coupling condition is fulfilled twice within the incident angle range for each Fabry-Pérot interference. The first time happens at a small incident angle (normal incidence for the first interference). The second time happens around 82°. This leads to the high absorption areas at large oblique incident angle.

Moreover, the absorption in the diffuse field has been calculated, while considering the anisotropy. This study shows that the metamaterial has overall high absorption at low-frequency range for all incidences and anisotropic compositions considered. Meanwhile, the material is overall angle and frequency selective in terms of absorption.

The current stage of the study on the straw-inspired metamaterial has paved the way for several different directions of future researches.

Firstly, the theoretical and numerical model of the homogenised problem allows us to analyse more versatile configurations of scatterers with more complex geometry. The anisotropy of a unit cell with only straight cylinder is limited by its simple external geometry. We can imagine configuration that can bring about more orientation selective in terms of absorption while considering oblique incidence and anisotropy.

Similarly to the rainbow trapping absorber design in Ref. [120], the theoretical model of the straw-inspired metamaterial can include such a series of QWRs with sequential inner radius or length, to form an acoustic rainbow, to achieve wider band-gap in the reflection regime, or even total absorption in the transmission regime.

Secondly, the metamaterial designed in this thesis is still artificial, and cannot be manufactured without precise 3D-printing and plastic material. This is against our initial idea of using eco-friendly and sustainable raw material to make better acoustic absorbers. Further study should be made using only naturally cultivated straws to form a truly natural metamaterial[1].

As the straw is made of the vascular bundle of natural cellulose, the tube wall can no longer be considered as perfectly rigid, especially at low-frequency range. A full poroelastic model should be theorised, which couples the flux interaction of the inner cavity and vibration modes of the tube. This requires deeper understanding and further development on the homogenisation method, and more sophisticated numerical model.

Thirdly, the anisotropy study shows the possibility of a surface wave conversion at extremely low frequencies[2]. It is very interesting to look at surface wave propagation at the interface of the metamaterial. This may also help to better understand the high absorption at grazing incidence, to design corresponding metasurface, similar as in Ref. [121].

Equally, the straw-inspired metamaterial is a good candidate for absorption in diffuse field, as it possesses efficient absorbing in the diffuse field. A further engineering study should be made for calculation of its diffusion coefficient, and possible effects on reverberation in room acoustics, similar as in Ref. [91].

Finally, as a general perspective, we want to see the in-field tests of the acoustic metamaterial, making full-scale wall-size penal tests as in Ref. [122].

[1] Initial study on natural straws is presented in Appendix D

[2] Initial results about grazing incident are presented in Appendix C

Appendix

Appendix A

Transfer Matrix Method

As shown in Fig. A.1, the unit of one HR and its adjacent slit space is defined. The cross-section of the unit is $S_0 = da$, the slit space $S_s = ha$.

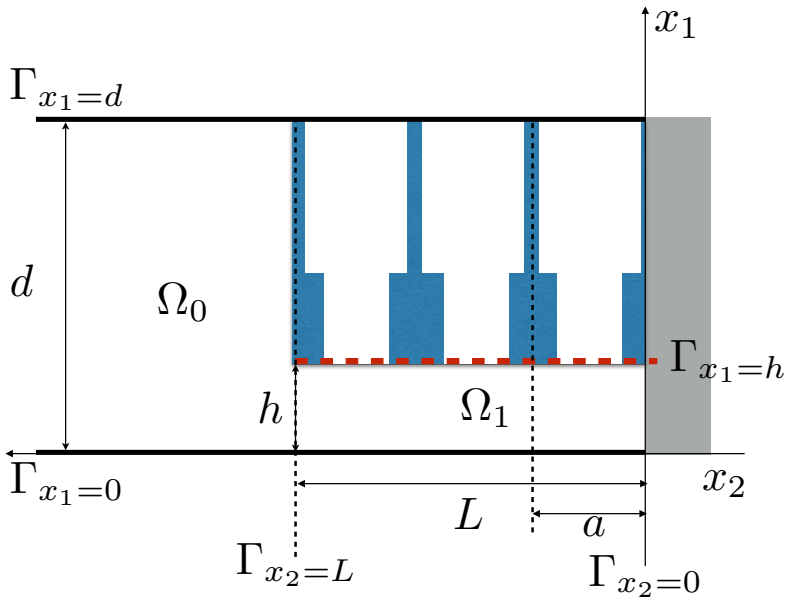

FIGURE A.1: 2D Schematic of the 3D unit cell of the panel composed of a set of $N = 3$ Helmholtz resonators.

It is assumed that the wavelength of the considered problem $\lambda \ll a$. Thus, a discrete model is developed accounting for the finite number of individual resonators using the Transfer Matrix Method (TMM).

Thus, for identical units of HR, the transfer matrix is written as:

$$\begin{pmatrix} P_{\mathrm{i}} \\ U_{\mathrm{i}} \end{pmatrix} = \mathbf{T} \begin{pmatrix} P_{\mathrm{o}} \\ U_{\mathrm{o}} \end{pmatrix}, \tag{A.0.1}$$

where the transmission matrix $\mathbf{T}$ is written as

$$\mathbf{T} = \begin{pmatrix} T_{11} & T_{12} \\ T_{21} & T_{22} \end{pmatrix} = \mathbf{M}_{\Delta l_{\mathrm{slit}}} (\mathbf{M}_s \mathbf{M}_{\mathrm{HR}} \mathbf{M}_s)^N .$$

Here, the transmission matrix for each lattice step in the slit, $\mathbf{M}_s$, is written as

$$\mathbf{M}_s = \begin{pmatrix} \cos\left(k^s \frac{a}{2}\right) & \mathrm{i}Z^s \sin\left(k^s \frac{a}{2}\right) \\ \frac{\mathrm{i}}{Z^s} \sin\left(k^s \frac{a}{2}\right) & \cos\left(k^s \frac{a}{2}\right) \end{pmatrix}. \tag{A.0.2}$$

with $Z^s = (B^s \rho^s)^{1/2}/S_s$.

The resonators are introduced as a punctual scatters by a transmission matrix $\mathbf{M}_{\mathrm{HR}}$ as

$$\mathbf{M}_{\mathrm{HR}} = \begin{pmatrix} 1 & 0 \\ 1/Z_{\mathrm{HR}} & 1 \end{pmatrix}, \tag{A.0.3}$$

and the radiation correction of the slit to the free space as

$$\mathbf{M}_{\Delta l_{\mathrm{slit}}} = \begin{pmatrix} 1 & Z_{\Delta l_{\mathrm{slit}}} \\ 0 & 1 \end{pmatrix}, \tag{A.0.4}$$

with the characteristic radiation impedance $Z_{\Delta l_{\mathrm{slit}}} = -i\omega \Delta l_{\mathrm{slit}} \rho_0 / \phi_t S_0$, where ρ_0 the air density and Δl_{slit} the proper end correction [123] , see Sec.2.2-2.4.

Then, the reflection coefficient is calculated as

$$R = \frac{T_{11} - Z_0 T_{21}}{T_{11} + Z_0 T_{21}}. \tag{A.0.5}$$

with $Z_0 = \rho_0 c_0 / S_0$, and finally the absorption as $\alpha = 1 - |R|^2$.

Appendix B

Viscous and thermal parameter for the analysed configurations

B.1 Configurations in Chapter 4

The configurations tested in Chapter 4 are Config.n°1 to Config.n°8. For the JCAL model only accounts for the air domain in the unit cell, the parameters of Config.n°3 and n°6, n°4 and n°7, n°5 and n°9 are the same. Also due to the 2D dimension of Config.n°1 and 2, only one set of parameters are calculated for the two. Their dimensions are listed as below:

Config.	R_x (mm)	ℓ_{II} (mm)	ℓ_x (mm)	ℓ_{I} (mm)
n°1	2.9	6	40	40
n°2	2.9	6	41	41
n°3,n°6	2.9	6	37	41
n°4,n°7	2.9	6	39	41
n°5,n°8	2.9	6	40	41

Table B.1: Dimensions of Config.n°1 to n°8.

The corresponding viscous and thermal parameters in JCAL model are listed in the following tables:

Config.	$K_{\mathrm{m}}^{\mathrm{I}0}$ (mm^2)	$\Lambda_{\mathrm{m}}^{\mathrm{I}}$ (mm)	$\tau^{\mathrm{I}\infty}$	$K_{\mathrm{m}}^{\mathrm{II}0}$ (mm^2)	$\Lambda_{\mathrm{m}}^{\mathrm{II}}$ (mm)	$\tau^{\mathrm{II}\infty}$
n°1, n°2	3.038×10^{-2}	0.5249	1.059	3.184×10^{-2}	0.4023	2.346
n°3, n°6	3.093×10^{-2}	0.5261	1.111	1.837×10^{-2}	0.4865	2.103
n°4, n°7	3.147×10^{-2}	0.5268	1.162	3.355×10^{-2}	0.5706	1.861
n°5, n°8	3.255×10^{-2}	0.5280	1.264	6.392×10^{-2}	0.7389	1.375

Table B.2: Viscous parameters of Config.n°1 to Config.n°8.

Config.	Θ_{m}^{0} (mm^2)	Λ'_{m} (mm)
n°1, n°2	6.365×10^{-2}	0.8656
n°3, n°6	7.923×10^{-2}	0.9943
n°4, n°7	9.561×10^{-2}	1.1
n°5, n°8	0.1276	1.4

Table B.3: Thermal parameters of Config.n°1 to Config.n°8.

B.2 Configurations in Chapter 5

The configurations without QWRs of which the theoretical results are shown in Fig. 5.9 are Configuration a), b) and c).Their dimensions are listed as below:

Config.	R_x (mm)	ℓ_{II} (mm)	ℓ_x (mm)	ℓ_{I} (mm)
a)	3.6	9	41	42
b)	4.4	9	41	42
c)	4.4	9	30	42

TABLE B.4: Dimensions of Configuration a), b) and c) in Fig. 5.9.

The corresponding viscous and thermal parameters in JCAL model are listed in the following tables:

Config.	$K_{\mathrm{m}}^{\mathrm{I}0}$ (mm^2)	$\Lambda_{\mathrm{m}}^{\mathrm{I}}$ (mm)	$\tau^{\mathrm{I}\infty}$	$K_{\mathrm{m}}^{\mathrm{II}0}$ (mm^2)	$\Lambda_{\mathrm{m}}^{\mathrm{II}}$ (mm)	$\tau^{\mathrm{II}\infty}$
a)	5.571×10^{-1}	3.550	1.022	1.837×10^{-2}	2.300	1.493
b)	1.203×10^{-1}	1.4569	1.126	1.857×10^{-2}	0.5528	2.256
c)	1.5779×10^{-1}	1.5504	1.517	3.498	1.985	1.338

TABLE B.5: Viscous parameters of Configuration a), b) and c) in Fig. 5.9.

Config.	Θ_{m}^{0} (mm^2)	Λ'_{m} (mm)
a)	5.615×10^{-1}	2.466
b)	1.258×10^{-1}	1.201
c)	3.700	4.255

TABLE B.6: Thermal parameters of Configuration a), b) and c) in Fig. 5.9.

Appendix C

Grazing incidence

The complex zero of the reflection coefficient corresponds to the zeros of the following complex function,

$$F(\omega,\theta) = \tan(\kappa D) - \mathrm{i}\frac{k_0\cos(\theta)}{\rho_0 H_{33}\kappa}. \tag{C.0.1}$$

In our case where $\alpha_{\mathrm{I}} = \alpha_{\mathrm{II}} = 0$, $H_{11} = H_{33}$, and $\psi = 0$, the complex function reduces to

$$F(\omega,\theta) = \tan(nk_0(\omega)D) - \mathrm{i}\frac{\cos(\theta)}{\rho_0 H_{33} n}, \text{with } n(\omega) = \sqrt{c_0^2/c_{33}^2 - \sin^2\theta}\,. \tag{C.0.2}$$

For each angle of incidence considered, there are multiple complex solutions which correspond to the respective order of Fabry-Pérot interferences.

Moreover, for the grazing incidence case where $\theta \to \pi/2$, with $\sin\theta = 1, \cos\theta = 0$,

$$F(\omega,\theta\to\pi/2) = \tan(nk_0(\omega)D), \text{with } n(\omega) = \sqrt{c_0^2/c_{33}^2 - 1} \tag{C.0.3}$$

One evident solution corresponds to the visco-thermal static case where $\omega = 0, \tan 0 = 0$.

C.1 Observation

Based on the observation of the complex zero trajectory of the 1st Fabry-Pérot interference, a small peak of absorption is found at extreme low frequency around 114 Hz at grazing incidence $\psi = 87$ °, shown in Fig. C.1. The absorption peak at 1290 Hz can be explained as the second time critically coupled. But the 1st one cannot be explained with the same observation in Sec. 6.4.

Furthermore, as the effective material layer is rigidly backed, and with the evidence of energy conversion to surface wave above 82^{o} , it can be determined that the major acoustic phenomena here correspond to a Love wave propagating along the interface of the metamaterial with ambient air. The Love wave propagates along x_1 direction at the surface of the layer in skin depth and quickly becomes evanescent in shallow depth in x_3 direction, shown in Fig. C.2.

C.2 2D problem

To simplify, a 2D surface propagation problem is proposed in plane $(x_1, 0, x_3)$ as $\psi = 0, \theta \approx \pi/2$, so that the wavenumbers $k_2 = 0, k_1 \neq 0$, see Fig. C.2. Thus, all elements

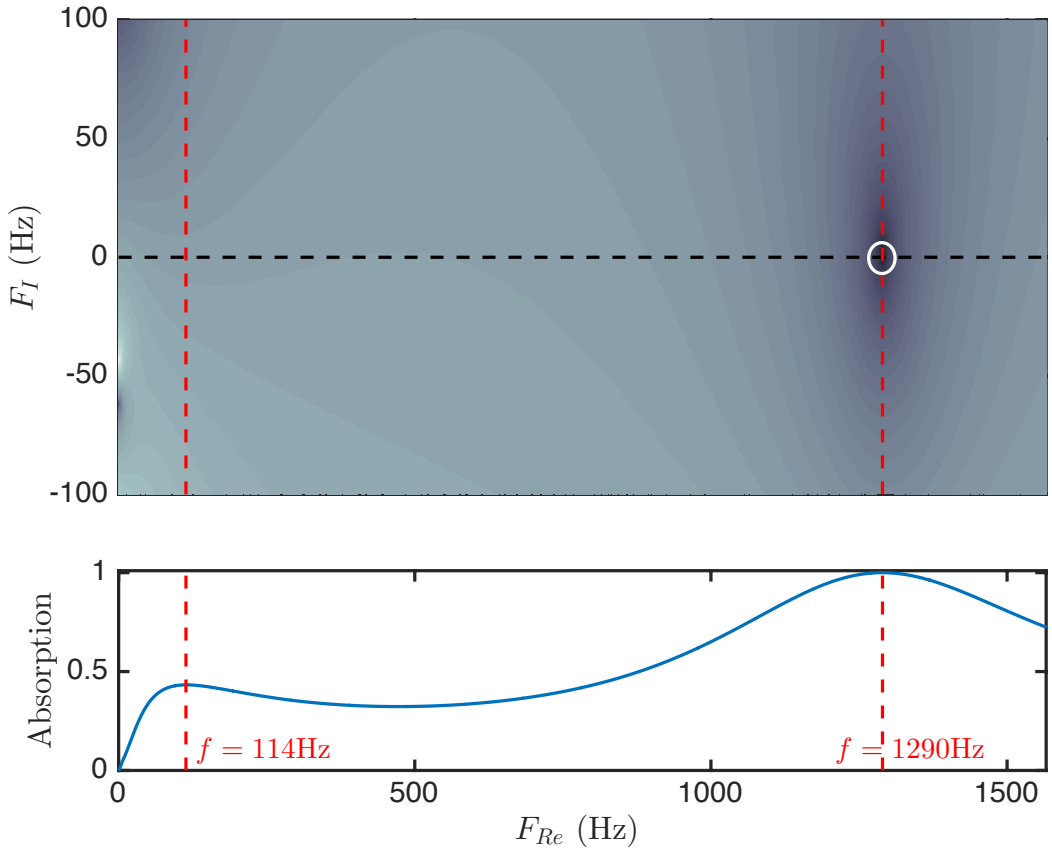

FIGURE C.1: Complex plane of $\ln|\ R\ |^2$ at $\theta = 87^o, \phi = 0$ with the corresponding absorption coefficient.

concerning the propagation simplifies accordingly,

$$\rho_{33} = \rho_{11} \ \Rightarrow\ H_{11}^* = \rho_{33}/\rho_{11} = 1, \tag{C.2.1a}$$

$$\Rightarrow\ \kappa(k_1) = \sqrt{k_{33}^2 - k_1^2} \tag{C.2.1b}$$

$$\sigma(k_1) = \frac{\rho_0 H_{33}\kappa(k_1)}{k_3^{(0)}(k_1)} = \frac{\rho_0}{\rho_{33}} \cdot \sqrt{\frac{k_{33}^2 - k_1^2}{k_0^2 - k_1^2}}. \tag{C.2.1c}$$

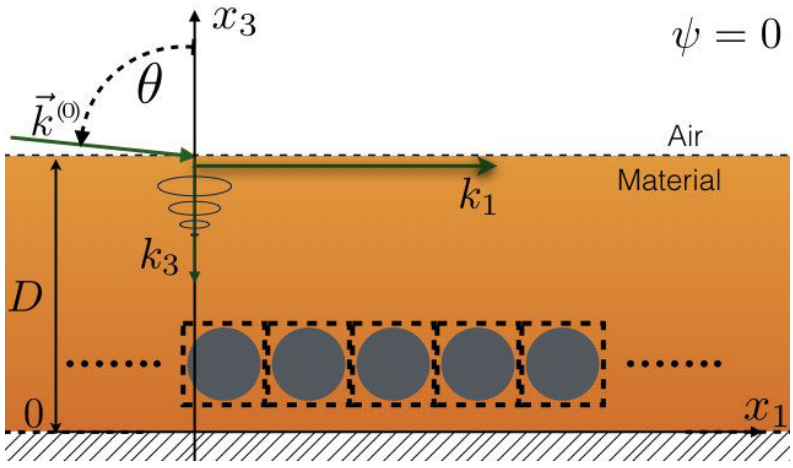

FIGURE C.2: Rigidly backed material layer representation: k_3 evanescent, tangential to the interface, k_1 propagating along the interface, solid array is positioned as shown, perpendicular to the k_1 direction.

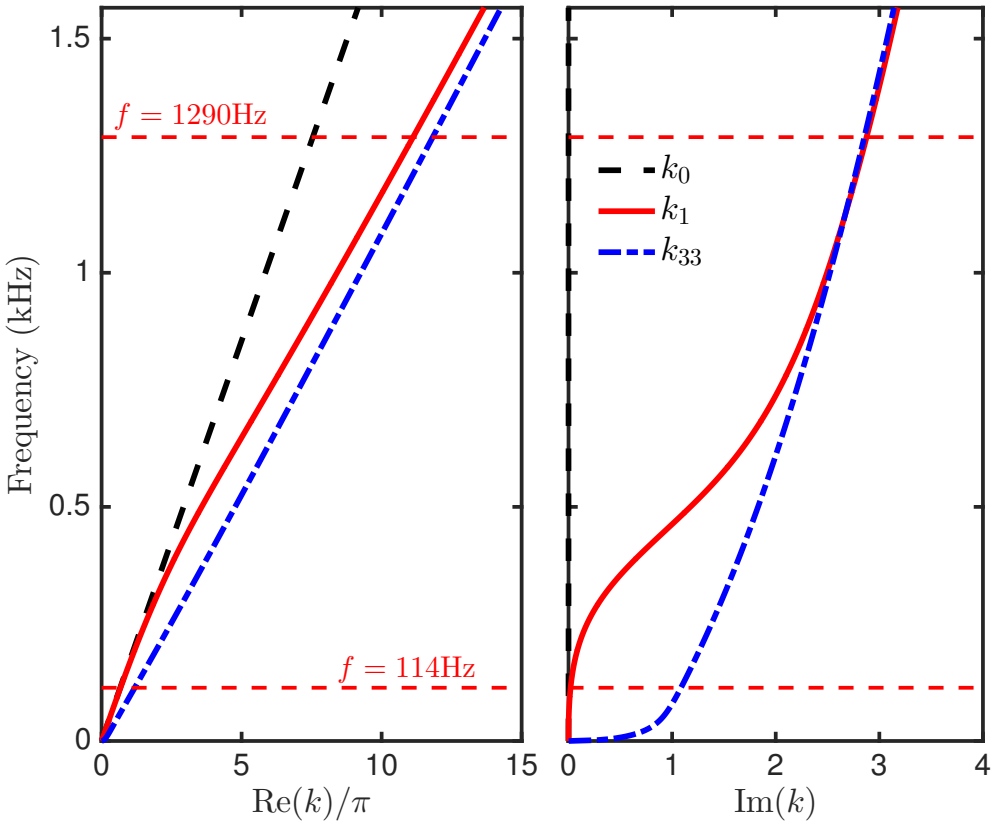

FIGURE C.3: Dispersion relations of the lowest frequency Love mode with various thickness $D = 110$ mm: a) Real part normalised by π; b) Corresponding imaginary part.

with $k_3^{(0)}(k_1) = \sqrt{k_0^2 - k_1^2}$ and $k_{33} = \sqrt{\omega^2/(BH_{33})}$.

A resolution of the denominator of the reflection coefficient is proposed, which gives out the dispersion relation of the lowest frequency Love mode in a rigidly-backed penetrable material layer [124],

$$\cos(\kappa(k_1)D) - i\sigma(k_1)\sin(\kappa(k_1)D) = 0. \tag{C.2.2}$$

Muller's method is applied to find the complex number solution of k_1. The result is shown in real and imaginary parts in Fig. C.3.

Appendix D

Natural Wheat Straw Bale

D.1 Introduction

An acoustic anisotropic metamaterial composed of natural straws is reported here for sound absorption. Natural wheat straws are harvest, cut, numbered and measured of their dimensions. Different configurations of straw stacks are tested in various impedance tube tests. Their visco-thermal parameters in different principal directions are retrieved by a Bayesian inversion method.

The measurements on the natural straw stacks show a perfect absorption at low frequency range which corresponds to a wavelength-to-width ratio of 9 times and an absorption plateau at higher frequencies. While, tests on the artificial straw-stack models with similar external porosity evidence a possible porous-skeleton resonance regime, responsible for the higher frequencies absorption plateau. Applications may concern sound absorption upon reflection, sound insulation for transmissions, and eco-friendly sound proofing material.

Many natural or natural-inspired materials with unconventional properties have emerged since the finding of natural metamaterials [31]. Natural straws as one of those materials have been utilized for thermal isolation for thousands of years worldwide. And acoustic panels made of natural straws are been well known as good candidates for sound absorption due to their air-flow resistivity [42]. The physics behind the idealized straw-like resonators stacks have revealed by the scale-separation techniques that the metamaterial with an anisotropic porous medium enriched by tailoring inner resonances induces multiple absorption peaks stemming from sub-wavelength Fabry-Perot interferences in the rigid-backed layer [125].

To further investigate into the real natural straw stack, we prepare natural straw samples with known dimensions to be tested by various impedance tubes tests, extract and simulate their visco-thermal parameters in different principal directions and the sound absorption results of natural and artificial straw stacks are compared with each other and possible theoretical predictions.

D.2 Preparation

Manually-harvested wheat straws are sun-dried, cut in the middle to expose their inner cavities, measured and numbered to determine their geometry. It is found out that the natural straw when cut in the middle of the stem forms a truncated cone shape with a slight declination angle, see Fig. D.1a). A total number of 98 straw sections are prepared

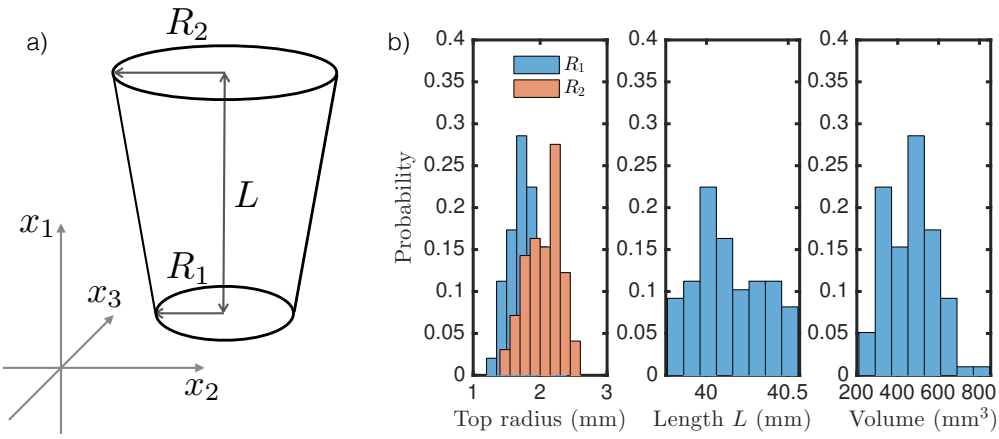

FIGURE D.1: Natural straws: a): Representation of the natural straw section; b): Histograms of the natural straw dimensions: Top radius R_1 and R_2, Length L and External volume of the truncated cone.

for further testing[1]. As natural straws are quite fragile, the numbering of the straws allows the damaged ones to be replaced by new sections with similar dimensions. Their dimensions are shown in Fig. D.1b).

As limited by the impedance tube, the length of the straw sections are cut to $L = 40$ mm $\pm$ 0.5 mm. The top radius of the truncated cones are centred around the mean values $\tilde{R}_1 = 1.76$ mm and $\tilde{R}_2 = 2.06$ mm. These mean dimensions will be used in the artificial straw stack design for 3D-printing. And the exterior volume can be calculated to later determine the theoretical external porosity of the straw stack.

D.3 Characterisation

In the first part, the prepared straws are plugged at both ends and then tested in the parallel direction (x_1) in an circular cross-section impedance tube. With the help of a Bayesian inversion algorithm [126], the visco-thermal parameters in parallel direction of the porous medium without the apparent quarter-wavelength resonances are extracted from the tests of the impedance tube in transmission regime.

As limited by the radius of the circular tube, only 49 straws can be tested, multiple tests are performed by randomising the configuration of the stack with the 98 straws.The mean-value result is presented here:

- the static permeability, intrinsic tortuosity and characteristic viscous length in parallel direction $K_{\parallel}^0 = 2420$ μm^2, $\tau_{\parallel}^{\infty} = 1.002$, and $\Lambda_{\parallel} = 0.114$ mm
- the static thermal permeability and characteristic thermal length $\Theta^0 = 2420$ μm^2 and $\Lambda_t = 1.89$ mm, with an external porosity $\phi = 0.351$.

The inversion method gives out valid and normal results, with exception of the thermal characteristic length Λ_t. It is an order of magnitude larger than the viscous characteristic length $\Lambda_{\parallel}$, whereas if the porous structure is indeed perfectly rigid and immobile, $\Lambda_{\parallel}$ should be equal to Λ_t. This drastic difference implies that the natural straw composed

[1] The authors are grateful to E. GOUEROU and C. MACH for their work during the preparation of this work.

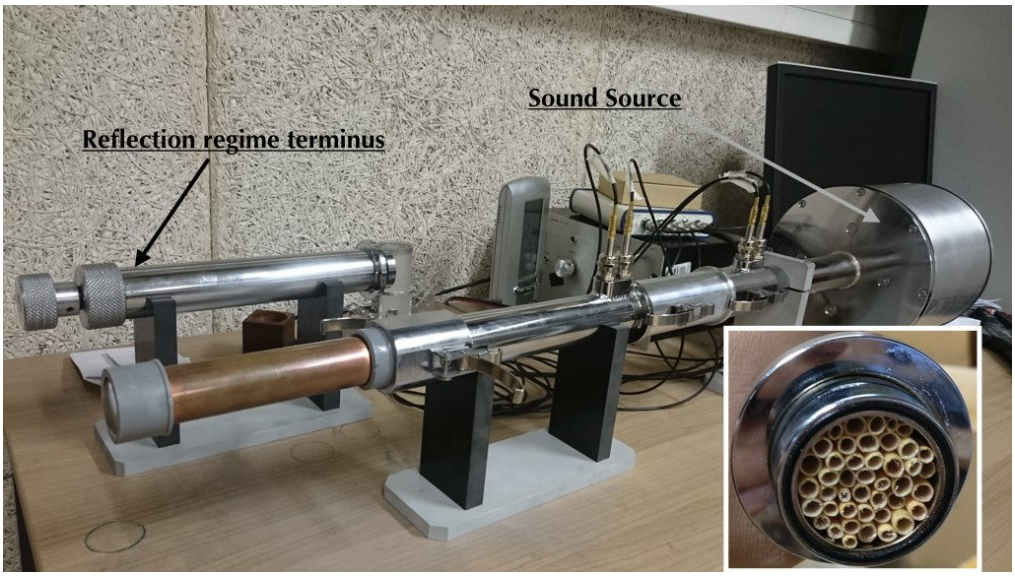

FIGURE D.2: Photo of the impedance tube used for the determination of the visco-thermal parameters, radius 30 mm, cut-off frequency 6.5 kHz, with a view of straw composition in the tube

material is not just a simple and ordinary porous medium and the straw stems should not be considered as perfectly rigid and immobile.

Similar to the added apparent-tube-resonance's effect on the effective bulk modulus in [125], the enlarged thermal characteristic length Λ_t and consequently-modified effective bulk modulus could indicate an extra resonance regime in lower and middle frequencies range, as the tube opening and the associated resonance are already eliminated by plugging the straws. This extra resonance regime may be the porous-skeleton resonance, as the whole structure is no longer considered immobile.

D.4 Experimental tests

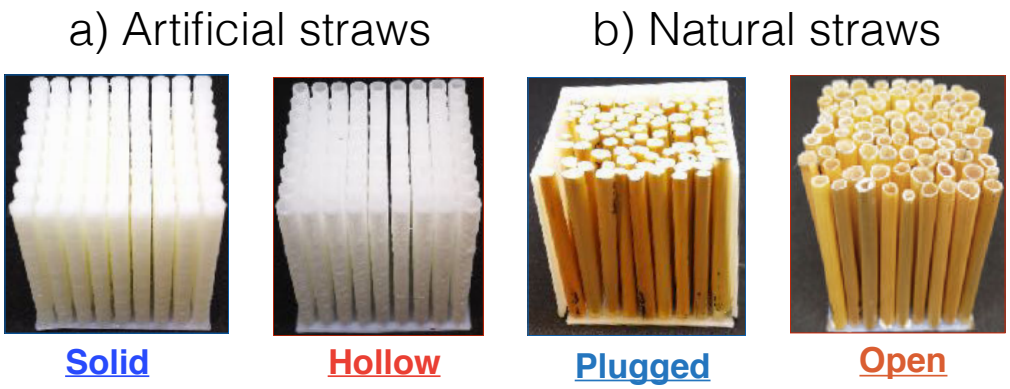

FIGURE D.3: Photos of the test samples: a) Artificial straws: Solid and Hollow and b) Natural straws: Plugged and Open.

In the second part, the straws are mounted onto the plastic support casing in a 9 by 9 square periodic arrangement, which limits the effective material space to a cube of 41

mm high by 40 mm by 40 mm wide. A figurative gap of 1 mm remains over the top of the straws. The straws are all plugged or empty for either configuration. Also two 3D-printed artificial models as mentioned in the earlier paragraph are manufactured as control group samples, one with hollow cones to mimic open straws, one with solid cones to mimic plugged straws. The photos of the 4 configurations are shown in Fig. D.3.

All four configuration are tested in perpendicular direction (x_2 and x_3) in a square cross-section impedance tube (42 by 42 mm). For natural straw samples, a necessary number of tests are performed to eliminate random effects from different incident directions (x_2 and x_3) or straw compositions (similar but different external porosity). The mean value of the test results are taken as the final results for natural straws cases.

In Fig. D.4a), the experimental results of absorption coefficient from the arrays of hollow and solid cones are compared with their respective theoretical predictions. In the artificial straws cases, the solid array gives an absorption corresponding to the usual quarter-wavelength resonance of a porous layer which is in good agreement with the theoretical one.

While the inner resonance of the hollow cones in the metamaterial only gives rise to a single absorption peak at 1.3 kHz and a gradually-rising higher frequencies range absorption plateau and no band-gap around the hollow cone's resonance frequency, rather than the multiple peaks and band-gap behavior predicted by the theoretical model. But the slow sound effect on the first resonance peak's frequency [75] is still clearly identified.

In Fig. D.4b), the experimental results of absorption coefficient are compared between the plugged and empty natural straw stacks cases. The measurements show greater absorption at lower frequencies than the artificial cases. A near-perfect absorption is observed for the plugged case, and a perfect absorption for the empty case, at low frequency of which the wavelength corresponds to 9 times of the effective material thickness.

No obvious slow sound effect is observed as the absorption peaks in the two case has almost identical frequencies, but the two cases differ in the frequencies surrounding the theoretical resonance frequencies of the natural straws. This could be an indication that the missing band-gap brought by the slow sound effect may be compensated by the porous-skeleton resonance regime, for the two regimes cohabit at the same frequency range.

A similar retrieval of the visco-thermal parameter is done with the Bayesian inversion method by combing the thermal data from the previous parallel direction test, which gives out the the viscous parameters in perpendicular direction for the plugged case: $K_\perp^0 = 605\ \mu\text{m}^2$, $\tau_\perp^\infty = 2.6$, $\Lambda_\perp = 0.78$ mm.

D.5 Conclusion

An acoustic anisotropic metamaterial composed of natural straws has shown interesting properties from the sound absorption viewpoint, particularly in comparison with the idealized rigid-frame straw-like resonators array.

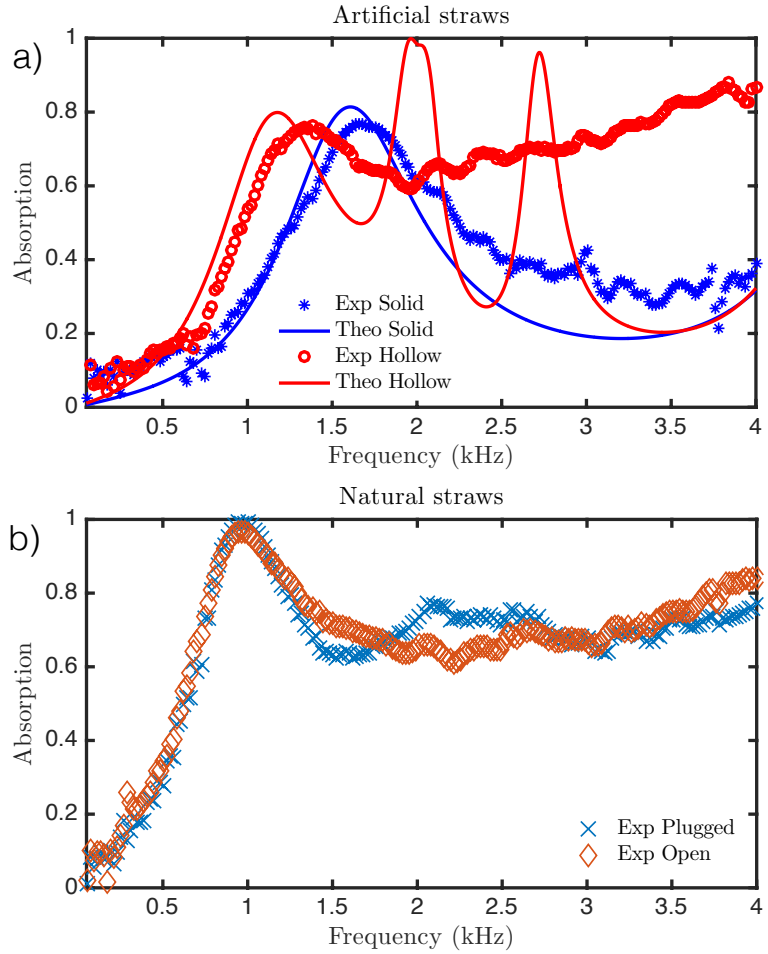

FIGURE D.4: Absorption coefficient for stacks: a) Comparison between solid and hollow artificial straws and their respective theoretical prediction; b) Experimental results of the plugged and open natural straws.

In particular, a vibratory porous-skeleton resonance regime is speculated to cohabit with the apparent unconventionally-negative compressibility and the associated slow-sound physics. This gives ways to the possibility to critically-couple the different scales to produce near-total or perfect sound absorption at low frequencies (perfect and near-total absorptions at 963 Hz observed in Fig. D.4b) for the natural straw cases).

Here, the characterisation process for different principal directions of the effective material well presents the anisotropy of the model, which could motivate studies on orientation-selective absorption based on bio-inspired acoustic metamaterials.

Bibliography

[1] B. Berglund et al. *Guidelines for community noise*. Stockholm University and Karolinska Institute, 1999.

[2] M. Basner and S. McGuire. "WHO Environmental Noise Guidelines for the European Region: A Systematic Review on Environmental Noise and Effects on Sleep". In: *International journal of environmental research and public health* 15.3 (2018), p. 519.

[3] L. Goines, L. Hagler, et al. "Noise pollution: a modern plague". In: *Southern Medical Journal-Birmingham Alabama* 100.3 (2007), p. 287.

[4] M. Basner et al. "Auditory and non-auditory effects of noise on health". In: *The lancet* 383.9925 (2014), pp. 1325–1332.

[5] A. Gidlöf-Gunnarsson and E. Öhrström. "Noise and well-being in urban residential environments: The potential role of perceived availability to nearby green areas". In: *Landscape and urban planning* 83.2 (2007), pp. 115–126.

[6] S. Stansfeld et al. "Noise and health in the urban environment". In: *Reviews on environmental health* 15.1-2 (2000), pp. 43–82.

[7] D. L. Johnson et al. "Theory of dynamic permeability and tortuosity in fluid-saturated porous media". In: *Journal of Fluid Mechanics* 176 (1987), pp. 379–402.

[8] Y. Champoux and J.-F. Allard. "Dynamic tortuosity and bulk modulus in air-saturated porous media". In: *Journal of Applied Physics* 70 (1991), pp. 1975–1979.

[9] J.-F. Allard and N. Atalla. *Propagation of sound in porous media: modelling sound absorbing materials 2e*. John Wiley & Sons, 2009.

[10] D. Lafarge et al. "Dynamic compressibility of air in porous structures at audible frequencies". In: *The Journal of the Acoustical Society of America* 102.4 (1997), pp. 1995–2006.

[11] C. Zwikker and C. W. Kosten. *Sound absorbing materials*. Elsevier, 1949.

[12] M. A. Biot. "Theory of propagation of elastic waves in a fluid-saturated porous solid. I. Low-frequency range". In: *The Journal of the acoustical Society of America* 28.2 (1956), pp. 168–178.

[13] M. A. Biot. "Theory of propagation of elastic waves in a fluid-saturated porous solid. II. Higher frequency range". In: *The Journal of the acoustical Society of america* 28.2 (1956), pp. 179–191.

[14] J. Siemiatycki et al. "Listing occupational carcinogens". In: *Environmental health perspectives* 112.15 (2004), p. 1447.

[15] *Man-made mineral fibres and radon*. Tech. rep. IARC Working Group on the Evaluation of Carcinogenic Risks to Humans, International Agency for Research on Cancer, and World Health Organization, 1988.

[16] *Man-made vitreous fibres*. Tech. rep. IARC Working Group on the Evaluation of Carcinogenic Risks to Humans, International Agency for Research on Cancer, and World Health Organization, 2002.

[17] M. Yang and P. Sheng. "Sound absorption structures: From porous media to acoustic metamaterials". In: *Annual Review of Materials Research* 47 (2017), pp. 83–114.

[18] J. Mei et al. "Dark acoustic metamaterials as super absorbers for low-frequency sound". In: *Nature Communications* 3 (2012), p. 756.

[19] G. Ma et al. "Acoustic metasurface with hybrid resonances". In: *Nature Materials* 13.9 (2014), pp. 873–878.

[20] X. Cai et al. "Ultrathin low-frequency sound absorbing panels based on coplanar spiral tubes or coplanar Helmholtz resonators". In: *Applied Physics Letters* 105.12 (2014), p. 121901.

[21] Y. Li and B. M. Assouar. "Acoustic metasurface-based perfect absorber with deep subwavelength thickness". In: *Applied Physics Letters* 108.6 (2016), p. 063502.

[22] C Lagarrigue et al. "Design of metaporous supercells by genetic algorithm for absorption optimization on a wide frequency band". In: *Applied Acoustics* 102 (2016), pp. 49–54.

[23] J.-P. Groby et al. "Acoustic response of a periodic distribution of macroscopic inclusions within a rigid frame porous plate". In: *Waves in Random and Complex Media* 18.3 (2008), pp. 409–433.

[24] C. Lagarrigue et al. "Absorption of sound by porous layers with embedded periodic arrays of resonant inclusions". In: *The Journal of the Acoustical Society of America* 134.6 (2013), pp. 4670–4680.

[25] A. Derode et al. "Robust acoustic time reversal with high-order multiple scattering". In: *Physical Review Letters* 75.23 (1995), p. 4206.

[26] M. Law et al. "Nanowire dye-sensitized solar cells". In: *Nature Materials* 4.6 (2005), pp. 455–459.

[27] Y. Chong et al. "Coherent perfect absorbers: time-reversed lasers". In: *Physical Review Letters* 105.5 (2010), p. 053901.

[28] A. Yariv. "Universal relations for coupling of optical power between microresonators and dielectric waveguides". In: *Electronics letters* 36.4 (2000), pp. 321–322.

[29] Y. Xu et al. "Scattering-theory analysis of waveguide-resonator coupling". In: *Physical Review E* 62.5 (2000), p. 7389.

[30] K. Y. Bliokh et al. "Colloquium: Unusual resonators: Plasmonics, metamaterials, and random media". In: *Reviews of Modern Physics* 80.4 (2008), p. 1201.

[31] P. Vukusic and J. R. Sambles. "Photonic structures in biology". In: *Nature* 424.6950 (2003), pp. 852–855.

[32] N. Jiménez et al. "Ultra-thin metamaterial for perfect and quasi-omnidirectional sound absorption". In: *Applied Physics Letters* 109.12 (2016), p. 121902.

[33] M. A. Meyers et al. "Biological materials: structure and mechanical properties". In: *Progress in Materials Science* 53.1 (2008), pp. 1–206.

[34] M. Miniaci et al. "Spider web-inspired acoustic metamaterials". In: *Applied Physics Letters* 109.7 (2016), p. 071905.

[35] Y. Cui et al. "A Thermally Insulating Textile Inspired by Polar Bear Hair". In: *Advanced Materials* 30.14 (2018), p. 1706807.

[36] D. Jones and D. Brischke, eds. *Performance of Bio-based Building Materials*. 1st ed. WoodHead Publishing, Elsevier, 2017.

[37] D. J. Oldham et al. "Sustainable acoustic absorbers from the biomass". In: *Applied Acoustics* 72.6 (2011), pp. 350–363.

[38] F. Asdrubali et al. "Sound absorption properties of reed". In: *Proceedings of the 22nd International Congress on Sound and Vibration, Florence, Italy2015*. 2015.

[39] H. Benkreira et al. "Sustainable acoustic and thermal insulation materials from elastomeric waste residues". In: *Chemical Engineering Science* 66.18 (2011), pp. 4157–4171.

[40] D. Aylor. "Sound transmission through vegetation in relation to leaf area density, leaf width, and breadth of canopy". In: *The Journal of the Acoustical Society of America* 51.1B (1972), pp. 411–414.

[41] M. Delany and E. Bazley. "Acoustical properties of fibrous absorbent materials". In: *Applied acoustics* 3.2 (1970), pp. 105–116.

[42] F. Asdrubali et al. "A review of sustainable materials for acoustic applications". In: *Building Acoustics* 19.4 (2012), pp. 283–311.

[43] R. G. Venegas Castillo. "Microstructure influence on acoustical properties of multi-scale porous materials". PhD thesis. Salford: University of Salford, 2011.

[44] B. Berge. *The ecology of building materials*. Routledge, 2009.

[45] R. Dalmeijer. "Straw bale sound insulation and acoustics". In: *The Last Straw, The International Journal of Straw Bale and Natural Building* 53.8 (2006).

[46] F. d'Alessandro et al. "Straw bale constructions: Laboratory, in field and numerical assessment of energy and environmental performance". In: *Journal of Building Engineering* 11 (2017), pp. 56–68.

[47] S. Goodhew et al. "Briefing: Challenges related to straw bale construction". In: *Proceedings of the Institution of Civil Engineers - Engineering Sustainability* 163.4 (2010), pp. 185–189.

[48] K. Wall et al. "Development and testing of a prototype straw bale house". In: *Proceedings of the Institution of Civil Engineers-Construction Materials* 165.6 (2012), pp. 377–384.

[49] S. H. Harper and J. M. Lynch. "The chemical components and decomposition of wheat straw leaves, internodes and nodes". In: *Journal of the Science of Food and Agriculture* 32.11 (1981), pp. 1057–1062.

[50] E. S. Palencia. *Non-homogeneous media and vibration theory*. Springer-Verlag, 1980.

[51] J.-L. Auriault et al. *Homogenization of coupled phenomena in heterogenous media*. Vol. 149. John Wiley & Sons, 2010.

[52] C. Boutin. "Acoustics of porous media with inner resonators". In: *The Journal of the Acoustical Society of America* 134.6 (2013), pp. 4717–4729.

[53] L. V. Hau et al. "Light speed reduction to 17 metres per second in an ultracold atomic gas". In: *Nature* 397.6720 (1999), pp. 594–598.

[54] A. Santillán and S. I. Bozhevolnyi. "Acoustic transparency and slow sound using detuned acoustic resonators". In: *Physical Review B* 84.6 (2011), p. 064304.

[55] G. Yu and X. Wang. "Acoustical "transparency" induced by local resonance in Bragg bandgaps". In: *Journal of Applied Physics* 115 (2014), p. 044913.

[56] G. Theocharis et al. “Limits of slow sound propagation and transparency in lossy, locally resonant periodic structures”. In: *New Journal of Physics* 16.9 (2014), p. 093017.

[57] A. Cicek et al. “Slow sound propagation in a sonic crystla linear wavegauide”. In: *Journal of Applied Physics* 111 (2012), p. 013522.

[58] M.-H. Lu et al. “Phononic crystals and acoustic metamaterials”. In: *Materials today* 12.12 (2009), pp. 34–42.

[59] Y. Auregan et al. “Acoustical behaviour of purely reacting liners”. In: *19th AIAA/CEAS Aeroacoustics Conference*. 2013, p. 2077.

[60] Y. Auregan and V. Pagneux. “Slow sound in lined flow ducts”. In: *The Journal of the Acoustical Society of America* 138.2 (2015), pp. 605–613.

[61] M. R. Stinson. “The propagation of plane sound waves in narrow and wide circular tubes, and generalization to uniform tubes of arbitrary cross-sectional shape”. In: *The Journal of the Acoustical Society of America* 89.2 (1991), pp. 550–558.

[62] N Sugimoto and T Horioka. “Dispersion characteristics of sound waves in a tunnel with an array of Helmholtz resonators”. In: *The Journal of the Acoustical Society of America* 97.3 (1995), pp. 1446–1459.

[63] C. Bradley. “Time harmonic acoustic Bloch wave propagation in periodic waveguides. Part I. Theory”. In: *The Journal of the Acoustical Society of America* 96.3 (1994), pp. 1844–1853.

[64] E. Redon et al. “Non-reflecting boundary conditions for acoustic propagation in ducts with acoustic treatment and mean flow”. In: *Int. J. Numer. Meth. Engng.* 86 (2011), pp. 1360–1378.

[65] D. Muller. “A method for solving algebraic equations using an automatic computer”. In: *Mathematical Tables and Other Aids to Computation* 10 (1956), pp. 208–215.

[66] P. Drude. “Transparent isotropic media”. In: *Wied. Ann* 43 (1891), p. 146.

[67] C. Simovski. “On electromagnetic characterization and homogenization of nanostructured metamaterials”. In: *Journal of Optics* 12 (2011), p. 013001.

[68] N. Fang et al. “Ultrasonic metamaterials with negative modulus”. In: *Nature Materials* 5.6 (2006), p. 452.

[69] J. Groby et al. “Acoustic response of a rigid-frame porous medium plate with a periodic set of inclusions”. In: *The Journal of the Acoustical Society of America* 126 (2009), pp. 685–693.

[70] J.-P. Groby et al. “Total absorption peak by use of a rigid frame porous layer backed by a rigid multi-irregularities grating”. In: *The Journal of the Acoustical Society of America* 127.5 (2010), pp. 2865–2874.

[71] G. Ma and P. Sheng. “Acoustic metamaterials: From local resonances to broad horizons”. In: *Science Advances* 2.2 (2016), e1501595.

[72] Z. Yang et al. “Membrane-type acoustic metamaterial with negative dynamic mass”. In: *Physical Review Letters* 101.20 (2008), p. 204301.

[73] A. Merkel et al. “Control of acoustic absorption in one-dimensional scattering by resonant scatterers”. In: *Applied Physics Letters* 107.24 (2015), p. 244102.

[74] V. Achilleos et al. “Coherent perfect absorption induced by the nonlinearity of a Helmholtz resonator”. In: *The Journal of the Acoustical Society of America* 140.1 (2016), EL94–EL100.

[75] J.-P. Groby et al. "The use of slow waves to design simple sound absorbing materials". In: *Journal of Applied Physics* 117.12 (2015), p. 124903.

[76] P. Leclaire et al. "Acoustical properties of air-saturated porous material with periodically distributed dead-end poresa)". In: *The Journal of the Acoustical Society of America* 137.4 (2015), pp. 1772–1782.

[77] J.-P. Groby et al. "Use of slow sound to design perfect and broadband passive sound absorbing materials". In: *The Journal of the Acoustical Society of America* 139.4 (2016), pp. 1660–1671.

[78] J.-P. Dalmont et al. "Radiation impedance of tubes with different flanges: numerical and experimental investigations". In: *Journal of Sound and Vibration* 244.3 (2001), pp. 505–534.

[79] J. Kergomard and A. Garcia. "Simple discontinuities in acoustic waveguides at low frequencies: critical analysis and formulae". In: *Journal of Sound and Vibration* 114.3 (1987), pp. 465–479.

[80] V. Dubos et al. "Theory of sound propagation in a duct with a branched tube using modal decomposition". In: *Acta Acustica united with Acustica* 85.2 (1999), pp. 153–169.

[81] F. P. Mechel. *Formulas of acoustics, 2nd ed.* Ed. by H. Springer-Verlag Berlin. Springer Science & Business Media, 2008, pp. 316–327.

[82] V. Romero-García et al. "Use of complex frequency plane to design broadband and sub-wavelength absorbers". In: *The Journal of the Acoustical Society of America* 139.6 (2016), pp. 3395–3403.

[83] J. R. Piper et al. "Total absorption by degenerate critical coupling". In: *Applied Physics Letters* 104.25 (2014), p. 251110.

[84] M. Yang et al. "Subwavelength total acoustic absorption with degenerate resonators". In: *Applied Physics Letters* 107.10 (2015), p. 104104.

[85] V. Romero-García et al. "Perfect and broadband acoustic absorption by critically coupled sub-wavelength resonators". In: *Scientific reports* 6 (2016), p. 19519.

[86] V. Pagneux. "Trapped modes and edge resonances in acoustics and elasticity". In: *Dynamic Localization Phenomena in Elasticity, Acoustics and Electromagnetism.* Springer, 2013, pp. 181–223.

[87] M. J. Powell. "A fast algorithm for nonlinearly constrained optimization calculations". In: *Numerical Analysis.* Springer, 1978, pp. 144–157.

[88] T. J. Cox and P. D'antonio. *Acoustic absorbers and diffusers: theory, design and application.* CRC Press, 2009.

[89] N. Jiménez et al. "Perfect Absorption of Sound by Rigidly-Backed High-Porous Materials". In: *Acta Acustica united with Acustica* 104.3 (2018), pp. 396–409.

[90] Y. Wang et al. "A space-coiled acoustic metamaterial with tunable low-frequency sound absorption". In: *EPL (Europhysics Letters)* 120.5 (2018), p. 54001.

[91] N. Jiménez et al. "Metadiffusers: Deep-subwavelength sound diffusers". In: *Scientific reports* 7.1 (2017), p. 5389.

[92] H. Darcy. *Les fontaines publiques de la ville de Dijon: exposition et application...* (French). Victor Dalmont, 1856.

[93] J.-L. Auriault and E Sanchez-Palencia. "Étude du comportement macroscopique d'un milieu poreux saturé déformable". (French). In: *Journal de mécanique* 16.4 (1977), pp. 575–603.

[94] J.-L. Auriault et al. "Dynamics of porous saturated media, checking of the generalized law of Darcy". In: *The Journal of the Acoustical Society of America* 77.5 (1985), pp. 1641–1650.

[95] M.-Y. Zhou and P. Sheng. "First-principles calculations of dynamic permeability in porous media". In: *Physical Review B* 39.16 (1989), p. 12027.

[96] C. Boutin and F. X. Becot. "Theory and experiments on poro-acoustics with inner resonators". In: *Wave Motion* 54 (2015), pp. 76–99.

[97] R. Venegas and C. Boutin. "Acoustics of permeo-elastic materials". In: *Journal of Fluid Mechanics* 828 (2017), pp. 135–174.

[98] P. D. Lax and A. N. Milgram. "Contributions to the theory of partial differential equations". In: Annals of Mathematics Studies 33. Princeton University Press, 1954. Chap. IX. Parabolic Equations.

[99] G. W. Milton and J. R. Willis. "On modifications of Newton's second law and linear continuum elastodynamics". In: *Proceedings of the royal society of london A: Mathematical, Physical and Engineering Sciences*. Vol. 463. 2079. The Royal Society. 2007, pp. 855–880.

[100] S. R. Pride et al. "Deriving the equations of motion for porous isotropic media". In: *The Journal of the Acoustical Society of America* 92.6 (1992), pp. 3278–3290.

[101] J. Auriault and C Boutin. "Deformable porous media with double porosity. Quasi-statics. I: Coupling effects". In: *Transport in porous media* 7.1 (1992), pp. 63–82.

[102] J. Auriault and C Boutin. "Deformable porous media with double porosity III: Acoustics". In: *Transport in porous media* 14.2 (1994), pp. 143–162.

[103] X. Olny and C. Boutin. "Acoustic wave propagation in double porosity media". In: *The Journal of the Acoustical Society of America* 114 (2003), pp. 73–84.

[104] F. Chevillotte et al. "Microstructure based model for sound absorption predictions of perforated closed-cell metallic foams". In: *The Journal of the Acoustical Society of America* 128.4 (2010), pp. 1766–1776.

[105] P Glé et al. "Acoustical properties of materials made of vegetable particles with several scales of porosity". In: *Applied Acoustics* 72.5 (2011), pp. 249–259.

[106] R. Venegas and O. Umnova. "Acoustical properties of double porosity granular materials". In: *The Journal of the Acoustical Society of America* 130.5 (2011), pp. 2765–2776.

[107] S. Yang et al. "Focusing of sound in a 3D phononic crystal". In: *Physical Review Letters* 93.2 (2004), p. 024301.

[108] A. Khelif et al. "Guiding and bending of acoustic waves in highly confined phononic crystal waveguides". In: *Applied Physics Letters* 84.22 (2004), pp. 4400–4402.

[109] S. Benchabane et al. "Evidence for complete surface wave band gap in a piezoelectric phononic crystal". In: *Physical Review E* 73.6 (2006), p. 065601.

[110] C. Lagarrigue et al. "Sustainable sonic crystal made of resonating bamboo rods". In: *The Journal of the Acoustical Society of America* 133.1 (2013), pp. 247–254.

[111] A. Lardeau et al. "Broadband transmission loss using the overlap of resonances in 3D sonic crystals". In: *Crystals* 6.5 (2016), p. 51.

[112] J. Sánchez-Dehesa et al. "Noise control by sonic crystal barriers made of recycled materials". In: *The Journal of the Acoustical Society of America* 129.3 (2011), pp. 1173–1183.

[113] J. Christensen et al. "Extraordinary absorption of sound in porous lamella-crystals". In: *Scientific reports* 4 (2014), p. 4674.

[114] J. Christensen and F. J. G. de Abajo. "Anisotropic metamaterials for full control of acoustic waves". In: *Physical review letters* 108.12 (2012), p. 124301.

[115] Y. Chen et al. "Enhanced acoustic sensing through wave compression and pressure amplification in anisotropic metamaterials". In: *Nature communications* 5 (2014), p. 5247.

[116] M. Kadic et al. "On the practicability of pentamode mechanical metamaterials". In: *Applied Physics Letters* 100.19 (2012), p. 191901.

[117] Y. Cui et al. "Ultrabroadband light absorption by a sawtooth anisotropic metamaterial slab". In: *Nano letters* 12.3 (2012), pp. 1443–1447.

[118] M. Islam et al. "Direct measurement of the polarized optical absorption cross section of single-wall carbon nanotubes". In: *Physical Review Letters* 93.3 (2004), p. 037404.

[119] U. Ingard. *Noise Reduction Analysis (Physics)*. Jones & Bartlett Publishers, 2010.

[120] N. Jiménez et al. "Rainbow-trapping absorbers: Broadband, perfect and asymmetric sound absorption by subwavelength panels for transmission problems". In: *Scientific Reports* 7.1 (2017), p. 13595.

[121] L. Schwan et al. "Complex dispersion relation of surface acoustic waves at a lossy metasurface". In: *Applied Physics Letters* 110.5 (2017), p. 051902.

[122] G. Ma et al. "Shaping reverberating sound fields with an actively tunable metasurface". In: *Proceedings of the National Academy of Sciences* (2018), p. 201801175.

[123] B. H. Song and J. S. Bolton. "A transfer-matrix approach for estimating the characteristic impedance and wave numbers of limp and rigid porous materials". In: *The Journal of the Acoustical Society of America* 107.3 (2000), pp. 1131–1152.

[124] J.-P. Groby. "Modélisation de la propagation des ondes élastiques générées par un séisme proche ou éloigné à l'intérieur d'une ville". PhD thesis. Université de la Méditerranée-Aix-Marseille II, 2005.

[125] W. Huang et al. "3D-printed straw-inspired metamaterial for sound absorption". In: *2017 11th International Congress on Engineered Materials Platforms for Novel Wave Phenomena (Metamaterials)*. 2017, pp. 157–159.

[126] M. Niskanen et al. "Deterministic and statistical characterization of rigid frame porous materials from impedance tube measurements". In: *The Journal of the Acoustical Society of America* 142.4 (2017), pp. 2407–2418.

UNIVERSITE BRETAGNE SCIENCES LOIRE POUR L'INGENIEUR

Le Mans Université

Titre : Propriétés acoustiques des Matériaux Naturels

Mots clés : Métamatériaux bio-inspirés, Anisotropie, Couplage critique, Absorption parfaite

Résumé : Dans cette thèse, nous étudions un métamatériau inspiré de la paille de blé pour l'absorption parfaite du son. Une botte de paille est idéalisée comme un milieu poreux anisotrope, composé d'un arrangement périodique très concentré de tubes creux cylindriques. L'approche théorique de ce métamatériau repose sur l'homogénéisation asymptotique à deux échelles d'un réseau perméable de résonateurs parfaitement rigides dont la physique est enrichie par des résonances internes. Les principales caractéristiques de ce milieu poreux sont la compressibilité effective négative autour de la résonance du tube et la réduction drastique de la vitesse de propagation du son (slow sound) à très basse fréquence. Une configuration optimale est conçue, basée sur la condition de couplage critique, pour laquelle la fuite d'énergie du système résonnant ouvert est parfaitement compensée par les pertes intrinsèques induites par les pertes visco-thermiques. Des mesures en tube à impédance sont effectuées sur des échantillons fabriqués par impression additive pour valider les résultats théoriques. Nous montrons que ce métamatériau est un absorbeur sub-longueur d'onde capable d'une absorption parfaite à très basse fréquence et d'introduire une quasi-bande interdite autour de la résonance du tube. De plus, la nature anisotrope de ce matériau conduit à une absorption globalement élevée à basse fréquence et ce pour toutes les incidences. Cette étude offre la possibilité de concevoir un absorbeur acoustique sélectif en angle et en fréquence. Pour conclure, les résultats de cette thèse montrent que la paille est un bon candidat pour une absorption acoustique parfaite, pouvant être performant dans le cadre de constructions durables et respectueuses de l'environnement.

Title: Acoustic properties of natural materials

Keywords: Bio-inspired metamaterial, Anisotropy, Critical coupling, Perfect absorption

Abstract: Straw-inspired metamaterials for sound absorption are investigated in this Thesis. A straw stack is idealized as a highly concentrated resonant anisotropic porous medium constituted of a periodic arrangement of densely packed cylindrical hollow tubes. The approach to this metamaterial relies on the two-scale asymptotic homogenization of a permeable array of perfectly rigid resonators, where the physics is further enriched by tailoring inner resonances. The main features of such sound absorbing medium are the possibility for the effective compressibility to become negative around the tube resonance and the drastic reduction of the effective sound speed (slow sound) at very low frequency in the system. Moreover, an optimal configuration for sound absorption is designed, based on the critical coupling condition, in which the energy leakage out of the open resonant system is perfectly compensated by the intrinsic losses induced by the visco-thermal losses both in the anisotropic matrix and in the resonators. Impedance tube measurements are performed on 3-D printed samples with controlled parameters to validate the theoretical results. This metamaterial is a sub-wavelength absorber that can achieve total absorption at a very low frequency and possesses a quasi-band-gap around the tube resonance. Furthermore, the anisotropic nature of the configuration gives rise to high absorption at low-frequency range for all incidences and diffuse field excitation. It paves the way to the design of angular and frequency selective sound absorber. To conclude, the results of this Thesis show that straw is a good candidate for perfect sound absorption as well as eco-friendly sustainable building materials.